A Study of Dusty Plasma Environment

Abul Khair Anuar, M.Eng.(UKM),

Submitted for the degree of Doctor of Philosophy

at Lancaster University,

February 2013.

Abstract

A Study of Dusty Plasma Environment

Abul Khair Anuar, M.Eng.(UKM)

Submitted for the degree of Doctor of Philosophy

February 2013

Future space explorations emphasize the need to understand the space environment in particular the effect they pose on crews and space-bound vehicles. One of such environment is the dusty plasma environment, where fine particles can be found in abundance. Dust particles interact with space plasma, get charged and are susceptible to the governing forces, hence are an important hazard to the space mission. This presents a challenge to accurately model the dust-plasma environment in order to predict and prepare crews and equipment for the harsh conditions.

This thesis makes three specific contributions. Firstly, the design and development of the dust module in Spacecraft Plasma Interaction System (SPIS) as well as the validation process involved. The software is then used to study plasma behaviour and spacecraft charging in the vicinity of dust particles. Results presented shows the capability of the software to model the dust charging process

and offers new observation on plasma properties in the vicinity of dust particles.

The second contribution of this thesis is on the study of lunar surface charging and dust dynamics. Several simulations have been performed to investigate the lunar surface charging and the effects on dust dynamics, especially on dust transport on lunar surface. The results of this investigation undertaking dust motion on various type of surface topography and various solar wind and solar UV flux condition, suggest strong correlation between dust motion and surface potential, hence confirming previous studies. In addition, simulation results indicate the minimum dust charge to mass ratio for possible levitation to take place which has not been previously reported.

Thirdly, several simulations are performed to investigate dust motion near space vehicle on lunar surface. Simulation reveals that the dust motion around the vehicle in the terminator and dayside exhibit distinguishable structures that has not been reported before.

Declaration

The material presented in this thesis is the result of my own work and has not been produced as a result of collaborations, except where specifically indicated. The material has not been submitted in substantially the same form for the award of a higher degree elsewhere.

Some of the material presented in this thesis has been , or in the process of being, published in journals (Anuar, Honary, Hapgood, Roussel 2013; Anuar, Farideh 2013).

Abul Khair Anuar

Farideh Honary

Acknowledgements

I would like to thank Allah for His guidance and for providing me with the will and good health to complete this work.

This dissertation would not have been possible without the help and guidance of my supervisor Farideh Honary, who never seems tired of teaching me, correcting me and providing me with ideas to move forward. Thank you for giving me the opportunity to do my thesis and supporting me all the way. Also to Mike Hapgood, who are full of ideas and guidance.

Jean-F Roussel and Jean Charles Mateo-Valez for the support and help they gave to me in writing the code. Also for their hospitality during my stay in Toulouse, France. I would have spent ages in a maze of codes if not for the training they provided.

The staffs and fellow students in the Space Plasma Environment and Radio Science (SPEARS) group, in particular to Matthew Beharrell who has been there almost every night in the office, providing me with company during my stay in Lancaster. The support and friendship of all members of the SPEARS group in encouraging and providing useful discussion during the course of my thesis.

To my sponsor, Universiti Tun Hussein Onn and the Government of Malaysia for the scholarship to come to the UK to do my PhD. There is no chance of me coming to Lancaster without their financial support.

The Malaysian community in Lancaster who has become my extended family, Fazrul Aizat who let me stay in his room during my final months in Lancaster.

I am deeply grateful to my parents Anuar Maarup and Salbiah Sawal for raising

me up to be what I am now. Also to my in laws Ahmad Hashim and Zainab Mustapha for their advice and support.

My biggest gratitude to my wife Anita Ahmad, and to my son Adham Haikal, and my lovely daughters, Alya Humaira and Aleesya Khadeeja for their support and understanding of the nature of this kind of adventure. Thank you for fulfilling my life, bringing me joy and being a rock behind me. I am indebtful for the missing days and nights, and for not being able to be with them especially during the last few months of this project.

Contents

List of Figures

List of Tables

Chapter 1

Introduction

Dust particles have been found in many space environments and form what is known as dusty plasma as they interact with space plasma. Dust refers to a collection of fine particles of nanometer to micrometer sized which are made of metallic or non-metallic materials and are present in space either naturally or as a result of human activities. Naturally, dust particles can be found in many astrophysical situations such as in the planetary ring of planets such as Saturn and Jupiter, in cometary tails, in interstellar cloud and in an airless planetary bodies and asteroid. Spacecraft emissions such as from propellant and material degradation also contribute to the presence of dust particles in space.

The interaction between dust particle and space plasma has produced many interesting phenomena and has became a major field of study in space physics. The study of dusty plasma has intensified in the late 20^{th} century as a result of the early space explorations, in particular after the Apollo missions, and the emergence semiconductor industry. In the first case, dust particles encountered during many of the missions have become a major problem to space vehicle operating on the lunar surface as well as on astronaut's life saving equipments. In the latter case, dust particles have been identified as main contaminant in wafer fabrication process which determines the wafer production yields. In both cases, dust particles are exposed to plasma causing them to get charge and eventually get involve in the overall plasma system.

Future space exploration such as the European Space Agency (ESA) Aurora Exploration Programme which is aimed at both human and robotic exploration of Mars and the Moon emphasis the need for further understanding of the dusty plasma environment. On lunar surface for example, charged dust particles have been observed to be levitated and accelerated into the lunar's upper atmosphere due to the electrostatic force generated by the lunar surface. The dust levitation process is most prevalent near the lunar terminator region and could possibly affect any mission taking place near the region. This thesis was motivated by the quest to understand dusty plasma and its interaction with any space vehicle that will be built to explore such regions.

This thesis presents simulation results of some of the process that are important in dusty plasma. In particular, the work tries to model processes that involve dust particles in plasma which are the dust charging process and the dust dynamics. The ionospheric dust charging process has been studied in order to examine surface charging in the vicinity of dust particles within a complex (dusty plasma) environment. In addition, the dusty environment found on the lunar surface has also been chosen as an example for the simulation of dust charging and dynamics.

1.1 Main Contributions

This thesis makes three specific contributions. Firstly, a new dust-plasma interaction module known as *Spacecraft Plasma Interaction Software - dust* (SPIS-dust) has been developed specifically to study dusty plasma environment. This process involves the design and implementation of a new module in Spacecraft Plasma Interaction Software, a freely available plasma simulation software. This code development will allow the dust plasma interaction and dust dynamics to be simulated.

Secondly, the dust environment on the lunar surface has been investigated using SPIS-dust. Various parameters and conditions related to dust on the lunar surface have been simulated with results showing many interesting phenomena happening

on the lunar surface. These include the lunar surface charging process and lunar dust dynamics which further illustrate the need of capable dust simulation software.

Finally, the first attempt of simulating dust particle dynamics on the lunar surface near a lunar exploration vehicle has been presented using SPIS-dust. Results show that dust particles could play an important role in the success of any future lunar exploration. This work is envisaged to provide a clear understanding on the lunar environment in order to prepare crews and equipment to the harsh reality of lunar environment.

1.2 Brief Description of All Chapters

This thesis presents a sequence of chapters that describes the works involved in the design, development and validation of the SPIS-dust code, followed by the application of the code on lunar environment, in order to study the behaviour of dust particles found in that environment. **Chapter 2** describes the theories and past works on both space plasma and dusty plasma. As dust particles can be found in most of the plasma environment it is important to have a good understanding on the plasma system in such environments. This includes a review of dusty plasma, plasma theory and space plasma environment found in the ionosphere and solar wind. Processes related to the behaviour of dust particles such as charging and dust dynamics are presented in this chapter.

Chapter 3 presents a review of plasma simulation theory. This includes methods and techniques used in plasma simulation and limitation and expectation of each technique. Plasma simulation theory that is covered in this chapter deals with the simulation of plasma particles in an unbounded plasma region, where interactions are between the particles themselves. Particle in cell method and Monte Carlo collision are introduced in this chapter. **Chapter 4** continues with the presentation of the Spacecraft Plasma Interaction Software that looks at interaction between plasma and spacecraft in space. Features of this software are presented and the advantages and limitations are discussed.

Chapter 5 describes the implementation of the dust module in SPIS-dust and the subsequent validation processes performed to gauge the output of the software. The dust interaction routine is validated and results are presented in this chapter. This chapter also investigates the effects of dust particles in the vicinity of a charged surface.

Chapter 6 further uses the SPIS-dust to study lunar dust environment. It starts with the description of lunar plasma and processes that charge the lunar surface. Simulations are performed to look at the response of the surface to different solar wind and solar UV flux conditions. The effects of having variations on the surface are also investigated and results are discussed. This is followed by the introduction of dust particles over the lunar surface where their dynamics are simulated and studied.

Chapter 7 looks at the effect of a lunar rover on dust dynamics. This is a culmination of the work from previous chapters which shows some of the different phenomena experienced by the rover in a dusty lunar environment. Simulations are performed for different regions of the lunar surface and results are presented and discussed in this chapter.

Finally, **Chapter 8** summarizes the works that has been investigated in this thesis. Observations found in the previous chapters are discussed. Future works in the subject are proposed in this chapter.

Chapter 2

Plasma Environment

2.1 Introduction

The vastness of space is filled with extremely tenuous gases of ionized particles; loose electrons and ions which form what is known as *plasma*. These ionized particles come form the heating of neutral atoms to the level where the excitation energy from the heating process exceeds the atom's ionization energy. These loose particles are affected by each others's electromagnetic field, binding them together such that they act collectively. In addition to the collective act, these particles have to adhere to other conditions; they are macroscopically neutral (quasineutral) as oppositely charged particles neutralize each other and are affected by electric and magnetic field. Plasma is sometime referred to as the fouth state of matter, with solid, liquid and gas forming the other three. It is estimated that 99% of the universe is made of plasma, with the remaining 1% representing other matter such as planets, planetary moons and asteroids and dust particles.

The heliospheric plasma originates mostly from the Sun in the form of the solar wind, travelling outward at approximately 450 km/s. The solar wind is believed to travel as far as several hundred AU (1 astronomical unit = 149, 597, 870, 700 meters), where it finally slows down from supersonic to zero. It was reported that the Voyager 1 spacecraft, which was launched back in 1977, had passed through the heliosheath, into a region of strong interstellar magnetic field, called the *magnetic*

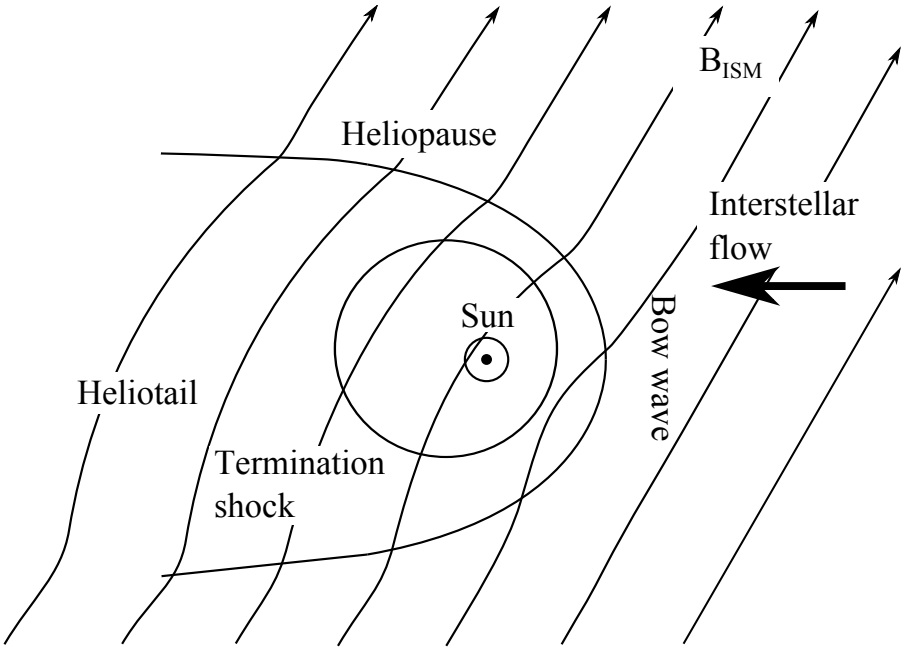

Figure 2.1: Current model of the Heliosphere. Recent finding by NASA's Interstellar Boundary Explorer (IBEX) shows no bow shock region (adapted from McComas et al. [2012]).

highway, which is an indication of the boundary separating the solar wind dominated heliosphere and the interstellar space [NASA, 2012]. This boundary is called the heliopause, a theoretical one where the solar wind pressure is considerably weaker than the pressure created by the interstellar wind from surrounding stars. Figure 2.1 shows the hypothetical structure of the heliosphere, a region in space where the solar wind dominates.

The solar wind in the Heliosphere travels along the Sun's magnetic field, sweeping past planetary objects in its path. For planet such as Earth where global geomagnetic field is strong, the solar wind is deflected by the Earth's magnetic field forming what is known as the magnetosphere. The deflection of the solar wind around the Earth's magnetosphere protects the surface inhabitants from possible hazardous conditions that maybe caused by the solar wind plasma. Figure 2.2 shows the schematic of the Earth's magnetosphere.

Although the Earth's magnetosphere appears to provide the much needed protection from the incoming solar wind, the response of the magnetic field during intense solar wind flux, coupled with favourable interplanetary magnetic field

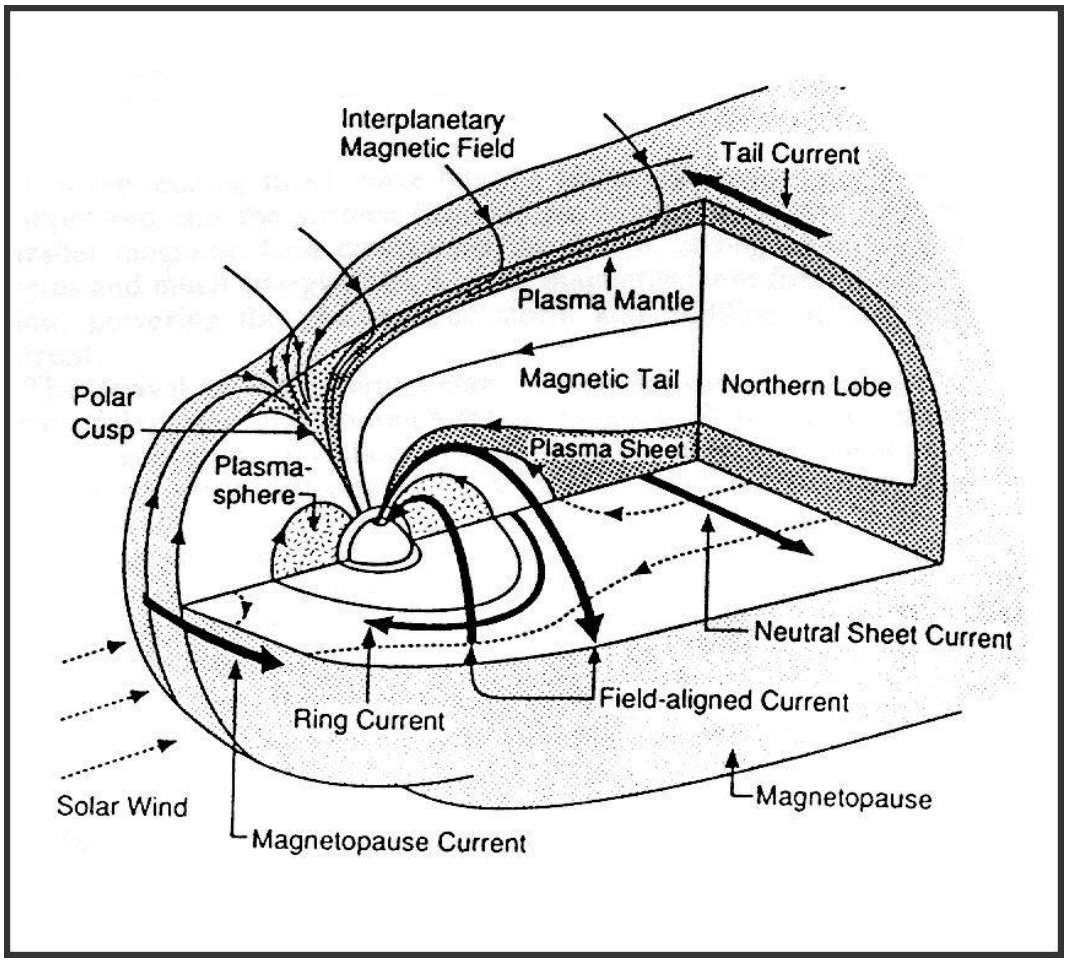

Figure 2.2: The Earth's magnetosphere.

direction, could provide a path for energetic electrons originating form the magnetosphere and the solar wind to enter the Earth's atmosphere via the North and South pole. These occurrences are the source of aurora display which are visible in the northernmost and southernmost part of the Earth's hemisphere, known as the auroral zone. The aurora is a result of collisions between highly energetic particles entering the Earth's atmosphere via the Earth's magnetic field lines and neutrals which happen in the atmospheric layer known as the ionosphere. The ionosphere is part of the upper atmosphere, beginning at altitude of around 80 km to around 600 km, and the main constituents of this layer are neutrals in addition to the charged electrons and ions. Particles precipitation are not the only source of charged particle in the ionosphere as the electron (and ion) productions are mostly due to photoionization process, secondary ionization by primary electrons (from photoionization) and charge exchange process.

The Earth's magnetic field is generated by the motion of the Earth's molten inner core, largely composed of iron and nickel. Combined with the Earth's gravitational force, the Earth is able to hold on to its atmosphere which provides protection not only from the solar wind but also from other cosmic influences such as the harmful ultraviolet radiation. The same is not always true for other celestial objects in the solar system where the lack of strong magnetic field means the solar wind is able to directly impact the surface of such bodies. For example, the lack of magnetic field and any appreciable atmosphere on the Moon's surface means the Moon's surface is subjected to the full force of the incoming solar wind. The solar wind contains large amount of charged particles (electrons and ions) and upon impact on the lunar surface (or any other surfaces in space), these particles can either be collected or produce secondary emission by transferring their energy to the surface. This process is known as charging and causes potential difference between the surface and the surrounding plasma. The surface is charged to what is known as *floating potential* in order for the net current entering and leaving the surface, is balanced. The potential developing on the surface can either attracts or repels plasma particles, depending on the polarity and the incidence plasma particles. The floating potential depends on several factors which include the solar wind conditions, surface material and the sun photon flux which controls the amount of photoionization on the surface.

The charging process is not limited to large bodies in space. Dust particles experience the same charging process when immersed in plasma. These fine particles with radii that vary from nanometer to micrometer collect and emit plasma particles when exposed to solar wind plasma. Similarly, these dust particles will be charged to a certain floating potential in order to balance the current entering and leaving the surface. As a result, these charged dust particles are affected by the electric and magnetic fields, similar to the ones experienced by plasma particles. Depending on the mass (or size) and the charge of an individual grain, their interaction with electric and magnetic fields could be stronger than their interaction with the

gravitational field. The combination of electrons, ions and charged dust particles form what is known as *dusty plasma* where all three elements interact collectively upon each other.

In addition to the dust particles in deep space, dusty plasma has also been observed in the Earth's atmosphere. During the summer months, a phenomena known as noctilucent clouds (NLCs) has been observed in the polar mesopause at altitude 80 - 90 km . These clouds are believed to contain charged ice particles which are formed due to the extremely low temperature [Havnes et al., 1996a, Cho and Kelley, 1993]. In addition to naturally occurring dusty plasma, human activities in space also contribute to the existence of dust particles in the Earth's atmosphere. These 'man made' particles have been found to be the reason for measurement errors in many occasions [Robinson et al., 1991].

Future space explorations such as the planned missions to the Moon require considerable assessment on the effect of dust particles on equipment and astronauts. This work contributes to the cause by providing a tool to study and analyse dusty plasma in space. This chapter will briefly describe space plasmas followed by theories of dusty plasma.

2.2 Physics of Space Plasmas

Plasma in space is made up from a very tenuous plasma compared to the laboratory plasma. Most of the plasma environment in the solar system originates from the Sun and can be classified into two main components; the high energy plasma ($E > 100\,\text{keV}$ for electrons and $E > 1\,\text{MeV}$ for proton) associated with solar events and low energy plasma ($E \approx$ tens of eV) that forms the background of the space environment. The high energy plasmas come from the sporadic burst of charged particles from events such as flares, coronal mass ejections, proton events and are highly correlated with the 11 year solar cycle. The low energy plasma on the other hand comes from the continuous emission of particles from the Sun's upper atmosphere that travel outward at speeds between 200kms^{-1} and 1000kms^{-1}

known as the solar wind.

2.2.1 Plasma Parameters

Number density and Temperature

The plasma environment can be represented by two important parameters, the number density and temperature. In plasma, number density for a particular species s, n_s, represents the number of particle for each plasma species per cubic volume with the subscript s representing the plasma species, i.e. e for electrons, i for ions and p for protons. The number density for different plasma species must be regarded as an independent variable as both electrons and ions react differently to electromagnetic force. When there is no external force, the plasma is macroscopically neutral where

$$q_i n_{i0} = e n_{e0} \tag{2.1}$$

where $q_i = Z_i e$ is the ion charge ($Z_i = 1$ for proton) and n_{s0} is the density where the plasma is neutral (net charge = 0) and e is the electronic charge given as 1.6022×10^{-19} C. The temperature of a plasma species is directly proportional to its average random kinetic energy. The velocity of a species in thermal equilibrium is given by the Maxwellian distribution

$$f_s(\mathbf{v}) = n_s \left(\frac{m_s}{2\pi k_B T_s} \right)^{3/2} \exp - \frac{m_s v^2}{2 k_B T_s} \tag{2.2}$$

where $f_s(\mathbf{v})$ is the distribution function, $\mathbf{v}$ is the velocity, m_s is the species mass, k_B is the Boltzmann's constant ($k_B = 1.38 \times 10^{-23}$ J K^{-1})and T_s is the species temperature in Kelvin (K). The Maxwellian distribution is normalized such that $f_s(\mathbf{v})$ integrated over all velocities gives the number density of the species s

$$\int_{\infty}^{-\infty} f_s(\mathbf{v}) \, \mathrm{d}x \, \mathrm{d}y \, \mathrm{d}z = n_s. \tag{2.3}$$

The species thermal velocity is given as

$$v_{th} = \sqrt{\frac{k_b T_s}{m_s}}. \tag{2.4}$$

A Maxwellian distribution is dependent only on the magnitude of the velocity $v^2 = v_{x_1}^2 + v_{x_2}^2 + v_{x_3}^2$. Using spherical coordinates, the velocity can be expressed as a function of speed v,the 'azimuth' θ and 'path angle' ϕ where $v_{x_1} = v \sin\theta \cos\phi$, $v_{x_2} = v \sin\theta \sin\phi$ and $v_{x_3} = v \cos\theta$. The increment of volume in velocity space is

$$\mathrm{d}\, v_{x_1}\, \mathrm{d}\, v_{x_2}\, \mathrm{d}\, v_{x_3} = v^2 \sin\theta\, \mathrm{d}\,\theta\, \mathrm{d}\,\phi\, \mathrm{d}\, v \tag{2.5}$$

and since f_M depends only on speed, the speed distribution function $F_M(v)$ is given by

$$F_M(v) == 4\pi \left(\frac{1}{\pi}\right)^{3/2} (v^2/v_{th}^2) \exp\left(-v^2/v_{th}^2\right)/v_{th}. \tag{2.6}$$

The species mean velocity is [Hastings and Garrett, 2004]

$$\langle v \rangle = \left(\frac{8 k_B T_s}{\pi m_s}\right)^{1/2}. \tag{2.7}$$

Figure 2.3a shows the single Maxwellian velocity distribution and 2.3b shows the Maxwellian speed distribution. In 2.3a, x-axis is in multiple of thermal velocity $(k_B\, T/m_s)^{1/2}$ while in 2.3b, x-axis is in multiple of mean velocity $\langle v \rangle$.

The average kinetic energy for the species is then

$$\langle E \rangle = \langle \frac{m_s v_{th}^2}{2} \rangle = \frac{3 k_B T_s}{2} \tag{2.8}$$

where the angle bracket indicates an average.

It is also common to give the temperature in the unit of electron volts (eV) where 1 eV $= k_B T/e = 1.6022 \times 10^{19}$ J is the energy that a particle carrying a charge e gains or loses in falling through a potential drop of 1V.

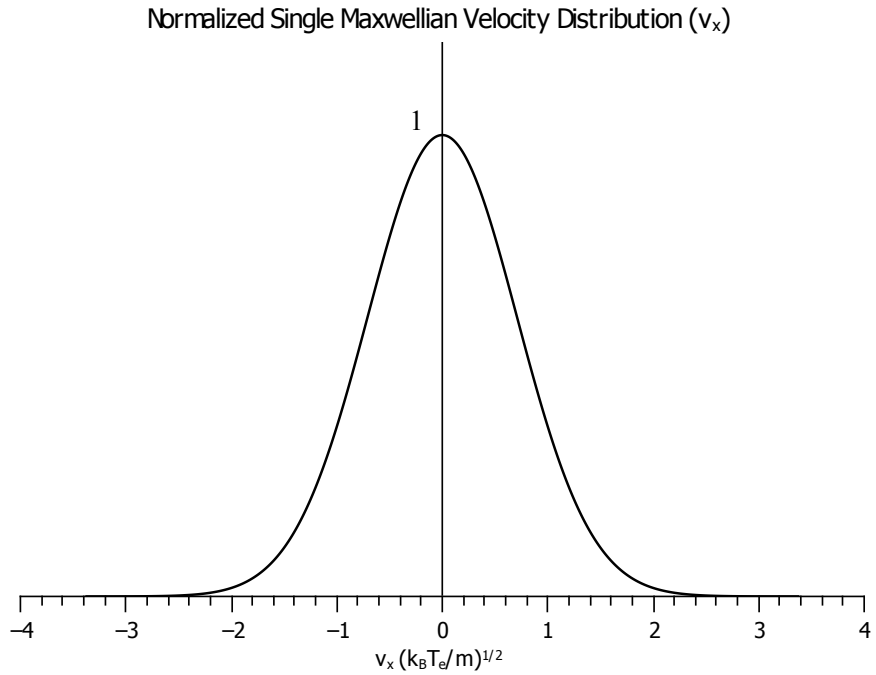

(a) Single Maxwellian velocity distribution

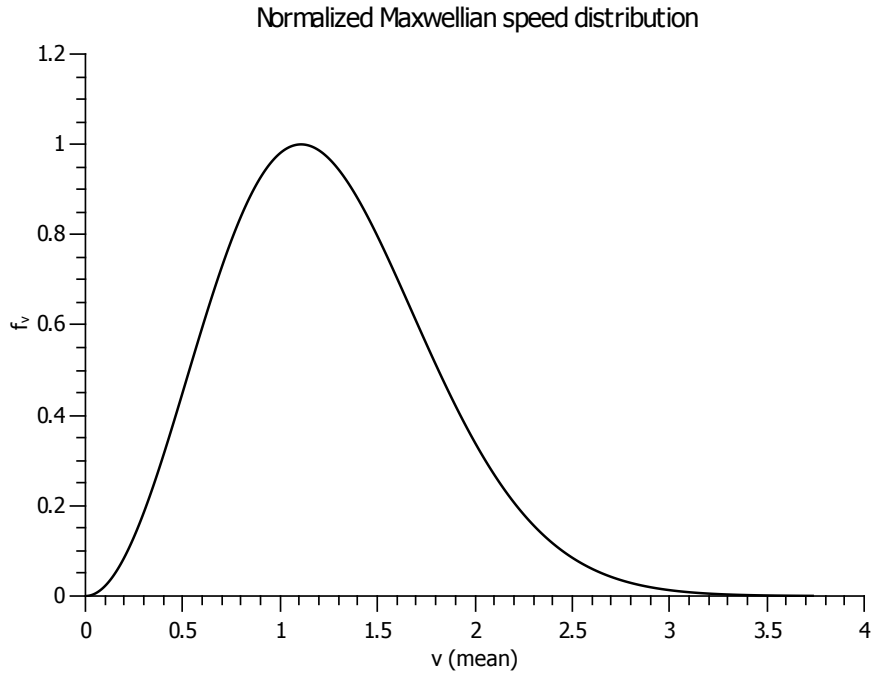

(b) Maxwellian speed distribution

Figure 2.3: Graph showing (a) the single Maxwellian velocity distribution and (b) the Maxwellian speed distribution. In (a) x-axis is in multiple of thermal velocity $(k_B\,T/m_s)^{1/2}$ while in (b) x-axis is in multiple of mean velocity $\langle v \rangle$.

Debye Length

Debye length is the plasma fundamental length scale that describes the ability of the plasma particle to shield the electric field of an individual particle or of a surface that is at non-zero potential. On a large scale, a plasma system is electrically neutral but on a smaller scale each particle species exerts Coulomb electrostatic force upon each other that drive the particle away and this creates a region where neutrality is not observed. The characteristic length where shielding occurs and charge neutrality is re-established is called the Debye radius or Debye length, after Debye and Hückel [1923] who first studied the effect in dielectric fluids.

The expression for Debye length can be obtained by placing a negative test charge in the plasma system with homogenous electron number density n_e and temperature T_e and fixed positive ions of density n_i. The presence of the test charge disturbs the plasma equilibrium state and particles realigned themselves to re-establish equlibrium. The electrostatic potential Φ for such plasma system is given by Poisson's equation

$$\nabla^2\Phi = \frac{\rho_q}{\varepsilon_0} = -\frac{e}{\varepsilon_0}\left(n_i - n_e\right) \tag{2.9}$$

where ε_0 is the permittivity of free space ($\varepsilon_0 = 8.8542 \times 10^{-12}\,\mathrm{F\,m^{-1}}$), ρ_q is the charge density and e is the electronic charge. Far away from the test particle, $\Phi = 0\mathrm{V}$ and assuming electrons and ions has velocity distribution described by Maxwellian distribution with density n_{s0} and temperature T_s, the density of the electrons and ions can be written as

$$n_e = n_{e0}\exp\left(\frac{-e\Phi}{k_B T_e}\right) \tag{2.10}$$

and

$$n_i = n_{i0}\exp\left(\frac{e\Phi}{k_B T_i}\right) \tag{2.11}$$

where $s = e, i$, $n_{e0} = n_{i0} = n_0$ and $T_e = T_i = T$. Substituting (2.10) and (2.11)

into the Poisson equation gives

$$\nabla^2\Phi = -\frac{en_0}{\varepsilon_0}\left(\exp\left(\frac{e\Phi}{k_BT}\right) - \exp\left(\frac{e\Phi}{k_BT}\right)\right). \tag{2.12}$$

However, since the ions are assumed to be stationary with respect to the test particle, (2.12) can be rewritten as

$$\nabla^2\Phi = -\frac{en_0}{\varepsilon_0}\left(1 - \exp\left(\frac{-e\Phi}{k_BT}\right)\right) \tag{2.13}$$

and expanding the exponential term in Taylor series and keeping only the first-order term gives

$$\nabla^2\Phi = \frac{n_0e^2}{\varepsilon_0k_BT}\Phi. \tag{2.14}$$

Since the plasma is isotropic, electrostatic potential can be assumed to be spherically symmetric which simplifies (2.14) to

$$\frac{\partial^2}{\partial r^2}(r\Phi) - \frac{n_0e^2}{\varepsilon_0k_BT}(r\Phi) = 0 \tag{2.15}$$

which has the general solution

$$\Phi = \frac{A}{r}\exp\left(\frac{-r}{\lambda_D}\right) \tag{2.16}$$

where r is the radius and A is a constant. The factor λ_D can be shown to be

$$\lambda_D = \sqrt{\frac{\varepsilon_0k_BT}{n_0e^2}}. \tag{2.17}$$

The constant A is the potential at which $r = 0$ and is given by

$$A = \frac{Q}{4\pi\varepsilon_0} \tag{2.18}$$

which gives the final solution for the electrostatic potential at distance r from the

particle to be

$$\Phi = \frac{Q}{4\pi\varepsilon_0 r} \exp\left(\frac{-r}{\lambda_D}\right) \tag{2.19}$$

which is known as the Debye-Hückel potential.

The length λ_D is the Debye length and is a measure of the shielding distance or thickness of the sheath. The Debye length gives rise to the concept of quasi-neutrality, that is at a scale length less than λ_D, plasma may not be charge neutral. It also represents the length scale over which the plasma collective effect is manifest, that is at length scale smaller than λ_D, particles behaves as individual charged particles whereas at larger length scale, collective coupling of particles is possible. The number of particles inside the Debye sphere is then given by

$$N_D = \frac{4}{3}\pi n_0 \lambda_D^3. \tag{2.20}$$

Table 2.1 shows the properties of typical plasma.

Table 2.1: Properties of typical space plasma (Kivelson and Russell [1995]).

Plasma type	Density (m^{-3})	Temperature (eV)	Debye Length (m)	N_D
Interstellar	10^6	10^{-1}	1	10^6
Solar wind	10^7	10	10	10^{10}
Solar corona	10^{12}	10^2	10^{-1}	10^9
Solar atmosphere	10^{20}	1	10^{-6}	10^2
Magnetosphere	10^7	10^3	10^2	10^{13}
Ionosphere	10^{12}	10^{-1}	10^{-3}	10^4

Plasma frequency

Another important plasma parameter is the natural frequency of plasma oscillation or simply plasma frequency. The collisionless Boltzmann's equation is given by

$$\frac{\partial f}{\partial t} + \mathbf{v} \cdot \frac{\partial f}{\partial \mathbf{r}} + \frac{q}{m}(\mathbf{E} + \mathbf{v} \times \mathbf{B}) \cdot \frac{\partial f}{\partial \mathbf{v}} = 0 \tag{2.21}$$

where f is the plasma distribution function given by $f_s(\mathbf{r}, \mathbf{v}, t)$ (eg. Maxwellian distribution as in equation (2.2)) in a 6-dimensional *phase space*, i.e. $\mathbf{r}$ is the position coordinates x, y, z and $\mathbf{v}$ is the velocity coordinates v_x, v_y, v_z, and $\mathbf{E}$ and $\mathbf{B}$ are the electric and magnetic fields respectively. Integrating the plasma distribution over velocity gives the plasma moments; the zeroth-order moment which is the density (equation (2.3) and the first order moment, the average velocity

$$\mathbf{u} = \frac{\int \mathbf{v} f \ \mathrm{d}^3 v}{\int f \ \mathrm{d}^3 v} = \frac{1}{n} \int \mathbf{v} f \, \mathrm{d}^3 v \tag{2.22}$$

where the operator $\mathrm{d}^3 v = \mathrm{d}v_x \, \mathrm{d}v_y \, \mathrm{d}v_z$. In a zero magnetic field, the collisionless Boltzmann's equation is reduced to Vlasov-Poisson equation

$$\frac{\partial f}{\partial t} + \mathbf{v} \cdot \frac{\partial f}{\partial \mathbf{r}} + \frac{q}{m} \mathbf{E} \cdot \frac{\partial f}{\partial \mathbf{v}} = 0. \tag{2.23}$$

Integrating equation (2.23) over the entire velocity space V gives

$$\int_V \frac{\partial f}{\partial t} \, \mathrm{d}^3 v + \int_V \mathbf{v} \cdot \frac{\partial f}{\partial \mathbf{r}} \, \mathrm{d}^3 v + \frac{q}{m} \int_V \mathbf{E} \cdot \frac{\partial f}{\partial \mathbf{v}} \, \mathrm{d}^3 v = 0. \tag{2.24}$$

The first integral term can be written as

$$\int_V \frac{\partial f}{\partial t} \, \mathrm{d}^3 v = \frac{\partial}{\partial t} \int_V f_s \, \mathrm{d}^3 v = \frac{\partial n_s}{\partial t}. \tag{2.25}$$

and the second term is

$$\int_V \mathbf{v} \cdot \frac{\partial f}{\partial \mathbf{r}} \, \mathrm{d}^3 v = \nabla \cdot \int_V \mathbf{v} f_s \, \mathrm{d}^3 v = \nabla \cdot (n_s \mathbf{u}) \tag{2.26}$$

where $\mathbf{u}$ is the average velocity in (2.22).

The third term is reduced to zero using Gauss' theorem by converting the

volume integral to surface integral at infinity, i.e.

$$\frac{q}{m}\int_V \mathbf{E}\cdot\frac{\partial f}{\partial \mathbf{v}}\,\mathrm{d}^3\,v = \frac{q}{m}\int_V \mathbf{E}\cdot\nabla f\,\mathrm{d}^3\,v = \frac{q}{m}\int_V \nabla\cdot\mathbf{E}f\,\mathrm{d}^3\,v = \frac{q}{m}\int_S \mathbf{E}f\,\mathrm{d}\,\mathbf{s}_v = 0. \tag{2.27}$$

Replacing the distribution function $f(\mathbf{r},\mathbf{v},t)$ in the Vlasov-Poisson (equation (2.23)) with its plasma moments density and average velocity $(n_s,\mathbf{u})$ gives

$$\frac{\partial}{\partial t}n + \nabla\cdot(n\mathbf{u}) = 0 \tag{2.28}$$

which is the *continuity equation*. Multiply (2.28) with charge e, the charge continuity equation can be obtained where

$$\frac{\partial \rho}{\partial t}n + \nabla\cdot(\mathbf{J}) = 0 \tag{2.29}$$

Since there is no collision, it can be assumed that forces acting on the particles are long range forces which are given by Newton's law

$$\mathbf{F} = m\frac{\mathrm{d}\mathbf{v}}{\mathrm{d}t} = q\mathbf{E} \tag{2.30}$$

for unmagnetized plasma. If both ions and electrons are assumed to be initially at rest, the introduction of small $\mathbf{E}$ will cause electrons to move while the ions remain in stationary position, i.e.

$$n_i = n_{i0} \tag{2.31}$$

$$n_e = n_{e0} + n_1(\mathbf{r},t) \tag{2.32}$$

where $n_1 \ll n_{e0}$. The average electron velocity after the perturbation is $\mathbf{u} = \mathbf{u}_0 + \mathbf{u}_1$ and since electrons starting from rest, $\mathbf{u} = \mathbf{u}_1$. Substituting both n and $\mathbf{u}$ in the continuity equation for electrons, taking only the first order term, assuming the

amplitude of the oscillation is small, gives

$$\frac{\partial n_1}{\partial t} + n_0 \nabla \cdot \mathbf{u}_1 = 0. \tag{2.33}$$

The *plasma frequency* can be derived by taking the derivative of (2.33)

$$\frac{\partial^2 n_1}{\partial t^2} + n_0 \nabla \cdot \left(\frac{\partial \mathbf{u}_1}{\partial t} \right) = 0, \tag{2.34}$$

and rewriting equation (2.30) as

$$\nabla \cdot \frac{\partial \mathbf{u}_1}{\partial t} = -\frac{e}{m_e} \nabla \cdot \mathbf{E}_1 \tag{2.35}$$

followed by substituting $\nabla \cdot \mathbf{E}_1$ with Maxwell's equation (i.e. Gauss's Law)

$$\nabla \cdot \mathbf{E}_1 = \frac{-e n_1}{\varepsilon_0} \tag{2.36}$$

which gives

$$\nabla \cdot \frac{\partial \mathbf{u}_1}{\partial t} = \frac{e^2 n_1}{m_e \varepsilon_0}, \tag{2.37}$$

and finally substituting (2.37) back into (2.34)

$$\frac{\partial^2 n_1}{\partial t^2} + \left(\frac{n_0 e^2}{\varepsilon_0 m_e} \right) n_1 = 0 \tag{2.38}$$

which is similar to the harmonic oscillator equation given by

$$m \frac{\mathrm{d}^2 x}{\mathrm{d}\, t^2} = -kx. \tag{2.39}$$

The electron plasma frequency ω_{pe}, is given by the term in the parentheses

$$\omega_{p,s}^2 = \frac{n_s e^2}{\varepsilon_0 m_s} \tag{2.40}$$

Plasma frequency is a result of a plasma particle being displaced from its

equilibrium position, creating a space charge field which tries to pull the particle back into its equilibrium position. Inertia causes the particle to overshoot from its original position and this process is repeated and the particle will continuously oscilate around its equilibrium position. The frequency of oscillation depends on the mass of the particle as shown in (2.40) with a light particle (e.g. an electron) oscillating much faster than a heavier particle (e.g. an ion). For multi-species plasma (electrons and ions), the plasma frequency is given by

$$\omega_p = \sqrt{\omega_{pe}^2 + \omega_{pi}^2} \tag{2.41}$$

which is approximately ω_{pe} since $\omega_{pe} \gg \omega_{pi}$.

2.3 Plasma Particle Dynamics

2.3.1 Single particle motion in constant E and B

Plasma particle motion is predominantly influenced by electromagnetic force given by the Lorentz-force law as

$$\mathbf{F}_L = q\mathbf{E} + q(\mathbf{v} \times \mathbf{B}) \tag{2.42}$$

where $\mathbf{E}$ is the electric field, $\mathbf{B}$ is the magnetic induction and $\mathbf{v}$ is the velocity vector of the particle comprising of the perpendicular($v_\perp$) and parallel ($v_\parallel$) components. It is also important to note that there are other forces that act upon the particle such as gravitational force $\mathbf{F}_g$, Coulomb drag force $\mathbf{F}_g$ and neutral drag $\mathbf{F}_n$ but in the context of this discussion, these forces are too small and are neglected. From equation (2.42), it can be seen that there are two main forces acting on a particle which are the electrostatic force ($\mathbf{F}_E = q\mathbf{E}$) and magnetic force ($\mathbf{F}_B = q(\mathbf{v} \times \mathbf{B})$). To resolve the particle motion, it is first assumed that the electric force component is zero ($\mathbf{E} = 0$). It can then be deduced that the magnetic force acting on a particle is always perpendicular to the magnetic field vector and the instantaneous velocity

vector (from the definition of cross product). Assuming a uniform magnetic field, the particle must then travel in circular motion perpendicular to the magnetic field vector. The radius of this motion, called the cyclotron radius or gyroradius is found by equating centripetal force to the Lorentz force

$$\frac{m_s v_\perp^2}{\rho_s} = q v_\perp B \tag{2.43}$$

where B is the magnitude of the magnetic field $\mathbf{B}$, $v_\perp$ is the velocity component perpendicular to B and ρ_s is the radius which gives

$$\rho_s = \frac{m_s v_\perp}{qB}. \tag{2.44}$$

The frequency for which the particle gyrates, the gyro frequency Ω_s is then

$$\Omega_s = \frac{qB}{m_s} \tag{2.45}$$

where Ω_s is given in radians per second.

The term $q(\mathbf{v} \times \mathbf{B})$ in (2.42) also implies that any particle motion parallel to B is unaffected by B since $v_\parallel \times \mathbf{B} = 0$. The particle's motion in a constant magnetic field $\mathbf{B}$ and in the absence of any other forces can be described as spiralling along the magnetic field direction; it gyrates around the field (due to $v_\perp$) while moving along the field (due to $v_\parallel$).

Inserting a constant $\mathbf{E}$ back into (2.42), the particle equation of motion is

$$m_s \frac{\mathrm{d}\mathbf{v}}{\mathrm{d}t} - q\left(\mathbf{v} \times \mathbf{B}\right) = q\mathbf{E}. \tag{2.46}$$

If the $\mathbf{E}$ is perpendicular to $\mathbf{B}$, the equation (2.46) has a solution for the case of $\frac{\mathrm{d}\mathbf{v}}{\mathrm{d}t} = 0$

$$\mathbf{v} = \frac{\mathbf{E}_\perp \times \mathbf{B}}{B^2} = \mathbf{v}_d \tag{2.47}$$

where $\mathbf{v}_d$ is the *drift velocity*. For this situation ($\mathbf{E} \cdot \mathbf{B} = 0$), the motion of the

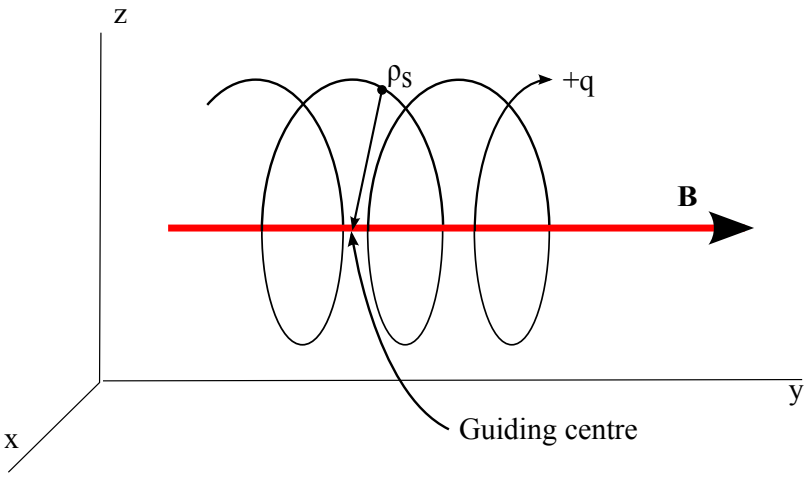

(a) Particle motion around a constant **B**.

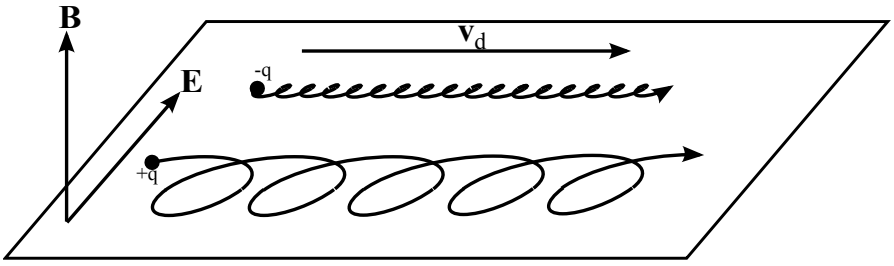

(b) Constant **B** and E, with **E** perpendicular to **B**

Figure 2.4: Single particle motion

particle can be described by gyration around the magnetic field, flow along the magnetic field and drift perpendicular to both **E** and **B**. This is what is known as *E cross B* drift velocity. Figure 2.4 shows the particle motion in the presence of constant magnetic and electric force. In Figure 2.4a, the particle's circular motion around the magnetic field generates a helical trajectory with clockwise direction for ions and counter-clockwise direction for electron. Figure 2.4b shows the $\mathbf{E} \times \mathbf{B}$ drift on a plane perpendicular to the magnetic field. Both ion and electron are accelerated when the velocity vector is parallel to the electric field, producing a larger gyroradius while the motion along the magnetic field is kept at a constant velocity.

The particle pitch angle, α, is the angle that the particle motion makes relative

to the field and is given by

$$\alpha = \arccos\left(v_{\parallel}/v\right). \tag{2.48}$$

The particle pitch angle is shown in Figure 2.5.

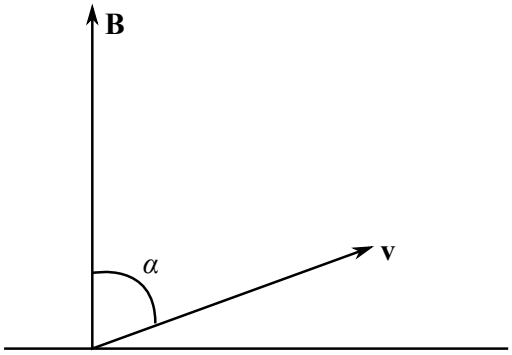

Figure 2.5: Particle pitch angle

2.4 Space Plasma Environment

The main driving force for the plasma environment in the solar system is the Sun which is responsible for the electromagnetic flux (radiation) and the emission of charged particles. The charged particle flux consists of the high energy ($E > 1$MeV) flux associated with sporadic burst of plasma and continuous low-energy background flux (E $\sim$ 10s eV) known as the solar wind. The high energy flux burst happens during solar events such as flares, coronal mass ejection (CME), proton events while solar wind, dominates the interplanetary environment and forms the ambient space plasma environment.

2.4.1 The solar wind

The space between the Sun and the planets was first thought to be completely vacuum with the exception of dust particles that causes light scattering in the zodiacal light. In the late 19th century, Richard C. Carrington observed that a solar flare event induces geomagnetic storm on Earth in the next day [Carrington, 1859].

It was then suggested that matter was being ejected from the sun forming a plasma bubble which periodically passes through the interplanetary space [Chapman and Ferraro, 1931].

The idea that the space is filled with continuous flow of plasma was not raised until 1950s when it became evident that the variation in Earth's magnetic field correlates with the event observed on the Sun. In addition, applying gas pressure law on the solar corona shows that the gas expansion on the sun's corona fills the inteplanetary space with solar atmosphere [Parker, 1958a]. Moreover, the observation of cometary tail that always pointing away from the sun also indicates the presence of huge pressure coming from the sun [Biermann, 1951]. It was later confirmed that there is a continuous flow of plasma particle from the sun which fills the solar atmosphere. It was later known as solar wind [Parker, 1958b], and was directly observed during the early years of space exploration.

The Sun is a giant gas ball and rotates on its axis roughly every 27 days at the equator and 31 days at the poles. The outward flow of solar wind is the results of a huge difference in gas pressure between the solar corona and interstellar space. This flow stretches the Sun's magnetic field lines such that a heliospheric current sheet (HCS) is formed at the equator, separating the field lines from the north and south of the Sun's equator. This current sheet move up and down in heliolatitude, due to the tilt in the Sun's dipole. The field lines are in opposite directions, outward in one hemisphere and inward in the other. The rotation and the tilt causes the magnetic fields lines to spiral outward, forming what is known as the Parker spiral, which is named after Eugene Parker [Parker, 1958a]. Figure 2.6 shows an artist impression of the HCS and the spiralling field lines.

Based on the gas pressure law, it is estimated that the Sun is emitting huge amount of matter into the heliosphere at a rate of 10^9kg/s. The properties of solar wind are often given at the Earth's orbit, that is at a distance of 1.5×10^{11}m or 1 astronomical unit (AU). It is made up largely from ionised hydrogen (protons and electrons) and small percentage ($\sim 5\%$) of ionised helium. The density at

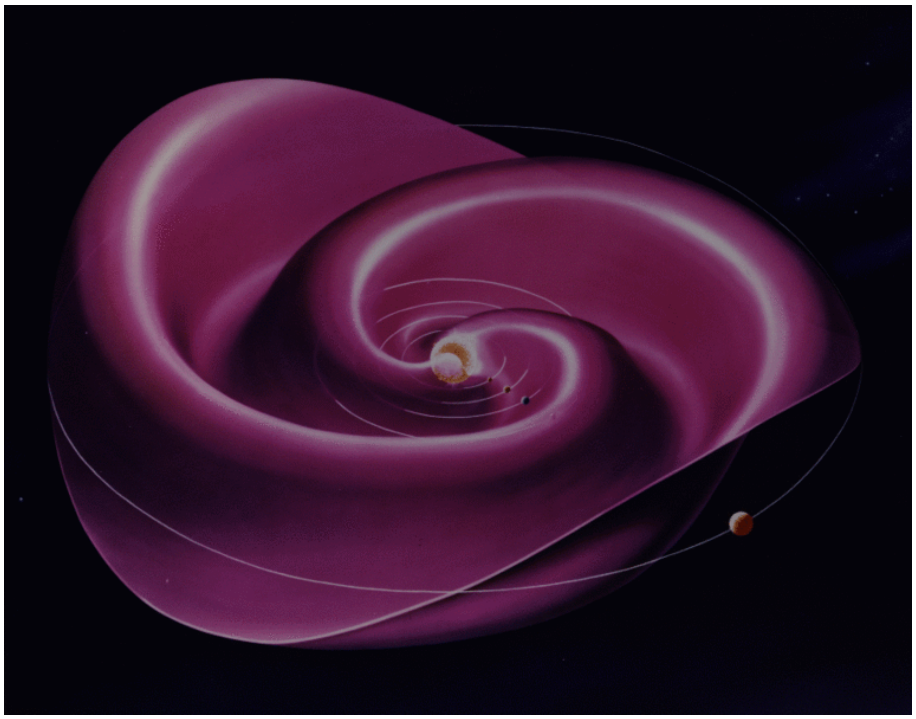

Figure 2.6: Artist impression of the Heliospheric current sheet which forms the Parker spiral (source: NASA).

Earth's orbit is about 6 ions and 6 electrons per cubic cm, with values fluctuating considerably between 0.1 - 100 per cubic cm [Prolss, 2004].

Solar wind is highly influenced by solar activity, which peaks every 11 years, and represents the major source of plasma that interacts with planets, comets, dust particles and other objects in space. This 11-year cycle also known as the sunspot cycle because of the high number of sunspot during the peak years. The sunspot number R is not the actual count of spots on the Sun surface but an index for the degree of the spottiness on the Sun which is calculated using $R = k(10g + s)$, where s is the number of individual spots, g is the number of sunspots group, and k is a subjective correction factor for different types of measurement equipment. The R values fluctuates over the 11-year cycle with maximum values of ≈ 150 and minimum values of ≈ 10 [Garrett and Whittlesey, 2000].

The solar cycle causes long term variation in the Earth's neutral atmosphere and ionosphere which is related to the increase in the extreme ultraviolet (EUV) radiation flux and increase in geomagnetic activity. EUV variations is believed to be correlated with the variations of solar radio flux observed at wavelength of 10.7

cm (2800 MHz), hence known as the $F_{10.7}$ index. The $F_{10.7}$ index varies from about 50 sfu ($1\,\text{sfu} = 10^{-22}\,\text{W}\cdot\,\text{m}^{-2}\cdot\,\text{Hz}^{-1}$) at solar minimum ($R$ minimum) to 240 sfu at solar maximum (R maximum) and varies with the 11-year solar cycle [Garrett and Whittlesey, 2000]. The short term geomagnetic activity on the other hand is represented by a 3-hour, semilogarithmic K_p or its linearised form a_p index. K_p and a_p represent magnetic-field disturbances induced by the changes in the solar wind which correlate with the variations of the upper atmosphere. The linearised form of a_p is often used to characterised the Earth's surface magnetic field at midlatitudes over a 3-hour period where the maximum variations can be obtained by multiplying the a_p value with 2γ ($1\gamma = 1\,\text{nanotesla}$) [Garrett and Whittlesey, 2000]. The index a_p and its daily average A_p values range from zero for no variation to maximum value of 400 which can be observed during major storm.

The solar wind can be classified as slow stream ($v \simeq 400\,\text{km/s}$) and high speed stream ($v > 600\,\text{km/s}$) with average velocity $\sim 450\,\text{km/s}$ [Prolss, 2004, Feldman et al., 2005]. The slow solar wind has temperature ranges from $1.4 - 1.6 \times 10^6\,\text{K}$ and a similar composition to the sun corona [Feldman et al., 2005]. It is observed to come from the mid heliographic latitude region known as the 'streamers belt' where emission occurs between latitudes of -30^o to 30^o during solar minimum (see Phillips [1995]). As the solar cycle moves towards maximum, this belt expand to higher latitude and the solar wind can eventually be emitted by the poles during the solar maximum period. On the other hand, the fast solar wind has temperature of $8 \times 10^5\,\text{K}$ and is believed to originate from coronal holes often found at high latitude in the Sun's photosphere. Tu et al. [2005] suggests that open magnetic field lines in the coronal hole forms a funnel that opens up at height of around 20,000 km above the photosphere. This is based on the observation using the Solar Ultraviolet Measurements of Emitted Radiation (SUMER) spectrometer and magnetograms on Solar and Heliospheric Observatory (SOHO) which shows that fast solar wind plasma flows from the funnel with outward initial speed of up tp 10 km/s [Tu et al., 2005].

Table 2.2 shows the mean properties of the solar wind at the Earth's orbit while Table 2.3 shows the solar wind value measured by Ulysses.

Table 2.2: Mean properties of the solar wind at Earth's orbit(extracted from Schwenn [1990])

Composition	$96\%\mathrm{H}^{+}, 4\%(0-20\%)\mathrm{He}^{++}, e^{-}$	
Density (cm^{-3})	$n_p \simeq n_e$	$\simeq 6(0.1-100)$
Velocity ($\mathrm{km\,s}^{-1}$)	$u_p \simeq u_e = u$	$\simeq 470(170-2000)$
Proton flux ($\mathrm{m}^{-2}\,\mathrm{s}^{-1}$)	$n_p\,u$	$\simeq 3\times10^{12}$
Momentum flux ($\mathrm{N\,m}^{-2}$)	$n_p\,m_H u^2$	$\simeq 2\times10^{-9}$
Energy flux ($\mathrm{mW\,m}^{-2}$)	$n_p\,m_H u^3/2$	$\simeq 0.50$
Temperature (K)	T	$\simeq 10^5(3500-5\times10^5)$
Plasma sound velocity (kms^{-1})	v_{PS}	$\simeq 50$

Table 2.3: Observed properties of the solar wind normalized at 1AU by Ulysses (extracted from Ebert et al. [2009])

Parameter	Fast solar wind 1 AU value ($\theta = 60\,\mathrm{deg}$)	Slow solar wind 1 AU value ($\theta = 0\,\mathrm{deg}$)
$v_p(\mathrm{km\,s}^{-1})$	745	392
$v_\alpha(\mathrm{km\,s}^{-1})$	769	399
$T_p(\times10^5\mathrm{K})$	2.46	0.80
$n_p(\mathrm{cm}^{-3})$	2.12	5.55
$n_\alpha(\mathrm{cm}^{-3})$	0.11	0.13
n_α/n_p	0.044	0.023
$\rho_i v_i^2(\mathrm{nPa})$	2.36	1.64
$\rho_i v_i(\mathrm{kg\,m}^{-2}\,\mathrm{s}^{-1})$	3.18	4.07

2.4.2 Ionosphere

The higher part of the Earth's atmosphere consists of layers of ionised particles of which the name *ionosphere* comes from. These layers are macroscopically neutral, where there is equal number of electrons and ions within a given volume. They have higher particle concentration than solar wind, although the free electrons and ions are less energetic than the ones found in the solar wind. The densities depend very much on the solar activity and solar flux because the two main processes that drive the ionisation process are photo-ionisations and collisions.

The ionosphere has been studied extensively due to its ability to reflect radio

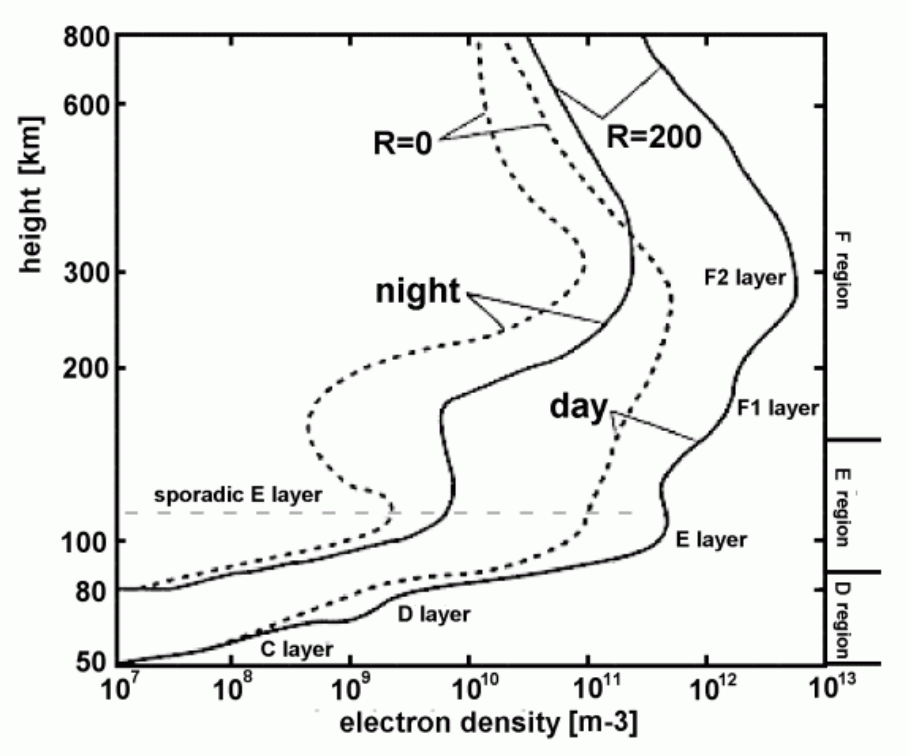

Figure 2.7: Typical day and night structure of an ionoshere. Also shown is the layer during solar minimum (dotted line) and solar maximum (solid line) (figure adapted from [Hastings and Garrett, 2004]).

signals. The first transatlantic radio transmission between Cornwall in England and Newfoundland in Canada in the early 20th century exploited this ionospheric feature since there was no line of sight transmission due to the Earth's curvature. This also means that radio reflection can be used as a tool to quantify the ionospheric plasma since reflection height is a function of electron density and signal frequency.

A typical ionospheric layers is shown in Figure 2.7. In the figure, the ionosphere can be classified into 4 main layers which are labelled as D, E, F1 and F2 layers. During night time, the F1 and F2 layers recombine forming the F layer. Table 2.4 lists the properties of the layers in the ionosphere.

These layers also are heavily influenced by the solar cycle where high electron density is observed during solar maximum. During high solar activity, an increase in electron precipitations in the ionosphere results in higher electron density, as shown in Figure 2.7. It is however more prevalence at higher latitude since energetic particles enter Earth's atmosphere through the magnetic field lines. As the stream

Table 2.4: Typical ionospheric layers properties (from Hastings and Garrett [2004])

Parameters	Layers			
	D	E	F	
			F1	F2
Height (km)	60 - 100	100 - 150	150 - 1000	
Ion Composition	NO^+/O^+	O^+	O^+/H^+	
n_e (m^{-3})				
day	$10^8 - 10^9$	$\sim 10^{11}$	10^{11}	10^{12}
night	-	$< 10^{10}$	10^{10}	

of high energy electrons reaches the upper atmosphere, they collide with neutral constituents. They excite and ionize the neutrals which is the source of the optical emission observed as auroras.

2.5 Dusty Plasma

2.5.1 Introduction to Dusty Plasma

Dusty plasma refers to a collection of dust particles which are charged upon exposure to space plasma and solar UV. The presence of charged dust particles affects plasma neutrality condition when the sheath (Debye sheath) created by the individual dust particle or cloud starts to screen plasma particles in its vicinity. These interactions result in a complex plasma behaviour such that the system is also known as *complex plasma*.

The dust physical properties such as its size, mass and density vary depending on its origin and surroundings. In most cases, dust particles are massive particles which weigh up to billion times of a proton and come in different sizes and shape ranging from nanometres to millimetres. The variation in shape and size means that each individual dust particle in the dusty plasma system behave differently making exact dusty plasma simulation complicated. This individuality affects for example the number of charges on the grain as each particle charges at different rates. Dusty plasma studies are normally limited to particles of size from few nanometres to 100 μm because for these sizes, particles are more likely to be affected

Table 2.5: The basic differences between electron-ion plasma and dusty plasmas (Shukla and Mamun [2002])

Characteristics	Electron-ion plasma	Dusty plasma
Quasi-neutrality condition	$n_{e0} = Z_i n_{i0}$	$Z_d n_{d0} + n_{e0} = Z_i n_{i0}$
Massive particle charge	$q_i = Z_i e$	$\|q_d\| = Z_d e \gg q_i$
Charge dynamics	$q_i =$ constant	$\partial q_d / \partial t =$ net current
Massive particle mass	m_i	$m_d \gg m_i$
Plasma frequency	ω_{pi}	$\omega_{pd} \ll \omega_{pi}$
Debye radius	λ_{De}	$\lambda_{Di} \ll \lambda_{De}$
Particle size	uniform	dust size distribution

by the electric and magnetic fields thus could participate in the overall plasma system.

In most cases, the dust radius $r_d \ll \lambda_D$, and the dust can be assumed to be spherical in shape with its radius and mass fall under certain type of distribution. The large radius also allows the dust particle to hold on to more than one electrical charge ($Z_d > 1$). The charge on a single dust particle is given by $q_d = qZ_d$ where $q = e$ positive for positively charged dust particle and $q = -e$ for negatively charged dust particle.

2.5.2 Dusty Plasma Characteristics

Important parameters of dusty plasma include dust grain radius (r_d), average distance between grains (a), plasma Debye radius (λ_D), and the dust cloud dimension. Two different regimes are recognised; (i) an isolated dust where $r_d \ll \lambda_D < a$ and (ii) ensemble dust grain where $r_d \ll a < \lambda_D$. The former case is referred to as dust-in-plasma where dust particles are electrically isolated from each other and resemble a probe immersed in plasma. The latter is known as dusty plasma where particles are closely packed and their properties can be describe collectively.

Macroscopic Neutrality

In a large scale, dusty plasma is said to be electrically neutral. In the absence of external forces, quasineutrality is observed at equilibrium which can be stated as

$$q_i n_i = e n_e - q_d n_{d0} \tag{2.49}$$

where n_{i0}, n_{e0} and n_{d0} are the density for ion, electron and dust respectively. $q_i = Z_i e$ is the charge for the ion species where $Z_i = 1$ for singly charged ion while $q_d = Z_d e(-Z_d e)$ is dust charge where Z_d is the dust charge number. The number of charge Z_d on a dust particle can vary from few unit charge to thousands of unit charge depending on plasma parameters, dust density and the dominant charging current. The charged dust changes the collective behaviour of the plasma which includes allowing the formation of electric field within the plasma, altering local plasma potential profile, modifying particle trajectories in the plasma, and modifying and introducing new plasma waves such as dust acoustic waves and dust ion acoustic waves [Shukla, 2001, Fortov et al., 2004].

Debye shielding

In this case of dusty plasma, Poisson's equation (2.9) is generalised to include the presence of dust particles, i.e.,

$$\nabla^2 \Phi = \frac{\rho_q}{\varepsilon_0} = \frac{e}{\varepsilon_0} \left(n_e - n_i - q_d n_d \right). \tag{2.50}$$

The solution to (2.50) is given by [Shukla, 1994]

$$\nabla^2 \Phi = \left(\frac{1}{\lambda_{De}^2} + \frac{1}{\lambda_{Di}^2} \right) \Phi \tag{2.51}$$

where λ_{De}^2 and λ_{Di}^2 are the electron and ion Debye length given by

$$\lambda_{De} = \sqrt{\frac{\varepsilon_0 k_B T_e}{n_{e0} e^2}} \tag{2.52}$$

and

$$\lambda_{Di} = \sqrt{\frac{\varepsilon_0 k_B T_i}{n_{i0} e^2}}. \tag{2.53}$$

The dusty plasma Debye length is given by [Shukla, 1994]

$$\lambda_D = \frac{\lambda_{De} \cdot \lambda_{Di}}{\sqrt{\lambda_{De} + \lambda_{Di}}} \tag{2.54}$$

where the dominant length depends on dust grain charge. In a negatively charge dust grains, the lack of free electrons means $n_e 0 \ll n_i 0$ which results in $\lambda_{De} \gg \lambda_{Di}$, consequently, $\lambda_D \simeq \lambda_{Di}$. In a positively charged dusty plasma, the opposite is true since $\lambda_{De} \ll \lambda_{Di}$.

Characteristic Frequencies

Dust plasma frequency can be derived in a similar fashion as in equation (2.40). In a cold, unmagnetized dusty plasma, the plasma frequency is given by [Shukla and Mamun, 2002]

$$\omega_p^2 = \sum_s \omega_{ps}^2 \tag{2.55}$$

where $s = i, e$ and d for electrons, ions and dust repectively. This is similar to (2.40) with additional dust plasma frequency given by

$$\omega_{p,d}^2 = \frac{n_d Z_d^2 e^2}{\varepsilon_0 m_d} \tag{2.56}$$

where the charge of the dust is taken into account in the calculation.

Collision frequency

Collision with neutral particles is also an important characteristic frequency in dusty plasma. There are three frequencies of interest, electron-neutral collision frequency, ν_{en}, ion-neutral collision frequency, ν_{in}, and dust-neutral collision frequency, ν_{dn}.

The collision frequency for species s is given by

$$\nu_{sn} = n_n \sigma_s^n v_{th,s} \tag{2.57}$$

where n_n is the neutral number density, σ_s^n is the scattering cross section and $v_{th,s}$ is the species thermal speed.

Coulomb Coupling Parameter

Coulomb coupling parameter Γ_c is the ratio of the dust potential energy to the dust thermal energy and is given by [Shukla, 2001]

$$\Gamma_c = \frac{q_d^2}{a k_B T_d} \exp\left(-\frac{a}{\lambda_D}\right). \tag{2.58}$$

It determines the coupling between the dust grain which indicates the likeliness of the cloud forming a dusty plasma crystal. Dusty plasma is strongly coupled when $\Gamma_c \gg 1$ and weakly coupled when $\Gamma_c \ll 1$. From (2.58) it is obvious that the grain charge q_d , the intergrain to Debye length ratio a/λ_D, and the dust thermal energy $k_B T_d$ play an important role in the formation of crystallised dust.

2.5.3 Dust Charging Process

The dust charging process can be described by three (3) elementary processes; (i) interaction with ambient plasma particles, (ii) interaction with energetic plasma particles, and (iii) interaction with photons from solar UV. Dust charging occurs when the surface tries to balance the current entering and leaving the surface. At this state the dust is considered to be in equilibrium, and the surface is charged to what is known as *floating potential*.

The whole process can be summed up by the current balance equation, i.e.

$$\sum I_e + I_i + I_{ph} + I_{sec} = 0 \tag{2.59}$$

where I_e and I_i is the current by the ambient plasma (electrons and ions), I_{ph} is photoelectron current and I_{sec} is the secondary emission current due to interactions with energetic plasma particles. The charging level will then depend on the dominant current flowing in and out of the dust particle which causes the dust to charge to either positive or negative potential.

Single dust charging

In the case of dust-in-plasma, the dust is in isolation when $r_d \ll \lambda_D \ll a$. The isolation implies that the motion of free electrons and ions are not affected by nearby dust particles such that any change on their approach towards the dust particle are only due to the space charge created by the dust particle. The dust-plasma interaction is then similar to the case of a probe immersed in plasma and the interaction can be approximately modelled by the Orbit Motion Limited (OML) theory [Bernstein and Rabinowitz, 1959, Chen, 1965, Whipple, 1981]. This approach uses the laws of conservation of energy and angular momentum to determine electrons and ions collection by the dust particle.

Consider a plasma particle species s with mass m_s and initial velocity v_s approaching a dust particle of radius r_d with charge q_d from infinite distance. Upon entering the Debye sheath, the particle experiences either attractive or repulsive force which alters its trajectory. Particle s could either hit the surface and be collected or could be scattered away from the dust particle depending on the resulting force between the dust and the particle. This collision process is shown in Figure 2.8. In the figure, an incident particle grazes past the dust particle and leaves with velocity $v_{g,s}$. Assuming the scattering process changes the particle's trajectory while maintaining the particle's speed, it can be deduced that collision can only happen when $\rho_c < \rho$, where ρ_c is the impact parameter for collision. The collision cross section between the two particles is a function of ρ_c which is given by

$$\sigma_s^d = \pi \rho_c^2. \tag{2.60}$$

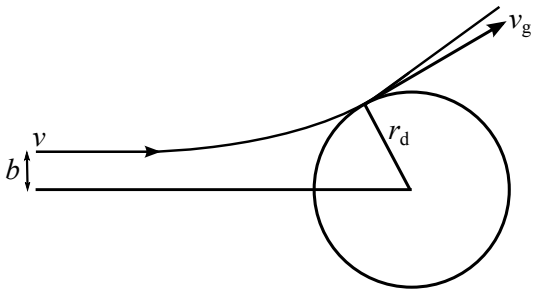

Figure 2.8: Grazing collisions between plasma particle s and a charged dust particle with $q_s q_d < 0$.

Conservation of momentum and energy require that

$$m_s v_s \rho_c = m_s v_{g,s} r_d \tag{2.61}$$

and

$$\frac{1}{2} m_s v_s^2 = \frac{1}{2} m_s v_{g,s}^2 + \frac{q_s q_d}{r_d}. \tag{2.62}$$

Solving for ρ_c^2 using (2.62) and (2.61), one ends up with [Shukla, 2001]

$$\rho_c^2 = r_d^2 \left(1 - \frac{2 q_s q_d}{r_d m_s v_s^2} \right) \tag{2.63}$$

and substituting into (2.60) gives

$$\sigma_s^d = \pi r_d^2 \left(1 - \frac{2 q_s q_d}{r_d m v_s^2} \right). \tag{2.64}$$

The dust charge q_d fluctuates because of the currents as in equation (2.59),

$$\frac{\mathrm{d}\, q_d}{\mathrm{d}t} = \sum_s I_s. \tag{2.65}$$

and is related to the dust charge number Z_d via $q_d = eZ_d$. The potential φ_d is the difference between the dust grain potential φ_g and plasma potential φ_p, i.e. $\varphi_d = \varphi_g - \varphi_p$, and is related to q_d by

$$q_d = C \varphi_d \tag{2.66}$$

where C is the capacitance of the grain approximated by [Whipple et al., 1985]

$$C \approx r_d \exp\left(-r_d/\lambda_D\right). \tag{2.67}$$

For $\lambda_D \gg r_d$, the capacitance can be approximated by r_d, i.e. $C \simeq r_d$, which gives $q_d = r_d \varphi_d$.

For a negatively charged dust particle, the collision cross section can be written as

$$\begin{aligned} \sigma_e(v_e) &= \begin{cases} \pi r_d^2 \left(1 + \frac{2e\varphi_d}{m_e v_e^2}\right), & \frac{2e\varphi_d}{m_e v_e^2} > -1 \\ 0, & \frac{2e\varphi_d}{m_e v_e^2} < -1 \end{cases} \\ \sigma_i(v_i) &= \pi r_d^2 \left(1 - \frac{2e\varphi_d}{m_i v_i^2}\right), \end{aligned} \tag{2.68}$$

where v_e and v_i are the electron and ion velocity respectively with ions are singly charged protons. From (2.68), a collision between electron and the negatively charged surface can only happen if the electron has sufficient energy to overcome the barrier induced by the dust's surface potential. On the other hand, ion is attracted to the dust particle and collision can happen over the whole velocity domain.

The flux of electrons and ions to the surface can be obtained by integrating their collision cross section with their velocity distribution function $f_s(v)$, i.e.

$$I_s = n_s \int v \sigma_s(v) f_s(v) \, \mathrm{d}^3 v. \tag{2.69}$$

Assuming the charging process happens in a Maxwellian plasma as in (2.2), the ambient plasma flux into the dust surface in (2.69) can be solved for the two cases of current collection; retardation and attraction current which are given by [Bernstein and Rabinowitz, 1959, Chen, 1965, Whipple, 1981]

$$I_s = 4\pi r_d^2 n_{s0} q_s \sqrt{\frac{k_B T_s}{2\pi m_s}} \left(1 - \frac{q_s \varphi_d}{k_B T_s}\right) \quad \text{for } q_s \varphi_d < 0 \tag{2.70}$$

and

$$I_s = 4\pi r_d^2 n_{s0} q_s \sqrt{\frac{k_B T_s}{2\pi m_s}} \exp\left(-\frac{q_s \varphi_d}{k_B T_s}\right) \quad \text{for } q_s\varphi_d > 0 \tag{2.71}$$

respectively.

In a case where the ions have some finite streaming speed, the Maxwellian velocity distribution for the ions can be written as [Whipple, 1981, Shukla, 2001]

$$f_i(\mathbf{v}) = n_i \left(\frac{m_i}{2\pi k_B T_i}\right)^{3/2} \exp\left[-\frac{m_i(\mathbf{v_i} - \mathbf{u_i})^2}{2k_B T_i}\right] \tag{2.72}$$

where $\mathbf{u}$ is the average ion velocity . For a negatively charged dust particle, the ion current collection can be calculated using the same procedure which gives

$$I_i = 4\pi r_d^2 n_i q_i \sqrt{\frac{k_B T_i}{2\pi m_i}} \left(F_1(u_0) - F_2(u_0)\frac{q_i \varphi_d}{k_B T_s}\right) \quad \text{for } q_i\varphi_d < 0. \tag{2.73}$$

where $F_1(u_0) = (\sqrt{\pi}/4u_0)(1+2u_0^2)\mathrm{erf}(u_0) + (1/2)\exp(-u_0^2)$ and $F_2(u_0) = (\sqrt{\pi}/2u_0)$ $\mathrm{erf}(u_0)$ are given by an error function $\mathrm{erf}(u_0) = (2/\sqrt{\pi}\int_0^{u_0}\exp(-t^2)\,\mathrm{d}t$ and $u_0 = v/v_{th}$. For ion drift speed less than the thermal speed, i.e. $u_0 \ll 1$, the solution for the ion current approaching the solution presented in (2.71). If $u_0 \gg 1$, ion current can be approximated by

$$I_i \simeq \pi r_d^2 q_i n_i v_i \left(1 - \frac{2q_i\varphi_d}{m_i u^2}\right) \tag{2.74}$$

Taking only currents due to the ambient plasma and assuming that $T_e \sim T_i$, an isolated dust particle is expected to charge to negative potential because of the higher electrons' thermal velocity compared to ions' thermal velocity. In this case, the particle's surface potential is $-2.51k_BT_e/e$ for hydrogen plasma and $-3.6k_BT_e/e$ for oxygen plasma [Northrop, 1992].

Validity of Orbit Motion Limited (OML) theory

One important assumption in the implementation of OML is the lack of consideration for the exact form of the electrostatic potential around the dust in the

determination of collision cross section (equation (2.68)). This limitation means the OML theory only valid if the potential satisfies certain condition. For example, the motion of an ion approaching a negatively charged dust particle depends on the *effective interaction potential* U_{eff}, in addition to the attractive electrostatic potential U_r. U_{eff} is a function of the attractive potential U_r and contains a component related to centrifugal repulsion due to ion angular momentum conservation. The effective potential normalised to the ion's kinetic energy is given by [Fortov et al., 2005]

$$U_{eff}(r,\rho) = \frac{\rho^2}{r^2} + \frac{U(r)}{E} \tag{2.75}$$

where r is the distance from the dust's surface, ρ is the impact parameter, and $U(r) < 0$ ($q_s q_d < 0$). The distance of the closest approach r_0, is the distance that determines whether the ion will be collected by the dust surface which happens when $U_{eff}(r_0,\rho) = 1$ for any given ρ. This means for $r_0 \leq r_d$, the solution for $U_{eff}(r_0,\rho) = 1$ dictates that the ion particle will be collected by the dust surface while for $r_0 > r_d$, ion is pulled towards the surface by elastic scattering but does not reach the surface. Replacing $r_0 = r_d$ and $U(r_d) = e\varphi_d$ in equation (2.75), the maximum impact parameter for ion is

$$\rho_c^{OML} = r_d\sqrt{1 - \frac{2e\varphi_d}{m_i v_i^2}} \tag{2.76}$$

which is the same as the impact parameter given in (2.63).

The equation $U_{eff}(r,\rho) = 1$ however does not necessarily results in one solution and has been shown to have multiple roots under certain condition [Allen, 2000]. Unique solution to the equation only exists if the decrease in electrostatic potential is more slowly than $1/r^2$. In reality, $|U(r)| \propto 1/r$ close to the particle, but further away, $U(r) \propto 1/r^2$. In this case, the solution to $U_{eff}(r,\rho) = 1$ can have multiple roots where the distance r_0 is given by the largest ρ. As a result, a potential barrier appear at $r_0 > \lambda_D > r_d$ where some of ions are reflected from the surface instead of being collected by the surface [Khrapak et al., 2003]. When this happens, OML

solution over-estimates ion current to the dust particle which gives lower stationary dust charge number. This effect is significant for slow ion species although in most cases the difference is small and can be neglected [Fortov et al., 2004]. Detailed explanation of this condition is treated in Fortov et al. [2005] and in Allen [1992, 2000] and references therein.

Charging of ensemble dust particles

In reality, dust particles can be densely packed such that $r_d \ll a \ll \lambda_D$. In this case, dust particles interact with each other and participate in the plasma collective behaviour. The dust particles are now not in isolation and the OML theory presented before needs to include the effect caused by the increase in dust density.

The charging of a dusty plasma system is done by considering the charge neutrality condition, i.e equation (2.49) which determines average charge on each dust particle. Increase in dust density results in a lower charge number per dust particle as there are more dust particles competing for the same number of plasma particles. Havnes et al. [1987] introduced the parameter $P = T_{eV} r_{d,\mu} n_{d0}/n_0$ which describes the collective behaviour of a dust cloud in space plasmas, where $r_{d,\mu}$ is the dust radius in micron and T_{eV} is the plasma temperature in eV. In a later paper, Havnes et al. [1990] reintroduced the P parameter as

$$P = 6.95 \times 10^6 T_{eV} r_d n_d / n_{e0} \tag{2.77}$$

where r_d is now the dust radius in centimetre and P is a factor 695 times larger than the old P parameter. At a low P value e.g. at $P < 1$, the dust particle has been shown to charge to the value similar to an isolated dust particle and plasma quasineutrality is a good approximation. However, as P increases, the high number of plasma particles absorption by the dust particles result in a perturbed plasma as the dust collective effects become increasingly significant [Havnes et al., 1987, 1990]. This results in on average lower number of unit charge on each dust particle

as the particles are now competing for the same number of plasma particles.

Secondary electron emission

There are many different processes that can happen when an electron strikes a dust grain surface. An incident electron with primary energy E_p can be reflected, scattered, absorbed, and can produce secondary emission or be tunnelled through the dust grain [Shukla and Mamun, 2002]. The type of interaction between the incidence electron and dust particle depends on the electron's primary energy, the dust particle's charge q_d and the dust radius. A negatively charged dust shields incoming electron such that any incidence electron needs to overcome the potential barrier before it can be collected. Low energy electrons ($E_p < \phi_d$) which are unable to overcome the potential barrier will be reflected or backscattered while ones with enough energy to overcome the potential barrier ($E_p > \phi_d$) could be absorbed by the surface. The absorption of electrons by the surface also depends on the dust radius (or diameter) because electrons with different energy levels will produce different types of interaction. Electrons with just enough energy to overcome the potential barrier are collected by the surface whereas ones with higher energy can either penetrate deep into the dust grain or tunnel through the grain. During these processes, energy from the primary electron is transferred to electrons residing inside the dust grain, exciting them with energy to travel towards the surface. These electrons are then emitted as secondary electrons and could reduce the number of unit electron on the dust.

The general theory on secondary electron emission has been developed by Sternglass [1954] who considered emission of electrons from a semi infinite slab of material using theoretical approximation of Jonker [1952]. The formula however will underestimate the secondary electron yield in the case of small dust particle since it only considers emission from one surface of the material, i.e. the plane surface where plasma particles are incidence. For a very small dust particle, secondary electrons could be emitted at any angle from the point of incidence, due to the

short travelling distance involved.

Chow et al. [1993] introduced a new model for the calculation of secondary electrons from small spherical dust grain also based on the work by Jonker [1952]. In the model, Chow et al. [1993] assumed (i) the energy loss of the primary electrons can be described by the Whiddington's law [Whiddington, 1912], (ii) the primary electron current density is conserved within the grain, (iii) the yield is proportional to the energy loss of the primaries, (iv) the secondary flux decreases exponentially with distance to the surface from the point of production and (v) primary electrons are incident normal to the grain. With these assumptions, Chow et al. [1993] modified the yield equation in Jonker [1952] and showed that the resulting secondary electron yield in dusty plasma is higher than the yield from slab of material as discussed by Sternglass [1954] and Jonker [1952] .

The secondary electron yield by primary electrons is given by [Chow et al., 1993]

$$\delta_s(E_p) = \frac{1}{2}\int_0^{\min(r_d, x_{\max})} K_s K_W \left(E_p^2 - K_W x\right)^{-1/2} f(x)\,\mathrm{d}x \tag{2.78}$$

where E_p is the energy of the electron just before impact, r_d is the grain radius, x_{max} is the maximum distance travelled before the electron is stopped by the grain, K_s is energy transfer efficiencies, K_W is the Whiddington's constant for energy loss with distance [Whiddington, 1912], x is the penetration depth ($x = 0$ at surface,$x = x_{max}$ at maximum penetration depth and $x = r_d$ if the electrons pass through the grain). The function $f(x)$ in (2.78) is given by

$$f(x) = \frac{1}{2}\int_0^{\pi} \exp\left(-\alpha\, l\,(x,\theta)\right)\sin\theta\,\mathrm{d}\theta \tag{2.79}$$

where

$$l(x,\theta) = \left[r_d^2 + (r_d - x)^2 - 2r_d\,(r_d - x)\cos\theta'\right]^{1/2} \tag{2.80}$$

with $\theta' = \theta - \sin^{-1}\left[(r_d - x)\sin\theta/r_d\right]$, α is the inverse of the absorption length for secondaries and $l(x,\theta)$ is the distance travelled by the excited electrons to reach the surface of the grain [Chow et al., 1993] . The model geometry for secondary

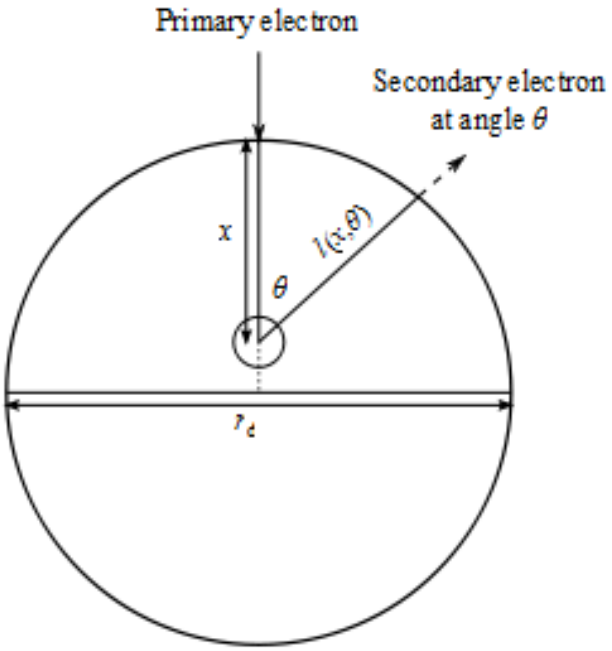

Figure 2.9: Primary electron entering a spherical grain at normal incidence. Along its path, electrons are excited and could make to the surface isotropically due to the small grain radius (after Shukla and Mamun [2002]).

emission by dust grain is shown in Figure 2.9.

The absorbed electron may stop at a distance x_{max} from the surface or continue travelling until it passes through the whole grain (r_d). At x_{max}, electron energy is $E(x) = 0$. From Whiddington's law, the amount of energy lost by the primary electron is given by

$$E(x) = \left(E_p^2 - K_W x\right)^{1/2} \tag{2.81}$$

where the maximum penetrating depth is $x_{max} = E_p^2/K_W$. Penetrating electron tunnels through the whole grain if their initial energy is

$$E_p > (K_W r_d)^{1/2}. \tag{2.82}$$

The secondary electron yield δ_s depends on the grain size as can be seen in (2.80), as well as energy of the incident electron (equation (2.78)). In summary, the secondary electron yield can be described to have the following characteristics;

1. At low primary electron energy, a smaller dust particle produces more sec-

ondary emission than a larger dust particle because of shorter penetration depth which means the resulting secondary electrons are closer to the surface hence are more likely to reach the surface. In addition, secondary electrons can be emitted isotropically from a small grain because of large x_{max}/r_d ratio, but are more likely to be emitted from just one side of the grain for a large dust particle due to smaller x_{max}/r_d.

2. At high primary electron energy, a smaller dust particle produces less secondary electrons than a larger dust particle because the primary electron is more likely to tunnel through the smaller dust particle than being stopped. Whiddington's law states that primary electrons lose more energy at the end of their path, i.e. when they are being slowed down which means the majority of secondary electrons are produced near x_{max}. A larger dust particle ensures that primary electrons are stopped inside the grain which would allow for higher secondary yield.

The secondary electrons current is given by Meyer-Vernet [1982] as

$$\begin{aligned} I_s &= \tfrac{8\pi^2 r_d^2 e}{m_e^2} \int_0^\infty E\delta_s(E) f_e(E - e\varphi_d)\,\mathrm{d}E && \varphi_d \leq 0 \\ I_s &= \tfrac{8\pi^2 r_d^2 e}{m_e^2} \exp\left(-\tfrac{e\varphi_d}{kT_{se}}\right)\left(1 + \tfrac{e\varphi_d}{kT_{se}}\right) \int_{e\varphi_d}^\infty E\delta_s(E) f_e(E - e\varphi_d)\,\mathrm{d}E && \varphi_d \geq 0 \end{aligned} \tag{2.83}$$

where $k_{T_{se}}$ is the thermal energy of the secondary electrons. Assuming the secondary electrons are emitted with Maxwellian energy distribution, $f(E - e\varphi)$ can be expressed following Goertz [1989] and Meyer-Vernet [1982] as

$$f_e(E - e\varphi_d) = n_e \left(\frac{m_e}{2\pi k T_e}\right)^{3/2} \exp\left(-\frac{E - e\varphi_d}{m_e}\right). \tag{2.84}$$

Goertz [1989] found that the energy of these secondary electrons are small (1-5 eV) regardless the energy of the incident electrons.

This gives secondary electron current for positively and negatively charged dust

particles as

$$\begin{aligned} I_s &= C\int_0^\infty E\delta_s(E)\exp\left(-\tfrac{E}{k_BT_e}\right)\mathrm{d}E & \varphi_d \le 0 \\ I_s &= C\exp\left(-\tfrac{e\varphi_d}{k_BT_e}\right)\left(1+\tfrac{e\varphi_d}{k_BT_e}\right)\int_{e\varphi_d}^\infty E\delta_s(E)\exp\left(-\tfrac{E}{k_BT_e}\right)\mathrm{d}E & \phi_d \ge 0 \end{aligned} \tag{2.85}$$

where

$$C = 4\pi r_d^2 n_e e\left(\frac{k_BT_e}{2\pi m_e}\right)^{1/2}\frac{1}{(k_BT_e)^2}\exp\left(\frac{e\varphi_d}{k_BT_e}\right).$$

Photoemission

Photoemission refers to emission of electrons from the material surface due to incident photons with energy (hv) greater than the material work function (Wf), where h is the Planck's constant ($h = 6.626068 \times 10^{-34}\mathrm{m^2kg/s}$) and v is the photon frequency. For dust particles, emission depends on three factors [Shukla and Mamun, 2002], (i) wavelength of the incident photons, (ii) dust surface area and (iii) dust grain material properties. On a positively charged dust grain, photoelectrons may return to the surface and be recollected because of the surface's potential barrier. These photoelectrons will only be emitted if they have sufficient energy to escape the attractive force of the surface.

The photoelectron current is given by [Rosenberg and Mendis, 1996]

$$I_{ph} = \pi r_d^2 e J_p Q_{ab} Y_p \exp\left(-\frac{e\varphi_d}{k_BT_{ph}}\right) \tag{2.86}$$

where J_p is the photon flux, Q_{ab} is the efficiency of the absorptions of photons, Y_p is the photoelectron yield and T_{ph} is their average temperature, assuming the emitted electrons have Maxwellian distribution with temperature T_{ph}. The exponential terms in the equation refers to the energy required by the emitted electrons to overcome the potential barrier of the dust.

In the case of a negatively charged surface, the emitted photoelectrons will not return to the dust grain surface, which results in constant current given as

$$I_p = \pi r_d^2 e J_p Q_{ab} Y_p \tag{2.87}$$

2.5.4 Dust Dynamics

A charged dust motion follow the same equation as the plasma species with the addition of multitude of other forces such as the gravitational force ($\mathbf{F}_g$), Coulomb drag force ($\mathbf{F}_c$) and neutral drag ($\mathbf{F}_n$) given by

$$\begin{aligned} m_d \frac{\mathrm{d}\mathbf{V}_d}{\mathrm{d}t} &= Q_d(t)\left(\mathbf{E} + \mathbf{V}_d \times \mathbf{B}\right) + \mathbf{F}_g + \mathbf{F}_c + \mathbf{F}_n \\ \frac{\mathrm{d}\mathbf{X}_d}{\mathrm{d}t} &= \mathbf{V}_d \end{aligned} \tag{2.88}$$

where d refers to dust.

Gravitational force

The study of gravitational force acting in tandem with electromagnetic force is known as gravito-electrodynamics [Mendis et al., 1982, Goertz, 1989]. Gravitational force is determined by

$$F_g = m_d g, \tag{2.89}$$

where g is the gravitational acceleration. Gravitational force is most significant when dust particles are in the vicinity of large celestial object. Nevertheless, smaller object such as asteroids or even spacecraft could also contribute to the total gravitational force acting on the dust particle.

Ion drag force

The interaction between dust particles and ions consists of (i) collision impact, (ii) electrostatic Coulomb collision and (iii) ion fluid flow effects [Khrapak, 2002], with the latter having a negligible effect [Northrop and Birmingham, 1990]. The first term refers to momentum transfer due to direct collision between the ion particle and the dust particle. It is a function of collision cross section ((2.60)) and can be expressed as [Barnes et al., 1992, Shukla and Mamun, 2002]

$$\mathbf{F}_i^{coll} = \pi r_d^2 n_i m_i v_{i,tot} \mathbf{v}_i \left(1 - \frac{2e\varphi_d}{m_i v_i^2}\right) \tag{2.90}$$

where $v_{i,tot} = (v_i^2 + 8k_B T_i/\pi m_i)^{1/2}$ is the total velocity of the ion, which is the ion drift and thermal velocity.

The electrostatic Coulomb collision, also known as Coulomb drag is the force related to the scattering of the ion as it passes close to the dust. It is given as [Barnes et al., 1992]

$$\mathbf{F}_i^{coul} = 2\pi b_0^2 n_i m_i v_{i,tot} \mathbf{v}_i \ln\left(\frac{b_0^2 + \lambda_{De}^2}{b_0^2 + b_c^2}\right) \tag{2.91}$$

where $b_0 = r_d \frac{e\varphi_d}{m_i v_i^2}$ is the impact parameter, $b_c = r_d \left(1 - \frac{2e\varphi_d}{m_i v_i^2}\right)^{1/2}$ is the direct collision impact parameter. The calculation of Coulomb drag force is to exclude the force from the direct impact.

Neutral drag force

A particle moving in a weakly ionised plasma experiences resistive force as it moves through the medium. The resistance is mainly caused by neutral atoms and molecules and is a function of the dust particles' average velocity u_d which is normally less than the neutral thermal velocity $V_{n,th}$. There are two regimes of neutral drag force depending on Knudsen number K_n, where $K_n = l_n/r_d$ and l_n is the molecular free path. The first regime where $K_n \ll 1$ is called the hydrodynamic regime [Fortov et al., 2004], and the expression for F_n is given by the Stokes' law

$$F_n = -6\pi\eta r_d u_d \tag{2.92}$$

where η is the neutral gas' viscosity and the negative sign indicates the vector is in opposite direction with the particle velocity. The second regime is when $K_n \gg 1$, which is often called as free molecular regime, is the most likely case for dusty plasma. For $u \ll v_{n,th}$, F_n is given by [Epstein, 1924]

$$F_n = -\frac{8\sqrt{2\pi}}{3}\gamma r_d^2 n_n T_n \frac{u_d}{v_{n,th}} \tag{2.93}$$

where γ is a coefficient depending on the subsequent process happening on the surface of the dust, for example $\gamma = 1$ for absorption or reflection and $\gamma = 1 + \pi/8$ for diffuse scattering [Fortov et al., 2004].

2.5.5 Dusty Plasma in Solar System

Dust particles can be found in abundance in solar system. It is believed that the formation of the solar system from its nebula stage to its present form is a result of processes involving dust particles. For example, meteorites, comets and planets are believed to form through coagulation of dust that happen when the solar system was still in its nebula stage [Goertz, 1989] . Dust particles however are not evenly distributed throughout the solar system, mainly due to the electric and magnetic forces that act on them, in addition to the gravitational force exerted by large celestial body.

Dusty Plasma in Earth Atmosphere

During the summer months, a *shining night cloud* also known as the noctilucent clouds (NLCs) can be observed in the high latitude mesosphere. Early observations have confirmed that the clouds are extremely low in temperature which lead to suggestion that they were composed of ice particles [Cho and Kelley, 1993, Havnes et al., 1996b]. These ice particles can be charged by free electrons or via UV irradiation thus creating a dusty plasma region. In addition to the NLCs, another phenomena that suggests the presence of ice dust particles in the polar mesosphere is the radar backscatter known as the Polar Mesospheric Summer Echoes (PMSE) which happens at frequencies of 50MHz to 1.3 MHz . At the PMSE altitude, there is electron depletion region and ion density enhancement which is believed to be caused by positively charged dust particles where the charge density is larger than electron and ion density. The high dust charge number is due to the photoelectron process [Goertz, 1989, Havnes et al., 1996b] as without it, dust particles would only be charged to low Z_d.

Table 2.6: Approximate values of some dusty plasma environment on Earth's atmosphere [Shukla and Mamun, 2002].

Characteristics	NLCs	Rocket exhausts	Flames
$n_e(\mathrm{m}^{-3})$	10^9	10^{19}	10^{18}
$T_e(\mathrm{K})$	150	3×10^3	2×10^3
$n_d(\mathrm{m}^{-3})$	10^7	10^{14}	10^{17}
$r_d(\mu\,\mathrm{m})$	0.1	0.1	0.01
$n_n(\mathrm{m}^{-3})$	$\sim 10^{14}$	10^{24}	10^{25}
a/d	0.2	≤ 5	≤ 1

Charged dust particles in the Earth atmosphere are not limited to the ice particles in the NLCs. Meteoric dust has been suggested to be another source of dust particles in the atmosphere [Peucker-Ehrenbrink and Schmitz, 2001]. In addition, man made pollutions also contribute a significant number in the Earth's atmosphere such as terrestrial aerosols where 90% of the dust is in the form of aluminium oxide (Al_2O_3) [de Angelis, 1992]. Table 2.6 list properties of dust usually found in the Earth's atmosphere and their origin.

Dusty Plasma in Space

Dusty plasma can be found in the interplanetary space, comets, and in the planetary rings of Jupiter, Saturn, Uranus and Neptune. Most of the interplanetary dust grains come form asteroid collisions in the asteroid belt as well as dust emission from comets. Another example of dust particles in space is the observation of zodiacal light which happens when sunlight is reflected off dust particles in the solar system [Nesvorny et. al, 2010]. It is found that majority of these grains are rich in carbon, with the rest are made from submicrometer mineral and interstellar silicates. Almost 40000 tonnes of the grains reach the Earth's atmosphere each year, and collection by NASA shows that most of them are 5 - 10 mm in size [de Angelis, 1992]. Typical parameters of dust-laden plasmas of the interplanetary dust and from Halley's comet are given in Table 2.7.

Dust in the form of ice particle is the main constituent in the rings of Jupiter, Saturn, Neptune and Uranus. Phenomena such as the formation of spokes in the Saturn ring is believed to be caused by charged dust particles which play an

Table 2.7: Typical parameters of dust-laden plasmas of the interplanetary dust and from Halley's comet [Shukla and Mamun, 2002].

Characteristics	Zodiacal dust disc	Inside ionopause	Outside Ionopause
$n_e(\mathrm{m}^{-3})$	5×10^6	$10^9 - 10^{10}$	$10^8 - 10^9$
$T_e(\mathrm{K})$	10^5	$\leq 10^3$	$\sim 10^4$
$n_d(\mathrm{m}^{-3})$	10^{-6}	10^{-3}	$10^{-8} - 10^{-7}$
$r_d(\mu\,\mathrm{m})$	$2 - 10$	$0.1 - 10$	$0.01 - 10$
$n_n(\mathrm{m}^{-3})$	–	10^{10}	–
a/d	5	≥ 1	≥ 10

Table 2.8: Typical parameters of Saturn's ring [Shukla and Mamun, 2002].

Characteristics	E ring	F ring	Spokes
$n_e(\mathrm{m}^{-3})$	~ 10	~ 10	$0.1 - 10^2$
$T_e(\mathrm{K})$	10^5	$10^5 - 10^6$	$\sim 10^4$
$n_d(\mathrm{m}^{-3})$	10^{-7}	≤ 10	~ 1
$r_d(\mu\,\mathrm{m})$	~ 1	1	~ 1
$n_n(\mathrm{m}^{-3})$	–	–	–
a/d	0.1	$\leq 10^{-3}$	$\leq 10^{-2}$

important role in the maintenance of these ring systems [Goertz, 1989]. Recent observations of the Saturn's ring from the Cassini mission has confirmed that the dust dynamics in the rings is due to Saturn's magnetic field acting on electrically charged dust particles, in addition to the effect of streaming solar wind [Hsu et al., 2012]. It is now accepted that the motion of dust in the planetary rings needs to be explained not only in terms of its Keplerian motion but also in terms of its electrostatic induced motion. This has led to a new field of study known as 'gravitoelectrodynamics'. Table 2.8 gives nominal values for Saturn's ring.

Chapter 3

Plasma Simulation

3.1 Introduction

The role of plasma simulation is to provide an insight into plasma behaviour without having to physically perform a laboratory experiment, especially when such experiment is not possible or highly expensive. From the previous chapter, it can be seen that almost everything in space is made of plasma; the sun, stars, the Earth's ionosphere, Van Allen belts and megnetosphere, hence understanding plasma process is very important. In addition, many man made processes involve working with plasma, from electrons and ion guns to nuclear power plant [Chen and Lieberman, 1984], which means it is imperative to have a degree of understanding on how the plasma would behave before any experiment is to be carried out. A comprehensive review on plasma simulation can be found in Birdsall [2005] and Hockney and Eastwood [1988].

Plasma can be simulated using fluid approach, a field known as magnetohydrodynamic (MHD), using kinetic approach, where individual particle is tracked by its 6-phase space parameters ($x, y, z, v_x, v_y \text{and} v_z$) or a combination of both [Hockney and Eastwood, 1988, Birdsall, 1991]. In all three models, it is important to correctly assume the velocity distribution of any species involved as not to lose any physics involved. In the fluid model, plasma is described by its macroscopic quatities, i.e. velocity moments of the distribution such as density, mean velocity and mean

energy. Plasma behaviour can be investigated by solving the Boltzmann's equation or the Vlasov's equation for these quantities, as well as finding the transport coefficients such as mobility, diffusion coefficient, collision frequency etc.

In simulations using kinetic approach, a group of particles (*superparticles*) are tracked from the moment the particles enter the simulation area/volume until they vanish by either simply leaving the area/volume or by other processes such as recombination, absorption, collision etc. These superparticles represent many particles (1000s) and they represent average quantities rather than each particles properties. This approach also require solving the same Boltzmann's or Vlasov's equations, but with the help of easily managed cells. The cell represent a small part of the entire area/volume, for which the equation of motion is solved for each superparticles located in the cell based on the forces present in the cell (for example E and B field). This process is performed on each cell in the simulation volume/area, and depending on correct choise of parameters, could present accurate description on the plasma behaviour.

The kinetic model is more accurate than the fluid model, but is more computationally and numerically expensive to perform. The combination of fluid and kinetic model, often called the hybrid model, enables the user to reduce the computational cost involved such as by simulating one species using the fluid model and another using the kinetic model.

This chapter will emphasis on the kinetic approach of the plasma modelling. Techniques discussed form the basis for the plasma simulation software, the Spacecraft Plasma Interaction Software (SPIS), which will be covered in the proceeding chapter.

3.2 Particle-In-Cell (PIC) method

The purpose of particle-in-cell (PIC) method is to solve the kinetic equations of plasma, i.e. Boltzmann's equation, Vlasov's equation and finally the equation of motion to determine the particle 6-dimensional phase space. Particles are

represented by the velocity distribution function ($f_s(\mathbf{r}, \mathbf{v}, t)$) where $\mathbf{r}$ and $\mathbf{v}$ are the spatial and velocity coordinate respectively. Instead of simulating all plasma particles, this method uses *superparticle* to represent a large number of particles (> 10000s). This would allow the extremely large number of particles in a plasma system to be efficiently simulated by considering only a fraction of the total number of particles in the system. This approach also takes advantage of the fact that plasma simulations are designed to study the collective behaviour of the plasma system rather than the motion of an individual particle in the system. Nevertheless, the number of superparticles used to represent the real particles in the simulation must be able to produce sufficient statistical characteristics of the plasma system in order to have a highly accurate representation of the system.

In essence, PIC method uses numerical techniques to solve (i) individual superparticles 6-phase space coordinate in a Langragian frame and (ii) self consistent field equations by solving the moments of distribution function on an Eulerian mesh [Birdsall, 1991]. PIC also known as Particle-Mesh (PM) method because particle motions are solved based on the average fields calculated on the mesh.

The self-consistent electric and magnetic fields can be calculated from the Poisson's equation ((2.9)) and Ampere's Law given by

$$\nabla \times \mathbf{B} = \mu_0 \mathbf{j} + \frac{1}{c^2} \frac{\partial \mathbf{E}}{\partial t}. \tag{3.1}$$

The charge density (ρ) and current density ($\mathbf{j}$) in (2.9) and (3.1) are calculated for a number of fixed point in space from the particles' moments of distribution function, i.e.

$$\rho(\mathbf{r}, t) = \sum_s q \int f_s \, \mathrm{d}^3 \, v \tag{3.2}$$

and

$$\mathbf{j}(\mathbf{r}, t) = \sum_s q \int \mathbf{v} f_s \, \mathrm{d}^3 \, v \tag{3.3}$$

where the summation is over all species present in the plasma.

Particles interactions can be summed up by interaction with a number of

particles (*cumulative effect*) rather than interactions with each individual nearby particle (by *Coulomb interaction*). A *mathematical spatial grids* or cells can then be introduced to simplify the problem of having to calculate interactions with each individual particle in the simulation area/volume by only measuring the quantities at fixed number of points (nodes). These cells or *mesh* are chosen such that they are fine enough to resolve the Debye length, and are used to measure the charge and current density and effectively calculate the electric field $\mathbf{E}$ and magnetic field $\mathbf{B}$.

An example of mathematical grid or mesh normally used in a plasma simulation is shown in Figure 3.1. In the figure, an equally spaced mathematical grid is applied on the plasma simulation area. A particle q with its own phase-space quantities is assumed to be located on the grid and surrounded by the grid points or *nodes*. The particle deposits its charge and current on the nearby nodes and face made by the nodes respectively using a *weighting* process, which takes into account the particle position and distance to the nodes. The ρ and $\mathbf{j}$ from this process are used to solve the field quantities using (2.9) and (3.1) for $\mathbf{E}$ and $\mathbf{B}$ on the nodes. The fields are then applied to the particle, again using a weighting process to solve the equation of motion (2.46) for the determination of the particle''s new position and velocity.

The overall computational process of PIC method is shown in Figure 3.2. The whole computational process (loop) is done over a time step (Δt) for a number of time steps, n, for a period of time t, i.e. $t = n\Delta t$. The number of time steps are usually user-controlled, but are often based on the total time for the plasma system to reach a certain condition, for example the equilibrium condition. Δt depends primarily on plasma frequency, and therefore can be varied based on each species' plasma frequency. For example, particles with relatively large ω_p such as electrons need to be moved over a smaller time step (Δt_e) compared to particles with lower ω_p such as ions (Δt_i), where $\Delta t_e < \Delta t_i$. This technique would allow for faster simulation because most of the time, calculations for particle's trajectory only involves one plasma species.

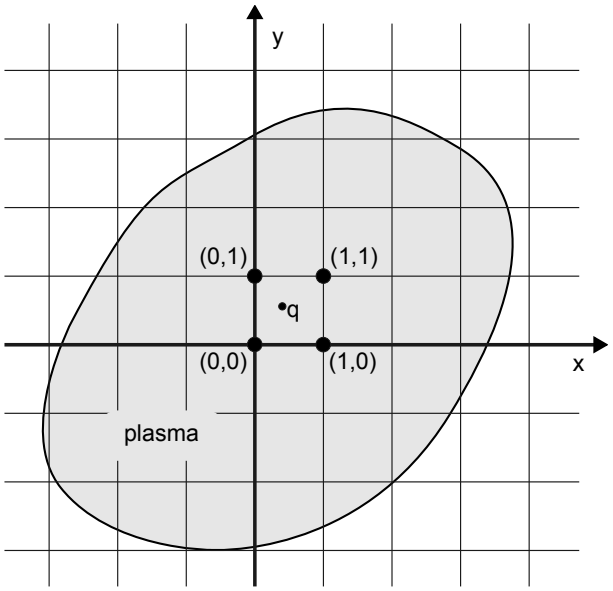

Figure 3.1: Example of mathematical grid use in plasma simulation. The simulation area/volume is divided into small manageable cells. Charge density ρ is measured on nearby nodes while current density $\mathbf{j}$ is measured on the face made by these nodes. These values are then used to calculate $\mathbf{E}$ and $\mathbf{B}$ which subsequently applied as a force on the particle q (adapted from Birdsall [1991]

.

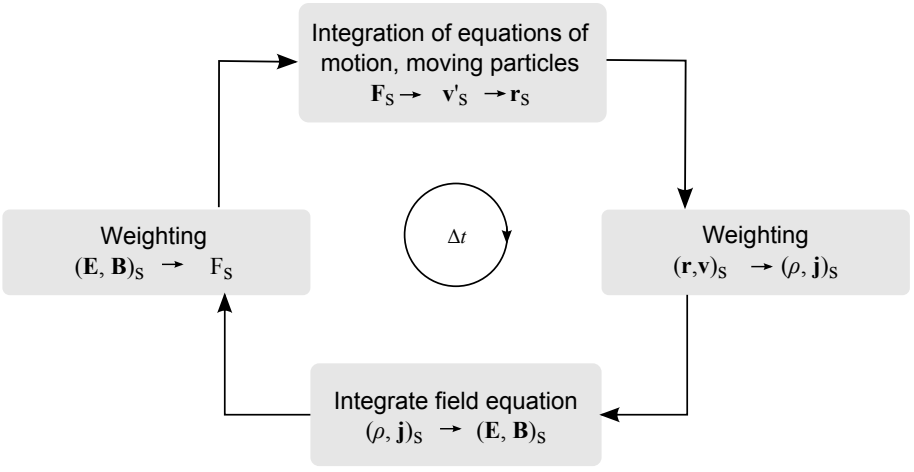

Figure 3.2: Particle In Cell computational method. The whole process is repeated for a number of Δt. Particles are introduced into the simulation domain adhering a set of *initial conditions* which govern their charge, initial position and velocity [Birdsall, 1991].

While moving faster particles more often than the slower particles reduces the number of computations needed to solve the plasma dynamics, it does not gives significant saving in computational time because solutions to the field equations are needed for every Δt, where in this case has to be solved for every Δt_e ($\Delta t = \Delta t_e$). Solving the field equations require solution to the Poisson's equation which in computational term is more expensive than solving the equation of motion. One technique that can be employed to reduce the computational time is by doing the reverse of this method, with the assumption that the faster particle is stationary over the course of a slower particle's motion. In this technique, both species are moved at the same small time interval ($\Delta t = \Delta t_e$) at the beginning of the simulation. Δt will be gradually increased towards Δt_i as the simulation approaches the steady state. As a result, the number of iterations needed for solving the field equations can be significantly reduced as $\Delta t_i > \Delta t_e$. This method will be further explored in the next chapter.

Finally, snapshots of plasma properties are taken at specified times or period to observe the change in global plasma behaviour and properties. Parameters of interest in plasma simulation include each species density, charge and current distribution, electric and magnetic fields, and plasma potential.

Integration method

Solving particle trajectory and field equation require solution to sets of differential and partial differential equations. Particle trajectory is a form of ordinary differential equation (ODE) while the electric and magnetic fields are a form of partial differential equations.

The force in the equation of motion (2.46) can be applied on the particle by

$$m\frac{\mathrm{d}\mathbf{v}}{\mathrm{d}t} = \mathbf{F} \tag{3.4}$$

$$\frac{\mathrm{d}\mathbf{r}}{\mathrm{d}t} = \mathbf{v} \tag{3.5}$$

where $\mathbf{F}$ is the force. These equations can be numerically solved by replacing it with the finite-difference equations

$$m\frac{\mathbf{v}_{new}-\mathbf{v}_{old}}{\Delta t}=\mathbf{F}_{old} \tag{3.6}$$

$$\frac{\mathbf{r}_{new}-\mathbf{r}_{old}}{\Delta t}=\mathbf{v}_{new}. \tag{3.7}$$

One method of solving these set of equations is by the *leap frog* method [Butcher, 1964, Romanelli, 1960, Hockney, 1966]. In Figure 3.3, $\mathbf{v}$ is advanced at time centred at $\mathbf{F}$ while $\mathbf{r}$ is advanced at time centred at $\mathbf{v}$. Knowing the initial conditions for particle velocities and positions at $t=0$, the solver had to first find $\mathbf{v}$ at $t-\frac{\Delta t}{2}$ using the $\mathbf{F}$ calculated at $t=0$. Integrations are then performed from $\mathbf{r}^t$ and $\mathbf{v}^{t-1/2\Delta t}$ to obtain the next $\mathbf{r}^{t+\Delta t}$ and $\mathbf{v}^{t+1/2\Delta t}$ by

$$m\frac{\mathrm{d}\,\mathbf{v}}{\mathrm{d}t}=\mathbf{F}\rightarrow m\frac{\mathbf{v}^{t+1/2\Delta t}-\mathbf{v}^{t-1/2\Delta t}}{\Delta t}=\mathbf{F}(\mathbf{r}^t,\mathbf{v}^t) \tag{3.8}$$

$$m\frac{\mathrm{d}\,\mathbf{r}}{\mathrm{d}t}=\mathbf{v}\rightarrow m\frac{\mathbf{x}^{t+\Delta t}-\mathbf{v}^{t-\Delta t}}{\Delta t}=\mathbf{v}^{t-1/2\Delta t}. \tag{3.9}$$

The advantage of this method is its fast implementation and since the two first-order equations are time centred, the integration of the two equations together is second order. This technique has been shown to be stable for simple harmonic motion such as plasma oscillations for $\omega_p\Delta t<2$, with good accuracy for $\omega_p\Delta t\leq 0.2$ [Birdsall, 1991].

Another commonly used method in solving an ordinary differential equation (ODE) is the Runge-Kutta method, with the fourth order version (RK4) is the most popular because of its high accuracy. This method can be used to solve ODE of the form

$$\frac{\mathrm{d}y}{\mathrm{d}x}=f(x,y),y(0)=y_0.$$

The method is based on the following

$$y_{i+1}=y_i+(a_1k_1+a_2k_2+a_3k_3+a_4k_4)h \tag{3.10}$$

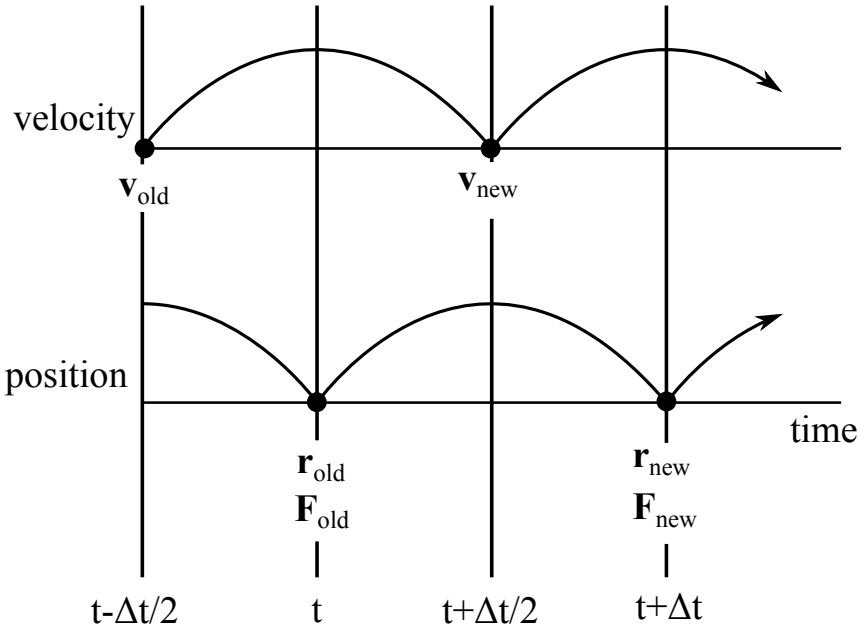

Figure 3.3: Leap frog method to solve the differential equations.

where by knowing the value of $y = y_i$, one would be able to find the value of $y = y_{i+1}$ at x_{i+1}, and $h = x_{i+1} - x_i$. One of the solution for the (3.10) is

$$y_{i+1} = y_i + \frac{1}{6}\left(k_1 + 2k_2 + 2k_3 + k_4\right) h \tag{3.11}$$

where

$$\begin{aligned} k_1 &= f(x_i, y_i) \\ k_2 &= f(x_i + \frac{1}{2}h, y_i + \frac{1}{2}k_1 h) \\ k_3 &= f(x_i + \frac{1}{2}h, y_i + \frac{1}{2}k_2 h) \\ k_4 &= f(x_i + h, y_i + k_3 h). \end{aligned}$$

Knowing the charge and current densities on each grid point (or nodes), one can find the electric and magnetic fields on the nodes by solving the Maxwell's equations, using the ρ and $\mathbf{j}$ as sources. It is first assume that the problem is an electrostatic one, i.e. $\nabla \times \mathbf{E} = -\partial \mathbf{B}/\partial t \approx 0$ hence $\mathbf{E} = -\nabla\varphi$. The two differential

equations that need solving are

$$\mathbf{E} = -\nabla\varphi \tag{3.12}$$

$$\nabla \cdot \mathbf{E} = \frac{\rho}{\varepsilon_0} \tag{3.13}$$

where together become the Poisson's equation

$$\nabla^2\varphi = -\frac{\rho}{\varepsilon_0} \tag{3.14}$$

Suppose that the equation needs to be solved in a 2-dimensional mesh as shown in Figure 3.1 The finite difference form of the Poisson's equation is then

$$\frac{(\varphi_{j-1} - 2\varphi_j + \varphi_{j+1})_k}{\Delta x^2} + \frac{(\varphi_{k-1} - 2\varphi_k + \varphi_{k+1})_j}{\Delta y^2} = -\frac{\rho_{j,k}}{\varepsilon_0} \tag{3.15}$$

where j, k are the grid number for x and y axis with separation of Δx and Δy respectively. This equation needs to be solved for every $\varphi_{j,k}$ using the appropriate boundary condition.

The three commonly used boundary conditions in plasma simulation are Dirichlet, Neumann and Robin boundary condition. Let $y'' + y = 0$ and $\nabla^2 y + y = 0$ are an ODE and a PDE respectively. In Dirichlet boundary condition, the solution of the ODE between the interval $[a, b]$ must take the form

$$y(a) = \alpha \quad \text{and} \quad y(b) = \beta$$

where α and β are given values. For PDE, the solution must satisfy

$$y(x) = f(x) \quad \forall x \in \partial\Omega$$

where $\partial\Omega$ is the boundary on a domain $\Omega \subset \mathbb{R}^n$. Neumann boundary condition on the other hand specifies the derivative of the solution to take on the boundary

domain, i.e. ODE between the interval $[a, b]$ must take the form

$$y'(a) = \alpha \quad \text{and} \quad y'(b) = \beta,$$

and for PDE

$$\frac{\partial y}{\partial \mathbf{n}}(x) = f(x) \quad \forall \mathbf{x} \in \partial\Omega$$

where $\mathbf{n}$ is normal to the boundary $\partial\Omega$ and f is a scalar function. The normal derivative $\frac{\partial y}{\partial \mathbf{n}}(\mathbf{x})$ is defined as

$$\frac{\partial y}{\partial \mathbf{n}}(\mathbf{x}) = \nabla y(\mathbf{x}) \cdot (\mathbf{x}).$$

Using the same example, Robin boundary condition for domain Ω where $\partial\Omega$ is the domain boundary is given by

$$ay(x) + b\frac{\partial y}{\partial \mathbf{n}} = g(y, x) \quad \text{on } \partial\Omega$$

for non-zero a and b which can be a constant or a function.

Having established the boundary condition for the problem above, the solution of E at point (j, k) can be found using the centred difference formula as

$$E_{j,k} = \frac{(\varphi_{j-1} - \varphi_{j+1})_k}{2\Delta x} + \frac{(\varphi_{k-1} - \varphi_{k+1})_j}{2\Delta y} \tag{3.16}$$

$$\frac{(\varphi_{j-1} - 2\varphi_j + \varphi_{j+1})_k}{(\Delta x)^2} + \frac{(\varphi_{k-1} - 2\varphi_k + \varphi_{k+1})_j}{(\Delta y)^2} = -\frac{\rho_{j,k}}{\varepsilon_0} \tag{3.17}$$

Figure 3.4 shows the 2-dimensional grid used for the above solution.

Finite element method

Another method often used in solving the partial differential equation such as the Poisson's equation is using the finite element method (FEM), also known as finite element analysis (FEA). Finite element analysis works by dividing the simulation domain into finite number of elements, where the solution of each element is solved

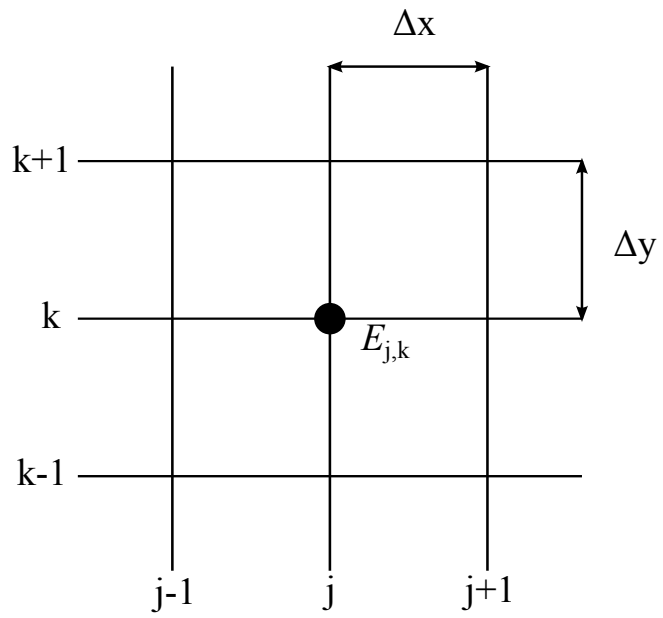

Figure 3.4: 2 dimensional uniformly spaced numerical grid. The charge density ρ and potential φ will be obtained only at x_j's and y_k's [Birdsall, 2005].

in relation to each other before an overall performance is obtained by adding the response of each elements. The elements in question here can be nodes, lines or edges, surfaces and small volumetric shape such as tetrahedron or cube. They can be constructed using equally sized elements (structured) or adaptive size (unstructured) depending on the geometry of the problem. Figure 3.5a shows an example of a 2-dimensional mesh of a probe (circle) in a plasma simulation domain. This unstructured mesh has the advantage over the structured mathematical grid as it can be used to model a more complex geometry or one with curve boundary such as in Fgure 3.5a. In the meshing process, triangles rather than squares are used in the meshing process to allow better representation of the probe located in the middle of the domain. The adaptive grids used enable the user to put more emphasis on the region close to the probe by employing smaller triangle in that area (high resolution) as compared to larger triangle in the boundary regions (low resolution).

In a 3-d simulation, the FEM describes the simulation domain in the form of non-overlapping tetrahedrons where each tetrahedron consists of 3 triangular faces,

6 edges and 4 nodes and is more suitable in applications where there is a need to have unstructured (unequal) mesh. The mesh forms a number of tetrahedrons where each tetrahedrons share its faces, edges and nodes with other tetrahedrons in a similar fashion as the equally spaced computational grid in finite difference method. In plasma simulation, the tetrahedrons are used to model the plasma volume while the tetrahedron's faces define the external or internal boundaries. The Poisson's equation is then solved using the specified boundary conditions. The boundary conditions used in solving the equation is similar to the case of finite difference method, i.e.

1. Dirichlet conditions on conductor boundary.
2. Neumann condition on dielectric boundary.
3. Robin condition on external boundary.

The Dirichlet condition on conductor boundary describes the potential of a conducting surface in the simulation volume. This is normally the case if there is a conductor such as a probe or spacecraft surface in the simulation volume where the potential of the surface is either biased to a certain value ($\varphi_s = \text{fixed}$) or allowed to float ($\varphi_s = \mathrm{d}\,I/\,\mathrm{d}\,t$). The Neumann boundary condition applies to dielectric boundary (on probe or spacecraft) when the normal component of the electric field is prescribed. The Robin condition often used on external boundary (free space boundary) and the parameter b is typically given by $1/r$, where r is the distance between one point in the computational domain to a point on the external boundary.

Weighting

In between the integration process shown in Figure 3.2, there are two weighting processes involved; one is the particle's charge density assignment on the grid from the particle's position, and the second is in the determination of force from the fields calculated at grid points at the particle's position [Birdsall, 1991]. In most

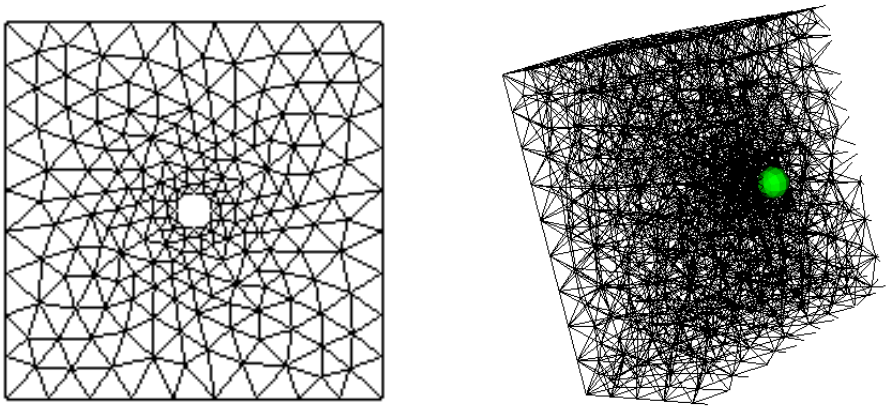

(a) Set of triangles are used to define the 2-dimensional simulation domain. This unstructured mesh which is used in defining the nodes and edges clearly capture the shape of the circular object located in the middle of the area.

(b) A 3-D representation of the same probe in the plasma simulation domain. The probe is now of spherical shape (green). The unstructured mesh can be seen where smaller tetrahedrons are used in the region closed to the probe and larger size are used at the boundary.

Figure 3.5: Finite element representation of a probe in a plasma simulation domain.

cases, the same weighting technique is employed for both weighting processes, as to avoid self force by the particle.

Figure 3.6 shows the close-up view of the 2-dimensional numerical grid in Figure 3.1. In the figure, particle q will have to deposit its charge to the nearby nodes for the determination of charge density at the grid points. This process can be performed using few techniques with the simplest one is the nearest grid point (NGP). In NGP, particle assigns its charge to the nearest grid point (hence the name) which in this case is point (x_j, y_k). The cell surrounding the point (shaded area), i.e. at distance of $\Delta x/2$ and $\Delta y/2$ from the point is then said to contain q number of charges. If there are more than one particle in the cell (which is normally the case), the charge density at the chosen grid point is

$$\rho(x_j, y_k) = \sum_n q_n \tag{3.18}$$

where n is the sum of all charged particles in that particular cell. The NGP technique is known as *zero-order weighting* and particle appears to be of rectangular shape of

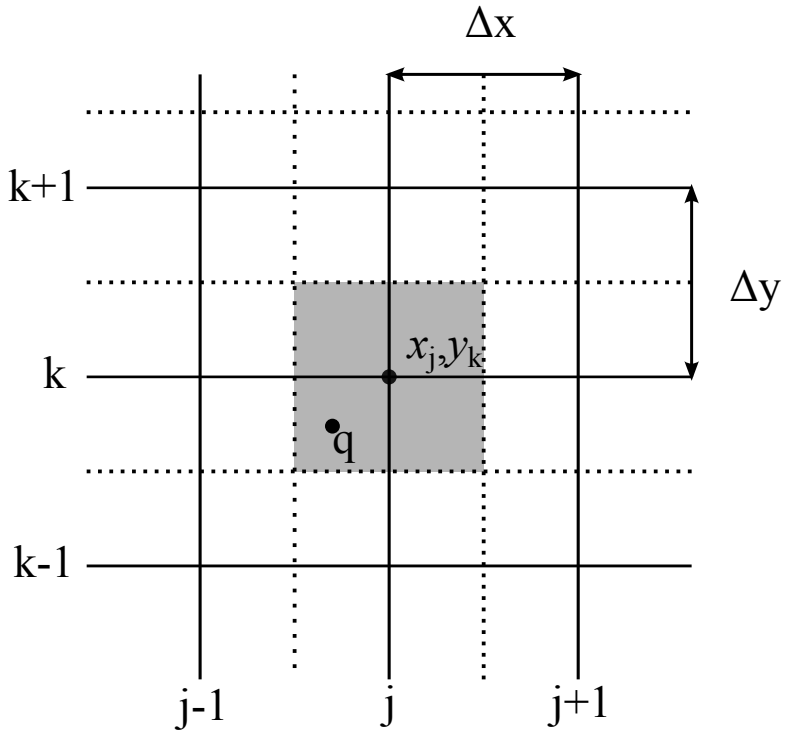

Figure 3.6: Weighting process [Birdsall, 1991].

size $\Delta x \times \Delta y$ because although the density is deposited on the grid, it is assumed that the whole cell area will have the same charge density. In the figure, assuming q is the only particle in the domain, the measured charge density is $\rho = q$ inside the cell and $\rho = 0$ outside it, giving it a staircase approximation of the charge density. This method although fast in term of calculation, will produce density and electric field which are relatively noisy both in time and space.

A first order weighting algorithm commonly known as cloud-in-cell can be used to smooth the the density and field fluctuations and reduce the noise caused by the weighting process, is shown in Figure 3.7. In the figure, the square shaded area is $\Delta x \times \Delta y$ in size, with the particle located at the centre. Area a, b, c and d belong to grid point A, B, C and D respectively and the charge of particle q is linearly assigned to all four grid points based on their respective area.

The same process is repeated in the assignment of force on particle. In NGP, all particles located in the same cell (a square $\Delta x/2$ away from a grid point) will

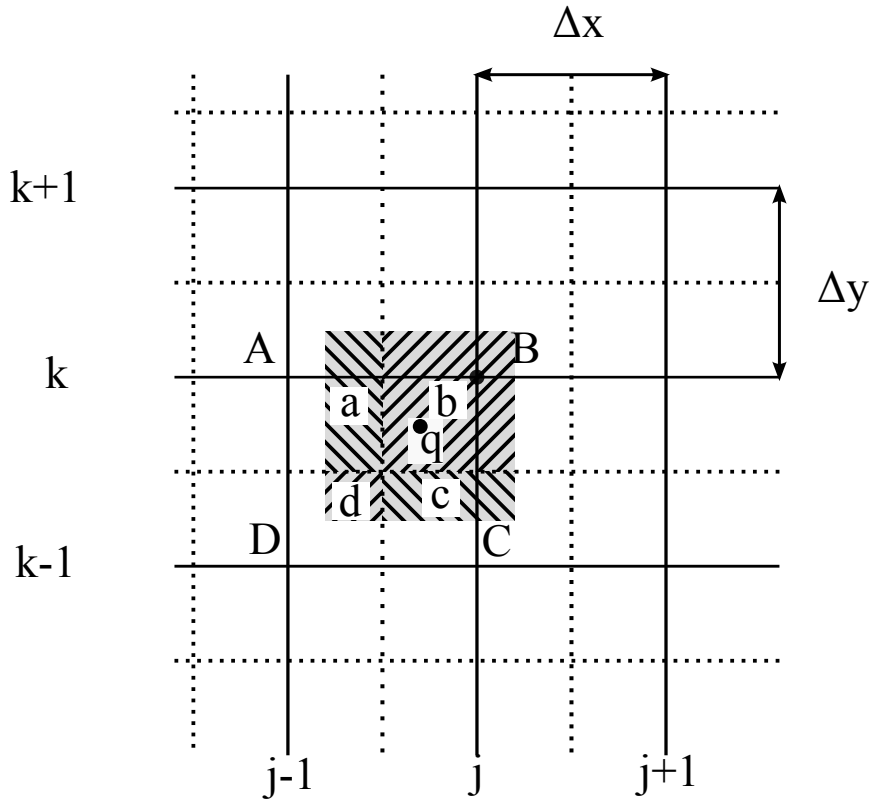

Figure 3.7: Cloud-In-Cell weighting process.

experience the same force coming from the grid point. In CIC, the force on each particle depends on the area the particle make with respect to the cell, i.e. linear assignment of force.

3.2.1 Monte Carlo Collision

The PIC method introduced so far deals with the motion of plasma particles in a computational grid (structured or unstructured) by implying the particles with the forces calculated on each nodes in the grid. In effects, this technique accounts for the long range forces experienced by each particle, but fails to deal with the short range interactions such as collision between particles. This type of interaction can be simulated using the Monte Carlo collision (MCC) algorithm which could be used to simulate interactions such as electron-neutral collision, ion-neutral collision and others short term interactions such as scattering, ionization, charge exchange and many more.

Burger [1967] first came up with a elastic electron-neutral collision algorithm for his simulation with low-pressure diodes. Assuming a 2-dimensional plasma simulation domain, a particle is represented by its velocity component in the x-direction $v_x(t_n)$ and in a direction perperdicular to x, $v_\perp(t_n)$ as well as its position on the grid $\mathbf{r}(t_n)$ where t_n refers to the current time in the simulation time step i.e $t_n - t_{n-1} = \Delta t$. The probability of a particle to undergo a collision during a time period Δt is given by

$$P_c(t_n) = 1 - \exp\left(-v(t_n)\Delta t/\lambda\left[v(t_n)\right]\right)$$

where P_c is the probability of the particle experiencing a collision during the interval $t_{n-1} \leq t \leq t_n$, and $\lambda(v)$ is the mean-free path given as a function of velocity. This function is evaluated for every particle in the simulation domain and a random process is done to determined which particle should undergoes the collision process. This method also assumes a conservation of momentum in calculating the output velocity of the collision which is also done using random process.

Using a similar approach to Burger [1967], the Monte Carlo works by finding the *collision frequency*, ν given by

$$\nu_{coll} = n_{target}\sigma(E)v_{rel} \tag{3.19}$$

where n_{target} is the density of the target particle, σ is the target cross section as a function of particle energy E and v_{rel} is the relative speed between the two colliding particle. The probability of a collision happening in a time step Δt is given by

$$P_c = 1 - \exp\left(-n_{target}\sigma(E)v_{rel}\Delta t\right) = 1 - \exp\left(\nu_{coll}\Delta t\right). \tag{3.20}$$

As an example, a collision between electron and neutral gas would gives us $n_{target} = n_{gas}$, and assuming that $v_{part} \gg v_{gas}$, $v_{rel} \approx v_{part}$. A uniform random number R is then generated and P_c is compared to R. A collision is assumed to happen during

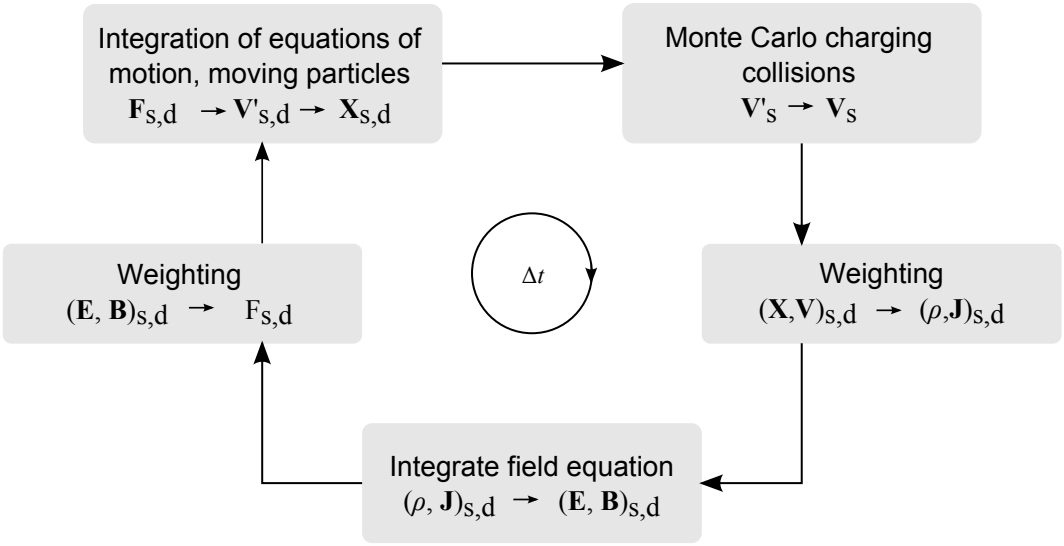

Figure 3.8: PIC-MCC computational algorithm. A collision probability process is added after all particles have been moved to their new positions.

the time period Δt if $P_c > R$. If the collsion process is an absorption type collision, the process is repeated for the next particle in the domain. A further probability process is performed if there is more than one type of interactions possible such as ionization, charge exchange or scattering by assuming this probability process p is propotional to $\sigma_p(E)$.

The MCC process is performed in the PIC technique after all particles have been moved to their next position as shown in Figure 3.8.

Chapter 4

Spacecraft Charging and Spacecraft Plasma Interaction Software (SPIS)

4.1 Introduction

The plasma environment represents a major challenge to any spacecraft operating in space due to a phenomena known as spacecraft charging. Spacecraft charging refers to the accumulation of charged particles from the surrounding plasma environment on the spacecraft's surface or the spacecraft's internal dielectric. This causes an electric field build-up to a level that could harm the spacecraft and any electronics instrument it operates. Spacecraft charging has been acknowledged to be one of the main reason for spacecraft malfunction and failure, with the effect ranging from operational anomalies to components malfunction, and in some cases could even lead to reduction in spacecraft life and complete spacecraft loss [McPherson et al., 1976, Rosen, 1976, Shaw et al., 1976].

The first *in situ* observation of high potential charging was reported by DeForest [1972] where the ATS 5 spacecraft was charged to potential exceeding 10kV during eclipse. This leads to the Spacecraft Charging At High Altitude (SCATHA)

experiment and its subsequent report and analysis that allow the formation of guidelines and standard regarding spacecraft charging [Koons, 1983, Purvis et al., 1984]. In spite of this, in 1994, two communication satellites own by Telesat Canada, Anik E-1 and Anik E-2 suffered malfunction which resulted in major disruption to telecommunication services in Canada [Rostoker, 1994, Lam et al., 2012]. The satellite's failure was later confirmed to be caused by electrostatic discharge (ESD) as a result of charging by high energy electrons and serves as a reminder of the potential disaster that can be caused by spacecraft charging [Baker et al., 1994, Baker, 2001].

4.2 Spacecraft Charging Process

Spacecraft in space reacts in the same way as any other object in space; it interacts with the environment to reach an equilibrium state. With no significant atmosphere to protect itself from the environment, its surface is exposed to the space plasma environment with continuous bombardment of charged particles and photons coming from the sun. The incidence charged particles can either stick to the surface, travel past the surface's protective layers, involve in some excitation process or can simply recombine on the surface depending primarily on the charged particle's energy. Meanwhile, photons interact with the surface by exciting electrons in the materials producing photoelectrons which are released from the surface into the surrounding plasma. All these processes result in a current system that flows into and out of the spacecraft, hence charging the spacecraft surface or the internal dielectrics into a potential level that could be hazardous to the spacecraft's operation.

The charging process is a result of the surface trying to balance the current arriving and leaving the surface, and is a function of the characteristic of the body (spacecraft materials, electrical properties etc.), spacecraft geometry, orbital parameters and local plasma condition [Rosen, 1976]. Table 4.1 list the parameters that determine the spacecraft-sheath potential with the functional dependencies.

Table 4.1: A list of variables important in the analysis of spacecraft charging [Rosen, 1976].

Environmental Parameters	As a function of:
Electron and proton fluxes	energy, direction, location, time
Illumination	area, direction, location, time

Material Parameters	As a function of:
Bulk resistivity	illumination, voltage stress
Surface resistivity	illumination, voltage stress
Arc discharge characteristics	capacitive configuration
Photoemissivity	incident direction, energy
Secondary emission coefficient	incident direction, energy
Backscatter coefficients	incident direction, energy
Surface contamination and imperfection	time (aging)
Dielectric constant	

Geometrical and orbital parameters	As a function of:
Exposed surface area	
apertures	incident flux
Capacitive configuration	illumination, time

There are two types of spacecraft charging problems commonly experienced by a spacecraft in space: surface charging and internal charging.

4.2.1 Surface Charging

Surface charging refers to the slow accumulation of charged particles on spacecraft's surface, normally due to plasma environment with low energy electrons, i.e. $E <$ 100keV. The charging process creates a potential difference between the spacecraft's surface and the plasma which results in electrostatic field that extends from the surface to the surrounding plasma environment. The effects of surface charging include surface damage from arc discharge, induced current on electronic system, payload error and in some cases could simply results in unnecessary station keeping process which could reduce spacecraft's life expectancy.

Surface charging could also lead to differential charging, a case where adjacent

surfaces are charged to different potential levels, which would normally happen between conducting and non-conducting surfaces. Differential charging happens when the adjacent surfaces are charged at different rates, possibly due to non uniform illumination or because of different materials involved. For example, two non-conducting material charged at a different rate if one is illuminated by sun flux and the other is in shadow. Another example of differential charging is when two differently charged surfaces come in contact to each other such as during extra vehicular activity (EVA) or during shuttle's docking process with the space station. During this process, current flows between the two differently charged surface as they come into contact. The flow can disrupt spacecraft equilibrium potential, or could become a significant hazard to astronaut performing extra vehicular activity (EVA).

The early work on surface charging can be traced back to the work of Langmuir and Blodgett [1924], Bernstein and Rabinowitz [1959] and Chen [1965] with a comprehensive reviews on spacecraft charging were provided by Whipple [1981] and Garrett and Whittlesey [2000]. The surface charging process can be simplified by looking at the current balance equation, which requires the spacecraft to be in equilibrium state, i.e. current entering and leaving the spacecraft is balanced. Considering all possible charging current, the current balance equation is given by

$$I_{TOT}(V_S) = I_E(V_S) - [I_I(V_S) + I_S(V_S) + I_{PH}(V_S)] \tag{4.1}$$

where

I_{TOT}	sum of incoming current
I_E	incident electron current
I_I	incident ion current
I_{SE}	secondary electron emission
I_{PH}	photoelectron current.

The first two terms in the equation are ambient currents collected from the surrounding plasma while the remaining terms are emission currents due to electrons and ions interaction, and natural radiation (photoemission) with the spacecraft

surface. In a similar manner to the dust charging process, the ambient plasma current to the surface can be generalised using the OML model [Bernstein and Rabinowitz, 1959, Chen, 1965, Whipple, 1981]. The charging process is then similar to the one experienced by a single dust particle with the exception of secondary current production due to the relative difference in size involved. Based on the equation, it is clear that the surface could charge to either negative or positive potential depending on the dominant current acting on the surface.

Considering only currents due to ambient plasma, spacecraft is charged to negative potential because of the large electron to ion current ratio. The large difference between electron and ion flux onto the spacecraft happens because electrons are more mobile compared to ions due to their much smaller weight. As negative potential develops on the surface, low energy electrons are repelled and ions are attracted to the surface by the sheath. Surface will continue to charge to negative potential until both currents are balanced. Using the OML theory, the equilibrium surface potential is a function of electron plasma temperature and is given by approximately $-2.5kT_e/e$ for hydrogen plasma and $-3.6kT_e/e$ for oxygen plasma [Northrop, 1992].

Most materials emit photoelectrons when illuminated by the UV component of the solar flux. The photoelectron yield is a function of material properties, solar flux, solar incidence angle and satellite potential [Hastings and Garrett, 2004]. Laboratory and space experiment have shown that the photoelectrons are emitted isotropically with a Maxwellian energy distribution [Whipple, 1981] with mean energy 2eV. Table 4.2 shows characteristics of photoelectrons at 1 AU for a variety of materials often used in spacecraft construction. In high orbit, photoelectron current dominates when compared to ambient current fluxes of $1 - 5\mu\text{A/m}^2$. The results is a positively charged surface in order to attract more ambient electron current to the surface as well as allowing the emitted photoelectrons to be recollected. As the yield is also highly dependent on the sun flux, non-conducting surface with cavities or ones that are shadowed could charged differently to sunlit part of the

Table 4.2: Photoemission characteristics for various material used in space (from [Hastings and Garrett, 2004])

Material	Work function (eV)	Flux (μA/m^2)
Aluminium oxide	3.9	42
Indium oxide	4.8	30
Gold	4.8	29
Stainless steel	4.4	20
Aguadag	4.6	18
Lithium fluoride on gold	4.4	15
Vitreus carbon	4.8	13
Graphite	4.7	4

spacecraft (differential charging). While a positively charged surface is the more likely outcome in the presence of photoelectrons, recent work shows the possibility of having a negatively charged surface in the presence of potential barrier that prevents low energy photoelectrons from leaving the surface [Lai and Tautz, 2006]. Since the photoelectrons are comparatively low in energy ($\approx$ 2eV), the presence of this barrier prevents these electrons from leaving the surface and are recollected by the surface.

High energy electrons incidence on the surface can either be reflected or absorbed by the surface. Absorbed electrons collide with atoms in the materials and could re-emerge back on the surface as backscatter electrons or end up exciting other electrons. These excited electrons travel to the surface and are emitted as secondary electrons. The backscattered electrons and secondary electrons can be differentiated by the amount of energy they have when leaving the surface. Backscattered electrons energy are slightly lower than the incident electrons energy while secondary electrons have mean energy of around 2 eV with Maxwellian energy distribution [Hastings and Garrett, 2004].

Similarly, incidence ions could also produce electron secondary emission. The resulting yield from both electrons and ions impact could be larger than the incident flux depending on the energy on the incidence particles and the material involved. Table 4.3 gives the maximum secondary electron yield $\delta_{e_{max}}$ and the incidence

Table 4.3: Secondary electron yield characteristics for various materials [Hastings and Garrett, 2004].

Material	$\delta_{e_{max}}$	$E_{\max}$ (eV)
Aluminium	0.97	300
Aluminium oxide	1.5-1.9	350-1300
Magnesium oxide	4.0	400
Silicon oxide	2.4	400
Teflon	3	300
Kapton	2.1	150
Magnesium	0.92	250

electron energy producing the maximum yield $E_{\max}$.

In geostationary orbit (GEO), ambient plasma is tenuous and collisionless compared to the dense and collisional plasma found in the ionosphere (LEO). However, the GEO orbit is characterized by sudden injection of high energy particles associated with substorm. This creates a non-Maxwelllian plasma system which needs to be properly modelled in order for any estimation on the charging level to be accurate. During this period, plasma environment in the geosynchronous orbit has been shown to be made of two different plasma populations; low energy particles from the background plasma (solar wind) and high energy particles from the solar event (mean energy of a few tens of keV) [Garrett and DeForest, 1979]. In a severe space weather condition such as during substorm, spacecraft surface could develop a much higher negative potential because of the increase presence of these high energy particles. SCATHA experiment has shown that these two populations can be adequately modelled using a bi-Maxwellian distribution [Garrett and DeForest, 1979]. The worst of negative charging happens when spacecraft is in eclipse during the charging event because of the absence of photoemission current which could help in lowering the overall surface potential.

In a region where ion speed is comparable to the spacecraft speed such as in the ionosphere, it is sometime more appropriate to model ion current as ram current as ion collection is most likely to happen at the spacecraft ram. Ion ram current is given by

$$I_{ram} = n_i q_i A_{ram} v_s \tag{4.2}$$

where A_{ram} is the spacecraft ram area and v_s is the spacecraft velocity. Another effect of this ram current is the formation of wake devoid of ions as the slower ions require slightly longer time to fill in the void as opposed to electrons [Al'pert, 1983].

4.2.2 Internal Charging

On the other hand, electrons with energy higher than 100keV can penetrate through spacecraft outer surface. This high energy electrons could be deposited on an ungrounded conductor or in spacecraft's internal dielectrics [Robinson Jr and Coakley, 1992]. This type of charging is known as internal or dielectric charging and normally happen during solar energetic event (SEE). As the charging process happens close to spacecraft electronics, this type of charging presents a much dangerous consequence to spacecraft [Violet and Frederickson, 1993].

4.3 Spacecraft Plasma Interaction Software, SPIS

As spacecraft becomes more sophisticated and carries both communication and scientific equipment, due care has to be made to ensure spacecraft is resistant to the charging effects. In addition, the presence of scientific equipment means any measurement on the environment must take into account the error caused by the electric field generated by the spacecraft surface. The needs for better understanding of the charging effects on each individual spacecraft has resulted in many computer simulation software that allow spacecraft builder and operator to assess the effect of space plasma on the spacecraft and vice versa.

Spacecraft charging software range from a simple 1 dimensional potential analysis software to a more complicated 3 dimensional simulation capable of simulating real spacecraft in any space plasma scenario. Examples of such software are the NASA/Air Force Spacecraft Charging Analysis Program (Nascap-2k) used

by the National Aeronautics and Space Administration (NASA) [Mandell et al., 2006, Katz et al., 1977], Multi-utility Spacecraft Charging Analysis Tool (MUSCAT) [Muranaka et al., 2008] by the Japanese Aerospace Exploration Agency (JAXA) and Spacecraft Plasma Interaction System (SPIS) [Roussel et al., 2008, Forest et al., 2006] by the European Space Agency (ESA). These software provide the necessary tools in ensuring the spacecraft charging process can be prevented and could provide a platform for the study of space plasma.

The Spacecraft Plasma Interaction System (SPIS) was developed under the Space Plasma Interactions Network in Europe. SPIS was funded by European Space Agency (ESA) and developed by contractors which include ONERA for the development of SPIS-Numerical Module (SPIS-NUM) and Artenum for the SPIS-User Interface (SPIS-UI). The code is designed on an open-source platform using object-oriented style coding which enable further development of the code. The SPIS framework also includes several other third party open source software such as Gmsh for mesh modelling [Geuzaine and J-F.Remacle, 2009] and Cassandra VTK for 3-D result analysis and display. SPIS has shown tremendous stability and accuracy in simulating spacecraft interactions with ordinary plasma, i.e. the one that consists only electrons and ions [Roussel et al., 2008, Forest et al., 2006].

The SPIS modelling chain is shown in Figure 4.1. It can be divided into three main processes which are the pre-processing, simulation and result analysis. The first and the last process are performed in the SPIS-UI while the simulation process is done by the SPIS-NUM module.

4.4 SPIS-User Interface, SPIS-UI

The SPIS-User Interface allows interfacing between the necessary user input and the SPIS-NUM module. Figure 4.2 shows the SPIS graphical user interface (GUI). The user interface is made of a series of icons that indicate the flow of the simulation process, 3 workspace windows and 2 console windows.

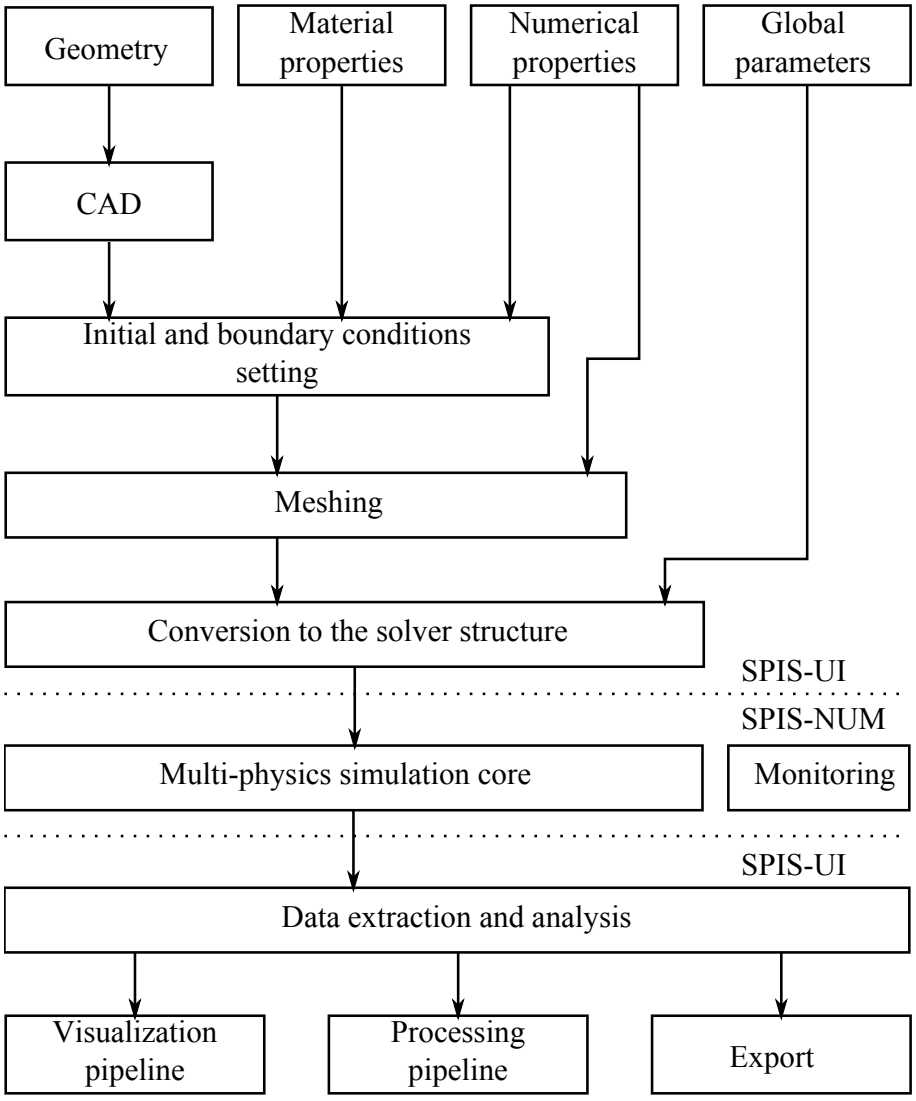

Figure 4.1: SPIS schemetic modelling chain

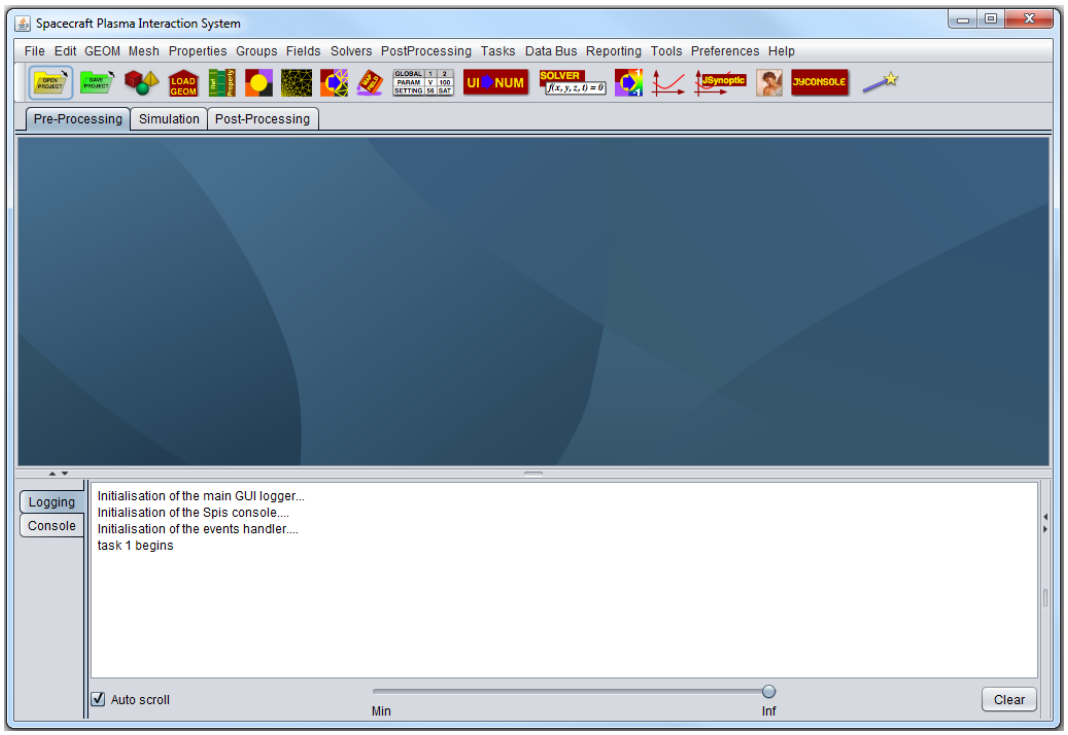

Figure 4.2: SPIS graphical user interface

4.4.1 Preprocessing

A spacecraft charging simulation in SPIS starts with the definition of the simulation model needed by the simulation kernel which are the model geometry, materials used in the construction of the spacecraft, numerical parameters of the simulation and global parameters such as the plasma environment. Model geometry is the representation of the simulation environment in the form of unstructured mesh. The geometry is prepared using the 'Gmsh' software which also serves as the meshing tool for SPIS. The geometry must represents at least 3 different 'physical models' which are the spacecraft surface, plasma boundary surface and plasma volume. Figure 4.3 shows an example of the geometry use to simulate the charging of a simple spherical probe in SPIS. In this example, the physical model for the spacecraft is represented by the probe's surface. Physical model for the plasma boundaries are the 6 enclosing surfaces which form a cube. The physical model for plasma volume is then defined as the space between the boundaries and the probe surface as shown in the Figure 4.3.

In the figure, the probe and the boundary surfaces are constructed from a

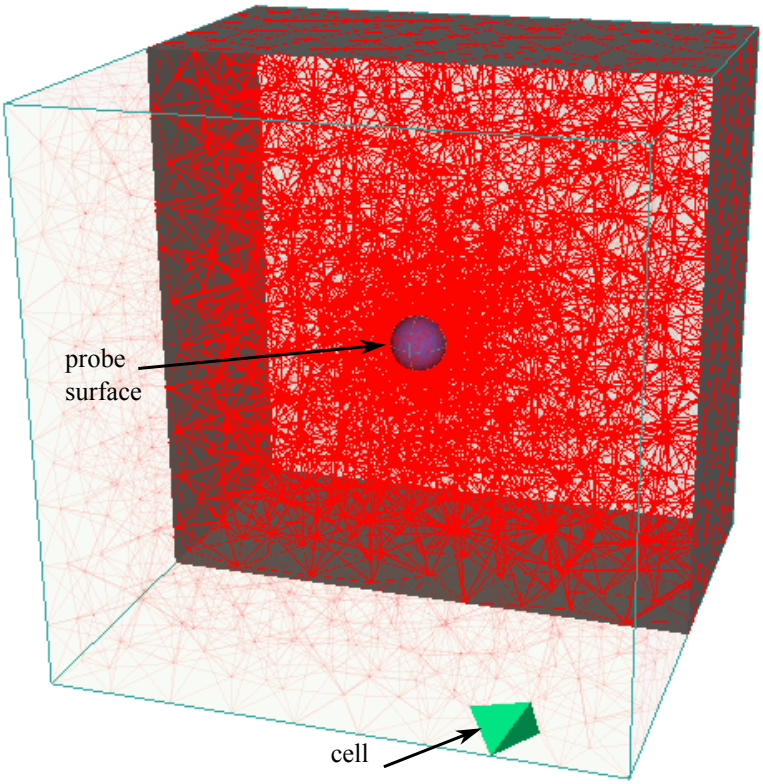

Figure 4.3: An example of a simulation geometry for simulating a spherical probe in SPIS-UI.

number of triangles. The size of each triangle depends on the level of accuracy needed for the simulation. In this example, the triangular surfaces that form the spherical probe are smaller than the ones on the boundary. This method increases field resolution close to the probe as well as producing a well constructed spherical probe. In the same time, a larger triangular surface at the boundary reduces the computational cost as there are less nodes where the field has to be resolved. The plasma volume is then meshed into 'cells' which are made from 4 interconnecting triangular surfaces. These cells form the volume for which particle dynamics are simulated.

The next step in the preprocessing stage is the setting up of the physical models based on the simulation geometry. This includes assigning the surfaces

with the relevant numerical materials properties, electrical nodes properties and plasma properties. An actual spacecraft can be made from different types of materials consisting of conducting and non-conducting surfaces such as indium titanium oxide (ITO) coated material and solar panels. SPIS provides a library of often used materials as well as the ability to implement a user-defined material for the surface. The material library contains information on the material's secondary yield properties such as photoemission yield, secondary electron yield, secondary proton yield and conductivity. Plasma properties defines the numerical properties and boundary conditions related to the plasma models. Among the plasma parameters that need to be defined include the material boundary (i.e. spacecraft surface), virtual boundary (plasma boundary) and the computational volume (plasma volume). The SPIS program will then mapped the corresponding numerical material properties, electrical nodes properties and plasma properties onto the simulation geometry. These parameters, which are directly related to the local surface and cells, are referred to as *local parameters* in the SPIS set up.

The final step in preprocessing stage is the *global parameters* set up. 'Global parameters' refers to parameters that define the space environment such as the plasma environment and the numerical parameters for the simulation. Plasma environment for example allows the selection of plasma distribution for each species of particle involves in the simulation. At the moment, SPIS allows two types of plasma environment which are single Maxwellian and bi-Maxwellian environment. Ambient electron and ion populations can be defined using either single or bi-Maxwellian model while emitted particles such as from photoemission and secondary emission can be defined using the single Maxwellian model. User also needs to set the species temperature and drift velocity (ions), average number of superparticles in the cells and type of particle interactions that are going to be performed during the simulation.

In addition to ambient and emitted plasma species, user also needs to set the simulation's numerical parameters. Numerical parameters are parameters related

to the numerical simulation itself such as the simulation duration, time step, output profile and the type of solver to be used in the simulation.

The order of the pre-processing process is explicitly shown by the arrangement of the icon on the top of the workspace window as in Figure 4.2. Both the local parameters and the global parameters are then passed to the simulation kernel (SPIS-NUM) for the simulation process to begin. Further information on the preprocessing are available on SPIS manual.

4.4.2 Analysis

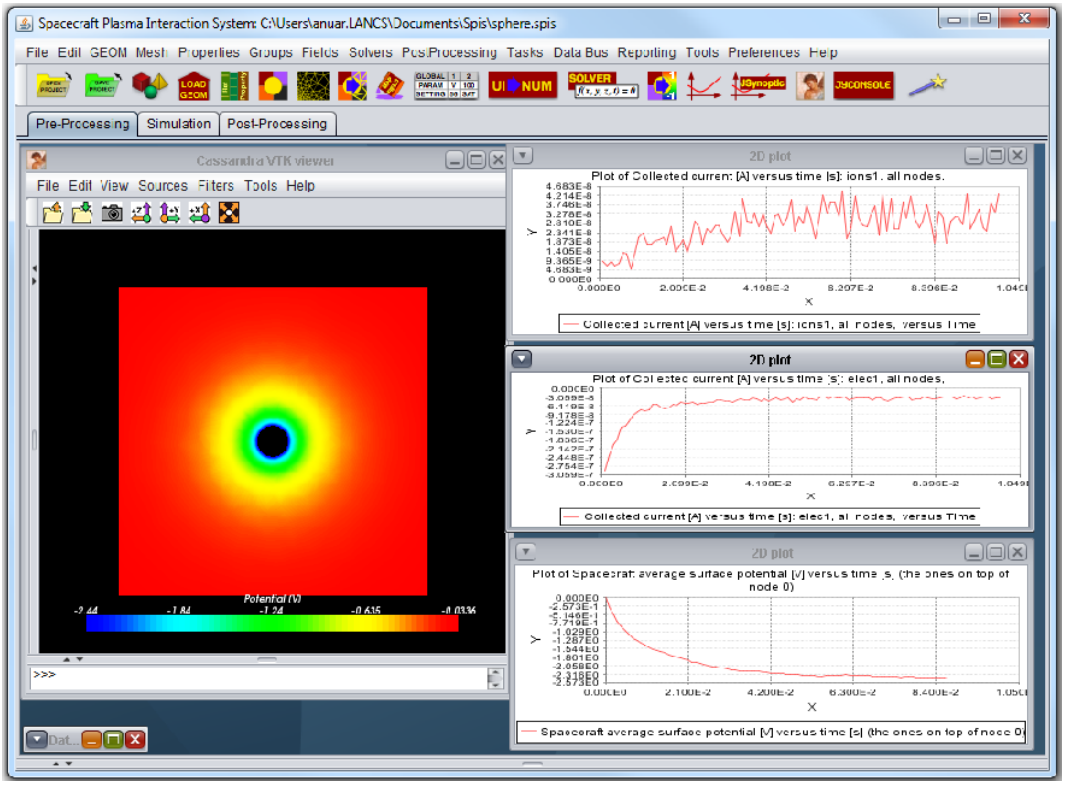

Figure 4.4: Example of results available in SPIS-UI for the probe in space simulation.

Upon completion of a simulation in SPIS-NUM, results are passed back to the SPIS-UI for post processing. The output includes 2 dimensional results such as surface's current (collected and emitted) and potential as well as 3-dimensional results such as plasma species density and energy distribution, current density, electric field and plasma potential. The 3 dimensional data are stored in the Virtualisation Toolkit format (VTK) and can be analysed using the default 'Cassandra VTK'

software or using third party software, 'Paraview'. Figure 4.4 shows an example of some the output produced by SPIS for the simulation of probe in space.

The results shown in Figure 4.4 are the 2 dimensional view of the plasma density and the potential and current of the probe versus time.

4.5 SPIS-Numerical Code, SPIS-NUM

SPIS-NUM is the numerical code that performs the integration process based on the information provided by the SPIS-UI. The simulation process of SPIS-NUM is shown in Figure 4.5.

Figure 4.5(a) shows the overall simulation process while (b) shows the particle sampling process. Simulation begins with the building up of the simulation model from the local parameters data, followed by setting up of plasma model using the global parameters data. During the first process, the numerical code builds the cell using the surface and volume mesh information contained in the local parameters which include the definition of boundary surface, spacecraft surface and plasma volume. It will then set up the related fields and solvers before building up the plasma environment based on the definitions provided in the global parameters. The code will also define any interaction process on demand which includes surface-plasma interactions as well as particle-particle interactions. In addition, numerical parameters such as time step are determined using either user-input value or based on the most suitable value which is limited by the constrain of cell size and particle's temperature.

4.5.1 Time step

An important parameter in SPIS is the iteration time step. The time step in SPIS is divided into three categories, plasma-spacecraft interaction time step (simulationDt), plasma time step (plasmaDt) and population time step (popNDt) as shown in Figure 4.6. The figure shows the three different level of time step

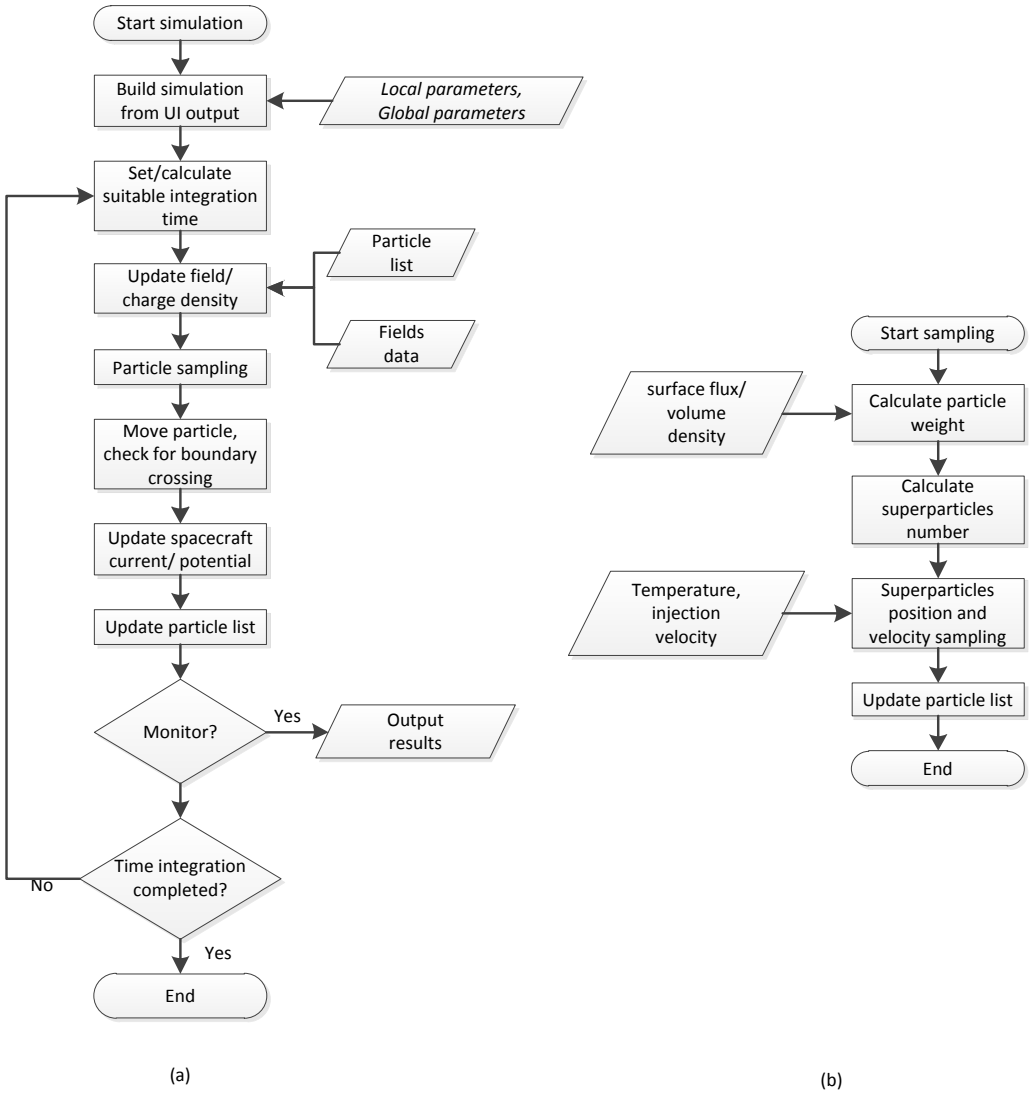

Figure 4.5: Flow chart showing the (a)simulation (integration) and (b)sampling process in SPIS-NUM.

available in SPIS. The upper level time step is the simulation time step which is the actual integration time step that reflects the physical interaction between the plasma particles and the spacecraft surfaces. The plasma time step is the lower level time step which is the duration for particle's trajectory calculation. This duration is normally restricted to a fraction of plasma frequency to ensure plasma stability. The plasma time step can be further classified into each population time step which represents the integration duration of each of the plasma population. During the simulation process, the numerical code will determine the suitable

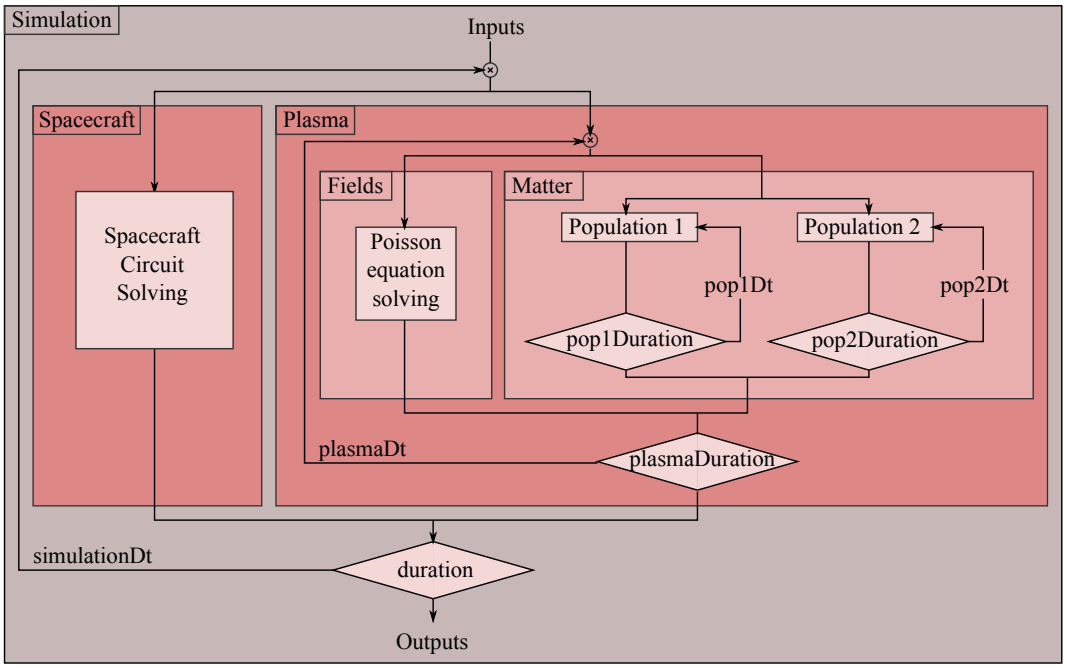

Figure 4.6: The three different level of time steps employ by SPIS.

integration duration which is the smallest time step between the three.

In most cases, simulations can be performed in real time where the same integration duration is used for all processes involved. There is however, a large difference in characteristic time between some of the processes. If a fast process can be assumed to happen on the background of a slower process, an assumption can be made that the fast process dynamics is quasi-static compared to the slow process. This assumption allows a larger time step to be used for the lower simulation level (plasma level) by emphasizing the slower process. In this case, the simulation time step is set to be the time step of the slower process. Since a fast process is assumed to be stationary during the slower process' simulation time step, integration for the fast process is performed at a fraction of the simulation time step. The duration of the fast process numerical integration must not exceed the inverse of the plasma frequency $1/\omega_{p,e}$ in order to maintain plasma stability. In this way the stationary state of the fast process is resolved without having to integrate over the complete duration of the upper level time step. This technique is known as numerical speed up and would enable a much quicker resolution of the simulation process as long as plasma stability is observed. Figure 4.7 shows the difference between the simulation

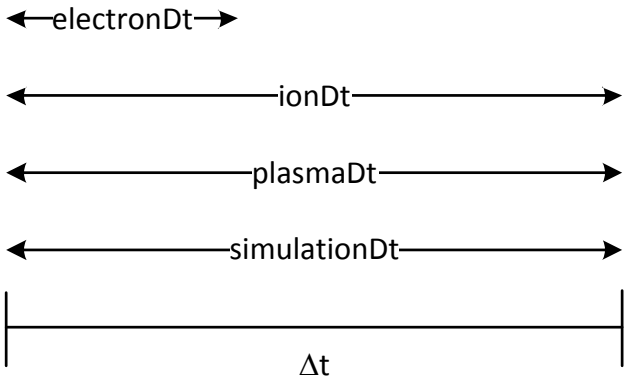

Figure 4.7: Example of the implementation of numerical speed-up.

time step and numerical time step with numerical speed up.

As an example, there can be a large difference between plasma species dynamics due to the mass ratio (electron and ion), or when there are two populations of the same species with large temperature difference (eg. high energy and low energy electrons). The fast species is assumed to be quasi-stationary with respect to the slow species such that its steady state can be obtained by only integrating over a fraction of the slow species time step. In the electron-ion example in Figure 4.7, the slower ion integration duration is set as the plasma duration (ionDt = plasmaDt = simulationDt) whereas the electron's integration duration is set to be a fraction of the plasma duration (electronDt $\ll$ plasmaDt). As a result, ion species trajectory is calculated over the full ion duration (real time) compared to the electron species where its physical trajectory is only calculated over a smaller duration (elctronDt $<$ ionDt). The electron however is assumed to have been physically integrated over the full duration (plasmaDt) as the ion species because of the quasi-static assumption. This technique however requires a reasonable integration durations being set up for both species, taking into account the velocity ratio between the two as well as the particles' plasma frequencies.

Another example where this useful feature of SPIS can be implemented is when simulating spacecraft's differential charging process. In this scenario, the two

simulation levels of concern are the plasma time step (plasmaDt) and plasma-spacecraft time step (simulationDt). In differential charging, potential evolution on the surface is few orders of magnitude slower compared to the plasma dynamics. Thus, plasma dynamics can be considered to be stationary with respect to the surface charging process. Therefore, it is possible to set the numerical plasma duration (plasmaDt) to be few orders of magnitude smaller that the simulation time step (simulationDt). This method could significantly reduce the actual simulation time as well as reducing computational needs. In all cases, a careful choice of each level time step is essential in order to retain plasma stability condition.

4.5.2 Density and Field solvers

When particle density is requested, each superparticle will deposits its density on the neighbouring nodes. This corresponds to depositing its volume density and charge on the four tetrahedron nodes that form the cell where the particle is located. The densities are deposited using linear weighting algorithm and the amount is proportional to the cell barycentric coordinates. These values are then used to solve the field equations (Poisson's) as described in Section 3.1.

4.5.3 Particle In Cell

The SPIS software offers the option to switch between fluid model, PIC model or a combination of both models. The choice of suitable model for the simulation depends mainly on the computational resources, accuracy as well as the required output from the simulation. While fluid model offers a fast and analytic way of obtaining the surface potential for a spacecraft charging problem, it is limited in terms of simulating some micro processes involved in the simulation process. SPIS for example only allows processes such as particle-particle interactions and potential barrier to be simulated using full PIC simulation. In some cases, the hybrid model can be employed to improve the simulation speed without compromising too much on the actual result, although it is still limited to the case where small scale

interactions are off interest. This section will only introduce the full particle in cell technique employed in SPIS.

The PIC simulation begins with the introduction of superparticles in the simulation volume. These superparticles are introduced in the simulation volume at the start of the simulation and are continuously injected from the boundary over the course of the simulation. One important attribute of a superparticle is the *weight*, which is the number of actual physical particles it represents. The weight also determines the number of superparticles available in the volume. High number of superparticles allows more precise representation of plasma parameters such as density and velocity distribution but will require more computational resources.

Particle sampling is the process of introducing these superparticles into the simulation domain either at the start of the simulation (volume sampling) or during the course of the simulation (surface sampling). Volume sampling is practically the process of representing the physical particles which were assumed to be readily available in the domain by taking each cell's volume density and dividing it with an appropriate particle weight. This is done once at the beginning of the simulation. On the other hand, surface sampling is the continuous process of injecting particles into the simulation volume either based on the conservation laws for the case of ambient plasma or when simulating particle source on spacecraft (eg. ion thruster). The former part refers to injection of particles from the plasma boundary while the later corresponds to particle injection from the spacecraft surface. Similarly, the number of superparticles injected from these surfaces depends on the particle flux through the surface and the weight of the superparticles.

The superparticle's weight in SPIS-NUM can be either a fix value or allowed to vary between two predetermine values. This flexibility enables more precise representation of physical particles especially during the later part of the simulation process. For example, as potential is developing on the spacecraft's surface, the initial boundary condition at the plasma boundary might no longer be the same as when the simulation started. This in turn affects the particle flux through that

boundary depending on the particle species and potential of the surface. Allowing a flexible superparticle weight means the accuracy and/or speed of the simulation can be sustained or improved by introducing either more superparticles with less weight or less superparticles with larger weight. This done by continuously monitoring and updating the particle's flux on the boundary.

The particle sampling process in SPIS-NUM is shown in the flow chart in Figure 4.5(b). After the creation of superparticles, their position's and velocity's are sampled based on their temperature (thermal velocity) and/or mach speed (drift speed for the case of ion particles). The list of these newly injected superparticles are then merged with the existing particle list i.e. particles that are already in the volume.

The next step in the simulation process is moving the particles in the simulation volume based on the force experienced by each superparticles. SPIS uses either exact integration method and/or iterative method using either leapfrog method (2nd order) or Runge-Kutta-Cash-Karp method (4th order). The switch between the exact trajectory and the iterative method depends on the type of fields present. Exact integration model is used only when constant electric field is present while the iterative method is used when both electric and magnetic fields are present and/or when any of the field is non-uniform. During this process, particles' next positions are recorded and they are marked for removal if they cross the plasma boundary (leaving the volume) or arrive at the spacecraft's surfaces (collected as current). The list is then updated by removing the marked particles from the simulation domain.

The moments of the simulation is recorded at predetermined intervals for future analysis. These include parameters such as density, energy, surface and plasma potential and electric field. The whole simulation process is repeated in the next integration duration and continue until the end of the simulation period. Upon the completion of the simulation, the results from the monitoring process are passed back to the UI for analysis.

Chapter 5

Spis-Dust: Implementation and Validation

5.1 Introduction

In addition to the naturally occurring dusty plasma, spacecraft in space has been acknowledged to be another source of dust particles [Goree ad Chiu, 1993]. These particulates are produced as a result of material degradation, waste dumping, thrusters firing or simply by the release of trapped dust particles from the spacecraft's surface. The introduction of dust particles into the space close to the spacecraft could create localized dusty plasma system which could present different types of problem to the spacecraft operation [Murphy and Chiu, 1991]. For example, dust particulates have been found to be the cause of measurement errors on many occasions [Robinson et al., 1991] due to the perturbation it causes to the surrounding plasma system.

In addition to the localized dusty plasma system, future space explorations such as to the Moon and asteroid require consideration on the global dusty environment often found near the lunar or asteroid surface. The lunar lander mission for example will require understanding on the behaviour and effects of dust on human and space equipments [Stubbs et al., 2007b]. Past experiences gathered during the Apollo

missions illustrate the potential hazard dust particles could poses to astronauts life saving equipment [Christoffersen et al., 2009]. As a result, a systematic and efficient method to understand the dusty environment is needed in order to anticipate future problem caused by dust particles.

One of the efforts undertaken to understand the behaviour of dust particles in space plasma is the development of dusty plasma simulation software that could realistically predict and simulate the dusty plasma systems. This chapter describes the implementation of SPIS to simulate the dust charging process, dusty plasma dynamics and their effects on spacecraft surface potential. The new software is called SPIS-Dust and was developed by taking advantage of SPIS open source and modularity which facilitates further development of the code such as the inclusion of dust charging and dusty plasma simulation.

New modules have been developed to accommodate the introduction of dust particle and the dust-plasma interaction. The code is modified in order to integrate dusty plasma environment into the SPIS framework, hence allowing simulation of dusty plasma dynamics and their effects on spacecraft charging. The MCC algorithm is introduced which allows the simulation of dust-plasma interaction by randomly checking for collision between dust and plasma particle in each time step. Dust-plasma collision is defined as an absorption type collision since plasma particles are assumed to stick to the dust surface. In reality, a collision between plasma particles and dust particle could produce many type of interactions such as scattering and ionization which are not addressed in this work. In the simulation, the number of absorption collision is a function of local plasma properties as well as the dust physical and electrical properties.

5.2 Dusty plasma in SPIS

The major difference between dust particles and any other elementary particles is the varying physical and electrical properties of the dust particles. Properties such as their size, mass, charge and density depends on the dust's origin and surroundings.

The size and mass of the dust particles also vary compared to elementary particles and are more likely to fall under certain size or mass distribution function. The charge on each dust particle on the other hand depends on the dust charging process involved and could range from few elementary charges up to tenths of thousand of elementary charges.

Dust particles are included in the SPIS-Dust environment by introducing an ion-like spherical dust species in the code default particle list. The inclusion of dust particles in the code is done in a way that it allows the introduction of dust particles with either equal mass and size, or ones that follows a certain size distribution. These particles can be injected into the simulation domain from the plasma boundary as for the case of drifting dust, or from spacecraft surface in order to look at problem arising from material erosion. It is also possible to inject dust particles with different value of dust charge number, representing either electrically neutral dust particles or ones that are charged to a certain potential. These dust parameters are set during the initial stage of the simulation process and are normally based on the ambient dusty environment.

As the dust particle density is likely to be much less than plasma particle density ($n_d \ll n_0$), special attentions are needed during the dust sampling process. Normal particle sampling method used in SPIS may result in a dust superparticle with weight less than unity. This could cause improper representation of the dust population in the simulation domain. Furthermore, in an environment where the microscopic dust-plasma interaction is important, having too many dust particles can lead to inefficient use of computational resources. Hence, depending on the environment, SPIS-Dust will require user to manually define the proper dust superparticle weight which is used for all dust particles in the simulation.

5.3 Dusty Plasma Simulation

A self consistent dusty plasma simulation requires solutions to the plasma and dust particle motions (equations (2.42) and (2.88)), dust charging (equations (2.70) and

(2.71)) and Poisson's equation (2.9). In PIC simulation, this is done by first solving the field equations on every node in the simulation domain. These fields are then reassigned as forces experienced by the particles in order to solve the motion of plasma and dust particles (equations (2.42) and (2.88)).

In a conventional 'structured' PIC simulation where the cells are of equal size, a correct choice of numerical parameters such as time step (Δt), cell size (Δx) and superparticle number per Debye length volume (N_d) are as important as the representation of physical model and properties. These parameters are chosen to ensure both the fields and particles spatial and temporal change are properly resolved during the course of the simulation. Commonly accepted values for Δt and Δx as suggested by Birdsall [2005] and Hockney and Eastwood [1988] are

$$\omega_p \Delta t \lesssim 0.2 \tag{5.1}$$

$$\frac{\lambda_D}{\Delta x} \gtrsim 2. \tag{5.2}$$

SPIS on the other hand employs an unstructured mesh design when constructing the cell for the PIC simulation. Rather than using an evenly spaced grid, the simulation model is constructed from tetrahedron cells where the size of each cell varies according to the intended spatial resolution. The choice of Δx is therefore not as straightforward as in the conventional PIC simulation as the variation in the cell size can be as much as few orders of magnitude. In addition, the variable particle weight method employed in SPIS means that the number of superparticles present in each cell is highly dependent on the cell's size and could vary from one cell to another. This could produce a large variation in both the number and weight of superparticles between larger and smaller cells which could reduce the accuracy of the Monte Carlo collision algorithm.

In order to minimize inaccuracies due to the implementation of unstructured mesh, a new imaginary cell is constructed in SPIS-Dust with the dust particle located at the centre of each cell. The purpose of this 'cell' is to ensure that the

number of samples (plasma superparticles) available for the collision algorithm is not limited to superparticles within the same tetrahedron cell as the dust particle but is determined by the distance between the plasma particles with the dust particle. This method will compensate for the variation in cell size caused by the unstructured mesh employed by SPIS.

This new 'cell' has a radius of r_s, which value is set based on the plasma density and superparticle weight. For example, in ionospheric plasma where the Debye length (λ_D) is of the order of centimeters and the simulation volume is of the order of tenths λ_D, the size of the cells can be set to be $\lambda_D/2$ from the location of the dust particle. In contrast, a cell in magnetospheric plasma where $\lambda_D \sim 10\,\mathrm{m}$ might require the radius to be a much smaller fraction of the Debye length due to the large Debye radius. In both cases, the choice of r_s also depends on the requirement of having at least certain number of surperparticles sample in the cell that will give the minimum numerical errors and at the same time avoiding unnecessary burden on computational resources.

5.3.1 PIC-MCC

The interaction between plasma species and the dust particle is simulated via Monte Carlo collision (MCC) algorithm which is based on the assumption that dust charging is a collisional event that can be modelled using MC technique [Birdsall, 1991]. The MCC method had been used extensively to simulate collision between plasma particles with neutrals and has been adopted for multistep dust collision by Gatsonis et al. [1994]. Multistep collisions allows MCC implementation in a highly collisional system and could enable a much larger time step to be used compared to the PIC recommended time step of $0.1\Delta t$ [Gatsonis et al., 1994]. Figure 5.1 shows the implementation of PIC-MCC in SPIS.

The determination of collision between the dust and plasma superparticles starts with finding the absorption collision frequency, ν_s for every dust superparticle in

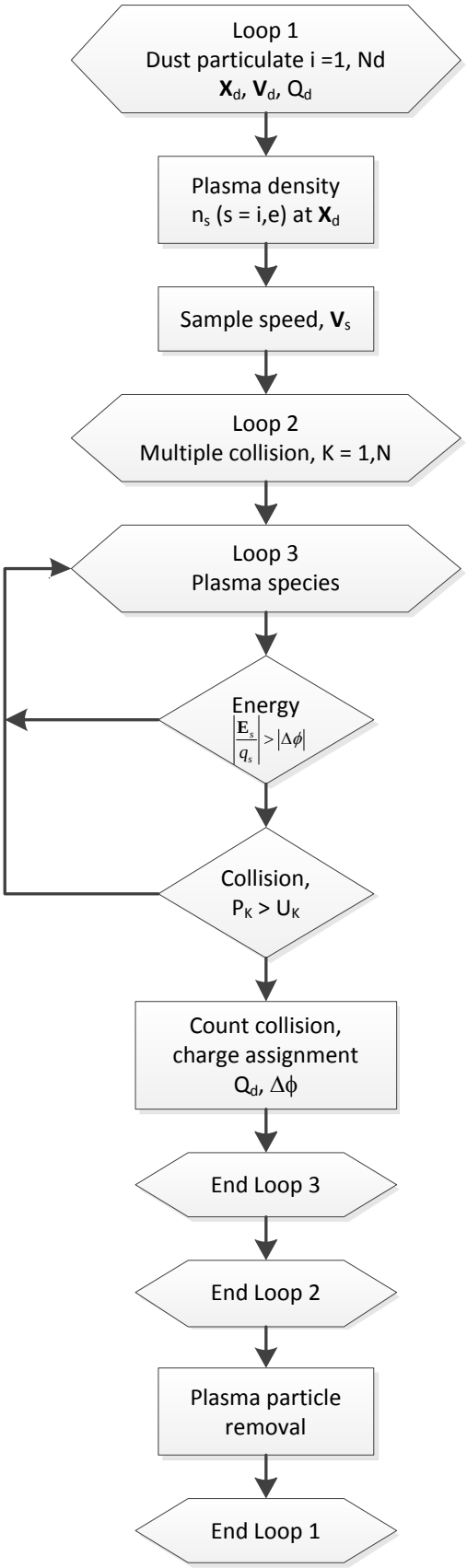

Figure 5.1: Flow chart of the computational sequence of the absorption collision

the simulation from

$$\nu_s = n_s \sigma_s v_{rel} \tag{5.3}$$

where n_s is the local density of the plasma species of the cell where the dust particle is located, σ_s is the absorption cross section and v_{rel} is the relative velocity between plasma species and the dust particle. Assuming that the dust particle mass is much heavier than the plasma species ($m_d \gg m_s$), v_{rel} can be estimated to be $\sim v_s$. The number of collision (N_{as}) allowed over a time step Δt is given by

$$N_{as} = \nu_s \Delta_t \tag{5.4}$$

where collision frequency, ν_s, corresponds to the local (cell) parameters. It can be seen from equations (5.3) and (5.4) that these parameters take into account local plasma density and particle speed in an area or volume where the dust is residing at its centre.

In the MCC scheme, the dust superparticle and plasma superparticle are randomly paired such that actual collision depends on the possibility of the pair producing a collision. In general, the probability of having a collision depends on the charge of both dust and plasma particles, energy of the incident plasma particles and collision frequency. In the event of collision, particle charge (q_s) is added to the dust charge but the colliding plasma species superparticle loses K_d number of particles, where K_d is the dust superparticle weight. This reflects the number of actual collisions that happened during that time step. In other words, every collision between plasma species superparticle and dust superparticle with weight K_s and K_d respectively represents K_d number of collisions and therefore require removal of K_d particles from K_s.

The dust collision cross section σ_s is calculated based on the following formula given by Havnes et al. [1987] as

$$\sigma_s = \pi r_d^2 \left(1 - \frac{\Delta\phi}{1/2 m_s |v_s|^2 / q_s}\right) \tag{5.5}$$

where r_d is the dust radius, $\Delta\phi$ is the potential difference between the dust particle and the incident plasma particle, m_s and v_s are the plasma species mass and velocity respectively and q_s is the species charge.

In the case of an isolated dust ($a > \lambda_D$), $\Delta\phi$ is equal to the dust surface potential $\phi_d(t)$ given by Whipple et al. [1985] as

$$\phi_d(t) = \frac{Q_d(t)}{C} = \frac{Q_d(t)}{4\pi\epsilon_0 r_d(1 + r_d/\lambda_D)}. \tag{5.6}$$

The plasma particle also needs to overcome the repelling potential of the dust in order for a collision to occur, i.e.

$$\left|1/2 m_s |v_s|^2 / q_s\right| > |\Delta\phi|. \tag{5.7}$$

Assuming a dust that is gaining negative surface potential which is normally the case when there is no other charging process involved, the condition set by equation (5.7) ensures that an absorption collision can only take place if the electron's kinetic energy is larger than the dust potential energy. Particles with kinetic energy less than the dust's potential energy will simply be reflected or scattered. The reflection and the scattering process however are not explicitly addressed by SPIS-dust version described here.

If the dust is in the form of a dust cloud ($a < \lambda_D$), competition for electrons/ions results in lower ϕ_d and the dust equilibrium charge number is reduced from the isolated case [Goertz and Ip, 1984, Whipple et al., 1985]. In the following simulations, $r_d \ll \lambda_D$ is assumed and hence

$$\Delta\phi = \frac{Q_d(t)}{4\pi\epsilon_0 r_d}. \tag{5.8}$$

The conventional MCC algorithm which allows only one collision in every time step is reasonable if the collision frequency between the two species is small or constant. As dust particles can vary in size, each individual particle is charged at

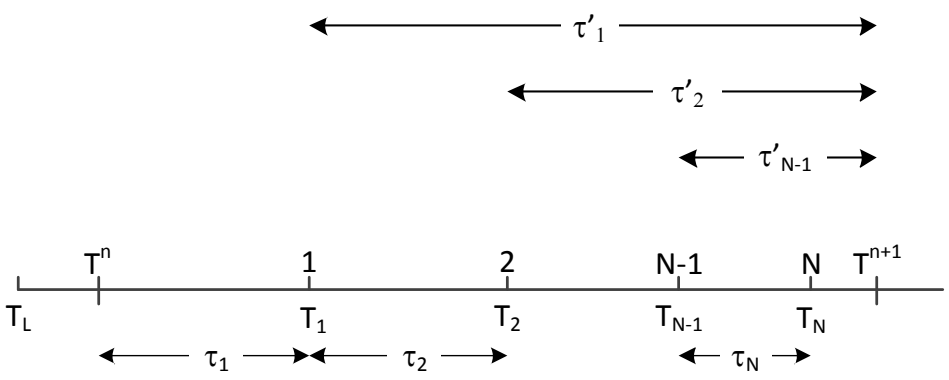

Figure 5.2: Multistep Monte Carlo collision algorithm.

a different rate to each other and this has to be taken into account in determining the number of collisions that a dust particle is likely to experience in each time step. For example, consider the collision process between a dust particle and electrons. An uncharged dust particle at the beginning of a simulation can undergo multiple collisions in one time step where this number decreases as the dust particle develops negative potential on its surface. At this stage, dust particle will experience less or occasional collision because the collision frequency which depends on the collision cross section (σ_s) is a function of dust surface potential as well as plasma particles properties such as energy and charge polarity, as shown in equation (5.5).

The need for different collision frequency for each dust particle requires a different approach to the normal MCC algorithm. This is done by employing multistep MCC algorithm first proposed by Gatsonis et al. [1994]. Figure 5.2 shows the implementation of multistep collision algorithm in MCC.

In a multistep collision algorithm, the probability of a collision in a time step Δt is given by Gatsonis et al. [1994] as

$$P_1 = 1 - exp\left[-\int_{T_L}^{T^{n+1}} \nu(t)\,\mathrm{d}t\right] \tag{5.9}$$

where T_L is the time of the last collision, T^n is the time at the beginning of the time step Δt and $T^{n+1} = T^n + \Delta t$. A uniform random number U_1 is then generated

where

$$U_1 = 1 - exp\left[-\int_{T_L}^{T_1} \nu(t)\mathrm{d}t\right] \tag{5.10}$$

where T_1 is the time for the particle to traverse the collision free path. Collision is assumed to happen if $P_1 > U_1$ which implies that $T_1 < T^{n+1} - T_L$, and T_L is then updated to T_1 ($T_L = T_1$) where the duration for the next collision is τ_1'. Multistep collision algorithm works by finding a new probability P_2 in the interval τ_1'. A second uniform random number U_2 is generated for the same interval where the time T_2 is the time for the particle to travel before the next collision occurs. Collision happens if $P_2 > U_2$ which implies $T_2 \leq T^{n+1}$. This process is repeated until all collisions for a given time step are accounted for.

5.3.2 Results and Discussion

The MCC algorithm is introduced by an interaction routine that checks for possible collision between dust particles and local plasma species based on techniques described in the preceding section. This process is performed after all particles have been moved to their next positions and includes interactions between all available plasma species with the dust particles. The dust-plasma interactions are limited to superparticles located in the same imaginary 'cell' as the dust particles. The dust-plasma interaction takes into account the number of collisions allowed within the specified time step using equation (5.4).

Particle sampling technique employed in SPIS-Dust injects superparticles on the cell's surface boundaries depending on the flux of each species on boundary surface, according to

$$N_{superparticle} = \frac{J_s \times A_{cell} \times \Delta_t}{weight} \tag{5.11}$$

where the area A_{cell} refers to the surface area of each individual cell which borders the unstructured mesh boundary, J_s is the particle flux passing through the boundary and weight is the number of particles represented by the superparticle. The flux depends on the particle mass and for a space plasma with equal electron and

ion temperature, the huge difference in the particle mass means that there will be considerable difference between electrons and ions flux. The sampling technique used allows injection of superparticles with weight ±50% of the predetermined average weight. This could lead to unequal number of superparticle if the superparticles representing the species with a low flux is injected with minimum weight whereas the one with higher flux is represented by superparticle with higher numerical weight. As a result, one could find a perfectly neutral plasma system where each species are represented by different number of superparticles with different numerical weight. Depending on the size of the interaction cell (r_s), the difference in the number of superparticles will also affect the Monte Carlo collision process as there will be a large number of particles to choose from for species with higher number of superparticles compared to the smaller choice for species with less number of superparticles. To resolve this, a new particle sampling method that uses fixed superparticle weight has been introduced to the SPIS-Dust software that enable both species' superparticles to be injected with equal weight while retaining the plasma neutrality condition of the plasma system. This technique also helps in reducing computational time and memory cost in some cases as well as maintaining uniformity in the MC collision algorithm.

5.3.3 SPIS-Dust Code Validation

In the validation process, the simulated dust particles are assumed to be spherical in shape with radius of 100 μm. This assumption is taken to allow the multistep collision process to be investigated and is also the maximum allowable particle size in most space mission [Brieda et al., 2010]. The assumption of spherical dust is valid when the dust radius is much less than the plasma Debye length [Cui and Goree, 1994], as is for the case of ionospheric plasma simulations used in this validation process. The modified SPIS-Dust software is validated for two different scenarios to investigate its performance against well established theories.

In the first scenario, a single dust particle is immersed in a dense ionospheric

plasma and the dust charging process via the PIC-MCC technique is monitored. The result is compared to the OML theory that provide analytical solution to the charging simulation [Whipple, 1981]. The next scenario involves charging of a cloud of dust particles in the same ionospheric plasma environment. In this scenario, a finite size dust cloud with three different densities are placed in the plasma and the response of the PIC-MCC algorithm for each densities are recorded. The results for the simulations are compared to the theoretical work by Havnes et al. [1990]. In both cases, the dust superparticles are set to be uncharged at the beginning of the simulation.

Single Dust Charging

Figure 5.3 shows the simulation model used for the single dust and the subsequent dust cloud charging simulations. In all validation simulations, the volumes are created with a 'dummy' probe that is kept at constant surface potential of 0V. The separation between the probe and the dust particle is maintained such that it will always be more than $5\lambda_D$ to negate any effect caused by the presence of the probe.

For single dust charging, simulation volume is set to be $10\lambda_D \times 10\lambda_D \times 20\lambda_D \mathrm{m}^{-3}$ and the volume is divided into two cubes. The top cube represents the plasma volume with the 'dummy' probe initialized as spacecraft surface. Dust particle is uncharged at the beginning of the simulation with $r_d = 100\mu\mathrm{m}$ and $q_d = 0$ and is positioned close to the centre of the bottom half of the simulation volume. The dust charging process is simulated for a typical ionospheric plasma with a Maxwellian distributions of electrons and singly charged oxygen O^+ ions. Secondary and photoelectron currents are neglected based on the assumption that both show negligible currents compared to thermal current in this type of space plasma [Whipple, 1981].

The ionospheric plasma with densities $n_e = n_i = 10^{11}\ \mathrm{m}^{-3}$ and temperature $T_e = 0.2\,\mathrm{eV}$ and $T_i = 0.1\,\mathrm{eV}$ is chosen for this validation purpose. Time step is taken to be approximately the inverse of the electron plasma frequency, Ω_e, with

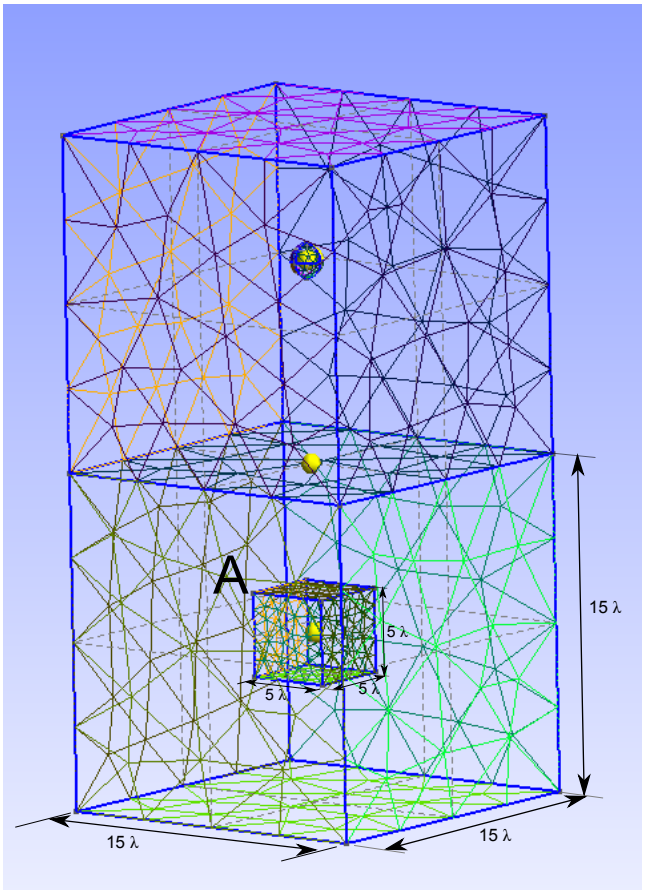

Figure 5.3: Simulation model used in the single dust charging. The mesh is constructed with a large cell at the boundary and smaller cell toward the centre of the volume, as shown by the surface mesh. At the location where the dust particle is placed, a finer mesh are employed to provide better resolution of the field whereas at the boundary, a much larger mesh is used to assist plasma species sampling process. The top half contain the 'dummy' probe and are not significant to the simulation as the 'dummy' probe's surface potential is kept at 0V. A single dust particle is introduced randomly close to the centre of the small 'cube' labelled A. Dust cloud is introduced inside the same 'cube' labelled A, with dust superparticles position is randomly set at the beginning of the simulation.

$\Delta t = 0.1\Omega_e^{-1} = 5.6 \times 10^{-9} s$ and the simulation is performed for over $15000\Omega_e^{-1}$ s. The spherical radius for interaction r_s is set to be $0.5\lambda_D$ and plasma particle weight, K_s set to 20,000.

The maximum number of collisions in the PIC-MCC over a time step in the ionospheric environment is calculated using (5.4), i.e. $N_{as} = \nu_s \Delta t = 5.6$, where it is assumed that the dust particle surface potential is zero. This number indicates that a single collision Monte Carlo process would not be able to keep up with the charging rate as there is more than one collision in a time step. In the simulation, the single dust particle is set to charge under two different charging rate; the first is when the particle is allowed maximum of 5 collision in every time step, and the second is when only single collision is allowed.

Figure 5.4 shows the surface potential of the dust particle at plasma drift speed, $V_d = 0$ as a function of time using the PIC-MCC method employed in SPIS-Dust, in comparison with the solution obtained from solving the OML charging equations. The figure shows an almost identical increase in dust surface potential between the PIC-MCC and the OML solution. The final surface potential between the two however differs as the dust particle reaches the equilibrium level with the MCC simulation underestimates the final surface potential of the dust particle.

Figure 5.4 also shows the need to have more than 1 collision per time step as the single collision per time step restriction causes an under-charging rate although the particle did reach the same potential as the one with multiple collision. The current collected by the dust particle is shown in Figure 5.5 for both ion and electron. This is compared to the one predicted by the OML theory. Both graphs clearly show the ability of SPIS-Dust to accurately perform the single dust charging process with almost identical charging rate.

Superparticle weight and the accuracy of the MCC

Superparticle weight has been discussed to be one major determinant on the outcome of any PIC-MCC simulation [Birdsall, 1991]. A single dust charging simulation is

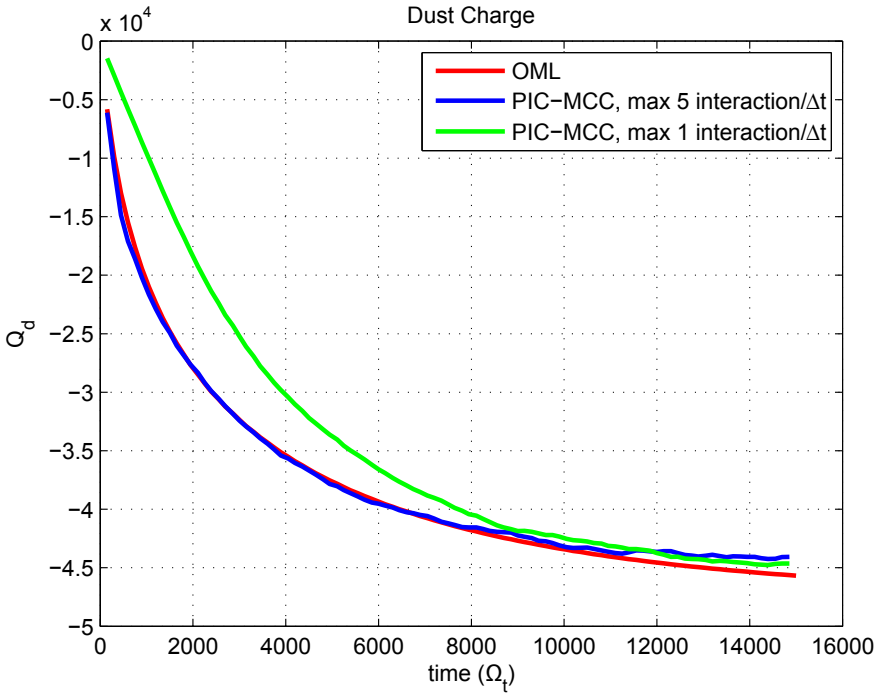

Figure 5.4: Dust particle surface potential compared to potential from OML approximation (red). Up to 5 collisions are allowed in every Δ_t (blue) and only 1 collision is allowed (green).

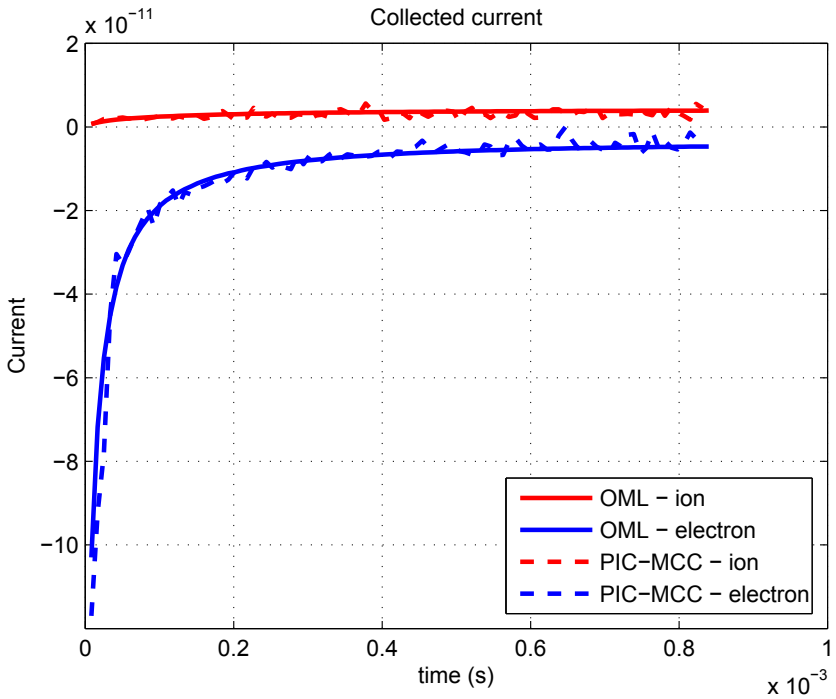

Figure 5.5: Current collection by the single dust grain shows almost identical result to the OML approximation. Solid lines are the OML current for electron (blue) and ion (red), while the dotted line are the results from the PIC-MCC simulation.

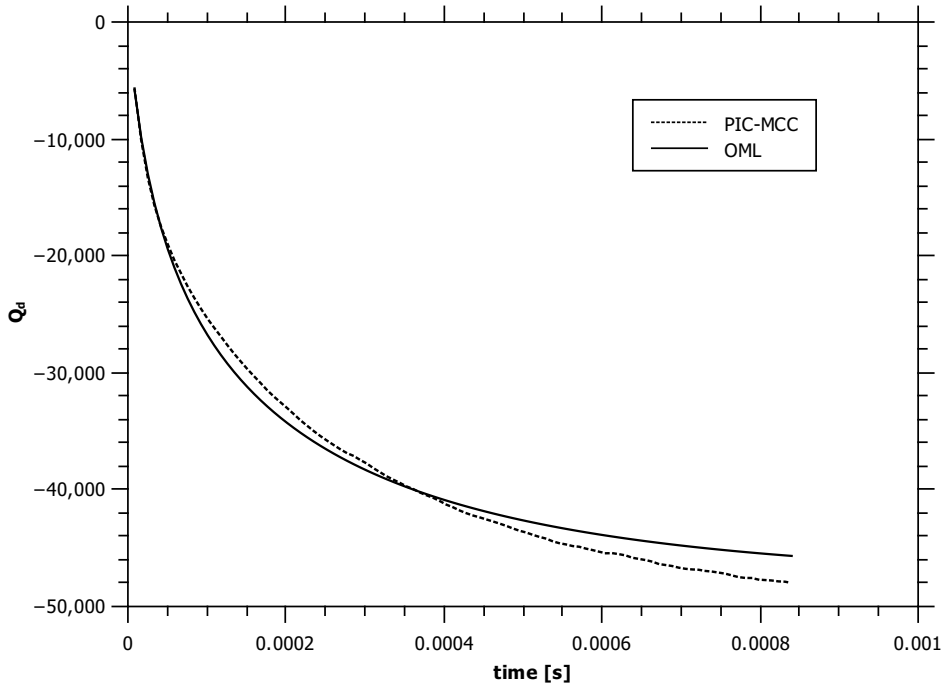

Figure 5.6: Dust charge for a case where superparticle weight is set to $K_s = 5000$. No significant advantage is obtained and simulation overestimates the final charge number.

repeated for plasma superparticles with weight $K_s = 5000$. A comparison of dust charge for this simulation and OML is shown Figure 5.6. Having almost twice the number of particles in the simulation volume does not necessarily gives better result than the one presented in the previous section. Simulation suggests an overestimate of the final dust charge number compared to the one solved analytically using the OML theory. In addition, having more particles also means increase number of computation which could slow the simulation process. At the moment there is no other way of determining the best number of superparticle weight except using the try and error method. Thus, a comparison between the numerical result and the analytic solution could provide user with evidence on the validity of the result. A few guidelines however are given by Birdsall [1991] and Hockney and Eastwood [1988] regarding the choice of this parameter.

Dust cloud charging in an unbounded plasma

It has been shown that increase in dust density causes the dust equilibrium charge to reduce significantly because of the dust collective effect [Whipple et al., 1985]. This is a direct results from the neutrality condition, i.e.

$$\frac{n_e}{n_i} = 1 - Z_d \frac{n_d}{n_i}. \tag{5.12}$$

In equation (5.12), the term $Z_d \frac{n_d}{n_i}$ can be used to determine whether the dust particle in the plasma system is in isolation or not. If $Z_d \frac{n_d}{n_i} \ll 1$, the dust particle is isolated and when it is comparable to 1 ($Z_d \frac{n_d}{n_i} \rightarrow 1$), the dust particles are no longer isolated. This equation also shows that an increase in n_d results in decreasing number of Z_d because there are more dust particle competing for the same number of electrons, in other word, the number of available electron per dust grain decreases.

For these simulations, finite cloud of uncharged dust with dimension of $5\lambda_D \times 5\lambda_D \times 5\lambda_D$ is introduced in the middle of the simulation volume at the beginning of the simulation. The simulation volume is set to $15\lambda_D \times 15\lambda_D \times 15\lambda_D$. The plasma is taken to be a typical ionospheric plasma with Maxwellian distribution, i.e. $n_e = n_i = 10^{11}\,\mathrm{m}^{-3}, T_e = T_i = 0.2\,\mathrm{eV}$. Ions are singly charged oxygen O^+ which is the usual constituent for this type of plasma. The dust particles have a uniform radius of 100 μm with mass density of $3000\,\mathrm{kg\,m}^{-3}$ and are randomly placed in the dust cloud. The density of the dust particles in the cloud are set for 3 different concentrations where $n_d = 10^6, 10^7$ and $10^8\,\mathrm{m}^{-3}$. The dust superparticle weight are set to 1,10 and 50 respectively producing 124, 133, and 254 dust superparticles. Each plasma superparticle represents 20000 real particles and simulation began with the loading of approximately 31,000 particle for each species. At every time step, new particles (electrons and ions) are injected into the simulation volume from each of the six boundary planes and particles leaving the simulation volume are discarded. Dust charging for all three different dust cloud densities are simulated

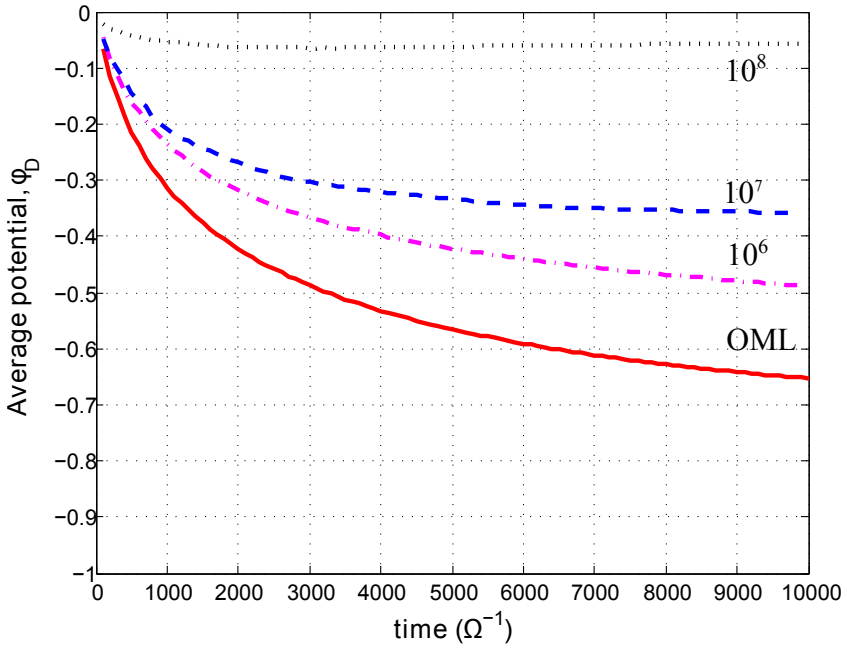

Figure 5.7: Average dust potential versus time in unit of plasma frequency (Ω_e) for different dust cloud densities. The graph shows decreasing dust potential for increasing dust cloud density.

for a period of $10000\Omega_e^{-1}$s and the resulting dust potential is plotted in Figure 5.7 as a function of time. For comparison, dust potential for a single dust particle is included in the same figure.

The average dust charge is calculated as $\overline{Q_d} = \sum_{i=1}^{N_d} Q_{id}/N_d$, where Q_{id} is the number of charge on the dust superparticle and N_d is the total number of particles in the dust cloud. Figure 5.7 clearly shows the effect of having more dust particles in the dust cloud on the average dust potential. It can be concluded that as the density increases, the $\overline{\phi_D}$ decreases together with the time it takes for the cloud to reach an average equilibrium potential.

Another important technique in determining the dust cloud collective behaviour is explained by the P parameter given by equation (2.77) [Havnes et al., 1987, 1990]. For ionospheric plasma with electrons and singly charged oxygen ions, P is evaluated for the three dust's densities which are 10^6 m^{-3}, 10^7 m^{-3} and 10^8 m^{-3}, giving P values of 0.139, 1.39, and 13.9 respectively. Figure 5.8 shows the average dust potential $\overline{\phi_D}$ versus P. The graph compares the results obtain from the simulations with the approximate rational functions for the evaluation

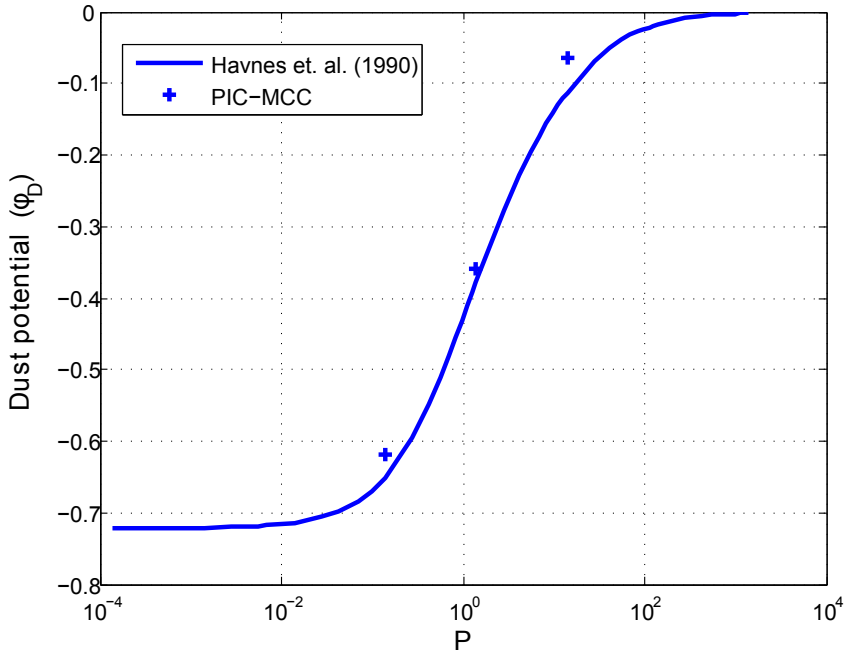

Figure 5.8: Average dust potential (+) compared to the analytical solution by Havnes et al. [1990] (solid line) as a function of P.

of P provided by Havnes et al. [1990]. It shows the effect of high P ($P > 1$) on the average dust potential. In the figure, dust potential $\overline{\phi_D}$ is calculated using the relation $Q_d = 4\pi\epsilon_0 r_d \phi_D$, where ϕ_D is the relative potential difference between the dust and the plasma [Havnes et al., 1990]. In Figure 5.8, $\overline{\phi_D}$ is obtained when the dust cloud has reached its average equilibrium dust charge. In all three cases, the simulation is in excellent agreement with the dust equilibrium potential given by Havnes et al. [1990] although a slightly lower average is observed for $n_d = 10^8 \mathrm{m}^{-3}$. Similar results were observed by Gatsonis et al. [1994] and it was argued that the difference was due to the fact that Havnes et al. [1990] does not include the effect of non-thermalized plasma in the derivation of the solution.

In a finite dust cloud, the collective effect of the dust cloud produces a larger resistance to incoming electrons and at the same time increases the attractive force on ions. At low dust cloud density ($n_d = 10^6$ m^{-3}), the dust cloud potential does not perturb the surrounding plasma and the result is very much similar to the case of isolated dust. As the density of the cloud increases, there is now more competition to electrons (and ions) among the particles inside the dust cloud. A cross section of dust cloud potential on x-y plane for dust cloud with densities

of 10^7 m^{-3} and 10^8 m^{-3} are shown in Figure 5.9. In Figure 5.9(a), a uniform potential can be observed across the dust cloud where $n_d = 10^7$ m^{-3}. This indicates that the all particles inside the cloud are charged at a similar rate to each other. Figure 5.9(b) meanwhile shows the dust cloud potential when density is increase to $n_d = 10^8$ m^{-3}. In the figure, a ring-like structure can be observed to appear at the cloud's boundary and the plasma is heavily perturbed with positive potential can be seen outside the dust cloud. The ring structure is negatively charge while the plasma inside the cloud is positively charged.

The ring structure is formed due to the dust collective effect. The high number of particles located inside the cloud created a potential barrier which shields incoming low energy electrons. At the same time, this barrier also reduces the flux of the high energy electrons into the innermost section of the cloud. This results in reduced number of electron collisions inside the dust cloud because there are now less number of electrons that are able to pass through the potential barrier created by the cloud. In addition, the negative plasma potential created by the dust cloud attracts more ions to the cloud hence increases the ion collision frequency.

The charge density cross section on the x-z plane for both electrons and ions are shown in Figure 5.10. As illustrated in Figure 5.10(a), electron density at the centre of the dust cloud is reduced to almost one tenth compared to ambient plasma. Figure 5.10(b) indicates that there is almost twice as much ions concentrating near the dust cloud's edge. This result agrees with the observation made by Gatsonis et al. [1994] although the boundary between the neutral and the disturbed plasma is not visible in the figure due to smaller simulation volume.

The radius of the dust cloud is increased to test whether the observation of the potential ring structure is dependent on the size of the dust cloud. The radius of the dust cloud is set to double from $5\lambda_D$ to $10\lambda_D$, and the density is maintained at 10^8m^{-3}. The system is simulated for a period of $10000\Omega_e$s and the resulting dust cloud and plasma potential is shown in Figure 5.11. The plot shows the development of similar potential structure around the dust cloud, where the outer

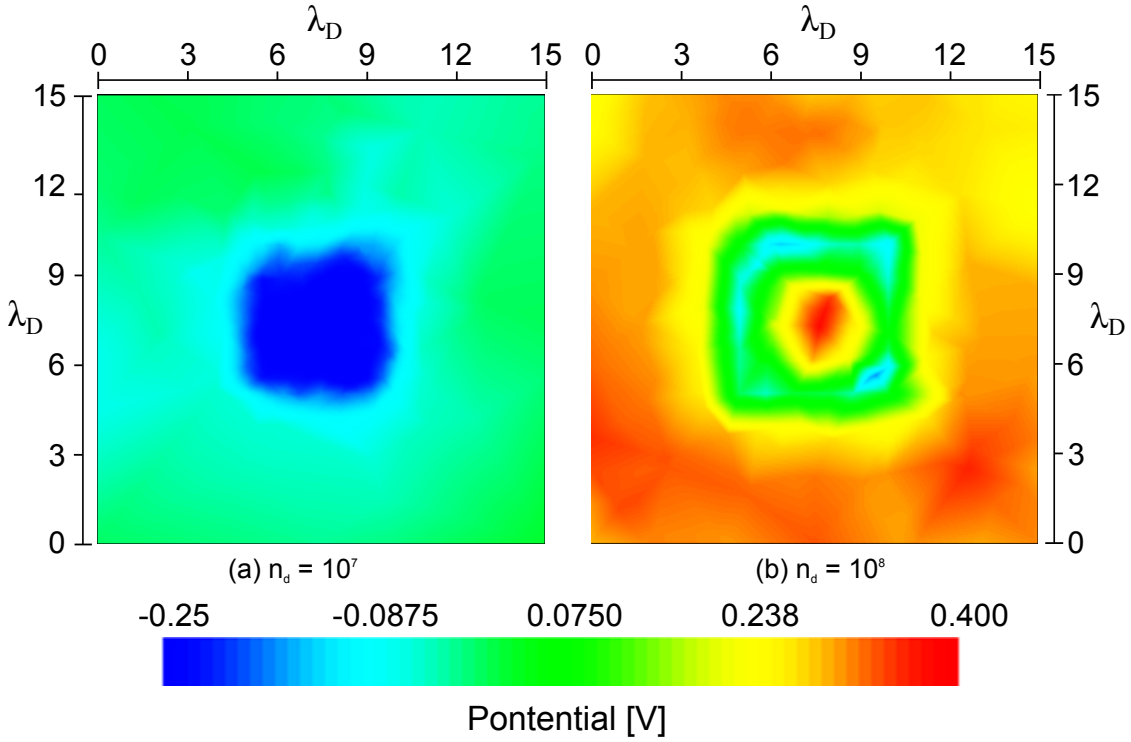

Figure 5.9: Plasma potential on the x-z plane at y = 0 for dust cloud with (a)$n_d = 10^7$ and (b) $n_d = 10^8$. The scale is in $\lambda/2$ with the snapshot taken at $t = 10000\Omega^{-1}$. In (a), a homogeneous negative plasma potential is observed at the dust cloud position while in (b), the centre of the cloud is positively charged due to screening effects caused by dust particle located at the edge of the cloud.

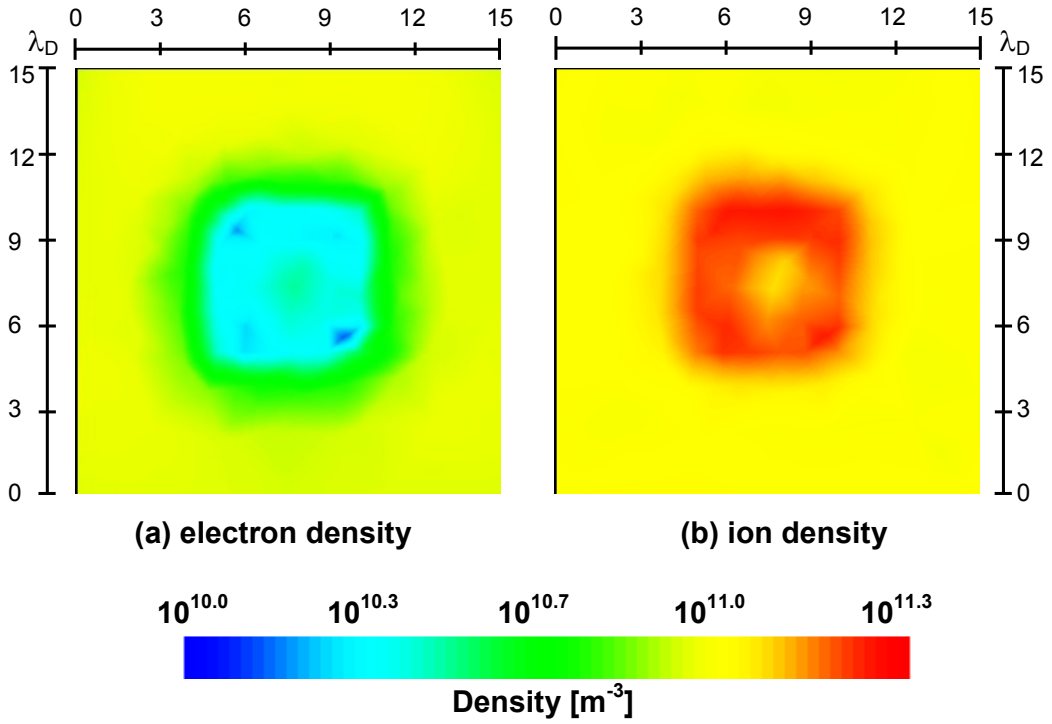

Figure 5.10: Plasma density on the x-z plane at y = 0 for dust cloud with $n_d = 10^8$. The scale is in λ_D with the snapshot taken at $t = 10000\Omega^{-1}$. In (a), a depleted electron region is clearly seen at the centre of the cloud with density around 1/10 of the ambient electron density. In (b), increase in ion density around the cloud with twice the ambient density is observed at the cloud edges. This is caused by negatively charged dust particles located at the cloud's edge as compared to the centre of the dust cloud where dust particles are positively charged.

edge of the cloud is more negatively charged compared to the inner cloud. This happen simply because the larger dust cloud requires a much longer time to reach its average equilibrium potential. Based on the results, it can be concluded that even though the development of the ring structure is time dependent, the formation of the potential well is a function of the dust cloud density rather than the size of the cloud.

In conclusion, at low dust density ($P < 1$), each particle in the dust cloud behave in a similar manner as a single dust particle and the charging process can be approximated by the OML theory. However when $P > 1$, the difference in electron and ion density around the dust cloud means that dust particles located on the edge are charged to negative potential while the ones in the middle of the cloud are positively charged.

5.3.4 Dust cloud near a charged surface

Simulations reported in this section considers a surface which represents a spacecraft in an ionospheric plasma environment releasing a cloud of trapped dust particles into its surrounding. The surface is assumed to be conducting with initial potential of 0V. No other surface interaction such as photoemission or secondary emission are included in the simulation. This condition is akin to the environment a spacecraft might encounter during its initial orbital injection.

The dust particles have the same basic properties (size, mass and cloud radius) as in the previous simulations, and the particles are assumed to be uncharged at the beginning of the simulation. The dust cloud has a radius of $5\lambda_D$ with densities of $n_d = 10^8$ and is initialised at two different distances from the spacecraft, at $1\lambda_D$ and at $5\lambda_D$. Plasma particles are injected from the boundary planes, and each superparticle represents 20,000 actual particles, as in the previous section. The 2-d view of the simulation model is shown in Figure 5.12.

The surface's current collection and surface potential are shown in Figure 5.13. In Figure 5.13(a), there is an increase in electron current for the two different cases

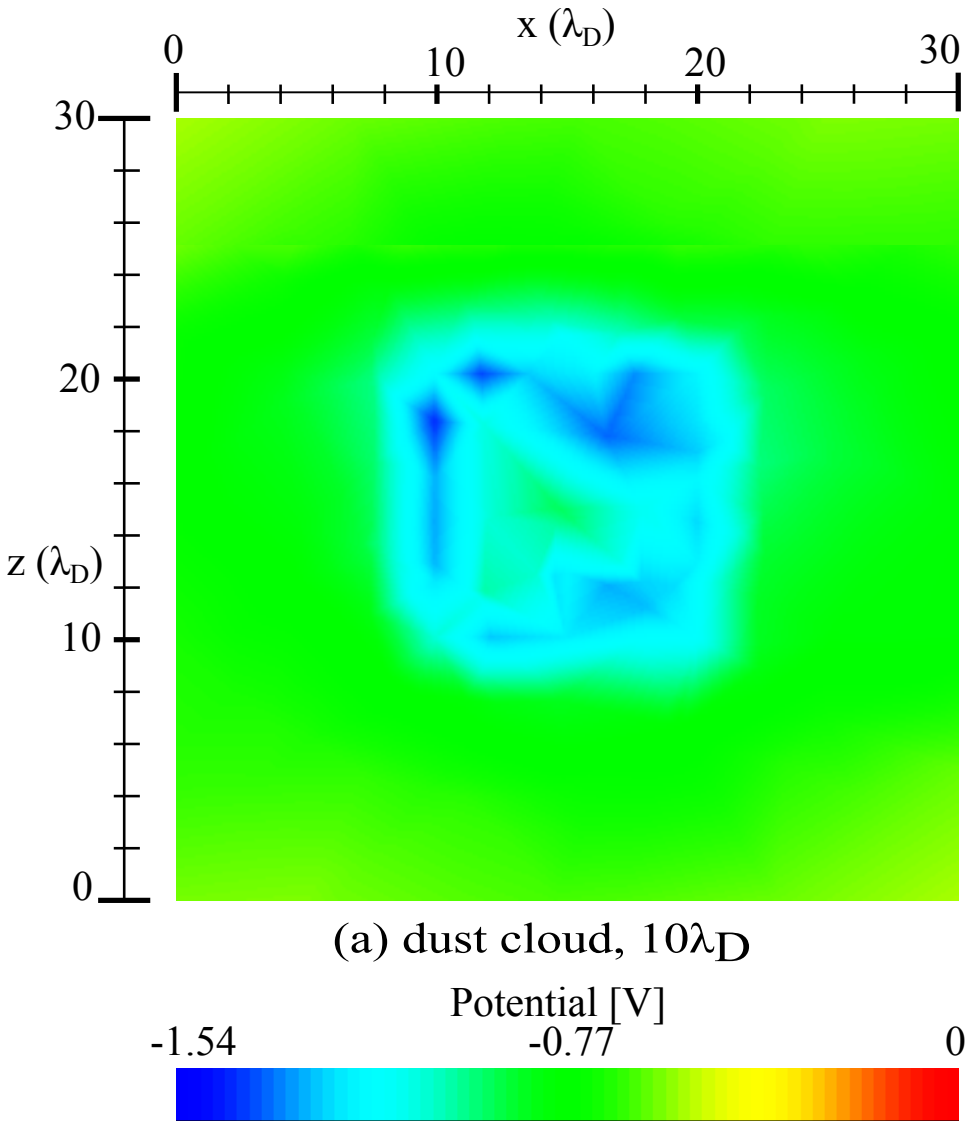

Figure 5.11: The 2-d view of the plasma potential surrounding a dust cloud with radius $10\lambda_D$ at $t = 10000\Omega_e$s. A similar ring structure can be since although the potential of both the outer edge and inner side is negative. The dust cloud requires a much longer simulation period for it to have a similar potential level as in Figure 5.9.

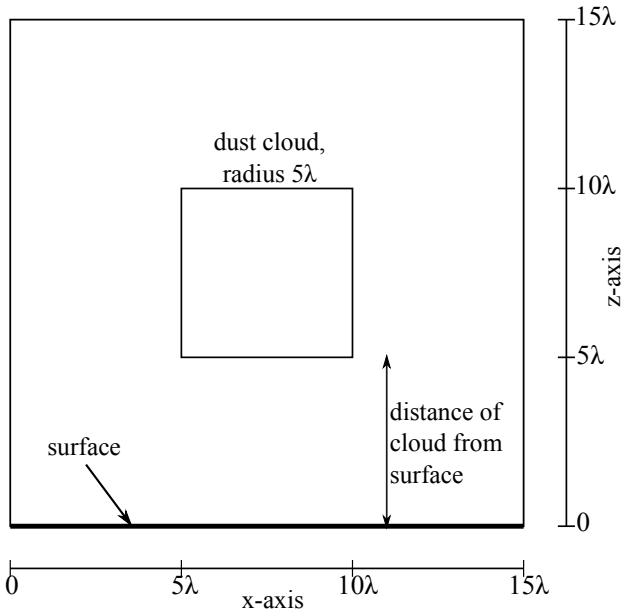

Figure 5.12: 2-d view of the simulation model.

of dust clouds when compared to the one without the dust cloud. There is however a slight increase in ion current when the dust cloud is closer to the charged surface as shown in Figure 5.13(b). The increase in ion current is an order of magnitude smaller than the electron current, making its contribution to the total net current almost insignificant as shown in Figure 5.13(c). This results in slightly higher negative potential on the surface when compared to the case with no dust particle as in Figure 5.13(d).

As the spacecraft surface is charged to negative potential, ions are accelerated towards the surface. The presence of dust cloud increases this attracting force, with the dust cloud closer to the surface contributing more to the attracting force than the one that is further away. This is clearly illustrated in Figure 5.14. Figure 5.14(a) and Figure 5.14(c) show ion densities for the cases where the cloud is $1\lambda_D$ from the surface while Figure 5.14(b) and Figure 5.14(d) show the ion densities when the dust cloud is located $5\lambda_D$ from the surface. The first 2 figures are taken at $t = 10000\Omega_e^{-1}$s while the latter 2 are taken at the end of the simulation at $t = 20000\Omega_e^{-1}$s. Halfway through the simulation at $t = 10000\Omega_e^{-1}$s, a high ion concentration can be seen in both dust clouds (Figure 5.14(a) and Figure 5.14(b)).

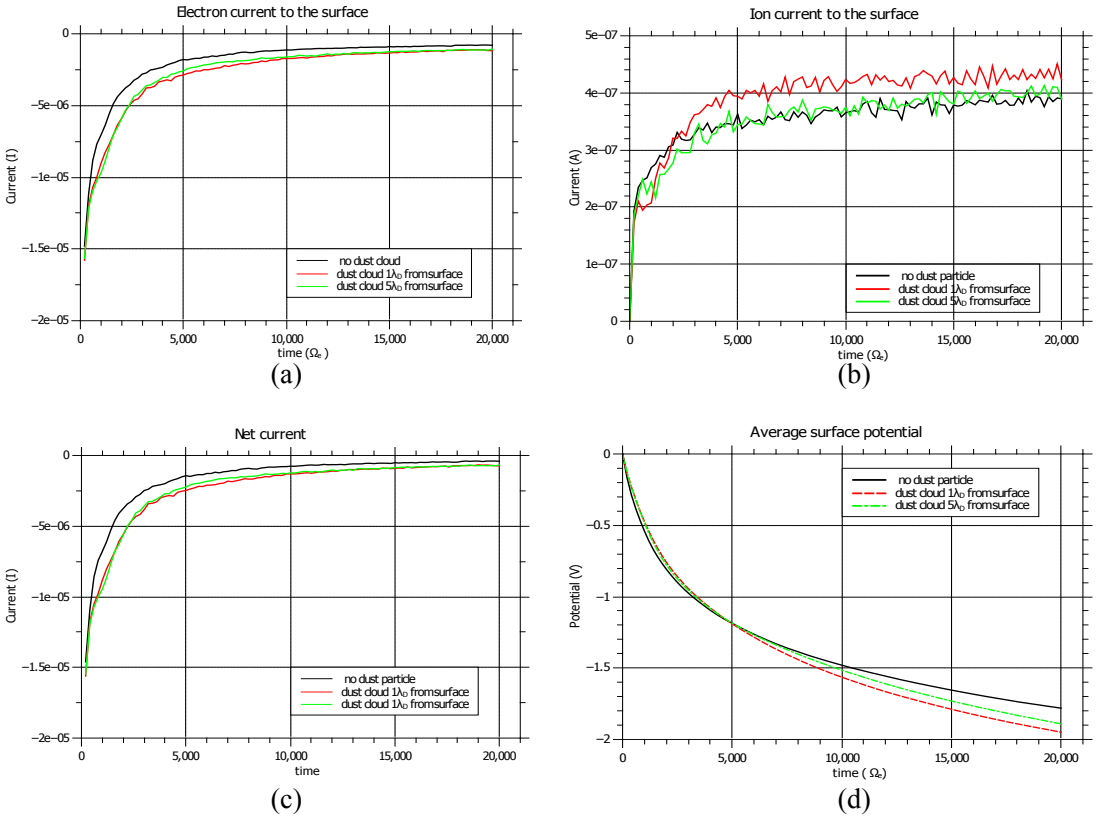

Figure 5.13: Current collection and surface potential for the three cases: no dust cloud (black), dust cloud $1\lambda_D$ from the surface (red), and dust cloud $5\lambda_D$ from the surface. (a) and (b) show increase in electron and ion currents in for both cases of dust cloud. The increase in ion current however is higher for the case where the cloud is much closer to the surface. (c) is the net current coming onto the surface and (d) shows the average surface potential where the dust cloud is observed to have caused the potential to decrease further.

As the surface is charged to a negative potential, ions that were previously trapped inside the dust cloud start to move towards the surface, where they are collected. As a result, for the cloud that is close to the surface, a region of depleted ions appears at the bottom edge of the cloud (Figure 5.14(c)).

The presence of a charged surface also creates a region of depleted electrons. Electrons are being repelled from the surface, and the effect is significant when the cloud is close to the surface. In Figure 5.15(a), electron density between the dust cloud and the surface is an order of magnitude lower than the one where the cloud is located at distance $5\lambda_d$ from the surface in Figure 5.15(b). The structure of the electron depleted regions is similar to a wake region often encountered when an object passes through a streaming plasma. Simulations also reveals that electrons inside both dust clouds are made of high energy electrons as illustrated in Figure 5.16, with more energetic electrons observed on the cloud closer to the surface. In both cases, low energy electrons appear to have been repelled by the cloud, creating a layer around the dust cloud. In addition, Figure 5.16(a) indicates that there is a region where low energy electrons are trapped between the dust cloud and the negatively charged surface as these electrons have less energy to overcome the potential barrier created by the surface and the dust cloud.

5.4 Summary and Conclusion

A modified SPIS software (SPIS-Dust) to simulate dust-plasma interaction has been presented. Modifications to the code include the introduction of (i) dust particle to the software, (ii) a new plasma sampling routine, and (iii) Monte Carlo collision algorithm which have all been integrated into the existing code. The results presented in this chapter illustrates that SPIS-Dust is more than capable to be used for simulation studies of dusty plasma with 3-D capabilities. The 3-D non-structured mesh used in SPIS however requires a different approach to the conventional PIC-MCC method. The 'cell' where dust-plasma interaction takes place needs to be redefined to improve stability of the results. The size of the

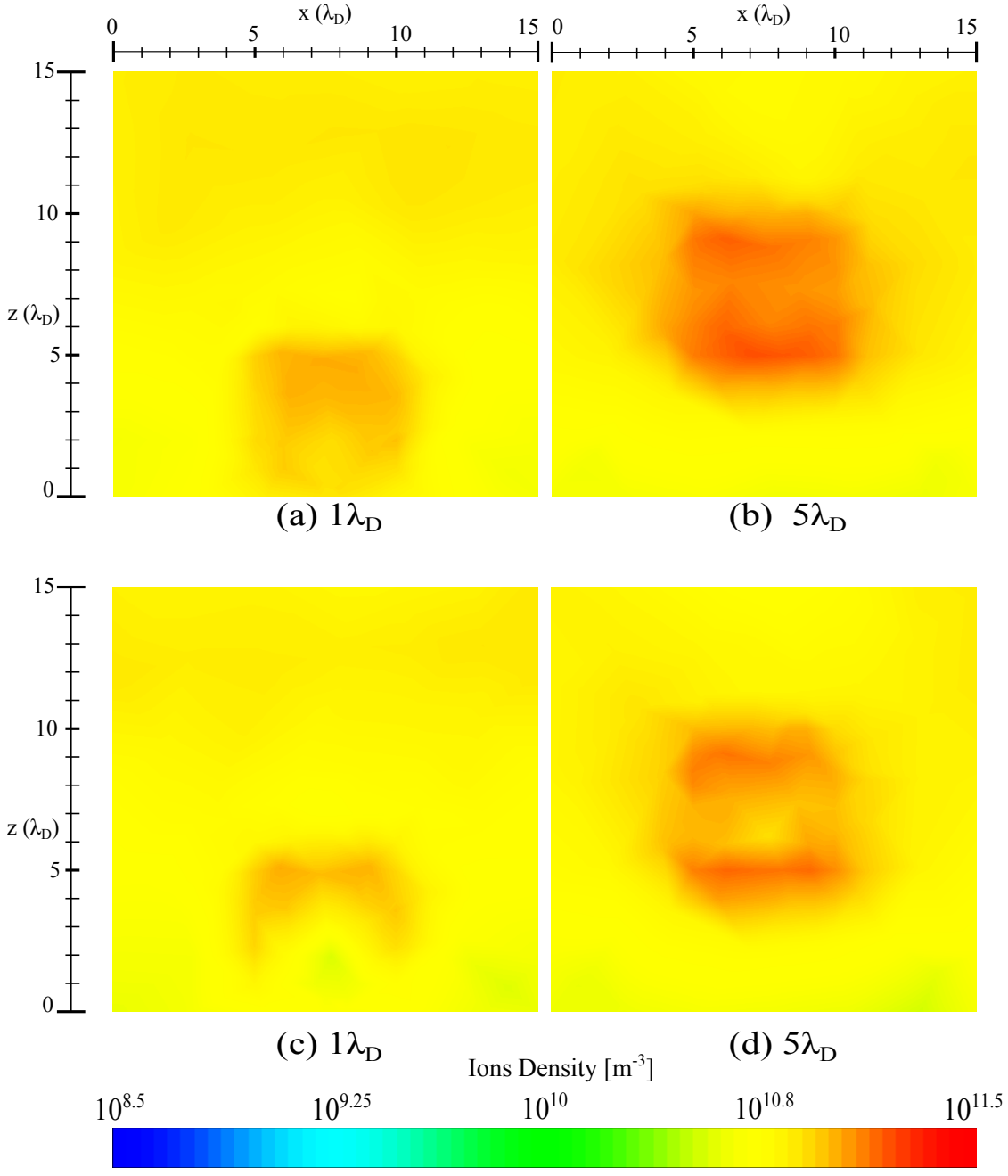

Figure 5.14: Ion density on the x-z plane at y = 0 for dust cloud with $n_d = 10^8$. The scale is in λ_D with the snapshot taken at $t = 10000\Omega^{-1}$ for (a) and (b), and at $t = 20000\Omega^{-1}$ for (c) and (d) . In (a) and (b), a high concentrartion of ions are observed on both dust cloud, and in (c) high ion density is observed only on the top edge of the cloud which is further away from the charged surface while in (d), high ion density can be seen forming a ring around the cloud edge. In (c), ions are attracted to the negative potential on the surface, leaving an area depleted of ions.

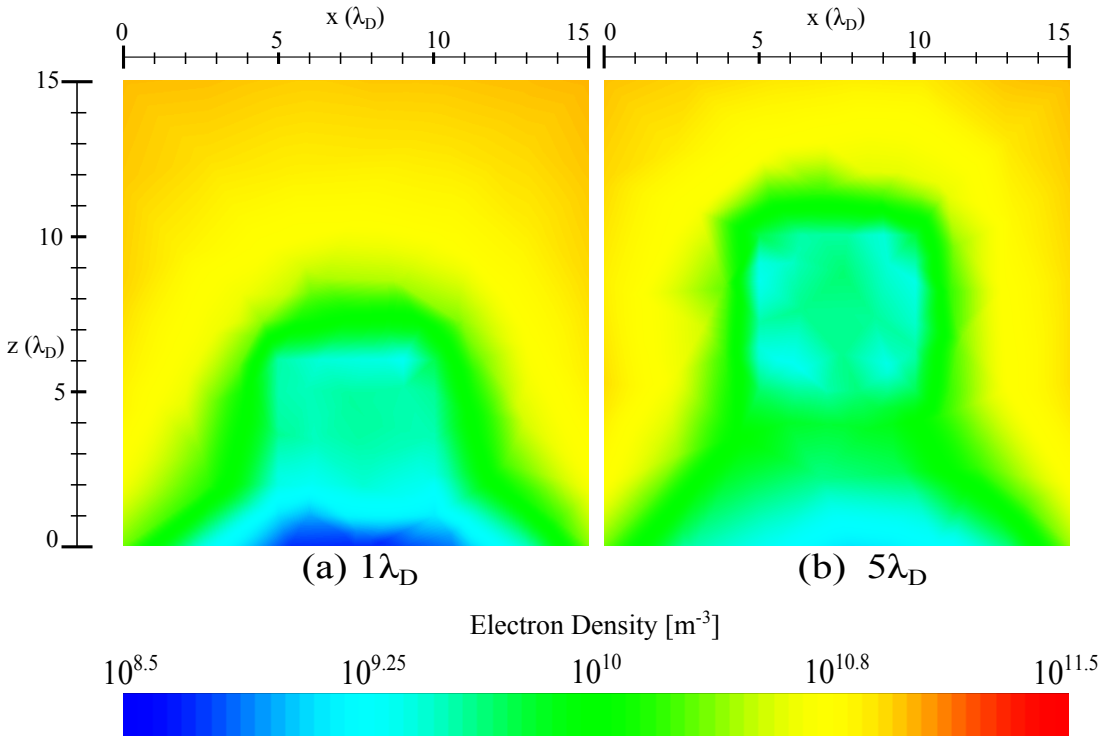

Figure 5.15: Electron density on the x-z plane at y = 0 for dust cloud with $n_d = 10^8$. The scale is in λ_D with the snapshot taken at $t = 20000\Omega^{-1}$. In (a), electron density between the cloud and the surface for the case where the distance in between them is $1\lambda_D$ is an order of magnitude lower than the one where the dust cloud is located at $5\lambda_D$. On both cases, the structure of the depletion region is similar to a wake region caused by object in flowing plasma.

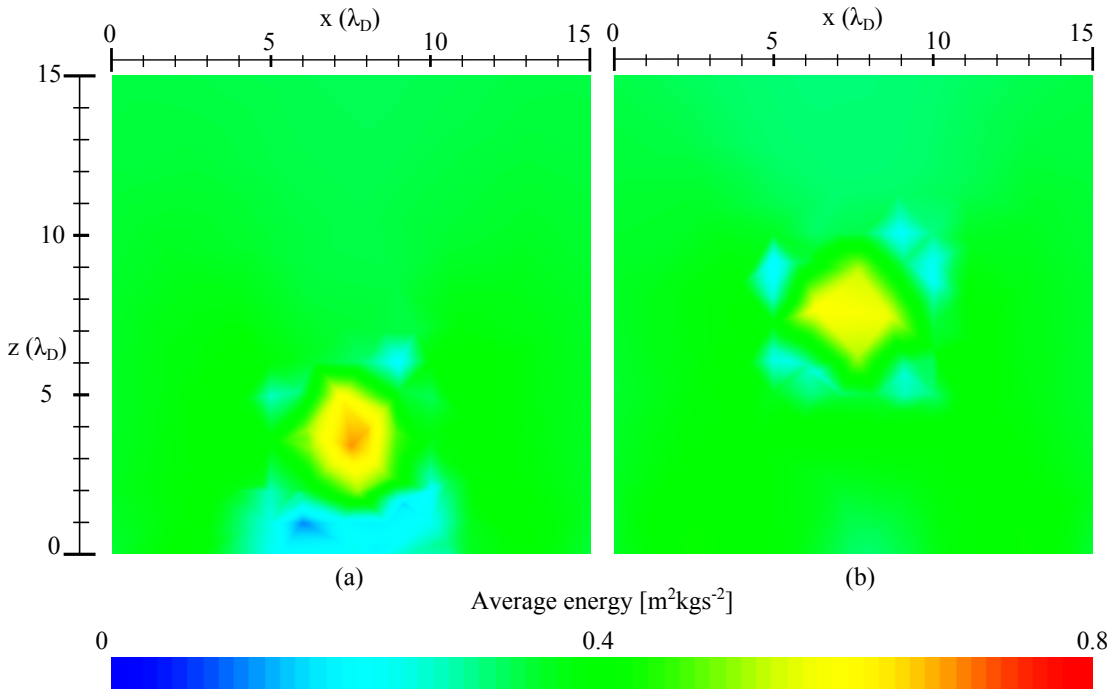

Figure 5.16: Electron energy map on the x-z plane at y = 0 for a dust cloud with $n_d = 10^8$ located at a distance of $1\lambda_D$ (a) and $5\lambda_D$ from the surface. The scale is in λ_D with the snapshot taken at $t = 20000\Omega^{-1}$. In (a), higher energy electrons can be found in the middle of the cloud because of the potential barrier created by both the surface and the dust cloud repels low energy ones. Also visible is the region of low energy electrons trapped between the cloud and the surface. These electrons have less energy to overcome the surface and the dust cloud potential barrier. In (b) high energy electrons can be observed in the middle of the dust cloud with low energy ones appear to have been repelled by the dust cloud potential barrier.

'cell' is based on dust-plasma sheath (Debye length) as well as the number of superparticles per 'cell' used in the simulation. In addition to the 'cell' structure, the simulation set up needs to be adapted to compensate for the need of a spacecraft surface which is necessary for the simulation to take place within the SPIS-Dust framework.

In the isolated dust scenario, the multistep MCC algorithm employed produces almost identical result when compared to the OML theory with both the final dust potential and dust current collection following similar charging curves. Allowing the dust to have more than one collision per time step will enable the exact charging rate to be simulated and this is indeed needed as single collision would results in under estimation of the collision frequency especially during the initial charging stage. This technique also provides a good approximation to the dust cloud scenario where the average equilibrium dust charge falls within the range of the analytical solution. In the dust cloud simulation, the effect of dust density to the dust cloud potential and its surrounding plasma has been presented which shows the formation of ring-like structure on the dust cloud for $n_d = 10^8\ \mathrm{m}^{-3}$. This ring-like structure is caused by plasma neutrality being violated as the outer dust particle creates a potential barrier when charged. This barrier prevents low energy electrons from reaching the inner cloud and at the same time attracts ions. As a result, a positive plasma potential is observed at distance of more than $5\lambda_D$ from the dust cloud as well as in the inner cloud itself.

In assessing the spacecraft charging in the presence of dust particles, simulations were carried out for two cases where (a) the dust was positioned at $1\lambda_D$ with respect to the spacecraft surface and (b) where the distance of dust cloud and the surface was kept at $5\lambda_D$. The simulation revealed that the spacecraft's surface was charged to a higher potential due to increase in electron current. Once negative potential is developed on the spacecraft's surface, ions become attracted causing the ring structure to disappear. This effect is more pronounced when the dust cloud is closer to the surface. In addition, the dust cloud creates regions of low and high energy

electrons and in one case,with low energy electrons being trapped between the dust cloud and the charged surface. This indicates that a cloud of dust particles, when released from a spacecraft surface, can affect electron and ion collection, resulting in a lower surface potential. Although the simulation performed can be attributed to a worst case scenario, where the maximum size of dust particles are released into space, the simulation results illustrates the importance of dust contamination when designing any space bound vehicle.

Chapter 6

Lunar Surface Environment

6.1 Introduction

Future space missions, particularly the proposed lunar exploration missions have reignited interest in the lunar plasma environment. Due to an almost non-existing atmosphere and global magnetic field, lunar surface is directly exposed to the solar wind and/or magnetospheric plasma, solar ultraviolet (UV) radiation and solar energetic particles (SEP) which creates what is known as the lunar exosphere. In addition, past observations (see for example Rennilson and Criswell [1974] and Berg et al. [1976]) have confirmed the presence of dust particles in the lunar exosphere which has created what is known as lunar dust-plasma environment [Stubbs et al., 2007a].

The Moon also orbits the Earth with a synodic period of ~ 29.6 days. This exposes the Moon's surface to the high dose of energetic particles found in the Earth's magnetotail as it completes its orbit around the Earth. This passage across the magnetotail lasts for around $4-5$ days during the full moon phase of the lunar cycle presents different solar environment to the one faced during the rest of the orbital period [Hapgood, 2007]. Consequently, the properties of the lunar exosphere depends on the solar wind condition, solar illumination, orbital position, localized magnetic field, lunar wake and to some extent the lunar topology itself.

Figure 6.1 shows an overview of lunar plasma environment [Stubbs et al., 2007a].

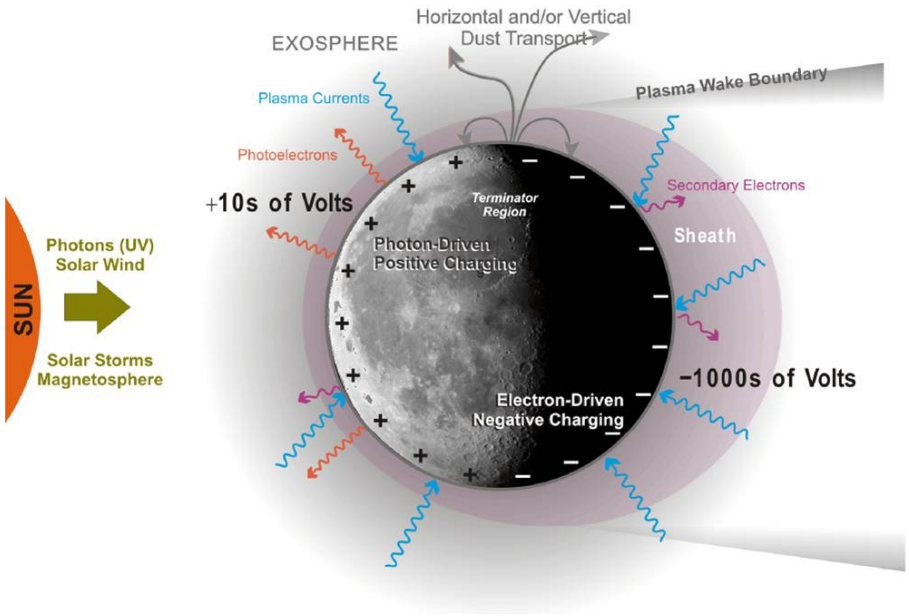

Figure 6.1: Overview of lunar plasma environment (adopted from [Stubbs et al., 2007a]).

Major processes depicted in the figure include charging processes by solar wind plasma and solar UV flux, lunar dusty exosphere, wake region and plasma sheath. This chapter will describe some of these processes which are important to the formation of lunar dusty plasma environment and their effects on dust dynamics. This chapter will also investigate some of the dust parameters that enable them to be levitated and accelerated over the lunar surface.

6.1.1 Lunar Surface Properties

The top layer of the lunar surface is made up entirely from lunar regolith which is formed as a result of continuous micrometeorites bombardment. This interplanetary micrometeorites with size approximately from $30 - 150\,\mu$m bombarded the lunar surface at speed of up to $\sim 72\,\mathrm{kms}^{-1}$ [Holsapple, 1993], turning the lunar surface into unconsolidated regolith [Grün et al., 1985]. These dusty regoliths are broadly distributed in size and loosely form the first few meters of the lunar surface. There is however significant increase in bulk density after around 0.1 m below the surface level due to compaction [Housen et al., 1983]. The mass density of an individual grain is typically $\sim 3000\,\mathrm{kg\,m}^{-3}$ with bulk density for the first 0.15 m from the

Table 6.1: Some Relevant Lunar Properties [Heiken, 1991].

Parameters	value
Lunar Radius (km)	1738.0
Grain density ($\mathrm{kg\,m^{-3}}$)	3340 [Hutton, 1969]
Gravitational acceleration (($m\ s^{-1}$)	1.623
Escape velocity (km/s)	2.38
Sidereal period (true rotation period)	27.322 days
Synodic period	29.531 days
dielectric constant	$1.84 - 2.47$ (Mare)
	$2.88 - 3.68$ (Upland)
Resistivity	10^{14}

lunar surface is around $\sim 1500\,\mathrm{kg\,m^{-3}}$ ([see Colwell et al., 2007] and references therein).

Few meters under the regolith is the lunar bedrock where its origin can be traced back to some 3.8 bilion years ago [Heiken, 1991] Interplanetary micrometeoroids impact is the only process believed to be responsible for the production of the lunar regolith and this process produces the ejecta that ended up being the suface's dusty regolith. As the dusty regolith starting to pile up above the surface, further impacts continue to grind these regolith, producing finer dust particles. Regolith with diameter smaller than 1 mm are often referred to as 'fines' and ones with diameter less than 100 μm as dust [Colwell et al., 2005].

The dust levitation process is believed to be the cause for the *horizon glow* observed by the astronauts during the Apollo mission in the seventies [Criswell, 1972, Rennilson and Criswell, 1974]. The first evidence of dust transport across the lunar surface was gathered by Apollo 17's Lunar Ejecta and Meteorite experiment (LEAM) which observed peak in impact flux during sunset and sunrise passage [Berg et al., 1973, 1976]. LEAM was intended to study dust levitation due to micrometeorite impact and was kitted with three sensors, one pointing up and two pointing in the east and west direction. The majority of these impact fluxes are observed coming from the east or west direction, suggesting both vertical and horizontal dust transport particularly around the terminator region [Berg et al., 1976]. The horizontal motion suggests the involvement of electric field in the

Table 6.2: Lunar soil parameters [Hutton, 1969].

Parameters	value
Composition (atomic percent)	
oxygen	60
silicon	20
aluminium	7
Iron content (percent)	
Mare terrain	5
Upland terrain	2
Grain size (microns)	2 to 60
Cohesion (N/cm^2)	0.02 to 0.2
nominal	0.05
Internal friction angle (deg)	31 to 39
Effective friction coefficient (estimated)	0.4 to 0.8
Adhesive strength (N/cm^2)	0.0025 to 0.01
Bulk density (gm/cm^3)	
at 5 cm	1.6
at 40 cm	2.0

transport of dust particles across the surface [Pelizzari and Criswell, 1978].

It has since been acknowledged that fine dust particles can be ejected or levitated from the lunar surface by means of mechanical activities, micrometeorites impact or by surface electric field [Colwell et al., 2005, Stubbs et al., 2006]. In the latter case, lunar dusty regoliths which are exposed to space plasma are charged to either positive or negative potential, depending on the main dust charging mechanism. These fine dust particles, upon acquiring enough charges could levitate into the exosphere creating a *dusty lunar exosphere*. The transport of these dust particles into the lunar exosphere is determined by the repelling electrostatic force generated between the dust particles and the lunar surface, and the attracting lunar gravitational force. The dust levitation properties such as its height, size distribution and density are directly dependent on the size of the dust particle itself and the strength of the electric field above the surface. Depending on the net force, particles could levitate to few centimetres on the dayside or accelerated to few tenths of kilometres in the terminator region [Stubbs et al., 2006].

In general, the lunar surface is charged to low positive potential on the dayside (< 10V) where it gradually decreases and changes in polarity towards the terminator

(~ -50 V) which trend continues well into the nightside region. The low levitation height in the lunar dayside is simply because of the low surface potential only creates weak electric field when compared to for example, the terminator region where surface is charged to high negative potential.

Criswell [1972] suggested a dust levitation model where dust particles acquire enough charge that allow electrostatic force in the upward direction to exceed the gravitational force pointing downward. This model however is incapable of explaining dust levitation observed at altitude above few tenths of meters [Stubbs et al., 2006]. Stubbs et al. [2006] proposed a new dynamic model where, rather than simply being levitated, the dust particle is accelerated by the electric field in the *plasma sheath*, thus allowing it to achieve altitude of few tenths of kilometers. Levitated dust particles can either follow a nearly ballistic trajectory before reimpacting back on the surface or continue to be suspended in the lunar exosphere if the gravitational and electric forces balances each other [Stubbs et al., 2006]. In some cases, dust particles could oscillate around a certain height and continue to do so until there is a change in the field sustaining the dust levitation process [Kuntz et al., 2011].

In addition, the lunar surface is made of craters which were formed by the micrometeorite impacts. Borisov and Mall [2006] suggested that the dust levitation on the lunar surface is caused by the strong electric field of mini craters especially near the terminator region. These mini craters have surfaces that are being shadowed from the incoming solar wind and solar UV flux which create the strong electric field needed for the dust levitation process.

These lifted dust particles can be a major environmental hazard to any space activities on lunar surface [Stubbs et al., 2007a]. Major effects include reduced material lifetime due to adhesion and abrasion, reduction in optical visibility due to dust levitation, astronauts health hazards and contamination of solar panels. It is therefore important to take into account the effects of lunar dusty exosphere in future lunar exploration to avoid any unwanted effects on the mission. Table 6.1

and 6.2 shows the Lunar surface properties and soil parameters [Heiken, 1991].

6.2 Lunar Surface Charging

The lunar surface charging process has been investigated since the early years of Apollo missions [see Manka, 1973, Freeman and Ibrahim, 1975]. This process is greatly influenced by solar driven processes which include solar wind plasma and solar ultraviolet (UV) radiation. The coupling between the lunar surface and the solar wind plasma for example creates a localized and distinctive plasma environment across the lunar atmosphere. The variation in solar UV exposure level on the other hand affects photoelectron yield which is also a main component in lunar surface charging process. In general, the lunar plasma environment can be classified into three regions based on the surface exposure to the solar wind and solar UV flux which are the dayside or the sunlit region, the terminator region and the nightside region (shadowed region).

The charging of the lunar surface is due to the collection of incidence solar wind particles and emission of secondary electrons and photoelectrons which charge the surface to a floating potential. The charging process can be described using the current balance equation given by [Manka, 1973, Whipple, 1981, Goertz, 1989]

$$I_e = I_i + I_{se} + I_{ph} \tag{6.1}$$

where I_e, I_i, I_{se} and I_{ph} are electron, ion, secondary electron emission and photoemission currents respectively. The charging process restores the equilibrium state between the surface and the plasma environment which is achieved when the net current entering and leaving a surface is zero [Whipple, 1981]. The resulting surface potential is due to the surface trying to counter the dominant charging current in order to balance the overall current collection and emission processes.

The orientation of the solar wind flow with respect to the surface normal (solar zenith angle, SZA) determines the amount of solar wind flux incidence on the

surface. This contributes to the large scale potential variation of the lunar surface. At sub solar point, the solar wind is incidence at SZA $\sim 0^o$ with respect to the surface normal which gives maximum solar flux intensity. As one moves away from the sub solar point towards the terminator, the increasing incidence angle reduces the flux intensity. At the terminator, the solar wind flow is parallel to the surface (SZA $\sim 90^o$) and incidence particles on the lunar surface are due to their thermal motion rather than the subsonic flow. Beyond the terminator is the wake region where direct interaction with both solar wind flow and solar UV flux diminished [Manka, 1973]. The plasma in this region is made of electrons of the tail distribution and ions from attraction, reflection and scattering processes.

In addition to the large scale variation of the surface potential, the lunar surface topology also contributes to the charging process where small scale variations have been observed and reported in many previous works (see for example Halekas et al. [2002], Farrell et al. [2007, 2008]). This small scale variation is possible because of the low conductivity of the surface. On a heavily cratered surface such as one found on the lunar surface, this characteristic allows the lunar surface to charge to different surface potentials (localized and differential charging) depending on the exposure level to both solar wind and solar UV. [Halekas et al., 2002]. These phenomena are normally observed near the terminator region as surface could be shadowed from both the ambient solar wind and solar UV flux due to the low sun angle.

The ambient plasma charges the surface to negative potential due to electrons having higher thermal speed than ions, which results in high electron to ion flux ratio ($J_e/J_i \gg 1$) on the surface. In addition, ions speed are more influenced by the solar wind flow speed which creates different plasma regions as it flows pass the lunar body known as the ram (facing the flow) and the wake (opposite the flow) sides. On the ram side, the ambient plasma currents are made of thermal electron current and subsonic ion current. Although the subsonic ion current is bigger than thermal ion current, it is still smaller than the ambient electron current

which means that the surface would charge to negative potential if there is no other charging process involved. On the wake side, the subsonic solar wind flow creates a cavity region which is dominated by high energy electrons of the Maxwellian energy tail and is depleted of ions because of the screening of the solar wind flow. The lack of ions means surface would have to charge to higher negative potential than the ram side, except for other charging current such as secondary electron emission that helps in reducing the surface negative potential.

For example, consider a typical solar wind with parameters $n_e \sim n_i \sim 1{\times}10^7 \mathrm{m}^{-3}$ and $T_e \sim T_i = 10$ eV with speed $v_{sw} \sim 400\,\mathrm{km\,s^{-1}}$ [Colwell et al., 2007]. This corresponds to proton thermal speed of $\sim 30\,\mathrm{km\,s^{-1}}$, electron thermal speed of $\sim 1300\,\mathrm{km\,s^{-1}}$ and solar wind's Debye length of ~ 7.5 m. In this example, ion drift speed is approximately an order of magnitude bigger than its thermal speed. Ion velocity components are then dominated by the solar wind flow speed when compare to the more random electron thermal motion. Consequently, ion flux on the surface is largely due to the collection of the ion subsonic flow than due to its thermal motion.

In the presence of solar UV flux, incidence photons excite electrons on the surface, emitting them as low energy ($E_{ph} \sim 2$ eV) photoelectrons. This process is highly dominant on the dayside of the lunar surface, with the photocurrent exceeds the ambient electron current, thus charging the surface positive [Singer and Walker, 1963]. The positively charged surface starts to attract more electrons to counter the electron loss, and recollects a majority of the photoelectrons because of their low energy profile. The recollection process happens because of the potential barrier that prevents photoelectrons from escaping the sheath, thus trapping photoelectrons in the sheath close to the surface. Only a small fraction of these photoelectrons, the ones with enough energy to overcame the attractive force, will leave the sheath and join the ambient plasma.

The main consequence of the recollection process is limiting the charging level on the sun lit side. The illuminated surface would never charge to high

positive potential as a high surface potential will create a stronger electric field or potential barrier that prevents further outflow of photoelectrons. These recollected photoelectrons helps in balancing the current on the surface because photoelectron yield, and hence photoelectron current depends on the photon flux and not the surface potential.

On the lunar surface, the charging process by both solar wind protons and solar UV flux outside the Earth's magnetotail happens on an overlapped area except for a small longitudinal area of $\sim 4^o$ at the equator where only one of these two processes is present [Colwell et al., 2007]. The discrepancies between these two processes at this region is due to the difference between the Moon orbital velocity around the Sun and the solar wind velocity which causes different level of shadowing of the solar photons and solar wind protons. At dawn, solar wind protons can still reach the surface but no photoemission is produced whilst at dusk, the surface is illuminated but has no incidence solar wind proton. In general however, charging on the day side surface by both proton and photoemission charge the surface to few volts positive (~ 5 V) with maximum surface potential is observed near the sub solar point Manka [1973].

Halfway between the sunlit and the night side region is the terminator region where the surface is exposed to near parallel solar wind flow with very little or no solar UV flux compared to the unhindered access by the fast thermal electrons. At this region, the main charging current comes from the ambient solar wind plasma but local surface topology such as craters and boulders could create localized regions of positively or negatively charged surfaces [Halekas et al., 2002, Farrell et al., 2007, 2008]. These localized regions are more prevalent in the terminator region because the almost parallel approach of solar wind and solar UV flux means a simple structure such as a boulder or a crater would have had a significantly shadowed region. A crater for example will have one side of the edge obscured from both solar wind and solar UV flux while the opposite edge is accessible to both. The shadowed region can be described as *mini wake* because it acts in a similar way

as the lunar wake, i.e. it reduces ion density and prevents photoemission [Farrell et al., 2007]. The variations in solar fluxes may result in strong localized electric field as photoelectron current varies between the illuminated and the shadowed regions. On a large scale, lunar surface in the terminator region is charged to $\sim$ -70V with the transition from positively charge dayside surface to negatively charge nightside surface happen inside the dayside region due to reduced solar wind and solar photon induced current (ion and photoemission current) [Colwell et al., 2007].

In the nightside region, the absence of solar UV photon and the screening of solar wind protons mean the main charging current is the energetic tail electrons which are the first to enter the lunar wake due to their high thermal speed. These high energy electrons charge the surface to high negative potential which is necessary in order to attract more solar wind ions into the cavity, as well as preventing more electrons from reaching the surface [Manka, 1973, Freeman and Ibrahim, 1975]. In addition to the high energy electrons of the Maxwellian tail, lunar surface also encounters high energy electrons during SEP events and during its passage in the Earth's magnetotail [Horányi et al., 1998, Hapgood, 2007]. During geotail passage, a surface potential of few thousands volt negative has been measured which is due to the high energy electron fluxes to the surface [Halekas et al., 2005] coupled with absence of solar wind protons in the plasmasheet. High energy electrons are however capable of producing secondary electron emission which could help in reducing the high negative potential of the surface. Observation has shown that secondary electron yield from electron with $E > 100\,\mathrm{eV}$ can exceed unity, and this process is believed to be one important factor in the determination of surface potential particularly in the night side region [Horányi et al., 1998]. Measurements of electron density on the lunar nightside by Lunar Prospector spacecraft suggests a surface potential of at least $-35\,\mathrm{V}$ with a more common potential of $-100\,\mathrm{V}$ when the Moon is in the magnetosphere [Halekas et al., 2002].

The potential on the lunar surface creates a non-neutral layer of plasma called the plasma sheath. The sheath, also known as the Debye sheath is a result of

potential on the lunar surface screening electrons or ions, creating a density gradient which in turn leads to electric field on the surface. On the nightside, the electric field is directed towards the surface which accelerates ions onto the surface. The opposite happens on the dayside, where the field is directed outward and accelerates electrons towards the surface. The plasma sheath layer, assuming a Maxwellian velocity distribution for electrons can be described by [Sickafoose et al., 2002]

$$\Phi(z) = -\Phi_0 \exp\left(\frac{z}{\lambda_D}\right) \tag{6.2}$$

where Φ_0 is the potential bias of the surface, λ_D is the plasma Debye length ($\lambda_D = \sqrt{\frac{\epsilon_0 k_B T}{n_0 e^2}}$) and z is the distance normal from the surface.

6.2.1 Photoelectron Layer

On the dayside, surface is exposed to the solar-UV producing photoelectrons. The photoelectron layer has been studied in several works as a result of the initial exploration of the lunar surface [Singer and Walker, 1963, Grard and Tunaley, 1971, Tunaley and Jones, 1973, Walbridge, 1973]. Similar to solar wind proton, the photoelectron flux leaving the surface is maximum at subsolar point and gradually decreases towards the terminator. These photoelectrons form what is known as photoelectron sheath, a layer of non-neutral plasma dominated by electrons which are produced by the photoemission process which extends to about ~ 1m in altitude [Freeman and Ibrahim, 1975]. In this layer, low energy photoelectrons experience a pulling force directing them towards the positively charged surface while ions are pushed further out by the electric field potential. As a result, the surface can only get charge to low positive potential because as the potential increases, more photoelectrons are attracted back to the surface rather than leaving the surface.

The properties of the photoelectron layer depends on the energy distribution of the photoelectrons. The photoelectron energy distribution on the other hand depends on the spectrum solar-UV radiation spectrum and the work function of

the lunar surface. Its density depends on the photoelectron current directed away from the surface and the resulting positively charged surface. The photoelectron current is determined by the solar photon flux with sufficient energy to dislodge electrons from the surface $F(\lambda < \lambda_{crit})$, and the quantum efficiency of the emitting surface $\chi(\lambda)$, given by [Singer and Walker, 1963, Grard and Tunaley, 1971]

$$I_{ph0} = \int_0^{\lambda_{crit}} F(\lambda)\, \chi(\lambda)\, \mathrm{d}\lambda. \tag{6.3}$$

The work function of the lunar surface for the longest-wavelength photon capable of producing photoelectrons at $\lambda_{crit} \sim 250$nm is given by Sternovsky et al. [2002] to be 5 eV. Direct measurement of photoemission efficiency ($\chi(\lambda)$) of the lunar regolith from Apollo 14 and Apollo 15 samples showed resulting photocurrent of $I_{ph} = 2.8 \times 10^{13}$ electrons $\mathrm{m}^{-2}\,\mathrm{s}^{-1}$ [Willis et al., 1973] which is roughly one tenth of photocurrent produced by a metal in solar flux [Manka, 1973]. The lunar surface is therefore a less efficient photoemitter when compared to metal and this could play an important role during any lunar landing mission. Manka [1973] and Goertz [1989] approximate the value for the photoelectron flux for lunar surface with photoemission efficiency $\chi(\lambda) = 0.1$ which gives $J_{ph} = 4\ \mathrm{A\,m^{-2}s^{-1}}$.

The density of the photoelectrons in the sheath is [Colwell et al., 2005]

$$n_{pe,0} = 2I_{ph0} \sin(i_s)/v_{pe} \tag{6.4}$$

where i_s is the solar elevation angle above the horizon, v_{pe} is the characteristic photoelectron emission velocity and the factor 2 is for the upward and downward photoelectron flux. Willis et al. [1973] measured the distribution of the photoelectrons energy and found it to be a narrow Maxwellian which peaked at $\Phi_{pe} = 2.2$ eV with maximum energy of about 6 eV [Feuerbacher et al., 1972]. The maximum energy value gives $v_{pe} = 8.8 \times 10^5\ \mathrm{m\,s^{-1}}$ and substituting this value in (6.4) gives photoelectron density at the surface of $n_{pe0} \sim 6 \times 10^7\ \mathrm{m^{-3}}$ [Colwell et al., 2007]. At this level, the ratio of photoemission-to-solar wind current at subsolar point

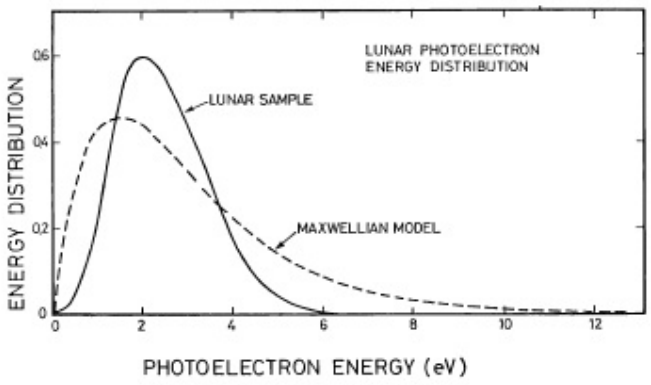

Figure 6.2: Photoelectron energy distribution by solar UV with area under the curves normalized to unity (extracted from Feuerbacher et al. [1972]).

can be calculated to be around $J_p h/J_e \sim 10$.

Assuming a Maxwellian distribution for the low photoelectron energies, the density of the photoelectron in the photoelectron sheath as a function of height can be derived analytically and is given by [Grard and Tunaley, 1971]

$$n_{pe} = n_{pe0}\left(1 + \frac{z}{\sqrt{2}\lambda_{D,pe}}\right)^{-2} \tag{6.5}$$

where z is the height above the lunar surface and $\lambda_{D,pe}$ is the effective Debye length for photoelectron given by

$$\lambda_{D,pe} = \sqrt{\frac{\varepsilon_0 k_B T_{pe}}{n_{pe,0} e^2}} \tag{6.6}$$

where T_{pe} is the photoelectron temperature and ϵ_0 is the permittivity of free space. The solution for $\lambda_{D,pe}$ for $n_{pe,0} \sim 6 \times 10^7\ \mathrm{m}^{-3}$ and maximum photoelectron energy $k_B T_{pe}/e = 6\ \mathrm{eV}$ yields $\lambda_{D,pe} \approx 2.35\ \mathrm{m}$ at the surface.

Feuerbacher et al. [1972] measured the photoelectron yield on lunar sample and showed that the photoelectron energy lacks the high energy tail of the Maxwellian distribution. Figure 6.2 shows the comparison between the photoelectron yield of lunar sample and the approximate Maxwellian distribution. A distinctive feature of the yield graph is the majority of the photoelectrons are emitted between 1 eV and 4 eV with mean kinetic energy of 2.2 eV. In addition, there is almost no photoelectron with energy exceeding 6 eV. These low energy photoelectrons are

more readily available for being recollected by the surface as they lack the energy to overcome the potential barrier created by the positively charged surface. Poppe and Horányi [2010] estimate the photoelectron yield curve to be a $f(v) \propto v^4 \exp^{-v^4/v_{th}^4}$ which enable several features of the distribution function to be replicated such as the strong peak at around the mean energy and the absence of the high energy tail.

6.3 Simulations and Results

6.3.1 Charging of the lunar surface using SPIS

SPIS-dust software is employed to model the lunar charging process using typical lunar plasma environment given by Colwell et al. [2005], where $n_e \sim n_i = 10^7\ \mathrm{m}^{-3}$ and $T_e \sim T_i = 10\ \mathrm{eV}$ with Maxwellian velocity distribution and ion drift velocity of $v_{sw} \sim 400\ \mathrm{km\,s}^{-1}$. Simulation is first performed for a flat lunar surface over an area $4\lambda_D \times 4\lambda_D$ where $\lambda_D = 7.5\ \mathrm{m}$ is the solar wind plasma Debye length. The simulation model is constructed where the bottom plane boundary ($z = 0$) is defined as the lunar surface, as illustrated in Figure 6.3. In the figure, arrows represent the direction of which superparticles are injected into the volume with the big arrow indicates the flow of subsonic ions in the case of $i_s = 0^o$. This injection process is in accordance to the expected flow of plasma particles near the lunar surface.

Parameters used for the lunar surface are lunar's dielectric constant $\varepsilon_l = 3$ and bulk conductivity $10^{-14}\ \Omega^{-1}\mathrm{m}^{-1}$ [Hutton, 1969]. Simulations are performed for different regions of the lunar surface by aligning both the solar wind angle and sun flux angle as shown in Figure 6.4. In the figure, the different area in longitude can be simulated by changing the incidence solar wind angle which can be seen to increase as one moves further away from the sub solar point.

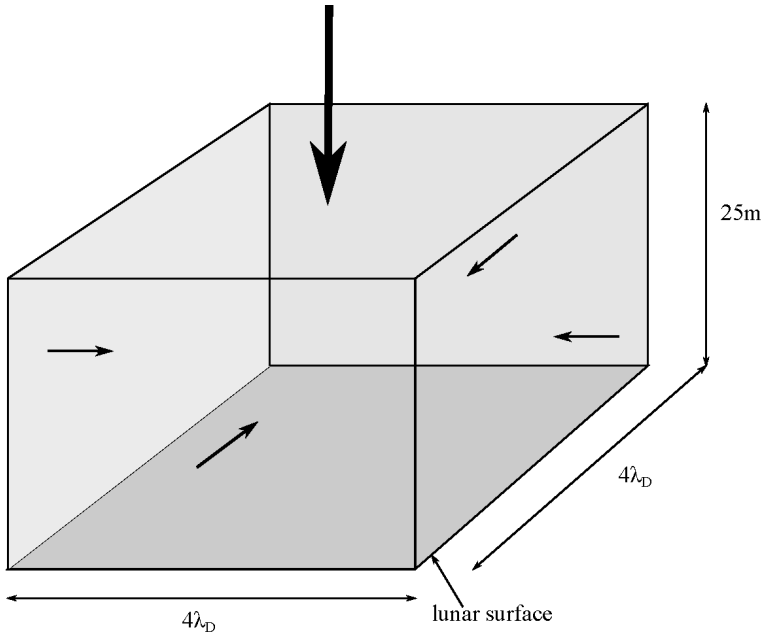

Figure 6.3: The model used for the simulation. Arrows indicate direction of superparticles injection. The big arrow refers to the case where solar wind and solar UV flux incidence angles are at subsolar point (0^o).

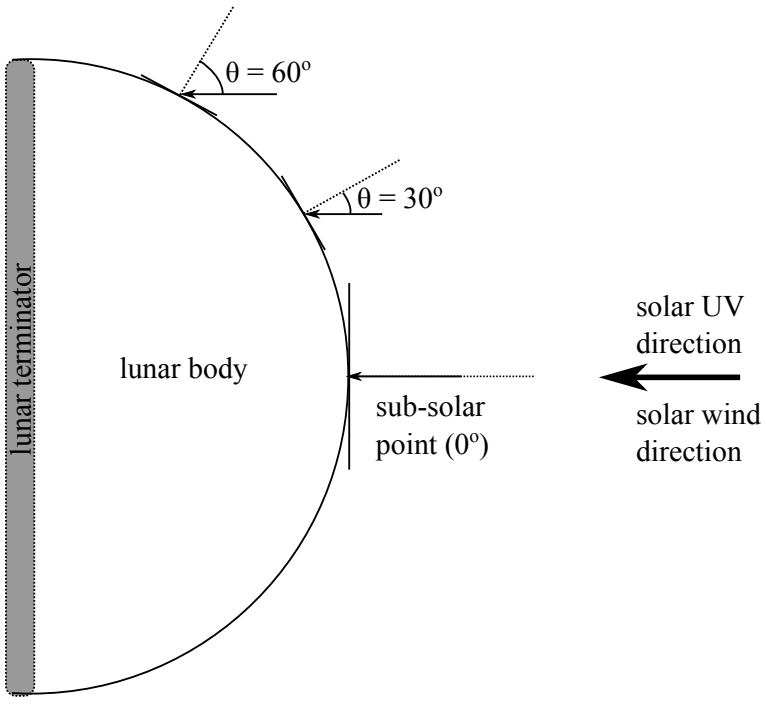

Figure 6.4: Solar wind and solar UV incidence angles with the surface (θ). Incidence angle increases towards the terminator reducing the solar wind flux and photon flux to the surface.

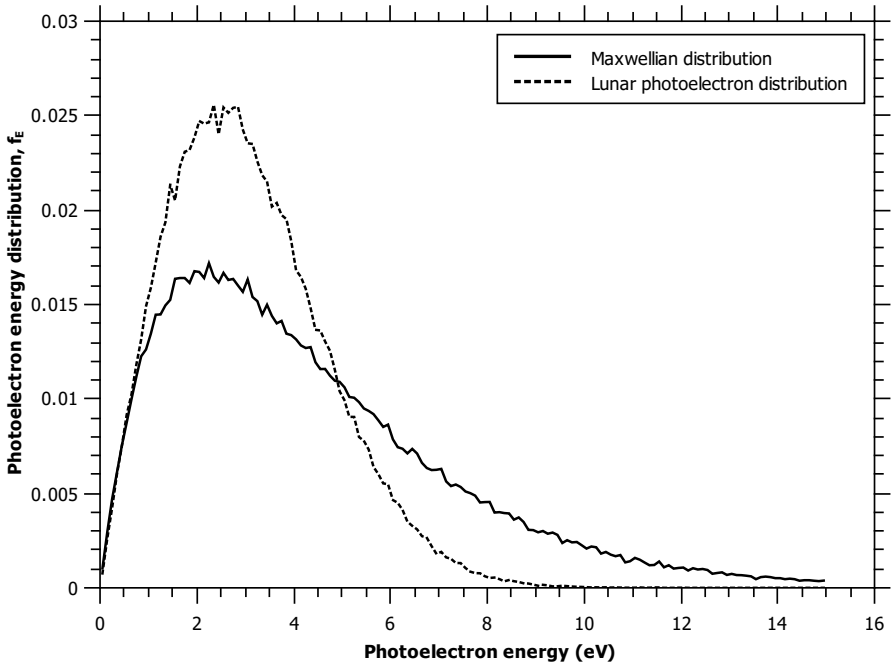

Figure 6.5: Actual photoelectron yield obtained from the simulation with the distribution function is plotted using $\sim 150,000$ samples. Solid line is the distribution using Maxwellian approximation (Lambertian distribution) while dash line is the lunar distribution based on Feuerbacher et al. [1972].

Photoelectron energy distribution

The sun flux is taken at 1 AU from the sun, where at this distance, photoelectron flux of $4.5\,\mu\mathrm{A\,m^{-2}}$ results in photoelectron current of 4.05×10^{-3} A in SPIS, which is the same value as calculated by Willis et al. [1973]. In the simulation, the energy distribution for photoelectron yield is modelled based on Poppe and Horányi [2010] estimation of $f(v) \propto \exp^{-v^4/v_{th}^4}$. The photoelectrons are assumed to have only the normal velocity component, and the samples (photoelectron superparticles) energy distribution is shown in Figure 6.5. In the graph, photoelectron yield for the case of Maxwellian (solid line) and the approximation based on Feuerbacher et al. [1972] and Poppe and Horányi [2010] are compared. Both lines show mean energy of around 2.2 eV, which is similar to the one measured by Feuerbacher et al. [1972]. The lunar photoelectron distribution however have a much shorter high energy tail when compared to the Maxwellian distribution. The simulation however produces photoelectrons with slightly longer high energy tail compared to Feuerbacher et al. [1972], where maximum photoelectron energy of 8 eV is recorded

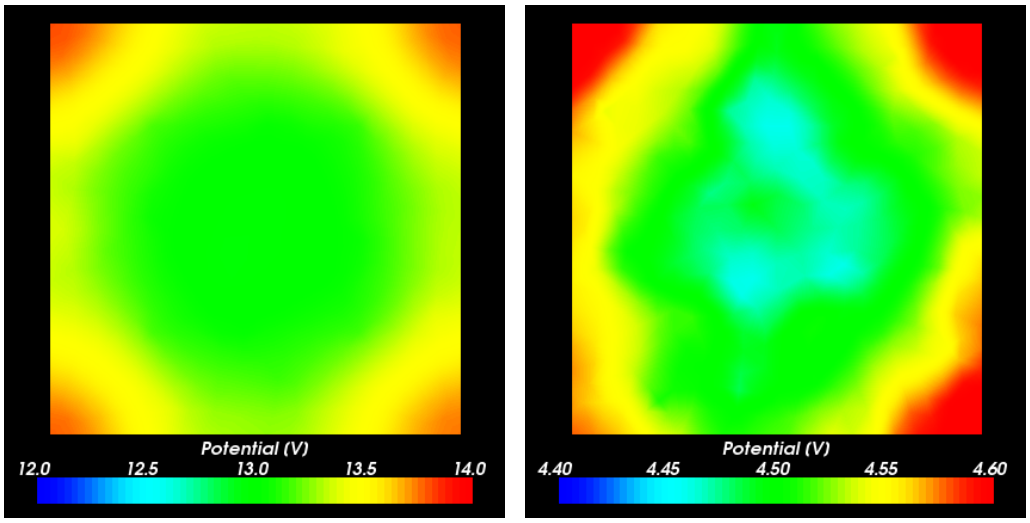

(a) Maxwellian distribution. (b) Lunar distribution.

Figure 6.6: Comparison of surface potential between Maxwellian and lunar photoelectron distribution. Surface with Maxwellian photoelectrons is charged to a higher potential because there are more electrons with energy to escape the potential barrier of the surface. Also notice the variation in surface potential. This is due to the very low conductivity of the surface which means charge are not equally distributed. In addition, the limit on the size of the simulation volume means some of the charging process, especially near the boundaries are not properly represented.

from the samples. The lack of high energy tail means there are less photoelectrons with enough energy to overcome the surface's potential attraction. As a result, most of these photoelectrons are recollected by the surface which will reduce the overall surface potential.

Lunar surface potential

Figure 6.6 shows the surface potentials for both Maxwellian and lunar photoelectron distribution. In the simulation, solar wind flow is incidence at 0^o with photoelectron flux for both cases are set to 4.05×10^{-3} A. In Figure 6.6a, surface is charged to $\sim$ 13 V which is approximately 3 times more than the potential of $\sim$ 4.5 V (Figure 6.6b) obtained using the narrowed Maxwellian distribution (after this will be known as lunar distribution). The large difference in surface potential can be attributed to the photoelectron energy distribution used in each case. The lack of high energy tail in the lunar photoelectron energy distribution means there are more photoelectrons to be recollected, as shown in Figure 6.7a. This contributes

to a lower positive potential on the surface. Figure 6.7b shows the currents for each charging process on the surface. The graph clearly shows that photoemission and photo-recollection are the two dominant currents in the lunar surface charging process at equilibrium. The dip in collected current for photoelectron and electron are due to the particles loading process at the beginning of the simulation. In both cases, currents will level up to their respective equilibrium value after around 0.05 ms.

The surface potentials observed in Figure 6.6 also show similarity in term of potential observed in areas close to the boundary. In both cases, higher potential are observed around the simulation boundaries and corners before settling down in the middle of the simulation area. The reason for this observation is mainly because of the limitation imposed by the finite simulation volume. A finite simulation volume results in some important plasma process such as particle injection can not be properly replicated especially on the boundaries close to the lunar surface. This can be explained by looking at the density of each of the plasma components. Figure 6.8 shows the density of electrons, ions, photoelectrons and plasma potential on the x-z plane at y = 0 from the simulation. In 6.8a, high electron density is observed at area close to the boundaries with the density levelling up at the centre of the simulation. During the simulation, superparticles are injected from the plasma boundary based on each species temperature and flux. As stated, electrons and ions are assumed to have Maxwellian velocity distribution, which is true if the observation is made far away from the sheath. During the injection process, ions are introduced with finite streaming speed whereas electrons motion are largely due to their thermal motion. The plasma sheath changes the species distribution; electrons are accelerated towards the surface because of the attractive potential whilst ions, due to their motion are largely dominated by their drift rather than their thermal motion, are less affected by the sheath (see Figure 6.8b). In addition, the simulation is performed for the case of sub solar point ($\theta = 0^o$) where solar wind protons approach the surface from the top boundary ($z = 25\,\mathrm{m}$) whilst electrons can

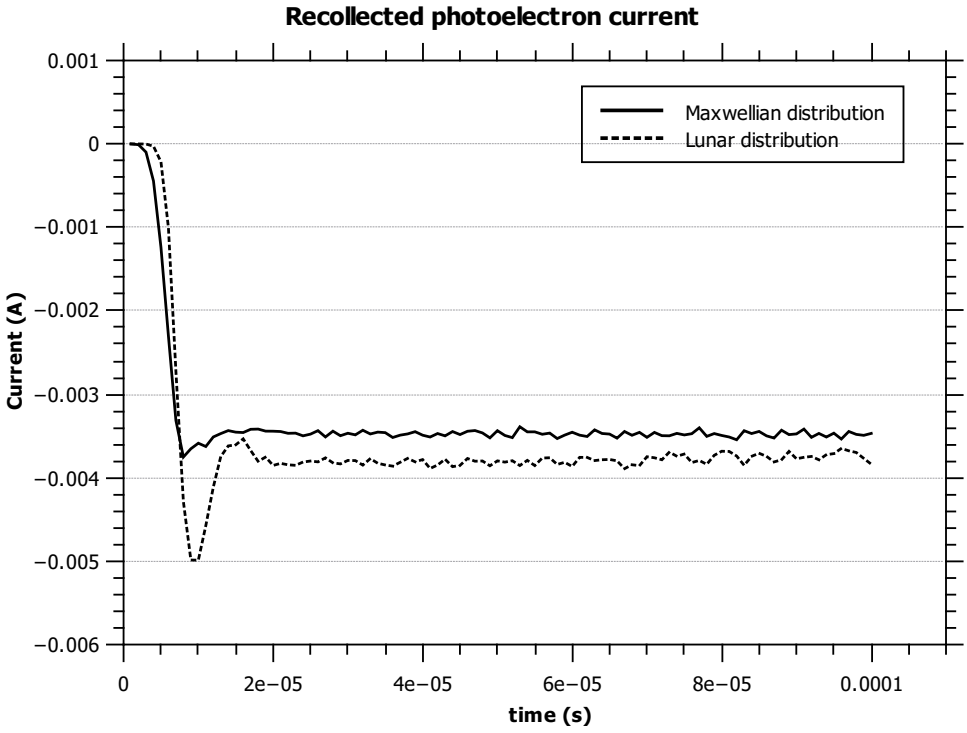

(a) Recollected photoelectron currents

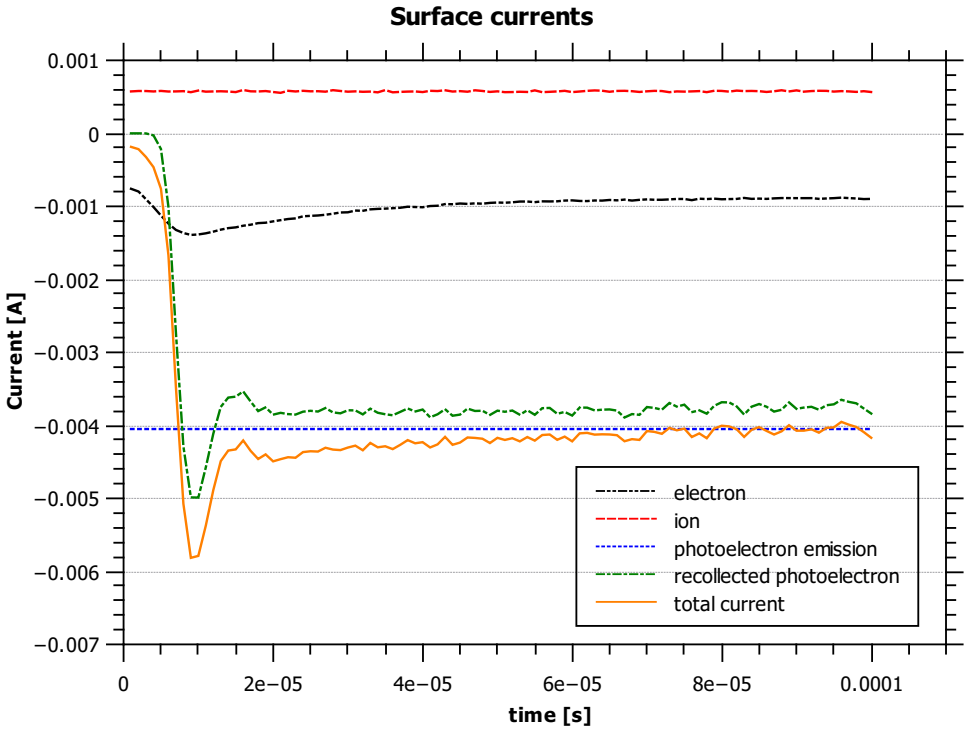

(b) Surface currents

Figure 6.7: (a) Recollected photo electron current using (solid) Maxwellian distribution and (dash) lunar distribution. (b) Surface currents. Surface is uncharged at the beginning of the simulation. Higher recollection for photoelectron with lunar distribution reduces surface potential.

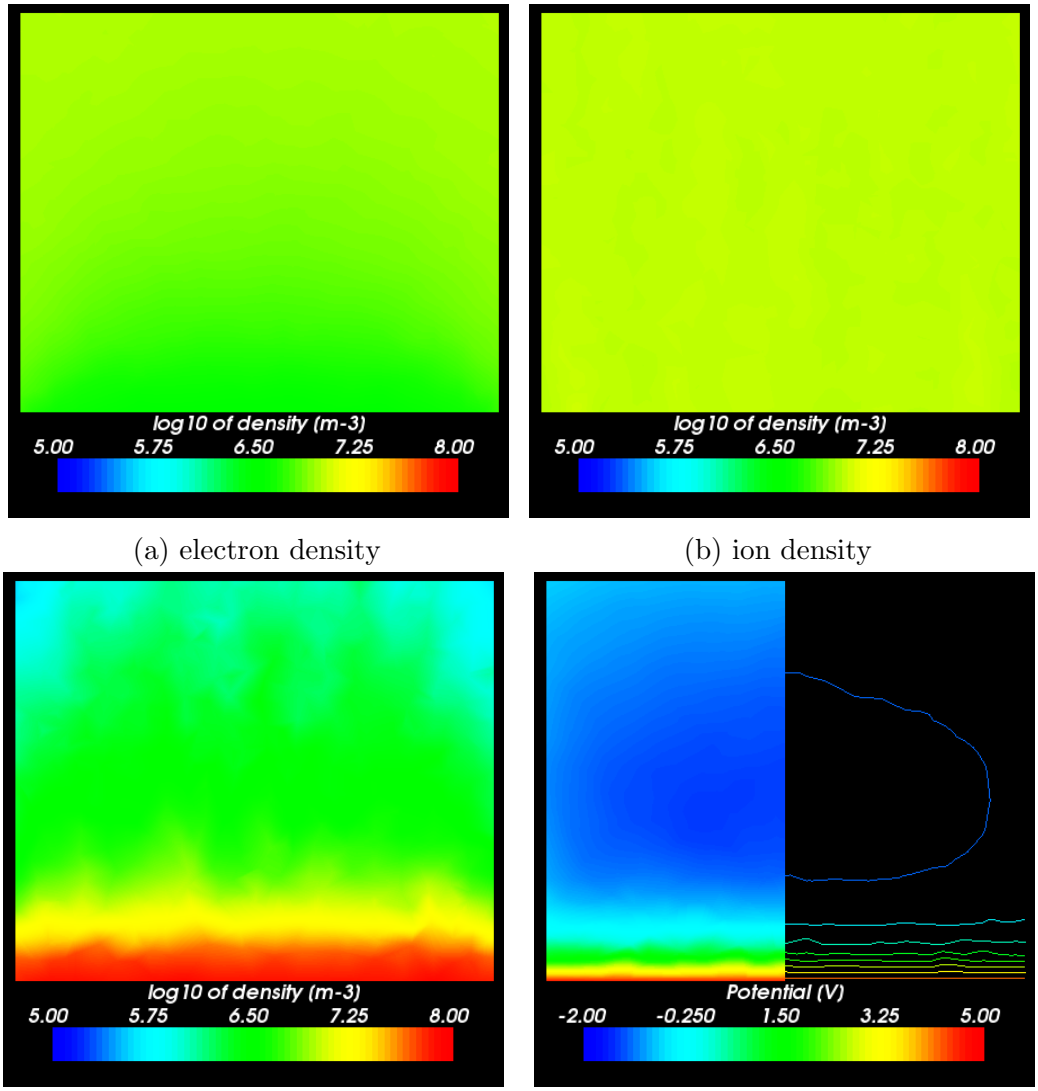

(a) electron density (b) ion density

(c) photoelectron density (d) Plasma potential

Figure 6.8: (a), (b) and (c) x-z plane view of electron, ion and photoelectron density respectively. The finite simulation volume affects electron density the most as its motion is dominated by thermal motion rather than solar wind drift. However, electrons contribute less current to the surface than photoelectrons, which means the surface potential is more likely to be influenced by photoelectrons. The high potential observed at the edge of the surface in Figure 6.6 is due to this particular limitation. (d) Plasma potential which shows the rapidly decreasing plasma sheath above the surface. All results are for a surface in the sub solar point (0°incident angle).

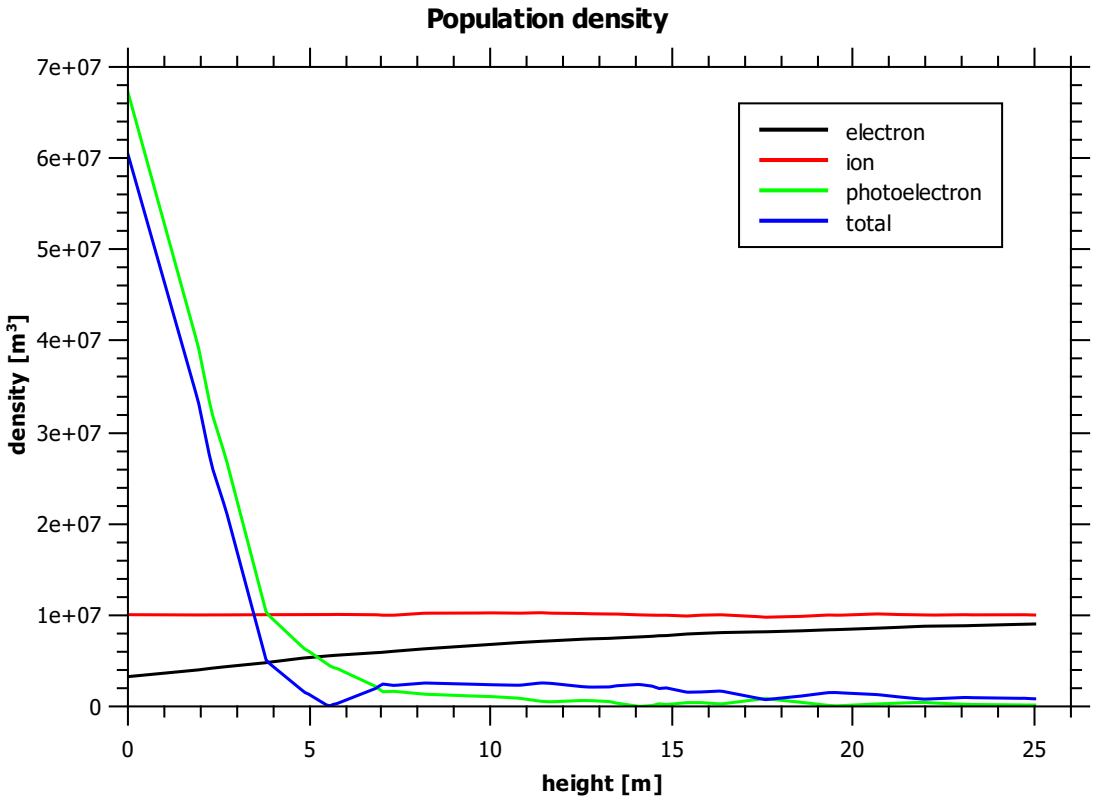

Figure 6.9: Plasma density vs height.

enter the simulation volume at all angles due to their thermal motion. Since the simulation cannot be performed over the whole surface area of the Moon because of limit in computational resources, the needs to limit the size of the simulation causes false approximation of Maxwellian velocity distribution for electrons, particularly ones that are injected from the side boundary.

However, because electrons flux is at least 4 times smaller than the photoemission current (see Figure 6.7b), and because surface conductivity is very low, the electron injection process only contributes to very small difference in surface potential. Figure 6.8c shows photoelectrons emission from the surface into the simulation volume. Form the figure, the density of photoelectron are observed to be lower at the side boundaries than at the centre of the simulation. As we recalled, photoelectrons are emitted with very low energy distribution, and almost 95% of photoelectrons are recollected as shown in Figure 6.7b. Instead of being recollected, photoelectrons which are produced on the surface near the side boundaries are

likely to leave the simulation domain via the side boundaries, thus reducing the recollected photoelectron current at that positions. Since photoelectron current is the dominant current, less recollected photoelectron in these areas causes surface potential at the edge to be slightly higher than the rest of the surface (middle of the simulation).

Nevertheless, since the area constraint is unavoidable, the rest of the simulations presented hereafter, are performed with photoelectrons having lunar distribution energy profile with the acknowledgement on the potential differences at the simulation boundaries. Figure 6.8d shows plasma potential near the surface. The figure clearly shows the formation of plasma sheath close to the surface, which is rapidly decreasing as we move further away from the surface. Another observation is that the potential drops to a negative level right after the sheath which is consistent with the work of Poppe and Horányi [2010] who predict a negative electric field right after the sheath. Figure 6.9 compares the density profiles for every plasma population. Maximum photoelectron density of $6 \times 10^7\,\mathrm{m}^3$ which has been observed at the surface is again in good agreement to the theoretical estimate given by Colwell et al. [2005].

Solar incidence angle

Surface potential decreases from the maximum positive potential observed at the sub solar point to negative potential at the terminator. Figure 6.10 shows the potential at 0°, 30°, 60° and at 90° incidence angles. At 0° and 30°, the surface is charged to around 4.50 V and 4 V due to the photoemission being the dominant current. At 60°, there are less photoelectrons due to less solar photon flux incidence on the surface, and the surface only charges to around ~ 1 V. At 90°, there is no photoemission taking place and surface is charged to negative potential as ambient electrons have become the dominant current. A surface potential of ~ -50 V is predicted in this area from the simulation. Figure 6.11 shows the photoelectron current emission and collection at 0°, 30° and 60°. It is clear from the graph that

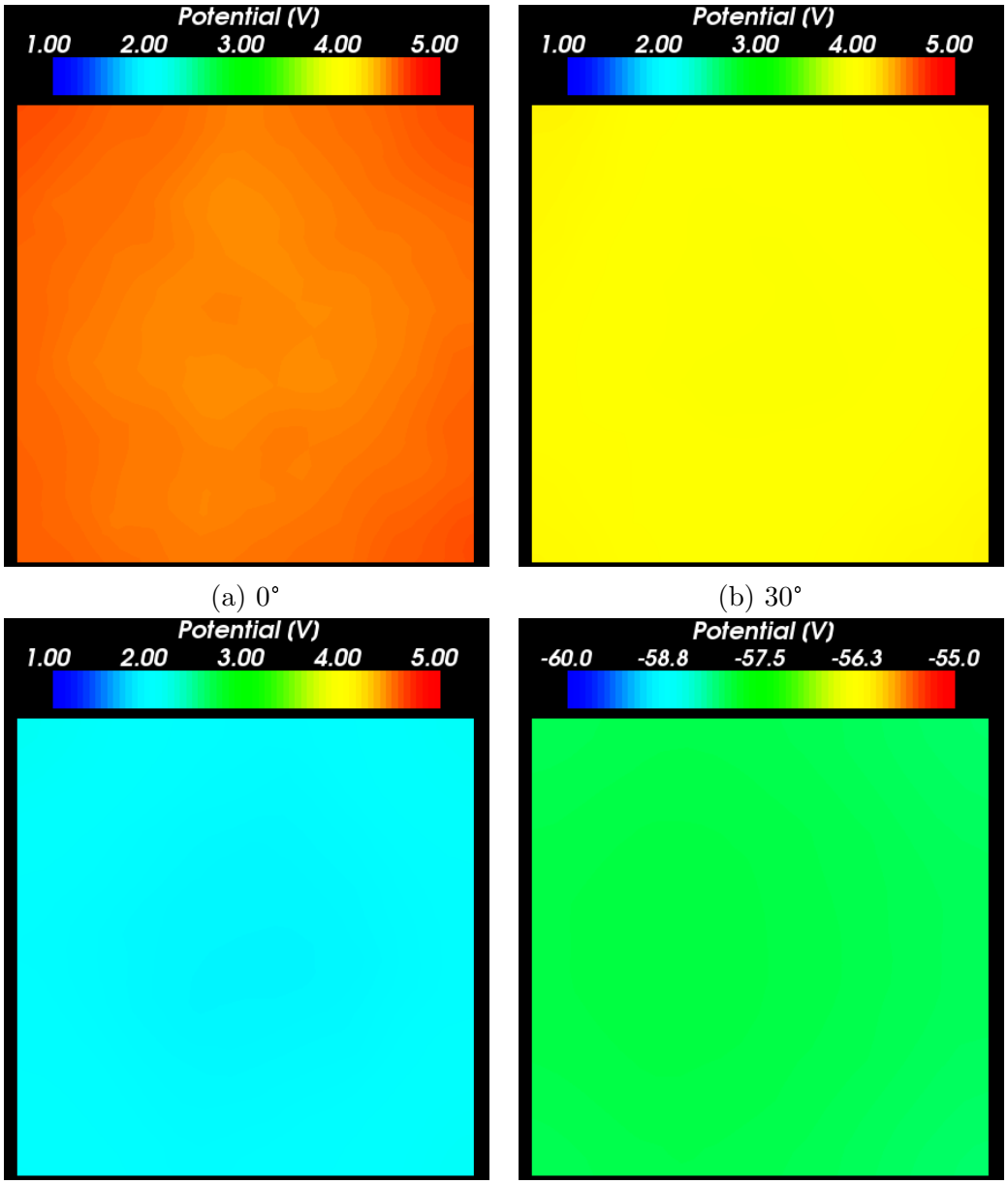

(a) 0° (b) 30°

(c) 60° (d) 90°

Figure 6.10: Surface potential for (a) 0°, (b) 30°, (c) 60°and (d) 90°. Notice the different scale used for 90°. Surface charged to positive potential at sub-solar point and gradually charged to more negative approaching terminator (90°, no photoemission).

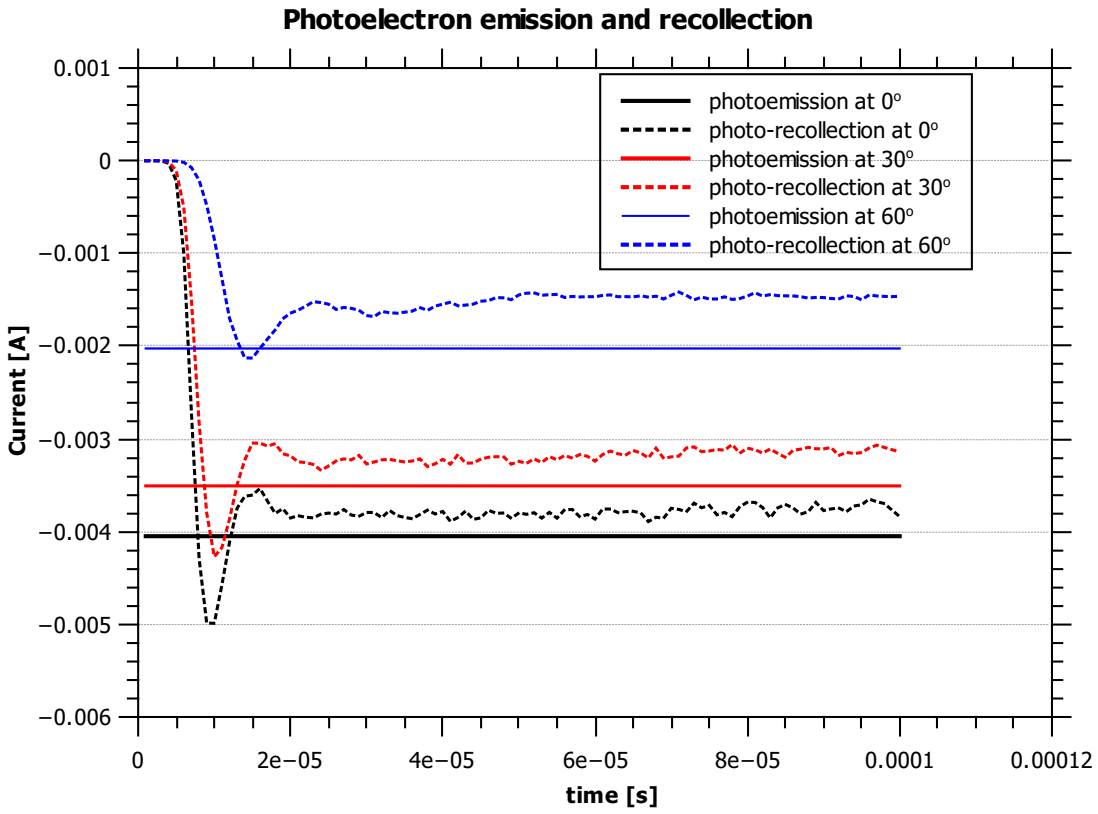

Figure 6.11: Photoeletron emission (solid line) and recollection (dotted line) at 0° (black), 30° (red), and 60° (blue).

photoelectron current is reduced when approaching the terminator region with the values can be calculated using

$$I_{ph} = \text{Area} I_{ph0} \cos i_s \tag{6.7}$$

where I_{ph0} is given by Willis et al. [1973] and i_s is the solar flux incidence angle.

Surface topography

Farrell et al. [2007] showed that surface topography plays an important role in surface charging process and could produce localized potential difference. Structures such as crater and boulder could disturb the natural solar wind flow and solar UV flux creating shadowed region. This shadowed region is charged to different potential than the illuminated region where the effects is more prevalent near the terminator region due to the low sun angle.

Figure 6.12 shows the potential of a 1-m deep, 5 meter in diameter crater at various sun incidence angles. In 6.12a and 6.12b, the crater is illuminated at low solar incidence angles, i.e. at 0^o and 30^o respectively. In both cases, the area outside the crater are charged to positive potential where small potential differences can be observed between the various crater's surfaces. The highest positive potential is found at the rim of the crater which is largely due to the potential barrier rather than the illumination level. At 30^o however, the effect of varying level of illumination is visible as opposite sides of the crater are charged to opposite polarity. The side facing the solar wind is charged to $\sim 9\,\mathrm{V}$ while the one in shadowed is charged to $\sim -3\,\mathrm{V}$.

Figure 6.12c and 6.12d show the surface potential when the crater is illuminated at 60^o and 90^o. In Figure 6.12c , the potential of the area outside the crater is approaching $\sim 0\,\mathrm{V}$ whilst in Figure 6.12d the value is close to $-70\,\mathrm{V}$. The first observation is due to the dominant photoelectron yield is reduced to a level close to the ambient electron current while in the latter case, electron current are the main source of charging current as photoelectron yield is almost zero. In Figure 6.12d, the crater's rim facing the solar wind is charged to positive potential due to increasing attraction by the surface towards thermal ion travelling parallel to the surface. The shadowed side on the other hand is charged to almost $\sim -100\,\mathrm{V}$ as there is now less ions able to reached the surface.

Figure 6.13 shows the densities and potential across a crater located at 90^o from the sub solar point. In Figure 6.13a, the electron density near the crater is reduced to almost 3 order of magnitude smaller due to the strong electric field created by the negatively charged surface. Further electron depletion can be observed at the shadowed region inside the crater where density dropped to $10^2\,\mathrm{m}^{-3}$ which is due to the strong potential barrier. In comparison, ion density in the area outside the crater is almost constant over the surface with its density approximately the same as its ambient density ($n_i \sim 10^7\,\mathrm{m}^{-3}$). However, near the shadowed region inside the crater, the density is reduced to almost zero as most of the subsonic

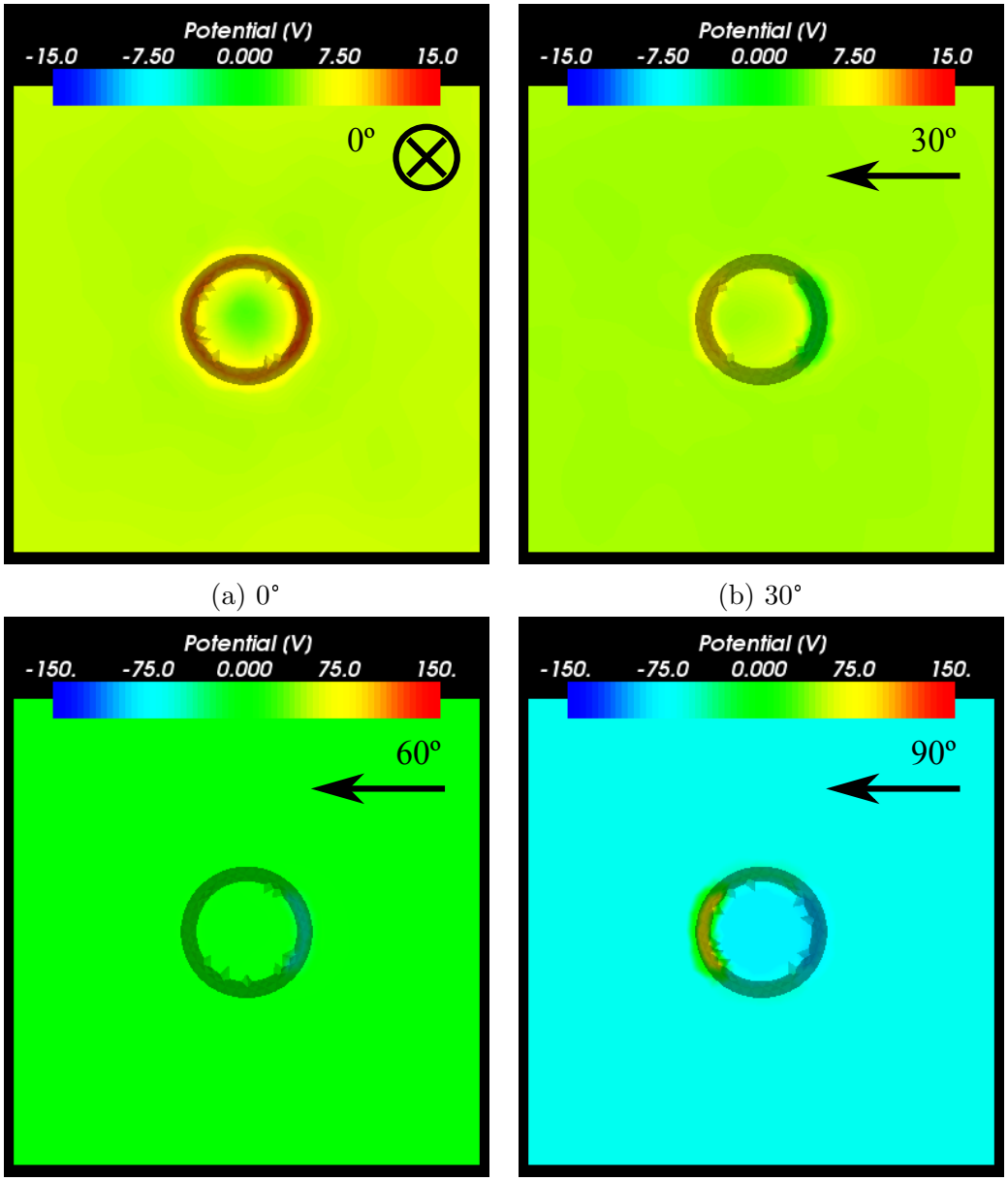

(a) 0° (b) 30°

(c) 60° (d) 90°

Figure 6.12: Surface potential around a 1 m depth, 5 m diameter crater for (a) 0^o, (b) 30^o, (c) 60^o and (d) 90^o solar incidence angles. Figures are represented in different sets of scales, one set for the top two figure and another two for the bottom figures. In (a), the whole surface of the crater is exposed to the solar wind and solar flux. Potential difference is observed between the crater rim and the rest of the surface. In (b), opposite edges of the crater are charged to opposite polarity. The edge in blue is the ones in shadow which is charged to negative potential because solar wind photons are being obstructed by the crater's rim. Surface facing the solar wind is charged to positive potential. In (c), the low solar angle has reduces the flux to the shadowed side even further with the surface is charged to $\sim -70\,\mathrm{V}$. In (d), surface facing the solar wind is charged to positive potential while the one in shadow is charged to negative potential. A potential close to -100 V can be seen on the shadowed side.

ions are completely obscured from the region. This causes the surface to charge to high negative potential as there is no ions to help lowering the magnitude of the surface potential. On the other hand, surface facing the shadowed region is charged to positive potential as ions are being collected by the surface. The surface and plasma potential are shown in Figure 6.13c.

Solar wind density and temperature are two parameters that could result in different potential level than the one observed in the preceding simulations. These two parameters vary over time and are highly dependent on solar activities. A simulation is performed for the case of crater near terminator ($\theta = 90^o$) in a more energetic solar wind plasma. The average temperature of the solar wind is doubled from 10 eV to 20 eV and the remaining parameters of the simulation are retained.

Figure 6.14 shows the surface and plasma potential for the crater after approximately 50 milliseconds. In 6.14a, the area outside the crater is charged to $\sim -90\,\mathrm{V}$ while the base of the crater is charged to approximately $-100\,\mathrm{V}$. Having more energetic populations results in higher negative surface potential and is largely due to the increase in electron thermal energy. As for ions, since their motion are largely dominated by the subsonic flow, they would contribute approximately the same charging current to the surface under these conditions.

The surface in shadow registers a potential of $\sim -200\,\mathrm{V}$ compared to approximately the same potential level on the sun-facing side as observed in the previous case. It is believed that the shadowed surface can charge to much higher potential since the surface has not reached its equilibrium potential after the simulation has ended as shown in Figure 6.15. This observation is consistent with theoretical work of Borisov and Mall [2006] who predicts potential in excess of $-200\,\mathrm{V}$.

In Figure 6.15, the area outside the crater reaches its equilibrium potential after approximately 10 ms whilst the one in shadow has yet to reach its equilibrium potential after 50 ms. The slow charging process of the shadowed surface is due to the lack of thermal ions reaching the surface. It is predicted that the surface will continue to charge to higher negative potential in order to attract more ion

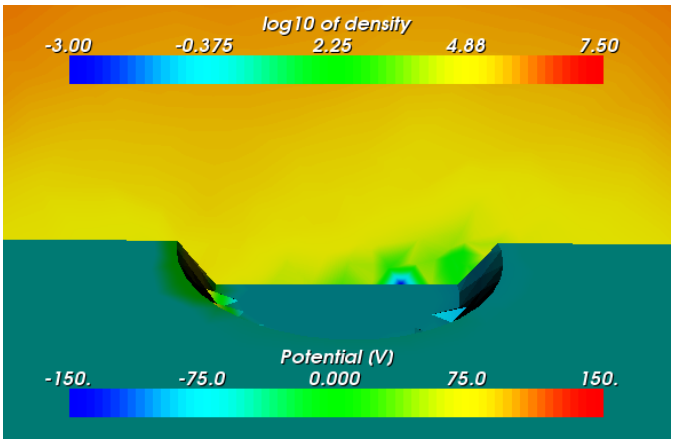

(a) electron density

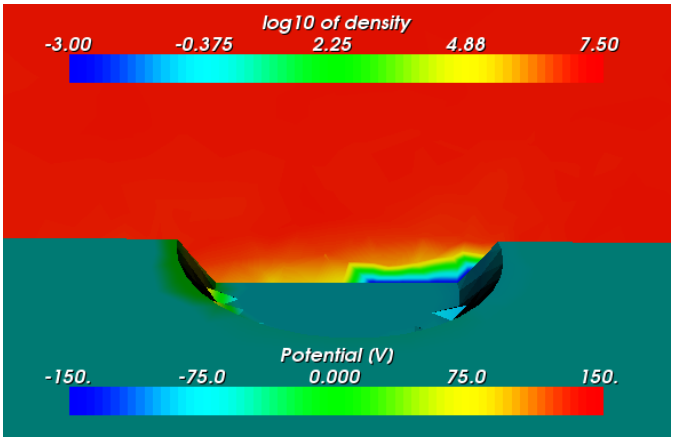

(b) ion density

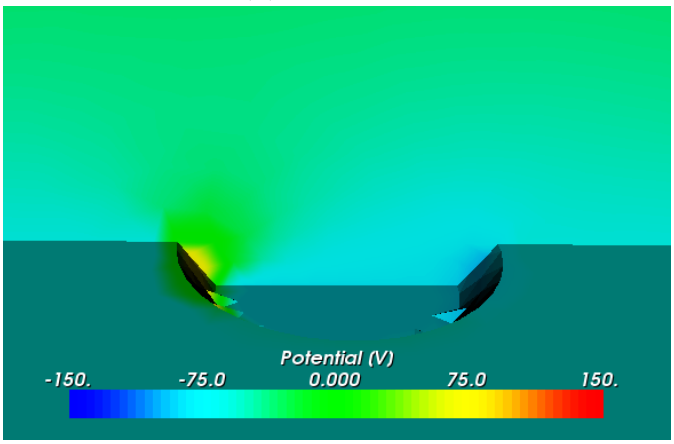

(c) plasma and surface potential

Figure 6.13: Densities and potential around a crater located 90^o from the sub solar point. In (a) and (b) the potential scale for the surface is given by the bottom scale, while the top scale shows the logarithmic of density. The negatively charged surface cause reduction in density for electrons in (a) compared to almost constant density for ions in (b). The shadowed part shows depletion for both electron and ion species but the worst is for ions where there is almost zero density observed. (c) shows the potential contour of the plasma which indicates the formation of potential barrier in the $x - z$ plane at $y = 0$.

particles to the surface. It is also believed that an increase in solar wind speed would only result in a more negative patch since ions will have larger horizontal velocity component, and thus are more likely to be shielded by the crater's edge.

In addition to the high negative potential found on the shadowed crater's rim, a small patch of highly negative surface can be seen appearing near the top of the positively charged crater's rim. The formation of this patch is believed to be the result of screening of ions by the positively charged sun-facing crater's rim. The positive barrier shown in Figure 6.14b causes incoming ions to be deflected over the area which is indicated by the slightly high ion density near the patch (see Figure 6.14c). This patch also repels incoming electrons creating small region of reduced electron density as illustrated in Figure 6.14d.

The solar wind near lunar surface is more likely to contain both the fast and slow solar wind components. A simulation is performed for the case of crater for this type of plasma condition where the slow solar wind component is made of plasma with $n_s = 10^6\,\mathrm{m}^{-3}$ and $T = 10\,\mathrm{eV}$ whilst the fast solar wind is set to $n_s = 5^6\,\mathrm{m}^{-3}$ and $T = 20\,\mathrm{eV}$. The streaming speed for both slow and fast solar wind are set to $400\,\mathrm{kms}^{-1}$ and $700\,\mathrm{kms}^{-1}$ respectively. Figure 6.16 shows the surface potential obtained from the simulation. From the figure, it is obvious that a similar pattern of surface potential can be observed near the lunar crater where the side in shadow is charged to negative potential whilst the one facing the solar wind is charged to positive potential. The simulation indicates an increase in the magnitude of the surface potential on both sides of the crater (shadowed and sunlit) but within the range anticipated by Colwell et al. [2007]. The simulation shows that there is around $\sim 200\,\mathrm{V}$ difference between the side in shadow and the one facing the solar wind which could create strong electric field. The changes in surface potential also confirm the time varying nature of lunar surface potential with regards to the change in solar wind plasma properties.

In addition to craters, the lunar surface also has other topological features such as one created by boulder. Figure 6.17 shows the potential and photoelectron

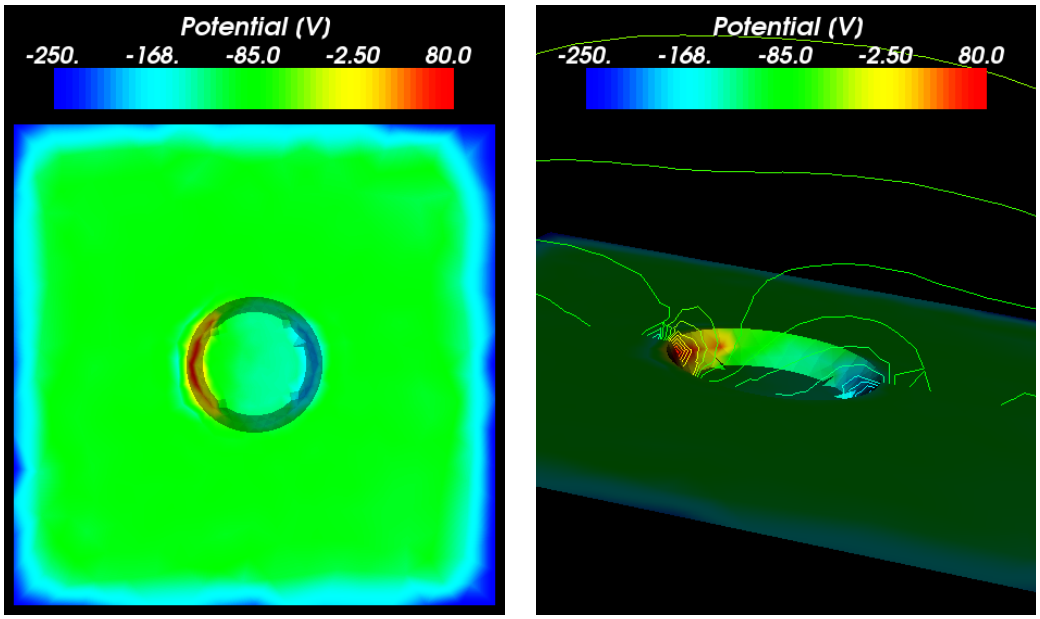

(a) Surface potential

(b) plasma potential

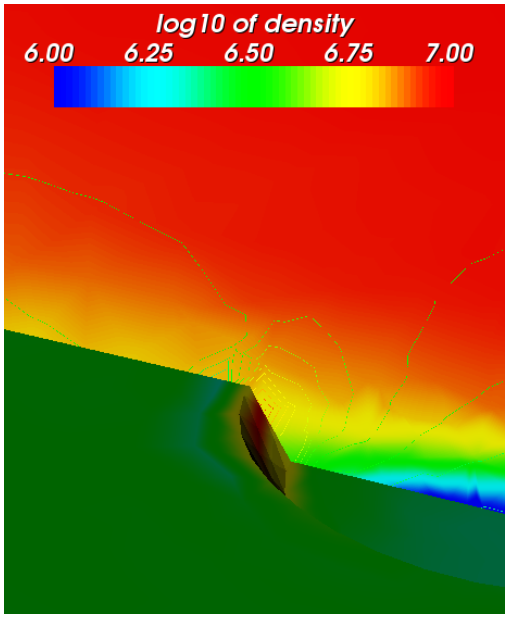

(c) ion density

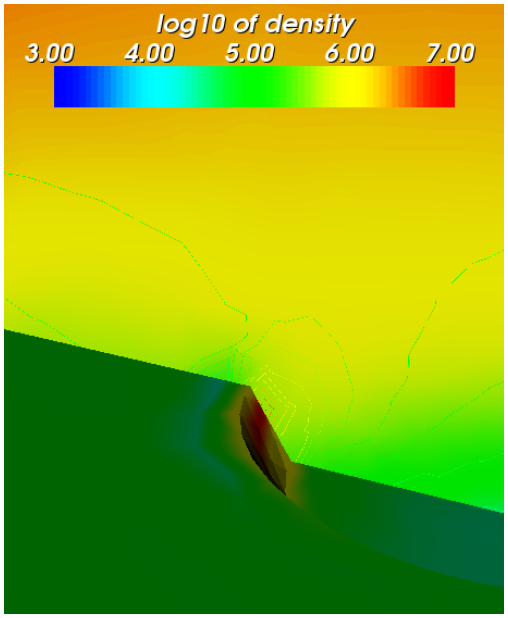

(d) electron density.

Figure 6.14: Surface, plasma potential and solar wind particle densities near a crater for a more energetic solar wind plasma. In (a), surface is charged to higher negative potential due to increase in particle energy. The carter's rim is charged to positive (sun facing) and negative (shadowed) potential with the negative side is almost 3 times higher in magnitude than the positive side. This creates 2 potential barriers (b) which affect both ions and electrons. In (c), the positive barrier deflects ions creating a negative patch on the top of the crater while in (d) this patch creates low density region for electrons.

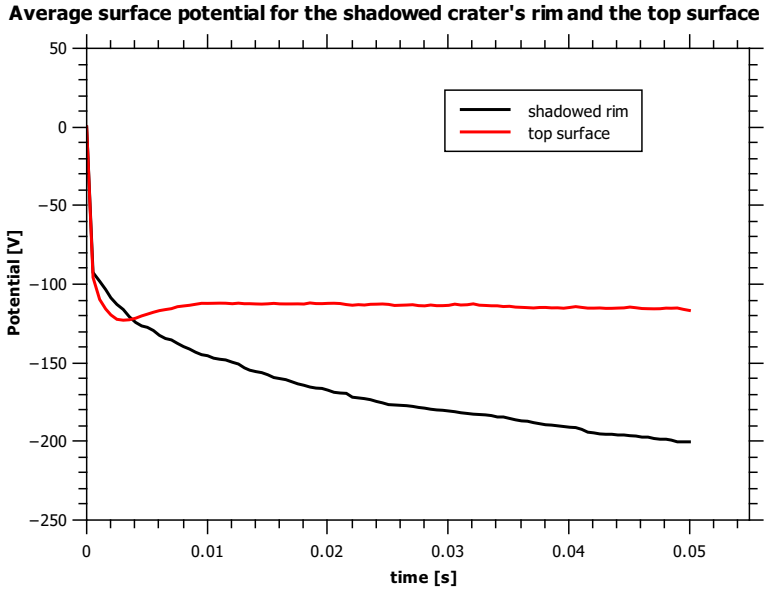

Figure 6.15: Average surface potential for the crater's rim in shadowed and the top surface. The final potential for the shadowed side has yet to achieve equilibrium level and the surface could charge to much higher potential.

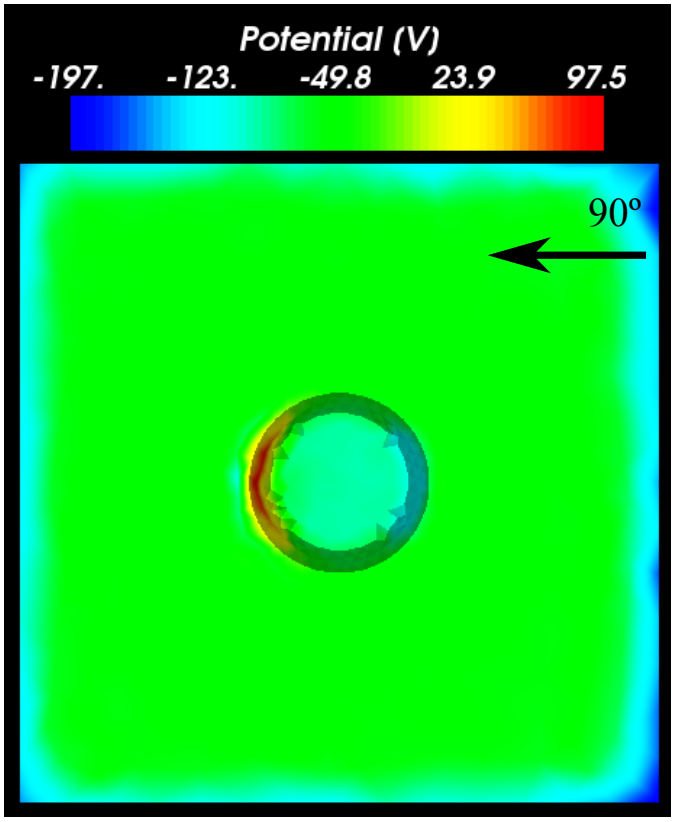

Figure 6.16: Surface potential near a crater for a Bi Maxwellian solar wind distribution. Simulation result shows that surface is charged in a similar fashion to single Maxwellian solar wind distribution except for the difference in the magnitude of the potential.

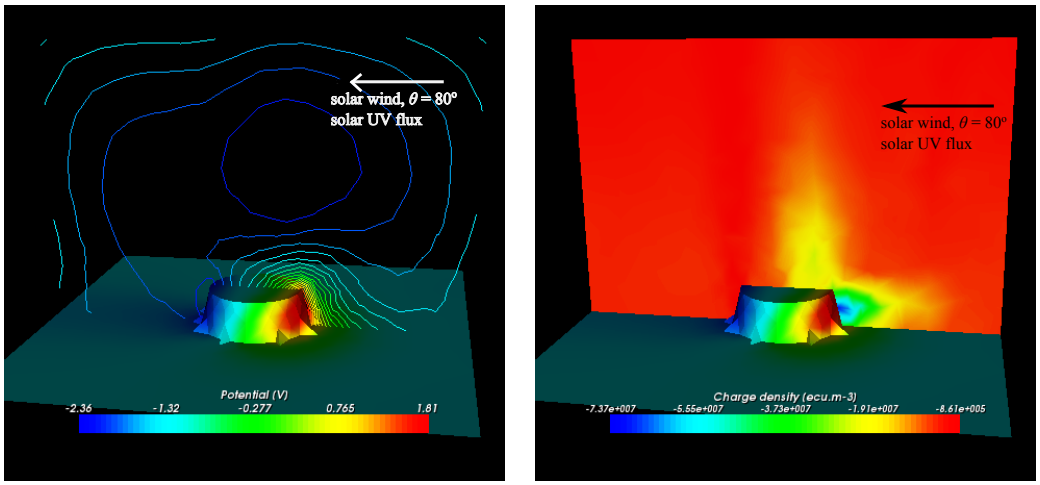

(a) Surface and plasma potential. (b) Photoelectron charge density.

Figure 6.17: Potential and photoelectron density cross section on a boulder. Solar wind and solar flux is set at $\theta = 80^o$. In 6.17a, positively charged surface is observed on the surface facing the incoming solar wind and UV flux, while in 6.17b shows the output photoelectron from the surface. Because the boulder's surface receives more UV flux than the flat lunar surface, more photoelectrons are emitted from the surface.

charge density for a boulder near the terminator region. The boulder has a base diameter of 5 m and height of 2 m, facing an incoming solar wind at $\theta = 80^o$ as shown in the figure. Figure 6.17a shows that the side facing the incoming solar wind and flux is charged to around ~ 2 V compared to the side in shadow which is charged to ~ -2.4 V. Since the incidence angle for both solar wind and UV flux are at $\theta = 80^o$, the whole lunar surface emits photoelectrons. However, at this angle, the photoelectron current is smaller than electron current, which results in the surface to be negatively charged.

6.3.2 Lunar Dust Dynamics

The loose dust particles on the lunar surface acquire charges from their interactions with ambient plasma and other processes such as from triboelectric charging, photoemission and secondary emission. The dust charging process causes the particles to develop repelling electrostatic force with the surface which enable them to levitate [Criswell, 1972]. Figure 6.18 shows sketch made by one of the astronauts during the Apollo mission illustrating the *horizon glow*, which was later attributed

to light scattering by charged dust particles [Criswell, 1972, McCoy and Criswell, 1974].

SPIS-Dust has been employed to study the dynamics of these charged dust particles over two regions which are the terminator region and at dayside ($\theta_{SZA} = 0^o$). The terminator has been shown to be the region where dust particles have been observed to levitate over to the lunar exosphere [McCoy and Criswell, 1974]. The subsolar point on the other hand represents the other end of the potential spectrum where surface is charge to positive potential.

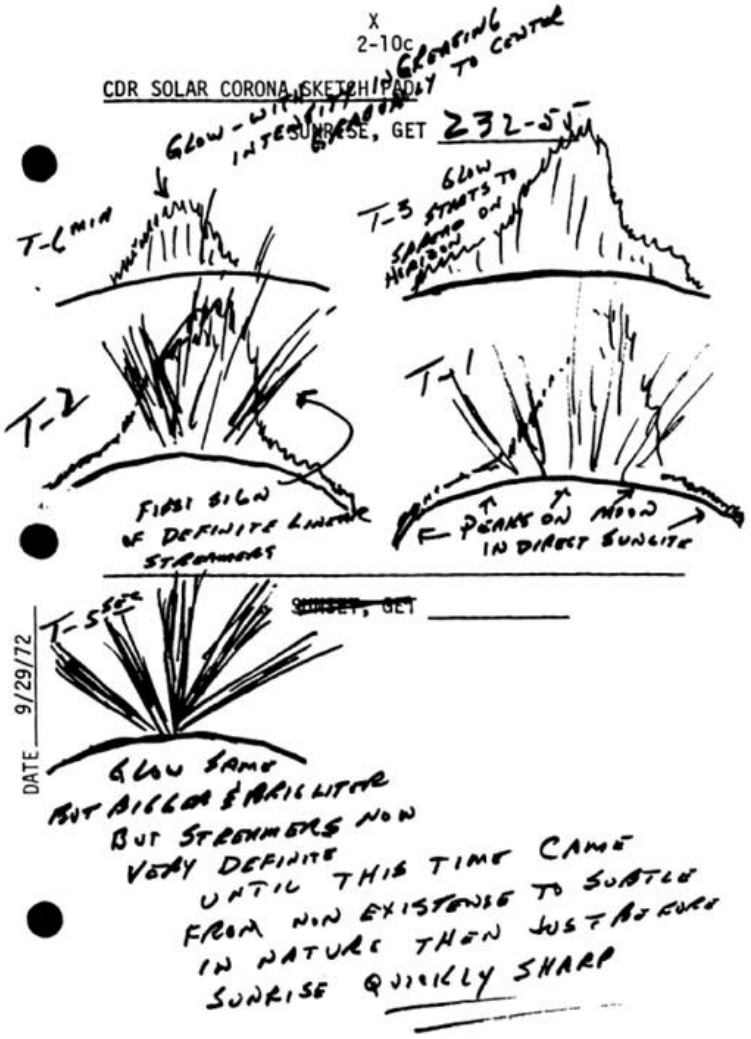

Figure 6.18: Lunar dust streamer as observed by the astronauts during the Apollo mission [McCoy and Criswell, 1974].

Dust particles can be levitated from the surface upon impact or by electrostatic force. In the latter case, dust particles acquire enough charge to overcome the

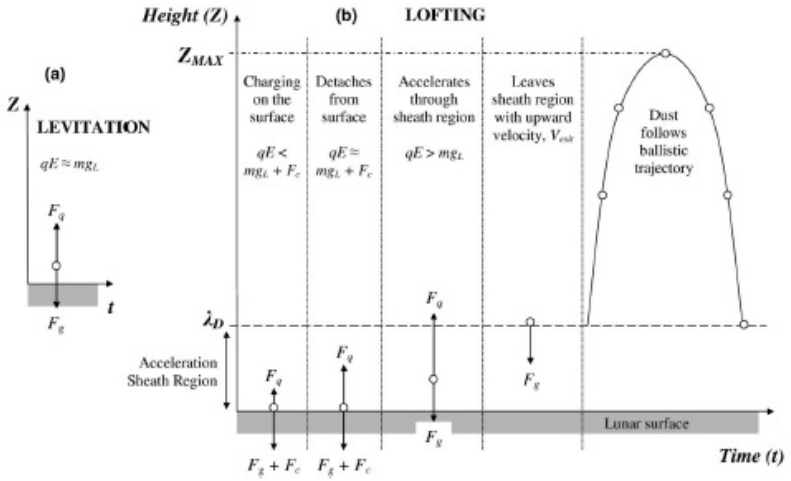

Figure 6.19: Dust levitation and acceleration model (from Stubbs et al. [2006]).

gravitational force of the Moon and has been predicted to travel up to 100km in altitude [Stubbs et al., 2006]. Two models has been proposed to explain the dust particle dynamics above the lunar surface which are the levitation model [Criswell, 1972] and the acceleration model [Stubbs et al., 2006]. The levitation model is adequate to explain the presence of micron size dust particles at sub-meter height but can not explain the discovery of submicron size particles high in the lunar exosphere. Stubbs et al. [2006] proposed a ballistic model which considers acceleration of the dust particle in the plasma sheath.

In both models, a charged dust particle is levitated into the plasma sheath once it electrostatic force exceeds the gravitational force. The acceleration model however predicts that the particle will be accelerated by the surface electric field once it enters the plasma sheath. This would enable it to reach much higher altitude than the one predicted by the levitation model as illustrated in Figure 6.19. This particle would then return to the surface or might oscillate over the surface.

Dust particle is levitated when the electrostatic force on the dust particle exceeds the gravitational force and other forces that hold the particle on the ground, i.e.

$$F_q > F_g + F_{other} \tag{6.8}$$

where $F_q = q_d E$ and $F_g = m_L g_L$, d stands for dust and L for lunar, and other forces

include adhesion and cohesive force. On the surface, dust particle is charged by the ambient plasma, photoemission and by contact with another dust and surface (triboelectric charging). The dust is levitated once it acquired enough charge (q_d) to overcome the gravitational and other forces. A large dust particle ($r_d \sim 1\mu$m) is more likely to levitate to a certain height where both forces are balanced. This is because large dust particles have smaller $|q_d|/m$ and would require significant number of charge before any levitation process can occur. A smaller size dust however can be accelerated once it enters the plasma sheath region and since its initial acceleration by the electric field is large compared to the gravitational force, the particle leaves the sheath regions with velocity pointing upwards. This is due to their large $|q_d|/m$ value and each additional charge have more impact on this value compared to the large particle. The accelerated dust particle continues to travel upwards, decelerates once it exits the sheath and travel until it reaches its highest altitude before returning back to the surface following a ballistic trajectory.

Dust particles on the surface are charged by various process which include triboelectric or contact charging. On the the lunar surface, loose dust particles can transfer charge between each other depending on the dust particles' work functions and the size of the contact area. Sternovsky et al. [2002] investigates the charging process of conducting and nonconducting materials that had been stored in vacuum. The materials are in the form of fine 'dust' with radii $\geq 25\,\mu$m to allow sufficient charge on the particle for measurement purpose. The particles are then placed sparsely on a conducting plate which can be biased to a potential.

The dust arrangement is to ensure charges that are being collected by the dust particle are due to the contact with the surface rather than with other particles. Result shows that dust resting on the surface are charged with approximately $q_d = CV$ where C is the capacitance between the grain and the conducting surface and V is the potential difference between the surface and the dust work function. In addition, dust particles are observed to have more charges when electric field is introduced on the plate's surface. This observation confirms that contact charging

is more likely to be the main charging mechanism for loose dust particle on the lunar surface than charging by ambient plasma. This theory is supported by the fact the solar wind plasma found in lunar orbit is more likely to be collisionless.

Sickafoose et al. [2001] investigates the triboelectric charging by placing a thick layer of dust particles, using a similar setting to the experiment conducted by Sternovsky et al. [2002]. The particles are then dropped into a container where their charge number are measured. In the experiments, it is found that the number of charges on the dust particle increases when it spent longer time in the dust layer. This experiment also shows that charge transfer can happen between surface and dust particle as well as between two particles which are in contact with each other.

Works related to dust charging on the lunar surface present another issue in simulating the separation mechanism of dust particles into the lunar exosphere. From Stubbs et al. [2006], it can be deduced that a dust particle could obtained approximately the same potential as the surface where the number of charge on the dust particle can be calculated using the capacitance rule. However the electrostatic force between the particles and the surface might causes it to levitate well before it reaches that potential level. On the other hand, the minimum charge from the electrostatic force is almost too small for the particle to have a significant levitation, or being accelerated in the sheath [Stubbs et al., 2006]. Borisov and Mall [2006] suggests that particle levitation near lunar crater in the terminator region is due to the high electric potential created by the presence of many mini craters in the region. He argues that a particle can only acquire few unit charges due to the high dust concentration on the ground. The presence of these mini craters create strong electric field ($> 200\,\mathrm{V/m}$) which allows particles to develop strong electrostatic force with the surface. As a result, levitating dust particles are more likely to have dust charge number far below the value calculated using the capacitance rule [Borisov and Mall, 2006]. The dust particle samples in the simulation therefore have to cover this possibility, i.e. a particle must have a minimum charge according to $F = q_d E$ and a maximum charge based on $q_d = VC$.

All simulations that are presented here consider dust particles that are charged between these two maximum and minimum values.

The electrostatic acceleration of the dust particle is given by

$$a_q = \frac{q_d E_s}{m_d} = \frac{3\varepsilon_0 \phi_s^2}{\rho \lambda_D r_d^2} \tag{6.9}$$

where E_s is the surface electric field given by ϕ_s/λ_D and $q_d = C\phi_s$ is the charge on the dust grain based on the capacitance rule ($Q = CV$), $C = 4\pi\varepsilon_0 r_d$ is the capacitance of a spherical dust particle, and ρ is the mass density of the dust particle of volume $\frac{4}{3}\pi r_d^3$.

Dust motion on flat lunar surface near terminator region

The simulation model is set as in the preceding section where one of the boundary is defined as lunar surface. Simulation is performed over an area of $6\lambda_D \times 6\lambda_D$ up to altitude of 60m. The lunar surface potential is set at 0 V at the beginning of the simulation and is allowed to float to its equilibrium potential as the simulation progresses. Dust particles are introduced into the simulation once the surface potential is at equilibrium and its motion is simulated for a total duration of 50 s.

In the simulation, 1000 dust particles are injected from a flat circular area located in the middle of the simulation volume as shown in Figure 6.20. This approach is due to the limitation caused by the size of the simulation volume that charges the edge of the surface to different potential to that of the centre, as discussed in the previous section. In reality, dust particles can be levitated from any point on the surface as long as it has the minimum number of charge as specify by Equation (6.8) . On the dayside, dust particles are positively charged, but the low surface potential means only particles with size of tenths of nanometer are more likely candidates for levitation. In contrast, surface near the terminator region can be charged to between -40V and -70V which presents a larger electrostatic force to the dust particles than surface in the dayside.

As there is currently no observation with regards to actual dust density and

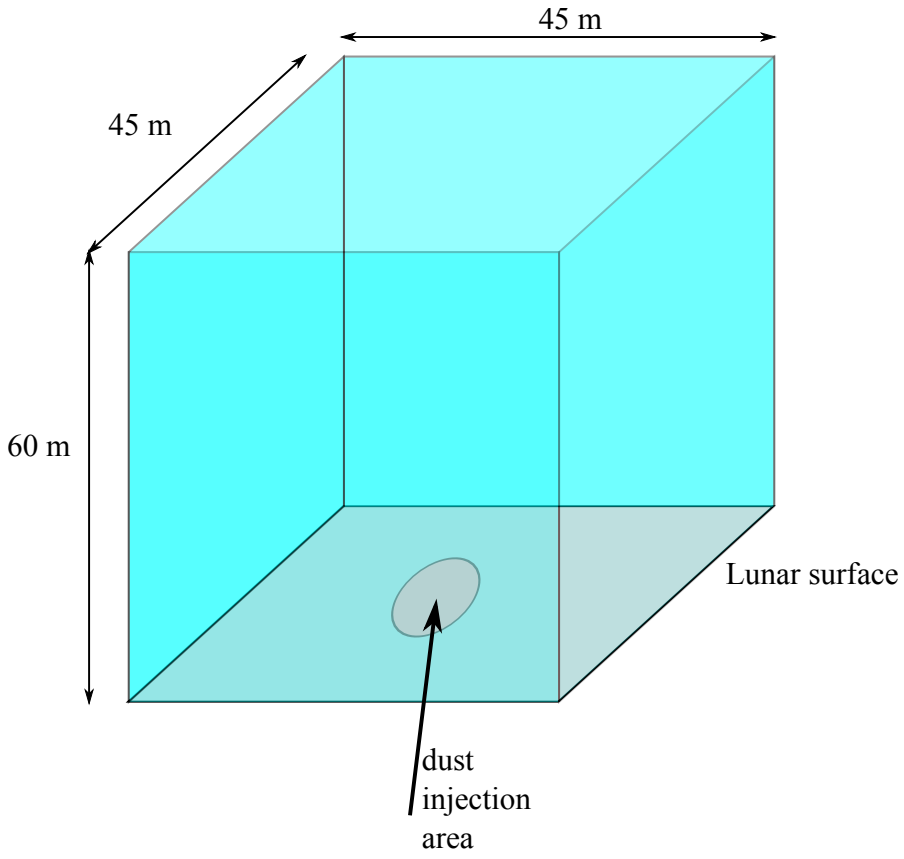

Figure 6.20: Simulation model used to simulate lunar dust.

the charge on each individual dust, the simulation is preformed by assuming each particles introduced would have a certain number of charges base on relation given in Equation (6.8). In the simulation, a dust particle can acquire any number of charge between the minimum required for levitation ($\sim q_d E_s \gtrsim F_g + F_c$) and the maximum number of charge based on the surface potential $q_{d,max} \sim \phi_d C$, where $\phi_d = \phi_s$ is the lunar surface potential and C is the spherical dust capacitance give by $C = 4\pi\varepsilon_0 r_d$. This assumption is based on the theoretical analysis of Stubbs et al. [2006] and experimental observations of Sternovsky et al. [2002], Sickafoose et al. [2001]. It is assumed that dust particles with sufficient number of charge to levitate might be held up by other forces such as adhesion, which cause them to continue to charge, either by interaction with ambient plasma while on the surface or by contact charging.

Once the dust particles leave the surface, they can continue to get charge from the interaction with plasma particles inside and outside the plasma sheath and

from photoemission. In the latter case, the charging process can be simulated using the PIC-MCC method presented in the previous chapter. However in the following simulation, no further charging process is assumed to happen once the particle leaves the surface.

The assumption that the dust charge can be justified in the following manner. The evolution of grain charge is given by

$$\frac{\mathrm{d}\,Z}{\mathrm{d}\,t} = I_i - I_e \tag{6.10}$$

where I_i and I_e are ion and electron current from the OML approximation [Whipple, 1981]. Assuming a nominal area current density of 10^{-14} Am^{-2} to represent all sources of current density including local plasma electrons, the time scale for change in charge can be calculated [Collier et al., 2011, Whipple, 1981]. Using the minimum charge limit, $q_{d,min}E = F_g$, $Z_{d,min} \sim 2600$ for 1μm radius particle, which gives $\phi_d = q_{d,min}/4\pi r_d \varepsilon_0 \sim 3.7$V and $q_{d,min} = -4.2 \times 10^{-16}$Coulomb. At this potential, current flux onto the dust is 8.6×10^{-18}A/m^2 and the time scale τ for the change in charge can be calculated following Collier et al. [2012]

$$\tau \sim \frac{q_{d,min}}{I} = \frac{-4.2 \times 10^{-16}}{8.6 \times 10^{-18}} \sim 48\text{s} \tag{6.11}$$

which shows that even at the largest dust particle size simulated here, with the lowest possible charge number $Z_{d,min}$, the time scale τ is the same order of magnitude with the maximum simulation time of 50 s. It is therefore possible to assume that the dust charge number will remain constant during the whole simulation process which will allow faster and more efficient simulations to be performed.

Particles with uniform size

SPIS-Dust is used to investigate the dynamics of evenly size dust particles of size 50 nm, 100 nm, 500 nm and 1 μm near the lunar terminator environment. For

Table 6.3: Dust properties on lunar surface charged to -50V.

Parameters	50nm	100nm	500nm	1μm
m_d[kg]	1.57×10^{-18}	1.257×10^{-17}	1.57×10^{-15}	1.257×10^{-14}
$Z_{d,min}$	1	5	300	3000
$Z_{d,max}$	1800	3600	18,000	36,000
$q_{d,min}/m_d$ [C/kg]	-0.1	-0.06	-0.03	-0.04
$q_{d,max}/m_d$ [C/kg]	-153	-38.25	-1.84	-0.45

each dust radius, 1000 particles are introduced into the simulation volume where each particle charge number is distributed uniformly in the $q_{d,min} > q_d > q_{d,max}$ range. Table 6.3 shows the maximum and minimum charge for the 4 different dust radii. The dust superparticle weight is set to 1, i.e. each dust superparticle represents an individual physical grain in the simulation volume. At equilibrium, lunar surface is found to charge to -52 V which is achieved after approximately 1ms. The dust particles are then injected into the simulation volume from the lunar surface after 5ms with zero initial velocity. This delay allows the potential on the surface to settle so that each dust particle experiences the same electrostatic force. The height of the simulation volume is limited to 60 m for computational reason. The properties of the released dust particles are tabulated in Table 6.3.

Figure 6.21 compares the maximum height achieved by dust particles of radius 50 nm, 100 nm and 500 nm. In the graph, the maximum height achieved by each particle is plotted against its $|q_d|/m$ value, limited to $q_d \sim 5$ C/kg. The first two smaller sizes can have $|q_d|/m$ that exceed 5 C/kg, where as the ones with $r_d = 500$ nm has maximum $|q_d|/m \sim 1.6$ C/kg. It is obvious from the graph that the maximum height achieved for each particle is proportional to the particle's $|q_d|/m$ value. Two particles with different radii but with the same $|q_d|/m$ value will levitate to approximately the same maximum height. In the graph, $|q_d|/m \gtrsim 0.6$ C/kg is required for any levitation to take place and at $|q_d|/m \sim 2.5$ C/kg, particles can exceed the simulation volume via the top boundary.

Dust particles trajectory have been found to follow the ballistic motion as suggested by Stubbs et al. [2006] where some particles experience oscillatory

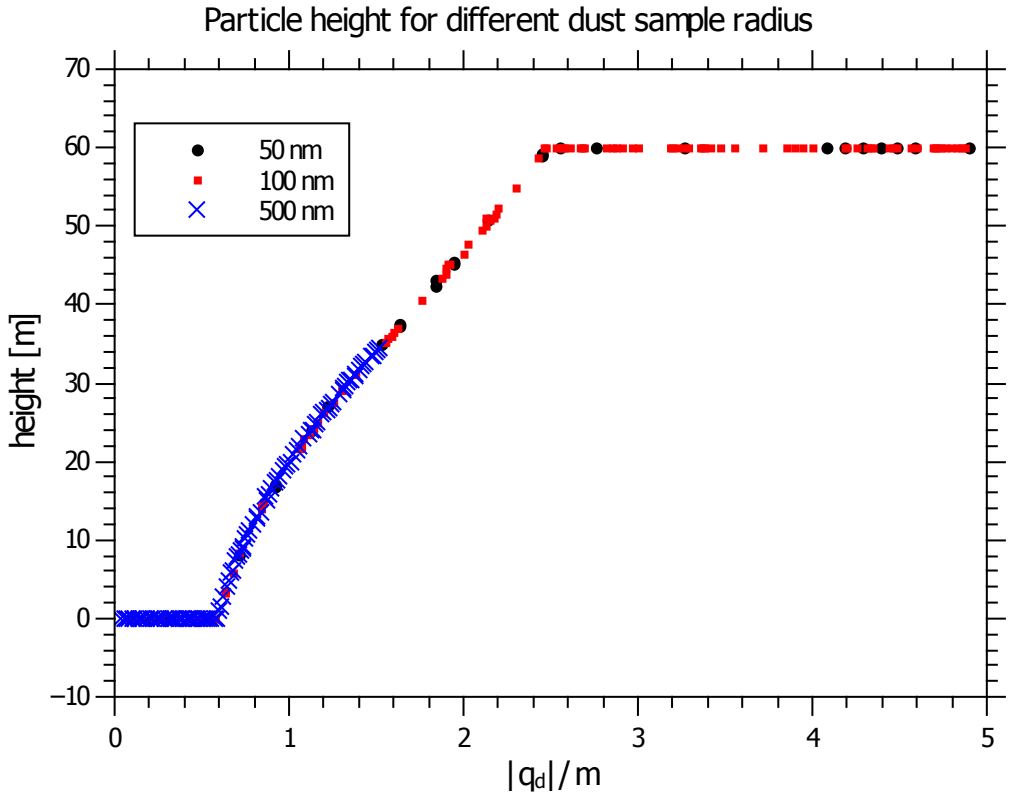

Figure 6.21: Maximum height achieved by dust particles of size 50 nm, 100 nm and 500 nm.

motions above the ground surface. Figure 6.22 shows motion for 5 dust samples of radius 500 nm with different $|q_d|/m$ values over 50 s. In the graph, particle maximum height increases proportionally with an increase in number of charge. The number of oscillations does not depend on the particle's $|q_d|/m$ C/kg value. For example, particle with $|q_d|/m = 0.68$ manages to complete 6 oscillations whereas particle with $|q_d|/m = 0.79$ only experiences 1 oscillation. This is due to the number of oscillations dependent on the instantaneous surface potential at the time of descend. As particles are levitating above the surface, temporal variation in lunar surface potential causes the particles to either return to the surface or accelerated upwards. The actual 3-d trajectory of a particle with $|q_d|/m = 0.68$ C/kg is shown in Figure 6.23. The trajectory suggests that the electric field due to the potential variation will accelerate the particle with horizontal velocity component.

For $r_d = 1\mu$m, there is no longer a clear pattern for the maximum dust height at $|q_d|/m > 0.6$ C/kg, as shown in Figure 6.24. The maximum $|q_d|/m$ from the

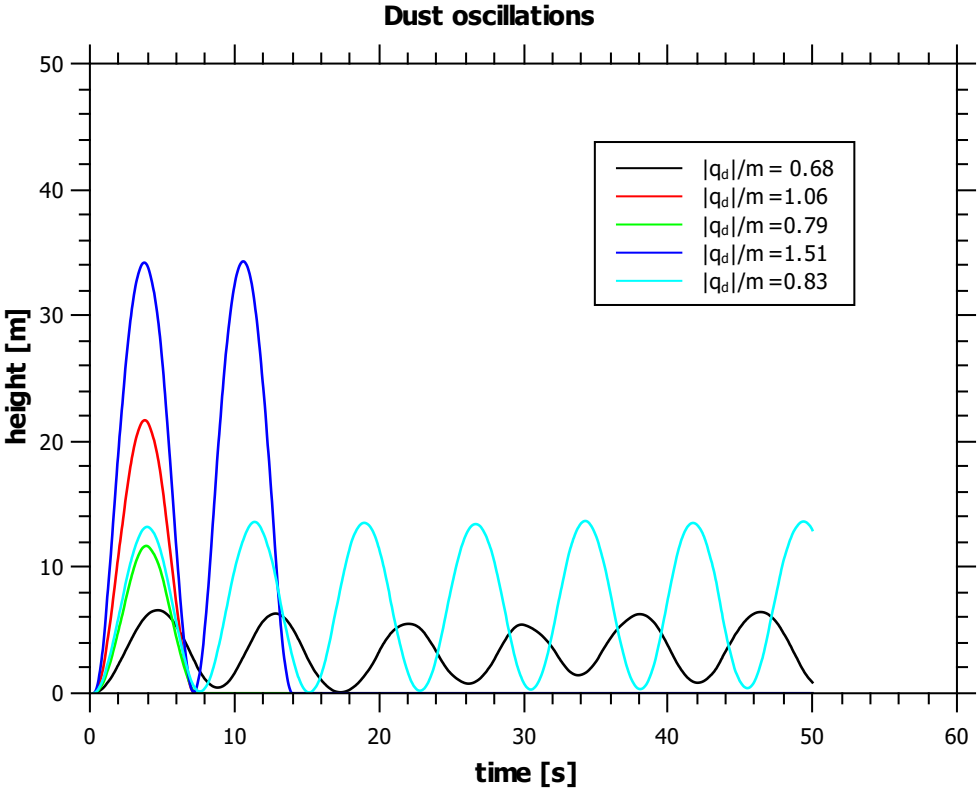

Figure 6.22: Oscillatory motion for dust particles of size 500 nm.

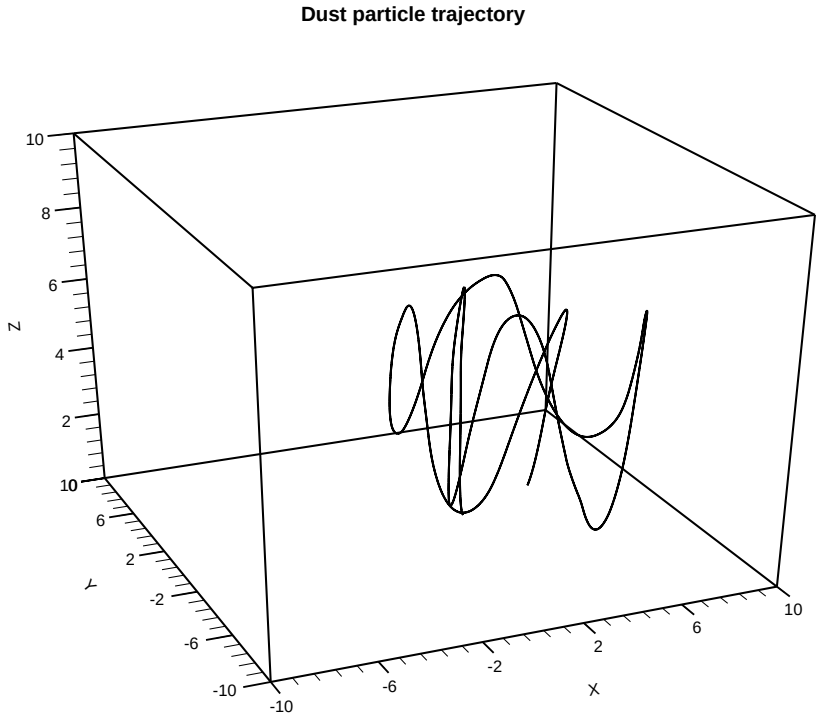

Figure 6.23: An example of dust particle trajectory where $r_d = 500$ nm. $|q_d|/m$ in this case is 0.68 C/kg .

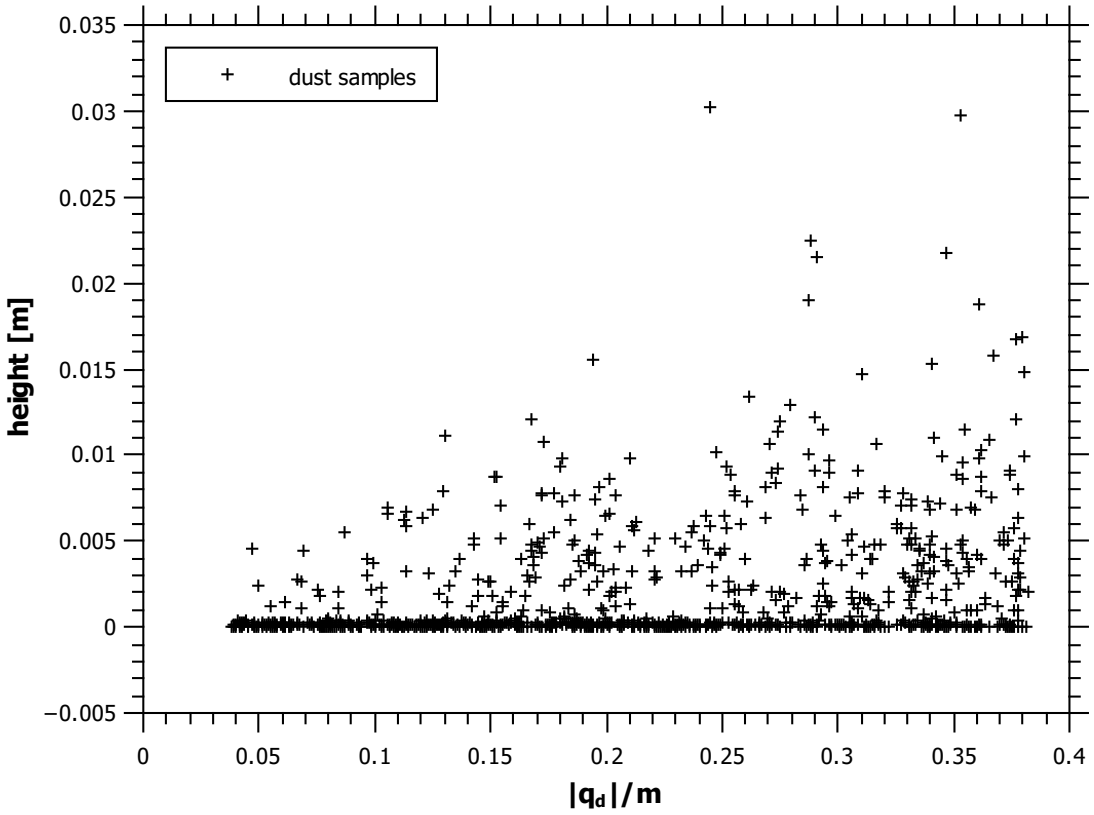

Figure 6.24: Levitation height for $r_d = 1\mu$m. The maximum height for each dust sample varies across the $|q_d|/m$ values with maximum height of $\sim 3\,$cm is observed.

samples is calculated to be around 0.38 C/kg. Particles of this size on average only achieve maximum elevation of few centimeters before returning to the surface due to the small $|q_d|/m$ value. This observation also suggests that particle of this size is unlikely to be accelerated out of the plasma sheath by the electric field.

Particles with varying size

The motion of dust particles with various sizes within the range of 10nm $< r_d <$ 1μm using the same simulation settings was investigated. These particles sizes are uniformly distributed in the log scale and have dust charge number Z_d randomly assigned between the $|q_{d,min,r_d}| < |q_d| < |q_{d,max,r_d}|$ range. The distribution of the dust particle samples is shown in Figure 6.25a. The resulting maximum height and maximum vertical velocity of the dust samples are shown in Figure 6.25b.

In Figure 6.25b, the black line represents the maximum height (left scale) while the red line represents the maximum vertical velocity (V_z). Result suggests that levitation height depends on the particles $|q_d|/m$ regardless of the dust radius distribution. Levitation only occur when $|q_d|/m > 0.6$ and particles below this value can only obtained maximum vertical velocity of $V_z \sim 0.1$m/s. Particles with $|q_d|/m > 1000$ obtained V_z in excess of 400 m/s.

Dust motion near lunar crater

The motion of dust particles near a lunar crater is simulated for two cases of crater near the dayside and the terminator regions. A continuous stream of dust particles are injected after the surface has reached its equilibrium potential. The size (radius) of the dust particles can vary but are limited to between 100 nm and 1 μm as particles of smaller sizes are more likely to exit the simulation volume via the top plasma boundary due to strong electrostatic force acting on them. The charge on each dust particle is set to vary between $|q_{d,min}|$ and $|q_{d,max}|$ as in the previous simulations. From the previous simulations, the surface is charged to different potentials according to its location which means that dust particles can either be

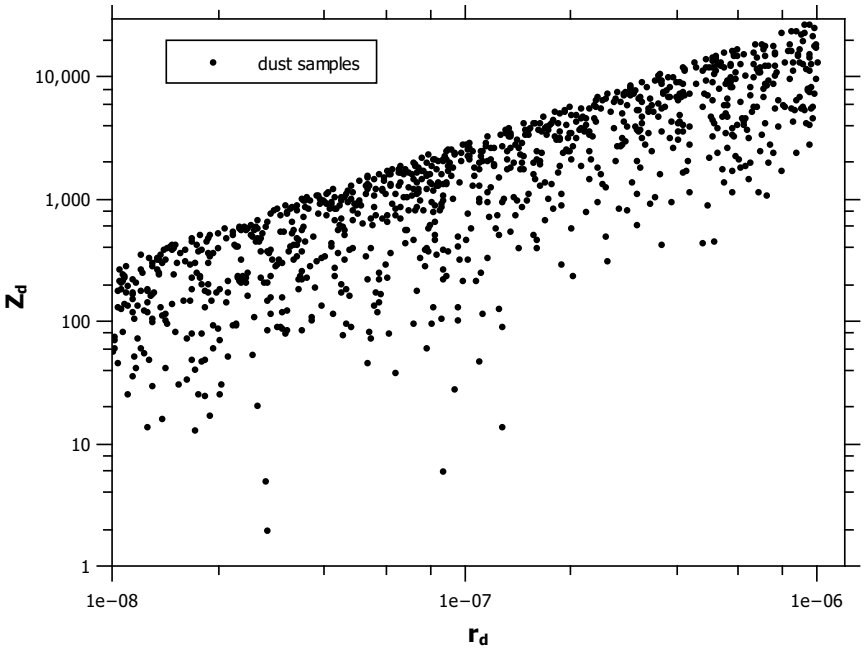

(a) Radius and charge distribution for the dust sample.

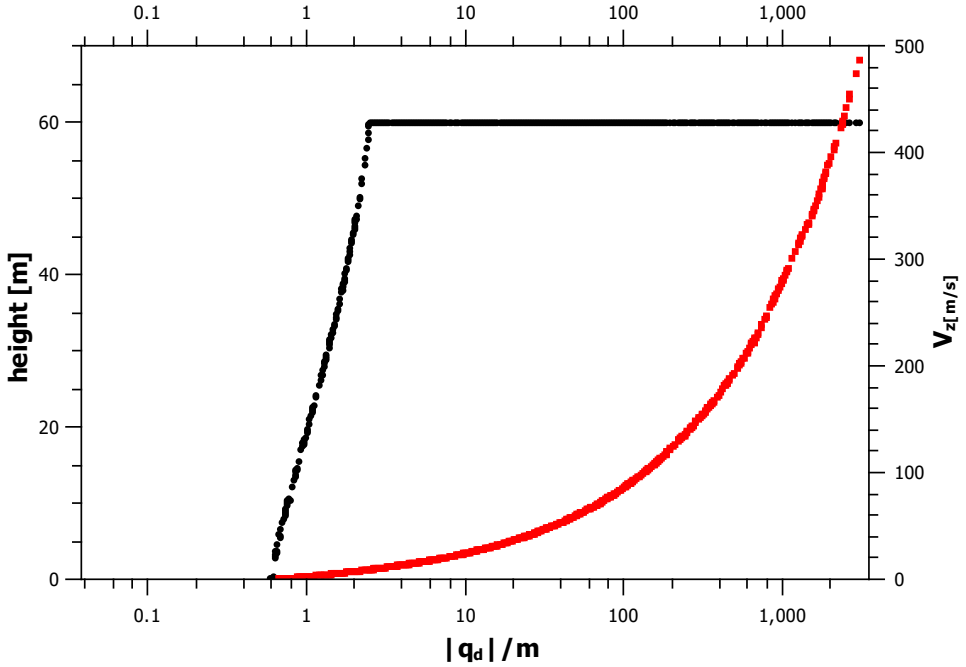

(b) Maximum height and maximum vertical velocity.

Figure 6.25: Graph showing (a) the radius and charge distribution and (b) maximum and vertical velocity observed from the simulation. Particles need to have $|q_d|/m$ ratio of more than 0.8 C/kg to have a significant levitation ($h_{max} > 1$ m).

positively or negatively charged when released by the surface.

Particles are injected from an area outside the crater and their motions are monitored at a specified interval. In the simulation, it is also assumed that the charge on each particle remains the same during the whole simulation period, eventhough they can change slightly over the course of the simulation because of the longer simulation period. In addition, it is also assumed that the background plasma is stationary with respect to the dust motion allowing the use of different time scales for each species in the simulation. About 1,000 dust particles are introduced to the simulation every 0.5 ms for over 0.5 s, producing about 1,000,000 dust superparticles during the injection period.

Figure 6.26 shows the cross section of a series of particle motion (density) around the crater in the dayside region beginning at $t = 5$ s until $t = 30$ s. The surface is found to charge to ~ 5 V with slightly higher potential is observed around the rim's surface (see Figure 6.12a). Figure 6.26a and 6.26b, show the initial levitation process of the dust particles where dust particles have been observed to levitate at an angle leaning towards the centre of the crater. This is due to the stronger electric field created by the high surface potential around the crater deflecting the motion above the crater. After reaching their maximum height, some of the dust particles which were injected from the crater's edge appear to follow a path into the middle of the crater as shown in Figure 6.26c and 6.26d. This motion happens because the deflected particles experience less electrostatic force over the middle of the crater than at the rim.

In reality, since this simulation is performed on the dayside where there is a layer of photoelectrons, there is a possibility of photoelectrons collection by the dust particles. Dust superparticles which were released into the simulation are positively charged which further increase their chances of collision with photoelectrons due to the attractive force involves and therefore reduces the electrostatic force between the dust particles and the surface. However, dust particles also experience photoemission while in flight which can balance the photoelectrons collision current. This

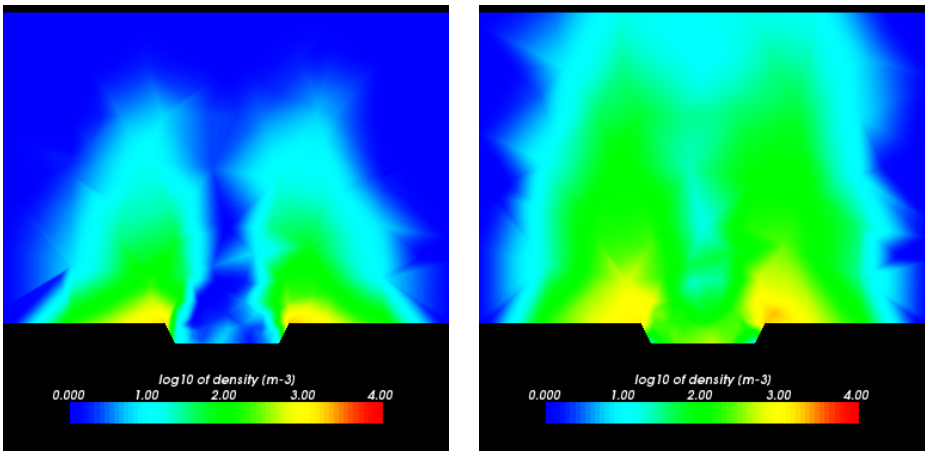

(a) $t = 5\,\mathrm{s}$ (b) $t = 10\,\mathrm{s}$

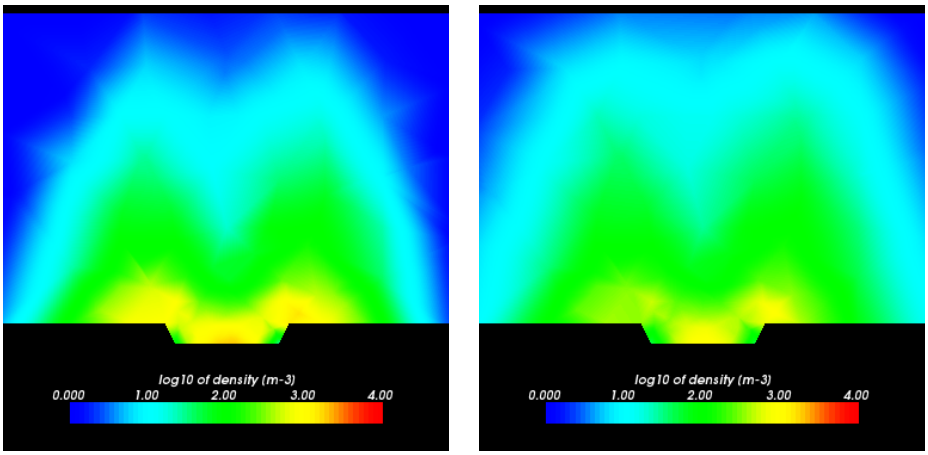

(c) $t = 15\,\mathrm{s}$ (d) $t = 20\,\mathrm{s}$

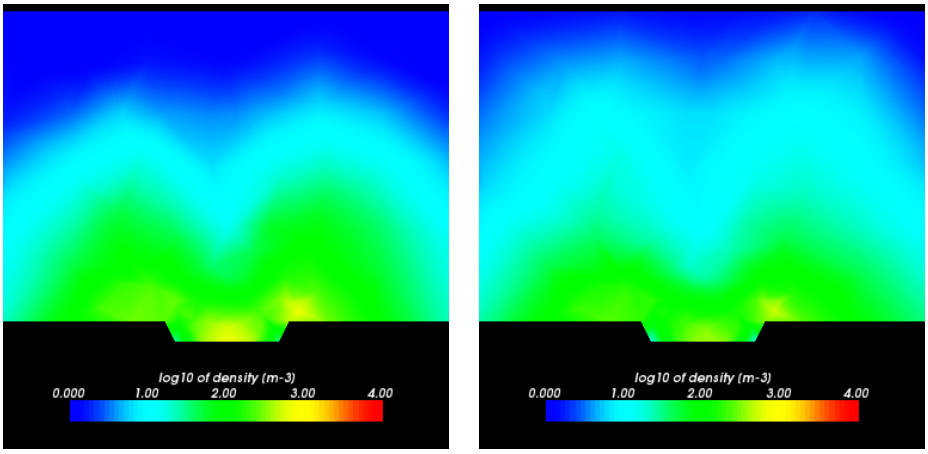

(e) $t = 25\,\mathrm{s}$ (f) $t = 30\,\mathrm{s}$

Figure 6.26: Dust motion near lunar crater during dayside ($\theta = 0^o$). The dust appear to be directed into the middle of the crater.

simulation then looks at the worst case scenario where the charged dust particles experience the strongest electrostatic force, because the have not lose any of the charge they carry when the leave the surface.

The motion of dust particles near the terminator region is simulated with slightly different arrangements. Because surface is charged to higher negative potential than the one on the dayside, streaming dust particles could move out of the simulation volume which could hide some of the dynamics involved. Simulation is performed using a bigger range of dust particles where the upper limit is set to 1 μm. In this simulation, dust particles are injected for a period of 0.5 s at an interval of 0.005 s, producing 100,000 dust superparticles and the simulation is ran for a period of 25 s.

Figure 6.27 shows a series of dust density at 2.5 s interval. From the figures, it appears that more particle are levitated from the more negatively charged surface (right) than the less negatively charged (left) surface due to the stronger electric field presents. Although the dust particles introduced in the simulation are negatively charged (since they come from outside the crater), there is little evidence of particles being attracted to the positively charged rim. A barrier can be seen which prevents all particles from entering the crater. This confirms the work of Borisov and Mall [2006] who predict a very strong electric field near the terminator and its function in accelerating particles into the lunar exosphere.

Cohesive force

Cohesion has been discussed as one parameter that determines the possibility of dust particles levitating over the lunar surface (see for example [Hartzell and Scheeres, 2011, Stubbs et al., 2006]). From equation (6.8), the electrostatic force required to enable a dust levitation can be expanded to include cohesion by

$$F_q > F_g + F_c \tag{6.12}$$

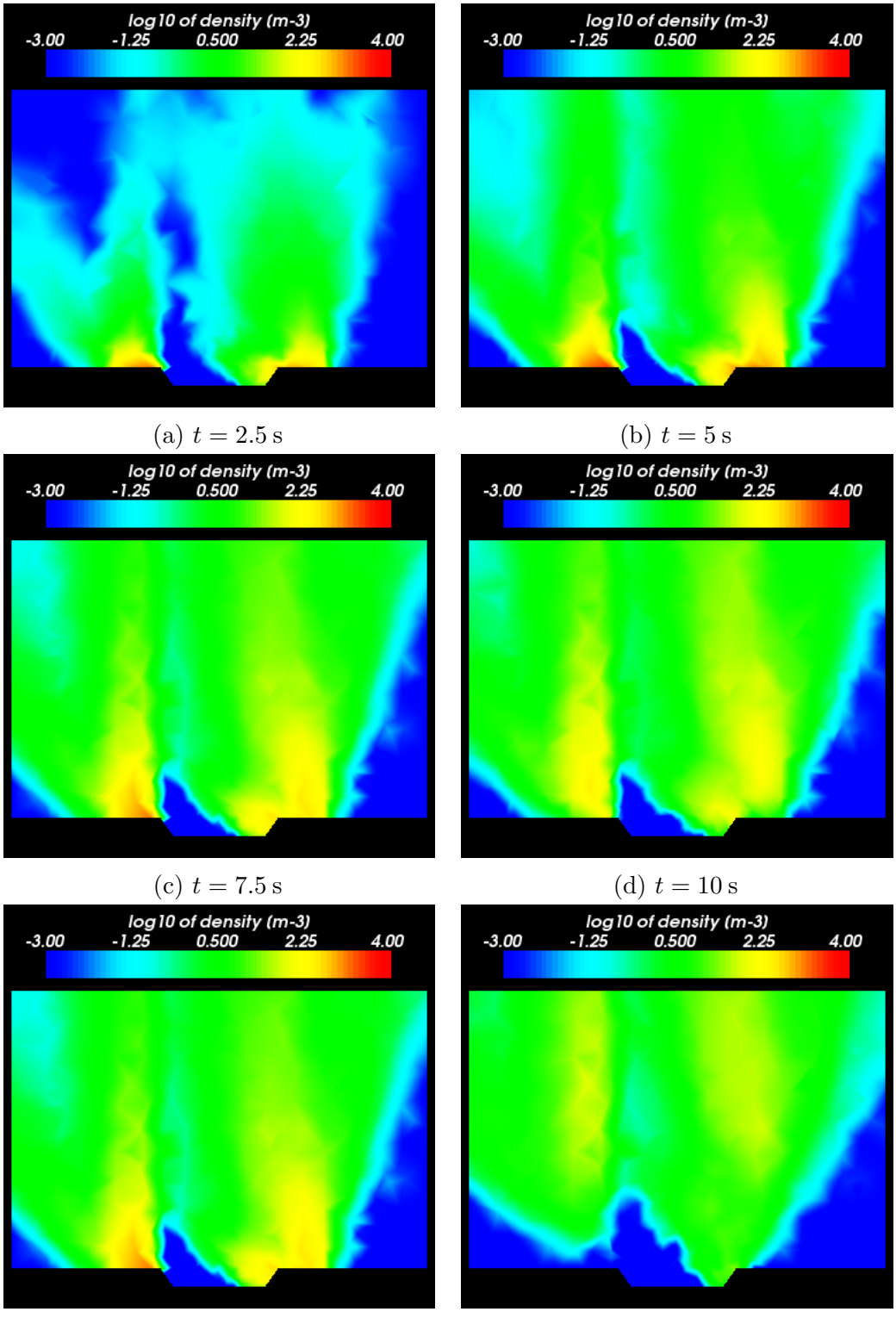

(a) $t = 2.5\,\mathrm{s}$ (b) $t = 5\,\mathrm{s}$

(c) $t = 7.5\,\mathrm{s}$ (d) $t = 10\,\mathrm{s}$

(e) $t = 12.5\,\mathrm{s}$ (f) $t = 15\,\mathrm{s}$

Figure 6.27: Dust motion in the first 15 s.

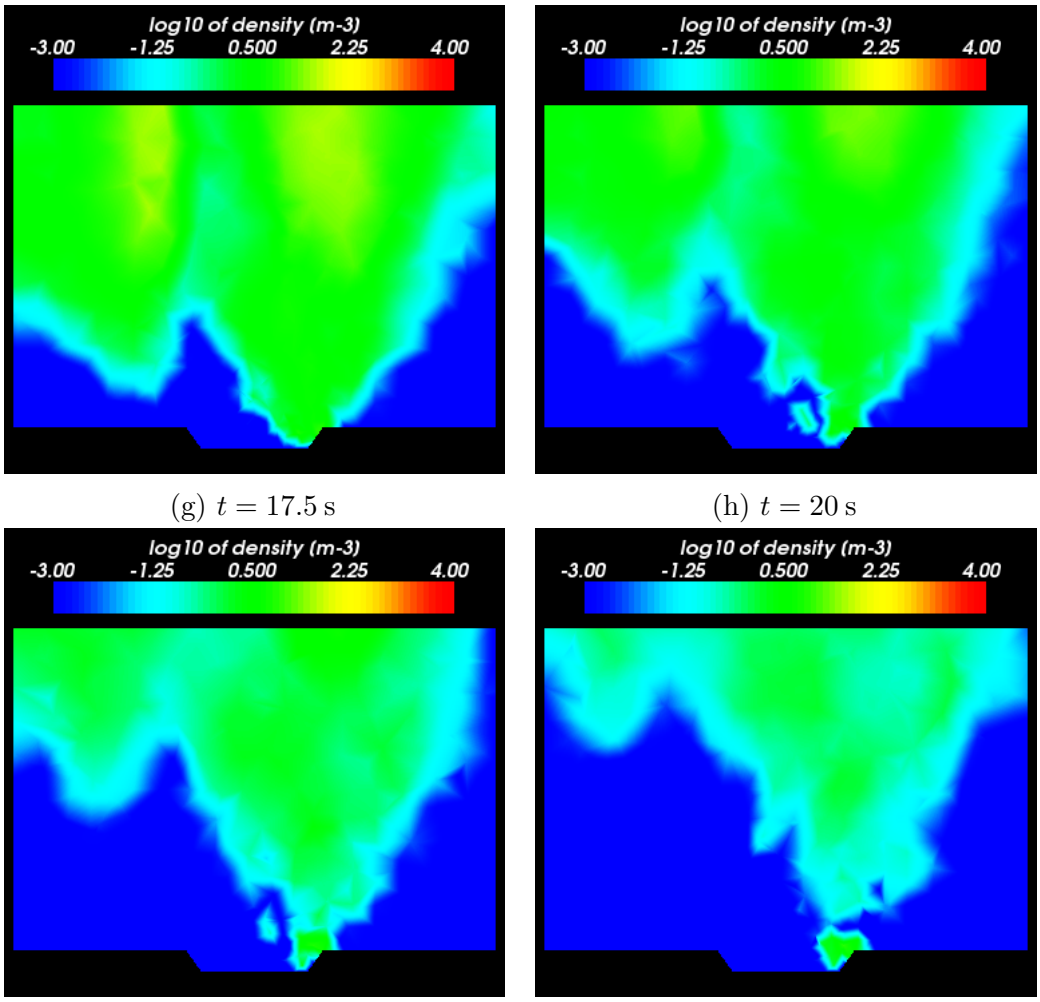

(g) $t = 17.5\,\mathrm{s}$ (h) $t = 20\,\mathrm{s}$

(i) $t = 22.5\,\mathrm{s}$ (j) $t = 25\,\mathrm{s}$

Figure 6.27: Dust motion near a crater close to the terminator region. Shadowed surface is creating a strong electric field which forms a barrier preventing any particle from entering the crater's basin.

where F_c is the cohesive force between two or more particles in contact to each other. Cohesive force is a form of van der Waals force where particles attract or repulse each other and is a function of the particle's size and shape. One early explanation of this type of force was by Hamaker [1937] who described the attraction between spherical particles based on the diameters and distance separating them.

An approximation of the cohesive force between two spherical particles of radius r_1 and r_2 is given by [Castellanos, 2005, Perko et al., 2001, Rognon et al., 2008]

$$F_c = \frac{D}{48(t+d)^2}\frac{r_1 r_2}{r_1 + r_2} \tag{6.13}$$

where $D = 4.3 \times 10^{-20}$ Joules is the Hamaker constant for lunar soil [Perko et al., 2001], t is the minimum distance between the particles due to adsorbed molecule and d is the distance between the particle surfaces. Assuming cohesion only occurs when particles are in contact, $d = 0$. The factor $\frac{r_1 r_2}{r_1 + r_2}$ approaches r_d if cohesion is assumed between the particle and a flat plane [Castellanos, 2005]. Perko et al. [2001] introduces the parameter $S = B/t$ where $B = 1.32 \times 10^{10}$ is the diameter of an O^{-2} ion. The parameter S represents an approximation of the surface cleanliness where $S = 1$ for a clean surface, and Perko et al. [2001] estimates a particle surface cleanliness of 0.88 during lunar day and 0.75 during the night. Equation (6.13) can be rewritten as

$$\mathbf{F}_c = CS^2 r_d \tag{6.14}$$

where C is a constant given by $C = 5.14 \times 10^{-2}\ \mathrm{kg/s^2}$.

The maximum levitation heights for 1000 particles injected with the effect of cohesion is compared to the one without any consideration for cohesion. Dust particles radius are varied from 100 nm to 100 μm and particles are injected (or released) from the lunar surface on the circular area as in Figure 6.20. In both cases, the maximum number of unit charge on each particle is set to be no more than the number of unit charge the particle could have obtained when its surface potential equal to the lunar surface potential, i.e. $\phi_d = \phi_{s,lunar}$, which can be solved

using spherical capacitance equation

$$Z_d = \frac{\phi_{s,lunar} 4\pi\varepsilon_0 r_d}{e} \tag{6.15}$$

This restriction is due to the fact that it is impossible for a dust particle to charge to a level where its surface potential exceeds the potential of the surface it resides because such level of charging would ultimately result in arcing.

The charge on the dust particles is calculated by solving the equality

$$\mathbf{F}_q \geq \mathbf{F}_g + \mathbf{F}_c \tag{6.16}$$

where $\mathbf{F}_q = q_d\mathbf{E}$ is the electrostatic force required to levitate the particle, $\mathbf{F}_g = m_d\mathbf{g}_l$ is the lunar gravitational force and $\mathbf{F}_c - CS^2 r_d$ is the cohesive force. Rearranging (6.16), we get

$$Z_d = \frac{1}{e\mathbf{E}} \left(m_d\mathbf{g}_l + CS^2 r_d\right) \tag{6.17}$$

where Z_d is the dust charge number given by

$$Z_d = \frac{q_d}{e}. \tag{6.18}$$

Considering only the normal component of the field, (6.17) can be simplified into

$$Z_d = \frac{1}{eE_0} \left(m_d g_l + CS^2 r_d\right) \tag{6.19}$$

where E_0 is electric field normal to the surface.

The SPIS software calculated the field by solving the Poisson's equation for every cell in the simulation volume and the field is assumed to be uniformed in that particular cell. The surface electric field E_0 is obtained by finding the electric field normal to the injection surface, in the cell where the surface is located, as shown in Figure 6.28.

Depending on the state of charging at the point of dust injection/release,

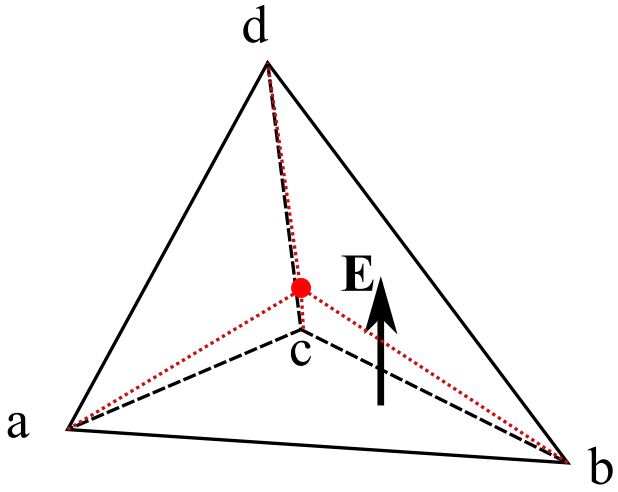

Figure 6.28: Interpretation of $\mathbf{E}_n$ in SPIS where $\mathbf{E}$ is assumed to be uniform in every cell. The field normal to the plane *abc* is obtained by calculating the potential gradient of the surface.

the potential or the charge on the dust can be solved using (6.19), assuming a uniformly distributed charge on the dust surface. At a region close to the terminator, simulation shows that the surface is charge to ~ -50V which is then used as the maximum potential limit for the dust particle. The comparison between the charge on the dust particles is shown in Figure 6.29. In the graph, a 100 nm particle only needs $\sim -46e$ to overcome the gravitational force (no cohesion) but would have to charge to the maximum limit of $\sim -3400e$ when cohesion is included. At roughly 1 μm, the number of charge on dust particles are at the same level for both cases of charging, where they are limited by the dust surface potential. The required charge on the dust particle in the case of cohesion exceeds the number it would have needed if the charge limit is not in place. One explanation of this rather high value is the consideration for cohesive force does not take into account the repulsive force between the two particles in contact. The formula given by Perko et al. [2001] and implemented by Hartzell and Scheeres [2011] might be applicable in a non-charging environment and it has not been able to explain the presence of small dust particles in the lunar exosphere. This effect has been shown by Wang et al. [2009] where a pile of dust on a bias plate spreads as they getting charged.

Figure 6.30 shows the maximum height achieved by each set of dust particles. When dust particles have more than the minimum charge for levitation, they will

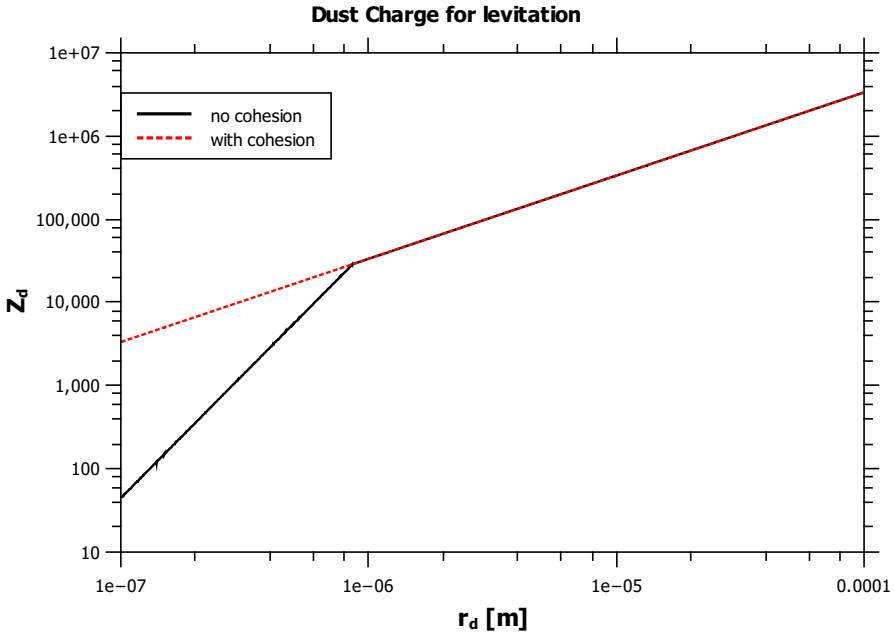

Figure 6.29: Charge on dust particle (Z_d)in the simulation when no cohesion (red, dotted line) and cohesion (black, solid line) is included in the simulation.

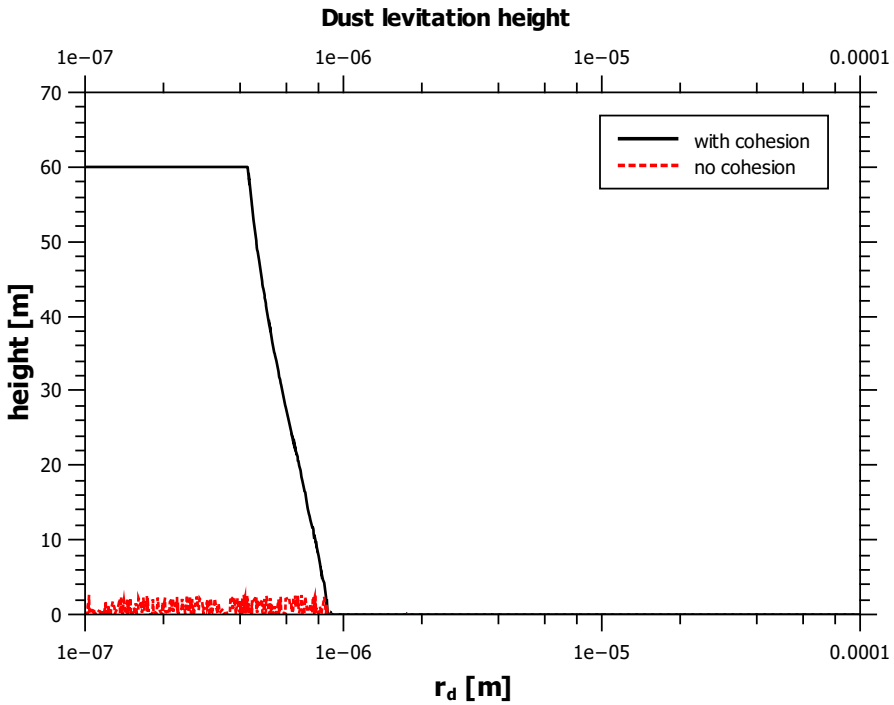

Figure 6.30: Maximum height achieved by dust particles with cohesion included (black, solid line) and no cohesion included (red, dotted line) in the charge determination.

only levitate to not more than few meters in height. Because of cohesive force, the particles acquire more than the minimum charge and can levitate to height higher than the simulation height of 60 m. The observation also shows that for this range of dust particles, the dust acceleration theory in Stubbs et al. [2006] can only happen when the particle has more than minimum required charge when it leaves the surface. This observation however does not rule out the possibility of a much smaller particle to be accelerated in the sheath as it may have a much larger $|q_d|/m$ ratio.

6.4 Summary and Conclusion

The charging process on lunar surface has been presented using SPIS software. On the dayside, lunar surface is charged to around +4 V and gradually reverses in polarity as it approaches the terminator region. Photoemission has been shown to be the main contributing current on the dayside, although almost 90% of the photoelectrons are recollected by the surface. The recollecting current is the main reason why the surface charged to a low positive potential because an increase in surface potential would only result in more photoelectrons being recollected due to emitted photoelectrons having low energy distribution. Past experiments have shown that these low energy distribution have a maximum energy of 6 eV but the model used in the simulation only manages to produce photoelectrons with maximum energy of 8 eV. The slight difference in energy distribution level leads to slightly higher potential observed in the simulation but still within the predicted level of ~ 5 eV [Manka, 1973].

On the terminator, simulation shows that the surface is charged to in excess of -40 V due to the limited solar UV flux with potential of ~ -55 V has been obtained from the simulation. The lack of solar UV is the main cause of this negative potential, in addition to the solar wind protons that flow parallel to the surface. Another issues with regards to the charging in the terminator region is the particle injection process that is not properly represented in the simulation.

As plasma species were assumed to have Maxwellian energy distribution, this condition is not observed particularly in the plasma sheath region. Plasma sheath region is a result of the surface being charged, and serves to either attract or reflect incoming particles in order to restore the current balance on the surface. As the surface beginning to charge, this sheath could cause an increase or decrease in particular plasma species density, hence changing the energy distribution of the species. However, simulations performed for plasma in this condition were able to produce surface potential within the potential range predicted by Colwell et al. [2005].

Simulation also confirms the possibility of having a negatively charged surface patch in the dayside area when crater or boulder is present. The simulation has shown that the sunlit facing side on both crater and boulder are charged to positive potential whereas the shadowed side are charged to negative potential. These phenomena is observed when the angle of incidence for both the solar wind and solar UV $> 30^o$. At these angle of incidences, the variations in surface topology create sunlit and shadowed region which causes incoming solar wind and solar UV to be obstructed. The simulations also suggest that these variations do not have to be big for the localized charging region to occur. This observation is consistent with observation made by Halekas et al. [2002] and the work of Farrell et al. [2007].

Charged dust particles have been shown to be present in the lunar exosphere, in particular near the terminator regions. The abundance of dust particles near the terminator region are simply due to the higher electric field which is present in this region. Simulations have been performed to compare the dust motion for different radius and $||q_d|/m_d$ ratio. Particles with radius less than 100 nm can be levitated to height in excess of 60 m, gaining speed of up to 400 m/s. Simulation also suggests that there is no significant electrostatic levitation for particle with radius of $1\,\mu$m with odd particles manage to achieve maximum height of around few centimeters. However, other ejection methods such as from meteorite impact has not been simulated where it is believed that this method is the most likely source of

levitation for particle with $r_d > 1\ \mu$m. Simulation also suggests that dust particles can travel in oscillatory motion near the surface, where it can be hazardous to human activity on the surface. These oscillatory motion can be sustained when the surface electric field produces equivalent force to the surface gravitational force. On lunar surface, the potential on the surface could vary because of the low surface conductivity and surface topography. These variation would also result in dust particles oscillatory motion as returning dust particles could experience bigger electrostatic force as they approach the surface.

SPIS has also been used to simulate dust particles motion near lunar crater for both dayside and terminator regions. In the first cases, dust particles appear to be deposited to the middle of the crater. These observations is due to the basin having a lower surface potential than the rim surface. In the latter case, no particle is deposited inside the crater because of the strong electric field created by the shadowed region. This electric field extends to the dayside creating a potential barrier preventing any particle from being deposited into the crater.

Recent paper by Hartzell and Scheeres [2011] suggests that cohesive plays a greater role in the determination of dust charge density in the lunar exosphere. SPIS was used to investigate the role of cohesive forces on dust motion by considering the cohesive force in the dust sampling process. Cohesion is believed to bind dust particles together, making it more difficult for the dust particle to leave the surface. It was suggested that cohesive would allow dust particle with size $> 100\ \mu$m to be levitated. However, simulation shows that the charge calculation method used by Hartzell and Scheeres [2011] would results in dust particles with surface potential larger than the lunar surface potential. By limiting the number of charge the dust particle could carry to the surface potential, dust particles with radius $< 1\ \mu$m are found to attain some levitation height but no levitation is observed for dust particles with radius $> 1\ \mu$m. This observation is due to dust particles with $r_d > 1\ \mu$m requiring number of charge greater than the limit imposed by the lunar surface potential.

In conclusion, SPIS has been used to simulate many possible scenarios on lunar surface which include lunar surface charging, shadowing phenomena and dust levitation. Some of observations agree with previous works with few new findings have been observed. One particular finding is the motion of dust particle near a crater where it has been suggested that the dust particles are attracted to the centre in the case of crater in the dayside region and are pushed away from the crater in the case of crater in the terminator region. Simulation result has shown agreement with the work of Borisov and Mall [2006] and suggests the the possibility of using SPIS-dust to investigate many phenomena on lunar surface.

Chapter 7

Lunar Dust Motion Near Lander

7.1 Introduction

The first successful lunar mission was launched by the USSR, when the first unmanned lunar probe made a hard landing on lunar surface under the country's *Luna* programme in September 1959. The USSR's *Luna* programme had achieved many first technological successes which include capturing the image of the far side of the Moon (*Luna 3*), the first soft landing (*Luna 9*) and the first artificial satellite to orbit the Moon (*Luna 10*). The United States of America had their own *Apollo* programme which mission was to send astronaut to lunar surface. In July 1969, National Aeronautics and Space Administration (NASA) successfully landed 3 astronauts on the Moon during the *Apollo 11* mission. It was followed by other 5 successful missions to the lunar surface with one mission had to be abandoned due to in flight system malfunction. In total, Apollo programme provided the space community with observations on lunar environment as well as bringing home 383 kg of lunar rocks and soil to Earth.

Major space agencies around the world (NASA, ESA, JAXA, Russia) have earmarked potential return to the Moon in the near future. The success of these future missions depends largely on the ability to understand and predict the effects of lunar environment in order to prepare crews and equipment to withstand such harsh environment. Observations and findings from previous Apollo and Luna

programmes are invaluable in the sense that they provide first hand experience on what to expect from the environment. One issue that has been anticipated involves dealing with the effect of lunar dust. NASA has for example conducted various studies on the impact of lunar dust on future space mission. These studies looked at many methods and ways to overcome issues such as dust adherence problem and its health hazard to astronaut which has increased public awareness on the importance to understand the dust behaviour.

The effects of lunar dust has been well documented by many [see for example Gaier, 2005, Stubbs et al., 2007b, Christoffersen et al., 2009] , which are mainly due to the dust's abrasiveness, adhesiveness and size. Among major issues with regards to the presence of dust particles are adherence to clothing and equipment, visibility reduction particularly during landing, and the effect on human health from breathing off the dust particles. Past lunar missions have found dust particles ability to adhere to all materials and could prove fatal if it involves life preserving equipment [Goodwin, 2002].

Previous chapter provides insight into the properties of lunar dust, which is a product of continuous meteorite bombardments that grind the regolith into 'fine' dust particles. On average, the dusty regolith grain size is $70\,\mu$m with roughly 10-20% are $< 20\,\mu$m (on weight scale) with samples of size $\sim 0.01\,\mu$m have been observed [Greenberg, 2005]. The properties of lunar dust and the dust charging process has been covered in Chapter 6. This chapter will investigate the lunar dust motion around man-made object such as the lunar exploration vehicle.

The rover size is based on the lunar *Space Exploration Vehicle (SEV)* as shown in Figure 7.1. The SEV is a 3-m height, 4.5 length rover that can house two astronauts. The chassis is 1.3 m from ground, and has 12 wheels to manoeuvre.

7.2 Dust motion near lunar rover

The motion of lunar dust near a rover has been investigated using the techniques and methods developed in SPIS-dust code. Although SPIS can be used to accurately

(a) Image showing the Habitat Demonstration Unit and Space Electric Vehicles. The two vehicles are at both sides of the habitat unit. (Image Credit: NASA)

(b) The Space Electric Vehicle. (Image Credit: NASA/Regan Geeseman)

Figure 7.1: NASA's lunar habitat and vehicle prototype.

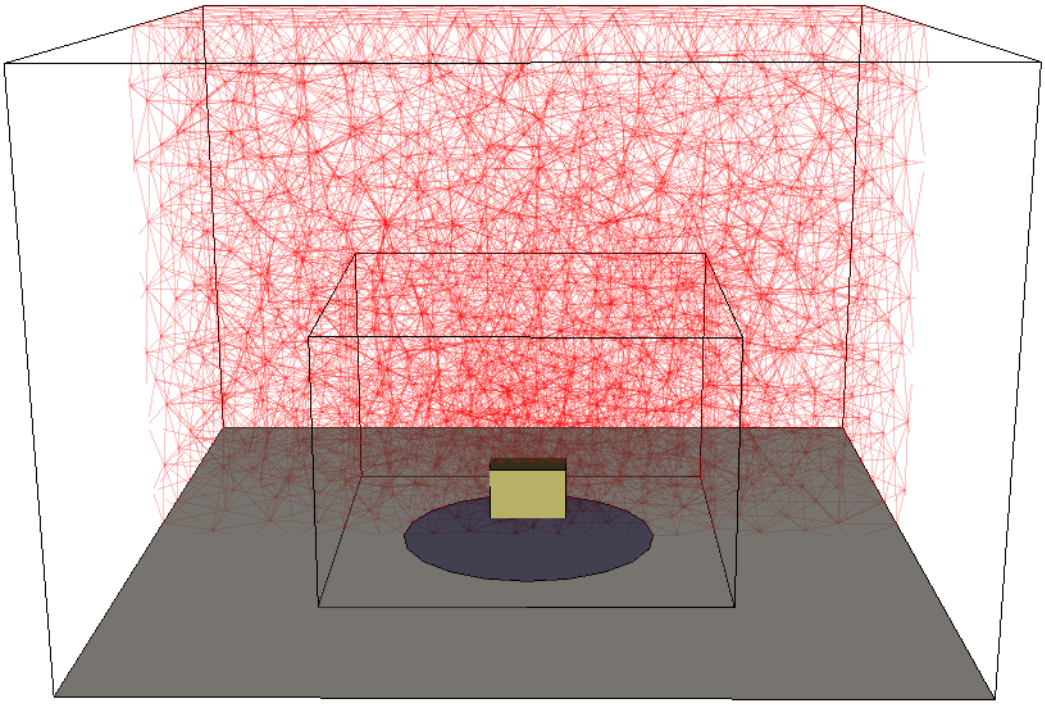

Figure 7.2: 3-D view of the lunar rover and the simulation domain.

model the SEV, no such attempt will be made for the reason that the focus of this work is to look at major dust movement around such vehicle. In this work, the vehicle is modelled as a rectangular box located in the middle of the simulation domain with the size given as $3\text{m} \times 1.5\text{m} \times 2\text{m}$ (LxWxH), and is placed 1 meter above the lunar surface. The simulation domain consists of an area of size $30\text{ m} \times 30\text{ m}$ with height of 20 meters.

7.2.1 Simulation profile

Dust particles are released from a circular area around the location of the rover as shown in Figure 7.2. For this simulation, a nested mesh method has been used to build the simulation domain, so that near the rover, in an area of $15\text{ m} \times 15\text{ m}$ with height of 10 meters, the length of each side of the tetrahedron that form a cell is limited to 1.5 meters, whilst outside this area th cell resolution is limited to 2.5 meters. The circular patch for dust release, the lander and the mesh design are shown in Figure 7.2.

The rover is constructed using material coated with indium titanium oxide (ITO). This highly conducting material allows the surface potential to be equally distributed over the surface. Each of the panels on the rover can be replaced with other type of materials such as solar panel and thermal coating depending on user's requirement.

A typical lunar plasma environment is chosen for this study, where $n_e \sim n_i = 10^7\,\mathrm{m}^3$ and $T_e \sim T_i = 10\,\mathrm{eV}$ [Colwell et al., 2007]. Simulation is performed over the near terminator region and over the dayside region. In the simulations, both the lunar and the rover surfaces are allowed to be charged to equilibrium level before any dust particle is introduced. Simulation period varies according to the regions, to ensure accurate depiction of the plasma and dust motion. It is also assumed that no dust charging process takes place after the dust leave the surface.

Terminator region

The time step employed in SPIS-dust is set to dynamic mode where, at the beginning of the simulation, is set to a fraction of plasma frequency ($\omega_{pe} \sim 5.66\,\mathrm{ms}^{-1}$). Taking the time step to be approximately 0.1Ω, where $\Omega = 1/\omega_{pe}$, the initial time step of the simulation is set to $\Delta_t = 1 \times 10^{-7}\,\mathrm{s}^{-1}$. As the simulation approaches the equilibrium state, the simulation time step is increased gradually until $\Delta_t = 1 \times 10^{-4}\,\mathrm{s}$. Detailed explanation on time step arrangement in SPIS-dust can be found in Chapter 4. The dust motion is simulated with a time step of $\Delta_{t,d} = 1 \times 10^{-3}\,\mathrm{s}$ in a cell with minimum size of 0.5 m. Assuming maximum dust velocity of $500\,\mathrm{ms}^{-1}$, the dust motion can therefore be assumed to not cross more than 1 cell during each time step, thus ensuring the motion is adequately monitored. The assumption of dust size and velocity are based on results obtained in Chapter 6. The simulation is performed for 10 s.

The equilibrium state is achieved at roughly 1 ms into the simulation, where at equilibrium the lunar surface is charged to $\sim -57\,\mathrm{V}$ which is slightly around the estimate value given by [Colwell et al., 2007]. In the figure, the presence of rover

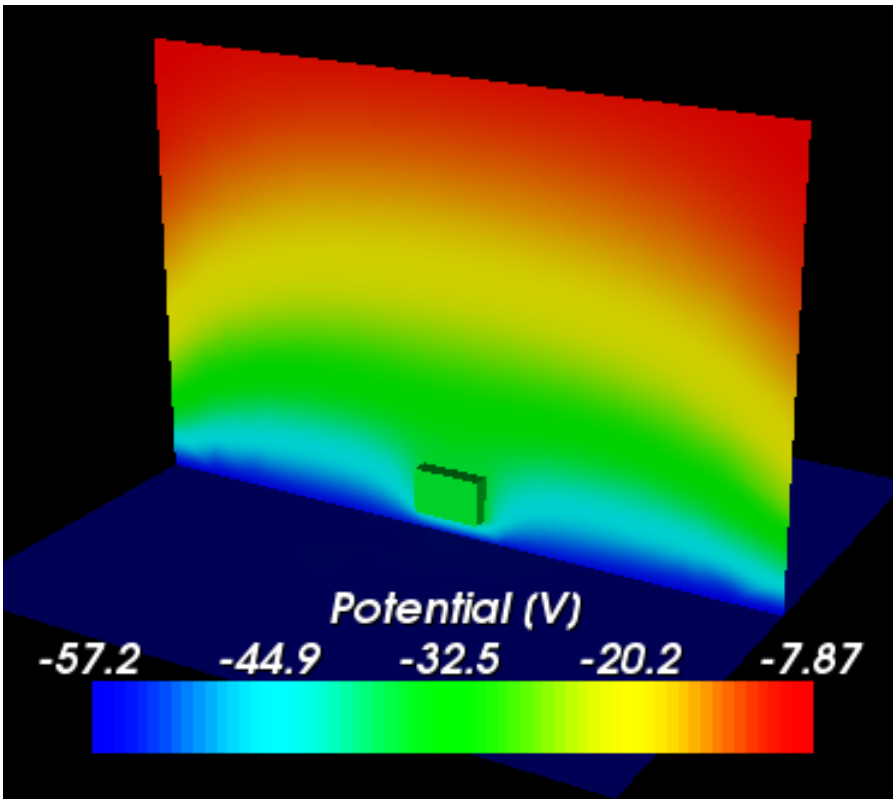

Figure 7.3: Potential of the lunar surface and the rover at $t = 0.001$ s. The rover is charged to around -32 V while the lunar surface is charged to around -57 V.

disturbs the lunar Debye sheath as the rover is charged to a potential of ~ -32 V. Since the rover surface is set to be made of conducting material, rover's surface potential is equally distributed over the rover's surface. Potential shown in the figure is taken at $t = 0.001$ s.

Dust particles are injected at approximately 5 ms, for a period of 0.1 s. 1000 dust superparticles are injected every 0.1 ms, which gives a total of 1,000,000 dust superparticles with superparticle's weight of 1. Using the assumption that other plasma processes are stationary when compared to the dust motion, the dust movement take place at every 1 ms compared to actual plasma simulation time step of 0.1ms. The dust particles are injected based on the lunar surface potential. In this simulation, the dust charge q_d ranges from the $q_{d,min}$ to $q_{d,max}$, where

$$q_{d,min}E > g_L m_d \tag{7.1}$$

and

$$q_{d,max} < \phi_s C \tag{7.2}$$

where $g_L, \phi_s and C$ are lunar gravitational acceleration, lunar surface potential and grain capacitance respectively. The dust particles radii are varied between 10 nm and 1 μm, which gives broad range of charge and mass distribution.

Figure 7.4 shows a sequence of figures of the simulation volume with the dust motion around the rover. The black box indicates the position of the rover. In Figure 7.4a and Figure 7.4a, dust particles are seen to be making their way upwards, where their paths are being obstructed by the rover. In Figure 7.4c and Figure 7.4d, dust particles reoccupy the void above the rover and continue their motion upwards. More dust particles are directed towards the space directly above the rover, which is shown by the triangular shape region in Figure 7.4e and Figure 7.4f.

Dayside region

A similar simulation is performed at the dayside region. Solar wind and solar UV flux is set to an incidence angle of 0^o from normal. Time step for the simulation is set to 1×10^{-6} s due to the presence of photoelectrons requires a higher time resolution. There are two photoelectron sources, one coming from the lunar surface and the other from the rover surface. Photoelectrons from the lunar surface are emitted with narrowed Maxwellian energy distribution from Feuerbacher et al. [1972] while the ones from the rover surface are emitted with the normal Maxwellian energy distribution. Figure 7.5 illustrates the plasma and surface potential obtained from the simulation.

The simulation indicates that lunar surface is to get charged to ~ 6 V while the rover surface is charged to ~ 3 V. The lunar surface potential in this case is slightly higher than the nominal value of 5 V due to the fact that the smaller simulation domain reduces the particle injection accuracy. One obvious observation from the simulation is the lack of disturbance on the lunar surface Debye sheath. In

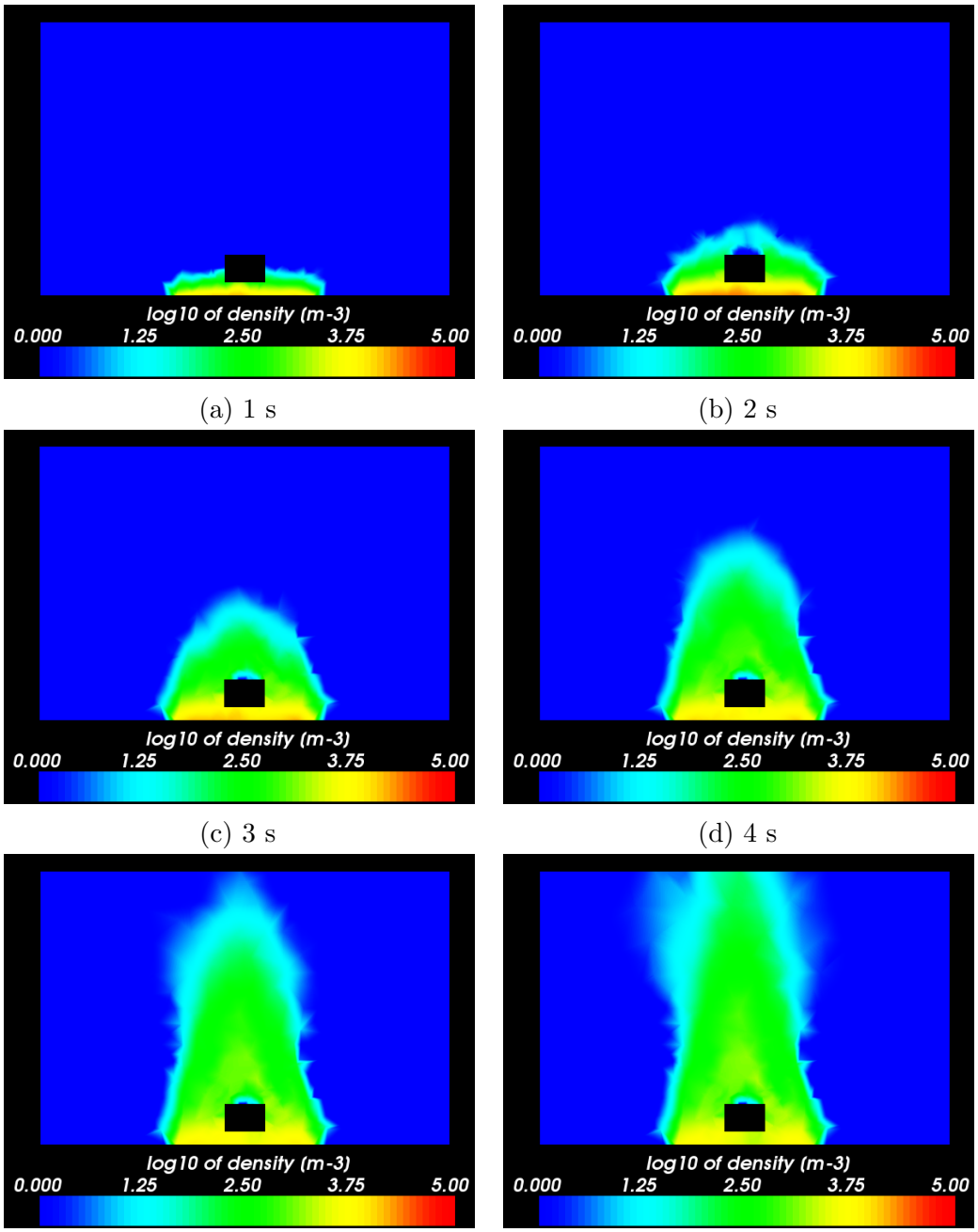

(a) 1 s (b) 2 s

(c) 3 s (d) 4 s

(e) 5 s (f) 6 s

Figure 7.4: Dust motion near the terminator region when a rover is present for the first 6 s. The rover is completely engulfed by the dust particle with a high dust concentration can be observed directly above the rover.

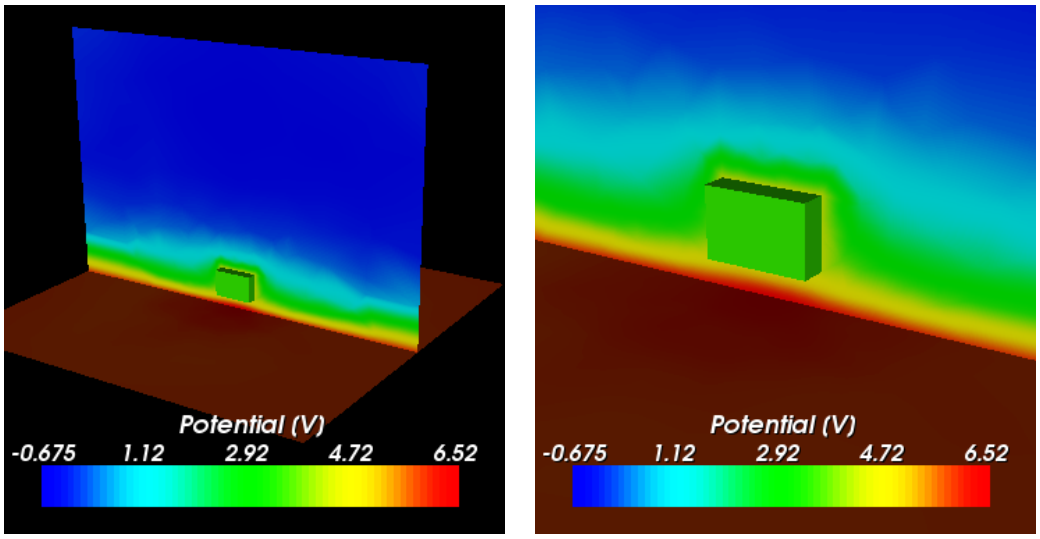

(a) Surface and plasma potential. (b) close up view

Figure 7.5: Plasma and surface potential on the rover and lunar surface during dayside. Also visible is Debye sheaths on both lunar surface and rover surface.

addition, the surface just under the rover is charged to slightly higher potential than the surrounding due to solar wind being obstructed by the rover.

The dust integration duration is retained at 1 ms, and dust particles are released from the surface at 0.1 ms when the surface is in equilibrium state. 1000 dust superparticles are released at every 1 μs for a period 0.1 ms, producing 100,000 particles over the 0.1 ms period. The dust superparticles size range between 10 nm and 1 μm and each superparticle has a number of charge between $q_{d,min}$ and $q_{d,max}$. Simulation is performed for a period of 20 s. The motion of the dust particles are shown in Figure 7.5. Due to the lower electric field on the surface compared to the terminator region, the time it takes for the particles to reach the bottom of the rover is more than 4s.

The rover acts as a complete obstacle to the dust particles streaming upwards, blocking dust particles which present on the surface underneath the rover. The result is different from the one in the terminator region where in this case, dust particles appear to create a funnel with the rover located at the centre. This is illustrated in Figure 7.7. In the figure, dust density is shown by the cell's mesh and surface. Almost no dust particles are observed above the rover, in contrast to the rover in the terminator where the particles appear to be attracted into the

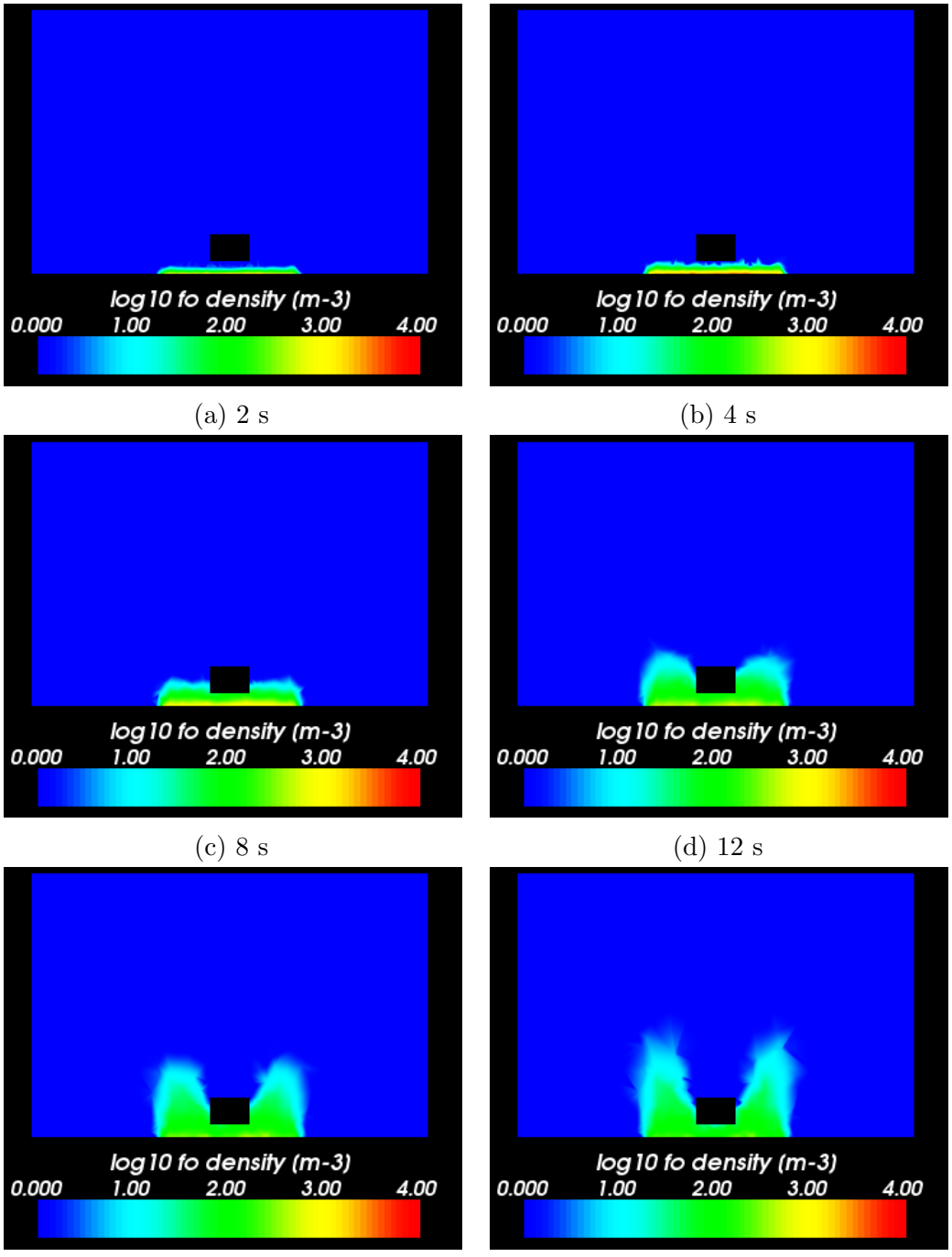

(a) 2 s (b) 4 s

(c) 8 s (d) 12 s

(e) 16 s (f) 20 s

Figure 7.6: Dust motion near the in the dayside region when a rover is present. The dust motion is slower compared to the terminator region because of the low surface potential means smaller electrostatic force, hence less acceleration on the particles. The rover forms an obstacle to the dust motion, and in 3-dimension is similar to a funnel with the rover sits in the middle.

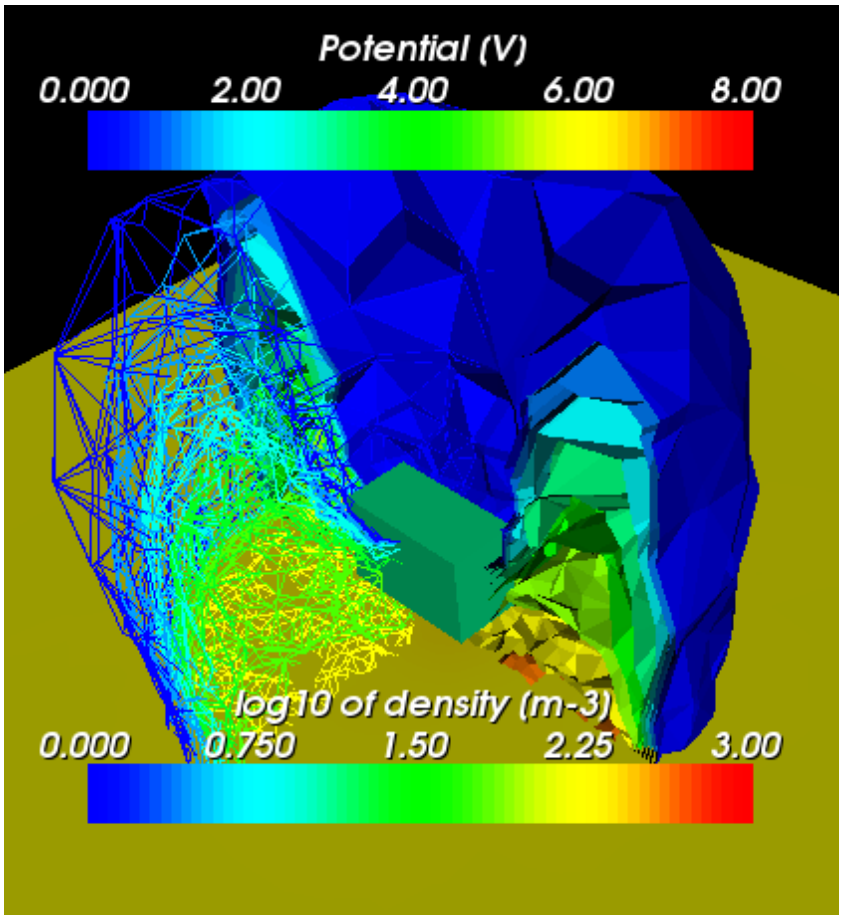

Figure 7.7: The rover blocks the levitated dust particle and forms a funnel on top of itself. Almost no particles are observed over the surface. The mesh and the cell surface shows the gradient of dust density (bottom scale). High dust density close to the ground and reduces with altitude.

top of the rover. In this case, particles seem to be pushed out by the rover surface electric field.

7.3 Conclusion

In this chapter, two simulations of rover near lunar surface have been carried out. In the first simulation, the rover is placed in the terminator region while in the second simulation, the rover is placed in the dayside region. Dust particles in the terminator region travel at higher speed than the one in the dayside due to the high surface electric field available near the terminator. Surface electric field comes from the lunar surface potential, where in the terminator region, is charged to higher negative potential due to lack of solar wind ions and solar UV flux. Near

the terminator, ion's flow is almost parallel to the surface which gives less ion current than on a surface in the dayside where ion's flow is normal to the surface. On the dayside, the presence of photoelectrons either from the surface or from the lander/rover contribute highly to the surface potential. Photoelectrons from the rover/lander are normally represented using Maxwellian energy distribution while the photoelectrons from lunar surface has energy distribution narrower than the Maxwellian. As a result there will be two different photoelectrons population, one coming from the surface and the other from the lander/rover which alters the potential around the surface. In both cases, absolute potential on the conducting rover is less than the one found on the surface.

The impact of photoelectrons collection by dust particles are not simulated in order to reduce the simulation's computational needs. Since dust particles are emitted from a positively charged surface will attract electrons, which in this case are the low energy photoelectrons. This interaction reduces the dust charge number on the positively charged dust particles, which would mean smaller electrostatic force acting on the dust particles.

Dust particles are introduced into the simulation over a period of time, when both the surface and the rover have achieved equilibrium potential. In both cases, the dust particles travel upwards, exceeding the rover's height, but results suggest that they move in different directions. In the terminator, the dust regroup in the space above the rover while on the dayside, the particles are pushed outwards. Both sets of dust samples are charged to the same polarity as the lunar and rover surface, therefore dust particles are expected to travel in the same direction. On the terminator region, the presence of dust in the void above the the rover's surface is more likely due to returning dust particles. On this occasion, dust particles travel upwards and inwards above the rover. Initially a void region of dust was created but was later filled by lunar-bound dust particles.

The result of the simulation of dust motion near a SEV suggests that a structure such as a rover might collect a lot of dust originating from nearby surface. This

process is more likely to happen if the vehicle is located in the terminator region and dust particles are negatively charged, and is less likely to happen in the dayside region as the particles are pushed outward. As the dust is being deposited on the top of the rover/lander, it is preferable to have a structure that allows natural dust movement towards the ground surface such dome-shaped structure which would result in less maintenance.

In conclusion, the motion of dust particles near a charged object above lunar surface has been simulated. These results are first attempts to model the dust motion around an SEV on lunar surface using SPIS-dust. Results suggest that dust motion are different for dayside and terminator environment.

Chapter 8

Conclusion and Future Works

Works presented in this thesis were motivated by the need to have a clear understanding of the role of dust particles in space, in particular near spacecraft or planetary exploration vehicle. Dust particles have been observed to be present in almost all space environment, such as in the ionosphere, interplanetary space and large celestial bodies. These 'fine' particles are present either by natural occurrences or due to human activities which can cause significant problems to space mission.

Dust particles are charged when exposed to space plasma and solar UV flux which is believed to be the reason for many of the space observations reported in the literature. The charging processes caused by ambient space plasma, photoemission and secondary emission have been investigated and explained by many authors (see Whipple [1981], Goertz [1989] and references herein). Some of these theoretical work can be implemented in computer model in order to have a fair amount of knowledge of the dust behaviour in space. The orbital motion limited theory (OML) has been implemented into a plasma simulation software, Spacecraft Plasma Interaction Software (SPIS). The SPIS capability in simulating spacecraft-plasma simulation has been complemented by the introduction of dust simulation module which covers important aspect of dust-plasma simulation such as dust charging and dust dynamics.

The particle-in-cell (PIC) technique use by SPIS has been extended to include Monte Carlo collision (MCC) algorithm. In this case, a multi-step MCC is used to

provide the tool for dust charging mechanism. Multi-step MCC allows variation in the charging rate of each individual dust samples, which is largely dependent on the dust instantaneous potential. This is an important requirement in dust charging process as individual particle could vary in size and potential, and therefore could hold different number of charges at any instantaneous moment.

The first task was to verify the suitability of SPIS to handle dynamic dust particles where their mass, charge and radius could be varied as compared to ordinary elementary particles such as electron and ion. The work was then proceeded with the implementation of PIC-MCC into SPIS, as well as handling of the dust dynamics in SPIS simulation environment. Simulations have been performed to validate the dust charging process for two different scenarios; an isolated dust and an ensemble of dust. In the first scenario, the charging process of a single dust particle has been compared to the theoretical result obtained using the Orbital Motion Limited (OML) theory. In the second scenario, the result is compared to the theoretical work by Havnes et al. [1990]. In both occasions, results showed good agreement between the theoretical work and simulation. Simulations were also performed to study the plasma behaviours near charged surface in the presence of dust particles. The result showed that dust cloud affects plasma equilibrium condition and is responsible to a change in surface potential. All results have been presented in Chapter 5.

The SPIS-dust software was then used to simulate the lunar surface charging. Lunar surface has been acknowledged to be made of thick layer of dust which have been observed to form what is known as lunar dusty exosphere. The lunar surface is charged in the same fashion as a probe immersed in plasma, and this charging process is believed to provide suitable environment for dust levitation process. A new material model that represent the lunar surface was first introduced in SPIS. The lunar material model was designed based on the observations and experimental data which were obtained from previous lunar missions. One important findings was the lunar surface photoelectrons yield which was found to have a much narrow

energy distribution than Maxwellian distribution, and this property in particular has profound effect on lunar surface potential. Simulation performed using SPIS showed that the different photoelectron model produces a large difference in surface potential, with the Maxwellian model estimation of surface potential is almost twice the nominal value presented in previous work. The photoelectron model based on the narrowed Maxwellian energy distribution has been developed and used in the simulation and result obtained was in good agreement with past observation. The model was then used to investigate the surface charging at various solar wind and solar UV flux incidence angle. The effect of lunar surface topology such as crater and boulder were also simulated using the lunar module in SPIS. It was found that SPIS can adequately model the lunar surface charging process with results being in good agreement with previous lunar charging model and observations. All results were presented in Chapter 6.

The SPIS-lunar was used to investigate dust dynamics on lunar surface. Dust particles were introduced to the simulation which originated from the lunar surface and their dynamics were simulated. These particles are varied in size and charge number which was based on limited observational data. Simulations were performed for dust particles in the terminator region. The particles maximum levitation height were found to be directly proportional to the particles' charge-over-mass ratio (q_d/m) with $q_d/m > 0.6$ to be the minimum value for levitation. Further simulations were performed to investigate dust motion near lunar's crater. It was found that the electric field developed from the charging of the surface causes dust originating from around the crater to be deposited inside the crater on the dayside and pushed away when the crater is near the terminator region. Simulation results were presented in Chapter 6.

In the final set of simulations, the dynamics of lunar dust near a simple conducting lunar exploratory vehicle were investigated. Simulations were performed for two different lunar regions, the terminator and dayside regions. Results showed two different observations; the dust particles appear to engulf the rover in terminator

but move outward from the rover in the dayside as they make their way upward. Simulation results for these observation have been presented in Chapter 7.

PIC-MCC modelling requires a number of particles present in a cell for it to be accurate. The dust charging process introduced in Chapter 5 uses dust-centered cell for collision determination, in order to have sufficient number of particles for the process. Future code development to increase efficiency can include technique such as particle rezoning to address this issue. This technique involves superparticle weight reassignment procedure, where superparticles number in each of the variable sized cell are maintained at a certain number by combining or splitting superparticles in the cell. This method would allows not only better plasma resolution but enable simulation to be performed over a large domain.

The plasma model presented in this work can be further improved in order to have a perfect representation of the lunar dusty plasma environment. One particular area of concern is the representation of plasma energy distribution function. It has been assumed that space plasma can be represented in the simulation by Maxwellian or bi-Maxwellian energy distribution during solar energetic particle event, which is true if the simulation is performed over a domain of size of several Debye length. In the case of simulating plasma environment near large celestial body, the potential developed by the body from charging process has been found to alter the energy and particle distributions. It is therefore important to have the instantaneous plasma distribution to be accurately modelled as it could have an affect on the outcome of the simulation. In addition, introduction of specific plasma distribution such as kappa distribution in SPIS would allow simulation to be performed in the nightside of the moon, where depleted ion density and high energy electrons are the major plasma constituents. A future work into this particular issue is recommended.

The dust dynamics simulated in this work only took into accounts two major forces on the lunar surface, gravitational and electrostatic force. Dust motion are affected by other forces such as magnetostatic force (Lorentz force) and radiation

pressure that could alter the motion of the particles. Lunar surface has been found to have magnetic anomaly regions, where localized magnetic field has been discovered. Introduction of magnetic anomalies requires more work on the magnetic field modelling to be implemented in SPIS for future simulations.

And finally, more simulations can be performed to study the dust motion around a lander or space exploration vehicle. Also, further simulations covering a larger space of the lunar surface can provide more detailed explanation of lunar dust exosphere and provide a good foundation for future lunar exploration mission.

Bibliography

Allen, J. E. . Probe theory - the orbital motion approach. *Physica Scripta*, 497--, 1992.

Allen, J. E., B. M. Annaratone and U. De Angelis. On the orbital motion limited theory for a small body at floating potential in a Maxwellian plasma. *Journal of Plasma Physics*, 63:299--309, 2000.

Al'pert, Ya. L.. *The Near-Earth and Interplanetary Plasma*, vol 1 and vol 2. Cambridge University Press, 1983.

Anuar, A.K., F. Honary, M. Hapgood and J.-F. Roussel 3-Dimensional simulation of dust charging and dusty plasma using SPIS *J. Geophys. Res., in review.*

Baker, D. N. , S. Kanekal, J. B. Blake, B. Klecker, and G. Rostoker. Satellite anomalies linked to electron increase in the magnetosphere. *Eos, Transactions American Geophysical Union*, 75 (35): 401--405, 1994.

Baker, D. N.. Satellite anomalies due to space storms. In I.A. Daglis, editor, *Space Storms and Space Weather Hazards*, volume 38 of *NATO Science Series*, 285--311. Springer Netherlands, 2001.

Barnes, M. S., J. H. Keller, J. C. Forster, J. A. ONeill and D. K. Coultas. Transport of dust particles in glow-discharge plasmas. *Phys. Rev. Lett.*, 68(3):313--316, 1992.

Berg, O., H. Wolf, and J. Rhee. Lunar soil movement registered by the Apollo 17 cosmic dust experiment. *Interplanetary dust and zodiacal light*, 233--237, 1976.

Berg, O., F. F. Richardson, and H. Burton. Lunar ejecta and meteorites experiment. In *Apollo 17: Preliminary Science Report*, 330:16, 1973.

Bernstein, I. B. and I. N. Rabinowitz Theory of Electrostatic Probes in a Low-Density Plasma *Physics of Fluids*, 2:112, 1959.

Biermann, L. Kometenschweife und solare korpuskularstrahlung. *Zeitschrift fur Astrophysik*, 29:274, 1951.

Birdsall, C. K. Particle-in-cell charged-particle simulations, plus monte carlo collisions with neutral atoms, PIC-MCC. *Plasma Science, IEEE Transactions on*, 19(2):65--85, April 1991.

Birdsall, C. K. and A. B. Langdon *Plasma Physics via Computer Simulation* Taylor & Francis Group, 2005.

Borisov, N. and U. Mall. Charging and motion of dust grains near the terminator of the moon. *Planet. Space Sci.*, 54(6):572--580, 2006.

Brieda, L., A. Barrie, D. Hughes, and T. Errigo. Analysis of particulate contamination during launch of the MMS mission. In *Proceedings of SPIE- The International Society for Optical Engineering*, volume 7794. SPIE, P. O. BOX 10 Bellingham WA 98227-0010 USA, 2010.

Burger, P. Elastic collisions in simulating one-dimensional plasma diodes on the computer. *Physics of Fluids*, 10(3):658--666, 1967.

Butcher, .J. C. Implicit Runge-Kutta processes *Math. Comp*, 18:50--64, 1964.

Carrington, R. C. Description of a Singular Appearance seen in the Sun on September 1, 1859. *Monthly Notices of the Royal Astronomical Society*, 20: 13--15, November 1859.

Castellanos, A. The relationship between attractive interparticle forces and bulk behaviour in dry and uncharged fine powders. *Advances in Physics*, 54 (4): 263--376, 2005.

Chapman, S. and V. C. A. Ferraro. A new theory of magnetic storms. *Terrestrial Magnetism and Atmospheric Electricity (Journal of Geophysical Research)*, 36: 171--186, 1931.

Chen, F. F. Electric probes. In R H Huddlestone and S L Leonard, editors, *Plasma Diagnostic Techniques*, Academic Press, New York, 1965.

Chen, F. F. and M. A. Lieberman. *Introduction to plasma physics and controlled fusion*, Plenum Press, New York, 1984.

Cho, J. Y. N. and M. C. Kelley. Polar mesosphere summer radar echoes: Observations and current theories. *Rev. Geophys.*, 31(3):243--265, 1993.

Chow, V. W., D. A. Mendis, and M. Rosenberg. Role of grain size and particle velocity distribution in secondary electron emission in space plasmas. *J. Geophys. Res.*, 98 (A11): 19065--19076, 1993.

Christoffoersen, R., J. F. Lindsay, S. K. Noble, M. A. Meador, J. J. Kosmo, J. A. Lawrence, L. Brostoff, A. Young and T. McCue Lunar Dust Effects on Spacesuit Systems: Insight from Apollo Spacesuits NASA/TP-2009-214786, Johnson Space Center, Houston, Texas, 2009.

Collier, .M. R., H. K. Hills, T. J. Stubbs, J. S. Halekas, G. T. Delory, J. Epsley, W. M. Farrell, J. W. Freeman, R. Vondrak Lunar surface electric potential changes associated with traversals the Earth's foreshock. *Planet. Space Sci.*,59(14):1727:1743, 2011.

Collier, .M. R., W. M. Farrell, and T. J. Stubbs. The lunar dust pendulum *J. Adv. Space Res.*, 2012.

Colwell, J. E., A. A.S. Gulbis, M. Horányi, and S. Robertson. Dust transport in photoelectron layers and the formation of dust ponds on eros. *Icarus*, 175(1):159--169, 2005.

Colwell, J. E., S. Batiste, M. Horányi, S. Robertson, and S. Sture. Lunar surface: Dust dynamics and regolith mechanics. *Rev. Geophys.*, 45(2): RG2006--, June 2007.

Criswell, D. R. Horizon-glow and motion of lunar dust. *Proc. Lunar and Planet. Sci. Conf. 3rd*, 163, 1972.

Cui, C., and J. Goree. Fluctuations of the charge on a dust grain in a plasma. *Plasma Science, IEEE Transactions on*, 22(2):151 --158, Apr. 1994.

de Angelis, U. The physics of Dusty Plasma *Physica Scripta*, 45(5):465, 1992.

Debye, P. and E. Hückel. De la theorie des electrolytes. i. abaissement du point de congelation et phenomenes associes. *Physikalische Zeitschrift*, 24(9):185--206, 1923.

DeForest, S. E. Spacecraft charging at synchronous orbit. *J. Geophys. Res.*, 77:651--659, 1972.

Ebert, R. W., D. J. McComas, H. A. Elliott, R. J. Forsyth, and J, T Gosling. Bulk properties of the slow and fast solar wind and interplanetary coronal mass ejections measured by Ulysses: Three polar orbits of observations. *J. Geophys. Res.*, 114(A1): A01109, 2009.

Epstein, P. S. On the resistance experienced by spheres in their motion through gases. *Phys. Rev.*, 23: 710--733, Jun 1924.

Farrell, W. M, T. J. Stubbs, R. R. Vondrak, G. T. Delory, J. S. Halekas. Complex electric fields near the lunar terminator: The near-surface wake and accelerated dust. *Geophys. Res. Lett*, 34(14):14, 2007.

Farrell, W. M, T. J. Stubbs, J. S. Halekas, G. T Delory, M. R. Collier, R. R. Vondrak, and R. P. Lin. Loss of solar wind plasma neutrality and affect on surface potentials near the lunar terminator and shadowed polar regions. *Geophys. Res. Lett*, 35(5):L05105, 2008.

Feldman, U., E. Landi, and N. A. Schwadron. On the sources of fast and slow solar wind. *J. Geophys. Res. (Space Physics)*, 110: A07109, July 2005.

Feuerbacher, B., M. Anderegg, B. Fitton, L. D. Laude, R. F. Willis, and R. J. L. Grard. Photoemission from lunar surface fines and the lunar photoelectron sheath. In A. E. Metzger, J. I. Trombka, L. E. Peterson, R. C. Reedy, and J. R. Arnold, editors, *Proc. Lunar and Planet. Sci. Conf.* , 3:2655, 1972.

Forest,F ., A. Hilgers, B. Thiebault, L. Eliasson, J.-J. Berthelier, and H. de Feraudy. An open-source spacecraft plasma interaction simulation code PicUp3D: Tests and validations. *Plasma Science, IEEE Transactions on*, 34(5):2103 --2113, 2006.

Fortov, V. E., A. G. Khrapak, S. A. Khrapak, V. I. Molotkov, and O. F. Petrov. Dusty plasmas. *Physics-Uspekhi*, 47(5):447--492, 2004.

Fortov, V. E., A. V. Ivlev, S. A. Khrapak, A. G. Khrapak, and G. E. Morfill. Complex (dusty) plasmas: Current status, open issues, perspectives. *Physics reports*, 421(1): 1--103, 2005.

Freeman, J. W. and M. Ibrahim. Lunar electric fields, surface potential and associated plasma sheaths. *Earth, Moon, and Planets*, 14 (1): 103--114, 1975.

Gaier, J. R. The effects of Lunar Dust on EVA Systems During the Apollo missions. *NASA/TM-2005-0213610*, Glenn Research Center, Cleveland, Ohio, 2005.

Garrett, H. B. and S. E. DeForest. An analytical simulation of the geosynchronous plasma environment. *Planet. Space Sci.*, 27: 1101--1109, 1979.

Garrett, H. B. and A. C. Whittlesey. Spacecraft charging, an update. *Plasma Science, IEEE Transactions on*, 28(6):2017--2028, 2000.

Gatsonis, N. A., R. E. Erlandson, and C. I. Meng. Simulation of dusty plasmas near surfaces in space. *J. Geophys. Res.*, 99(A5):8479--8489, 1994.

Geuzaine, C. and J-F. Remacle. Gmsh: a three-dimensional finite element mesh generator with built-in pre- and post-processing facilities. *International Journal For Numerical Methods in Engineering*, 79: 1309--1331, 2009.

Goertz, C. K. and W. H. Ip. Limitation of electrostatic charging of dust particles in a plasma. *Geophys. Res. Lett.*, 11(4):349--352, 1984.

Goertz, C. K. . Dusty plasma in the solar system. *Review of Geophysics*, 27:271--292, 1989.

Goodwin, R. *Apollo 17 NASA Mission Report*, 2002.

Goree, J. and Y. T. Chiu Dust contamination of the spacecraft environment by exposure to plasma. *Journal of Spacecraft and Rockets*, 30(6):765--767, 1993.

Grard, R. J. L., and J. K. E. Tunaley. Photoelectron sheath near a planar probe in interplanetary space. *J. Geophys. Res.*, 76(10):2498--2505, 1971.

Greenberg, P. S. Sensor development for the detection and characterization of lunar dust. *LPI Contributions*, 1287:41, 2005.

Grün, E., H. A. Zook, H. Fechtig, and R. H Giese. Collisional balance of the meteoritic complex. *Icarus*, 62(2):244--272, 1985.

Halekas, J. S., D. L. Mitchell, R. P. Lin, L. L. Hood, M. H. Acuña, and A. B. Binder. Evidence for negative charging of the lunar surface in shadow. *Geophys. Res. Lett.*, 29(10):1435--, May 2002.

Halekas, J. S. , R. P. Lin, and D. L. Mitchell. Large negative lunar surface potentials in sunlight and shadow. *Geophys. Res. Lett.*, 32(9):L09102--, May 2005.

Hamaker, H. C. The London van der Waals attraction between spherical particles. *Physica*, 4 (10): 1058--1072, 1937.

Hapgood, M. Modelling long-term trends in lunar exposure to the Earth's plasmasheet. *Annales Geophysicae*, 25(9):2037--2044, 2007.

Hartzell, C.M. and D.J. Scheeres. The role of cohesive forces in particle launching on the Moon and Asteroids. *Planet. Space Sci.*, 59(14):1758--1768, 2011.

Hastings, D. E and H. B. Garrett. *Spacecraft - Environment Interactions*. Cambridge University Press, 2004.

Havnes, O., C. K. Goertz, G. E. Morfill, E. Grűn, and W. Ip. Dust charges, cloud potential, and instabilities in a dust cloud embedded in a plasma. *J. Geophys. Res.*, 92:2281--2287, 1987.

Havnes, O., T. K. Asnesen, and F. Melandso. On dust charges and plasma potentials in a dusty plasma with dust size distribution. *J. Geophys. Res.*, 95:6581--6585, 1990.

Havnes, O., Næsheim, L. I., Hartquist, T. W, and Morfill,G. E., Melandsø, F., Schleicher, B., Trøim, J. , Blix, T. and Thrane, E. Meter-scale variations of the charge carried by mesospheric dust. *Planet. Space Sci.*, 44:1191--1194, 1996a.

Havnes, O., J. Trøim, T. Blix, W. Mortensen, L. I. Næsheim, E. Thrane, and T. Tønnesen. First detection of charged dust particles in the earth's mesosphere. *J. Geophys. Res.*, 101(A5):10839--10847, 1996b.

Heiken, G. H. *The Lunar Sourcebook: A user's guide to the Moon* Cambridge University Press, 1991.

Hockney, R. W. Computer simulation of anamolous plasma diffusion and numerical solution of Poisson's equation *Phys. Fluid*,9:1826--1835,1966.

Hockney, R. W. and J. W. Eastwood. *Computer simulation using particles*. Taylor & Francis Group, 1988.

Holsapple, K. A., The scaling of impact processes in planetary sciences. *Annu. Rev. Earth Planet. Sci.*, 21:333-373, 1993.

Horányi, M., B. Walch, S. Robertson, and D. Alexander. Electrostatic charging properties of apollo 17 lunar dust. *J. Geophys. Res.*, 103(E4):8575--8580, 1998.

Housen, K. R, R. M. Schmidt, and K. A. Holsapple. Crater ejecta scaling laws-fundamental forms based on dimensional analysis. *J. Geophys. Res.*, 88(B3):2485--2499, 1983.

Hsu, H.W, H. Krüger, and F. Postberg. Dynamics, Composition, and Origin of Jovian and Saturnian Dust-Stream Particles. *Nanodust in the Solar System: Discoveries and Interpretations.*,77--117, Springer Berlin Heidelberg, 2012.

Hutton, R. E. Lunar surface model. Technical report, National Aeronautics and Space Administration (NASA), 1969.

Jonker, J. L. H. On the theory of secondary electron emission. *Philips Res. Rep.*, 1952.

Katz,I., D.E. Parks, M.J. Mandell, J.M. Harvey, S.S. Wang, and J.C. Roche. Nascap, a three-dimensional charging analyzer program for complex spacecraft. *Nuclear Science, IEEE Transactions on*, 24(6):2276--2280, 1977.

Khrapak, S. A., A. V. Ivlev, G. E. Morfill,and H. M. Thomas. Ion drag force in complex plasmas *Phys. Rev. E*, 66(4):046414, 2002.

Khrapak, S. A., A. V. Ivlev, G. E. Morfill, and S. K. Zhdanov. Scattering in the attractive yukawa potential in the limit of strong interaction. *Phys. Rev. Lett.*, 90:225002, Jun 2003.

Kivelson, M. G. and C. T. Russell, editors. *Introduction to Space Plasma*. Cambridge University Press, 1995.

Koons, H. C. Summary of environmentally induced electrical discharges on the P 78--2 (SCATHA) satellite. *Journal of Spacecraft and Rockets(ISSN 0022-4560)*, 20: 425--431, 1983.

Kuntz,K. D , M.R. Collier, T.J. Stubbs, and W.M. Farrell. The lunar dust pendulum. In *AGU Fall Meeting Abstracts*, volume 1, page 1710, 2011.

Lai, S. T. and M. F. Tautz. Aspects of spacecraft charging in sunlight. *Plasma Science, IEEE Transactions on*, 34:2053--2061--, 2006.

Lam, H. L. , D. H. Boteler, B. Burlton, and J. Evans. Anik-E1 and E2 satellite failures of January 1994 revisited. *Space Weather*, 10: S10003--, October 2012.

Langmuir, I. and K. B. Blodgett. Currents limited by space charge between concentric spheres. *Phys. Rev.*, 24 (1): 49--59, Jul 1924.

Mandell, M.J. , V.A. Davis, D.L. Cooke, A.T. Wheelock, and CJ Roth. Nascap-2k spacecraft charging code overview. *Plasma Science, IEEE Transactions on*, 34(5):2084--2093, 2006.

Manka, R. H. Plasma and Potential at the Lunar Surface. In R. J. L. Grard, editor, *Photon and Particle Interactions with Surfaces in Space*, of *Astrophysics and Space Science Library*, 37:347, 1973.

McCoy, J. E., D. R. Criswell Evidence for a high altitude distribution of lunar dust *Proc. Lunar Planet. Sci. Conf. 24th*,1033--1034, 1974.

McComas, D. J., D. Alexashov, M. Bzowski, H. Fahr, J. Heerikhuisen, V. Izmodenov, M. A. Lee, E. Mbius, N. Pogorelov, N. A. Schwadron, and G. P. Zank. The heliospheres interstellar interaction: No bow shock. *Science*, 336(6086): 1291--1293, 2012.

McPherson, D. A. , R. W. Schober, and A. (editor) Rosen. Spacecraft charging athigh altitudes: The SCATHA satellite program. *Progress in Astronautics and Aeronautics, MIT Press*, 47, 1976.

Mendis, D. A., H. L. F. Houpis, and J. R. Hill. The gravito-electrodynamics of charged dust in planetary magnetospheres. *J. Geophys. Res.*, 87(A5):3449--3455, 1982.

Meyer-Vernet, N. Flip-flop of electric potential of dust grains in space. *Astronomy and Astrophysics*, 105:98--106, January 1982.

Muranaka, T., S. Hosoda, J.H. Kim, S. Hatta, K. Ikeda, T. Hamanaga, M. Cho, H. Usui, H.O. Ueda, K. Koga, et al. Development of multi-utility spacecraft charging analysis tool (MUSCAT). *Plasma Science, IEEE Transactions on*, 36(5):2336--2349, 2008.

Murphy, D. L. and Y. T. Chiu Dusty plasmas in the vicinity of a large dielectric object in space *J. Geophys. Res.*, 96:11291--11305, 1991.

NASA. Nasa voyager 1 encounters new region in deep space, December 2012. URL `http://www.jpl.nasa.gov/news/news.php?release=2012-381`.

Nesvorný, D., P. Jenniskens, H. F. Levison, W. F. Bottke, D. Vokrouhlický, and M. Gounelle. *Cometary origin of the zodiacal cloud and carbonaceous micrometeorites. Implications for hot debris disks.* The Astrophysical Journal, 713(2):816, 2010.

Northrop, T. G. Dusty plasmas. *Physica Scripta*, 45(5):475, 1992.

Northrop, T. G. and T. J. Birmingham. Plasma drag on a dust grain due to coulomb collisions. *Planet. Space Sci.*, 38(3):319--326, 1990.

Parker, E.N. Dynamics of the interplanetary gas and magnetic fields. *The Astrophysical Journal*, 128:664, 1958.

Parker, E.N. Interaction of the solar wind with the geomagnetic field. *Physics of Fluids*, 1:171, 1958.

Pelizzari, Michael A., and D. R. Criswell. Lunar dust transport by photoelectric charging at sunset. *Proc. Lunar and Planet. Sci. Conf. 9th*, 3225--3237, 1978.

Perko, H. A., J.D. Nelson, and W.Z. Sadeh. Surface cleanliness effect on lunar soil shear strength. *Journal of geotechnical and geoenvironmental engineering*, 127(4):371--383, 2001.

Peucker-Ehrenbrink, B., and B. Schmitz. *Accretion of Extraterrestrial Matter Throughout Earth's History.* Springer , 2001.

Phillips, J. L., S. J. Bame, A. Barnes, B. L. Barraclough, W. C. Feldman, B. E. Goldstein, J. T. Gosling. Ulysses solar wind plasma observations from pole to pole. *Geophys. Res. Lett.*, 22(23):3301--3304, 1995.

Poppe, A. and M. Horányi. Simulations of the photoelectron sheath and dust levitation on the lunar surface. *J. Geophys. Res*, 115:A08106, 2010.

Prolss, G. W. . *Physics of the Earth's space environment: An introduction*. Springer, 2004.

Purvis, C. K. , H. B. Garrett, A. C. Whittlesey, and N. J. Stevens. Design guidelines for assessing and controlling spacecraft charging effects,NASA TP-2361. Technical report, NASA, 1984.

Rennilson, J. J., and D.R. Criswell. Surveyor observations of lunar horizon-glow. *Earth, Moon, and Planets*, 10(2):121--142, 1974.

Robinson, P., P. Leung, J. Feynman, S. Gabriel, R. Wuerker, A. Wong, E. Seale, and O. Short. Observation and impact of dust particles on the Magellan mission to Venus. In R. Erlandson and C. I. Meng, editors, *Vehicle-Environment Interactions Conference*, volume 155. Applied Physics Laboratory, The Johns Hopkins University, 1991.

Robinson, P. A. Jr and P. Coakley. Spacecraft charging-progress in the study of dielectrics and plasmas. *Electrical Insulation, IEEE Transactions on*, 27(5): 944--960, 1992.

Rognon, P. G. , J.N. Roux, M. Naaim, F. Chevoir, et al. Dense flows of cohesive granular materials. *Journal of Fluid Mechanics*, 596:21, 2008.

Romanelli, M. J. Runge-Kutta methods for the solution of ordinary differential equations *Mathematical methods for digital computers*, 1:110--120, 1960.

Rosen, A. Spacecraft charging by magnetospheric plasmas. *Nuclear Science, IEEE Transactions on*, 23(6): 1762--1768, 1976.

Rosenberg, M. and DA Mendis. Use of uv to reduce particle trapping in process plasmas. *Plasma Science, IEEE Transactions on*, 24(3):1133--1136, 1996.

Rostoker, G. Commentary on the anik satellite upsets. *Report to Telesat Canada, Canadian Network for Space Research Report*, 1994.

Roussel, J.-F. , F. Rogier, G. Dufour, J.-C. Mateo-Velez, J. Forest, A. Hilgers, D. Rodgers, L. Girard, and D. Payan. SPIS open-source code: Methods, capabilities, achievements, and prospects. *Plasma Science, IEEE Transactions on*, 36(5):2360--2368, Oct. 2008.

Schwenn, R. *Physics of the Inner Heliosphere I,2.* Springer, 1990.

Shaw, R. R., J. E. Nanevicz, and R. C. Adamo. Observations of electrical discharges caused by differential satellite-charging. *Spacecraft charging by magnetospheric plasmas*, p. 61--76, 1976.

Shukla, P. K. Shielding of a slowly moving test charge in dusty plasmas *Physics of Plasmas*, 1(5):1362--1363, 1994.

Shukla, P. K. A survey of dusty plasma physics *Physics of Plasmas*, 8:1791,2001.

Shukla, P. K. and A. A. Mamun. *Introduction to Dusty Plasma Physics.* Institute of Physics, 2002.

Sickafoose, A. A. , J. E. Colwell, M. Horányi, and S. Robertson. Experimental investigations on photoelectric and triboelectric charging of dust. *J. Geophys. Res.*, 106:8343--8356, 2001.

Sickafoose, A. A. , J. E. Colwell, M. Horányi, and S. Robertson. Experimental levitation of dust grains in a plasma sheath. *J. Geophys. Res.*, 107(A11):1408, November 2002.

Singer, S.F. and E. H. Walker. Photoelectric screening of bodies in interplanetary space. *Icarus*, 1(1): 7--12, 1963.

Sternglass, E. J. Theory of secondary electron emission. *Sci. Rep. 1772*, 1954.

Sternovsky, Z., S. Robertson, A. Sickafoose, J. Colwell, and M. Horányi. Contact charging of lunar and martian dust simulants. *J. Geophys. Res.*, 107(E11): 5105--, November 2002.

Stubbs, T. J. , R. R. Vondrak, and W. M. Farrell. A dynamic fountain model for lunar dust. *Advances in Space Research*, 37(1):59--66, 2006.

Stubbs, T.J. , W. M. Farrell, J. S. Halekas, M. R. Collier, R. R. Vondrak, and G. T. Delory. The lunar dust-plasma environment. In *NASA, Berkeley, Lunar X-ray Observatory (LXO)/Magnetoseath Explorer (MagEX) meeting, Hilton Garden Inn*, 2007a.

Stubbs, T. J. ,R. R. Vondrak, and W. M. Farrell. Impact of dust on lunar exploration. URL `http://hefd. jsc. nasa. gov/files/StubbsImpactOnExploration`, 2007b.

Tu, C. Y. , C. Zhou, E. Marsch, L.D. Xia, L. Zhao, J.X. Wang, and K. Wilhelm. Solar wind origin in coronal funnels. *Science*, 308 (5721): 519--523, 2005b.

Tunaley, J. K. E. and J. Jones. The photoelectron sheath around a spherical body. *Photon and particle interactions with surfaces in space*, 59--71, 1973.

Violet, M. D. and A. R. Frederickson. Spacecraft anomalies on the CRRES satellite correlated with the environment and insulator samples. *Nuclear Science, IEEE Transactions on*, 40(6): 1512--1520, 1993.

Walbridge, E. Lunar photoelectron layer *J. Geophys. Res.*, 78(19):3668--3687, 1973.

Wang, X. , M. Horányi, and S. Robertson. Experiments on dust transport in plasma to investigate the origin of the lunar horizon glow *J. Geophys. Res.*,114.A5:A05103, 2009.

Whiddington, R. The transmission of cathode rays through matter *Proceedings of the Royal Society of London. Series A*, 86(588):360--370, 1912.

Whipple, E. C. Potentials of surfaces in space. *Reports on Progress in Physics*, 44(11): 1197, 1981.

Whipple, E. C., T. G. Northrop, and D. A. Mendis. The electrostatics of a dusty plasma. *J. Geophys. Res.*, 90:--, 1985.

Willis, R. F., M. Anderegg, B. Feuerbacher, and B. Fitton. Photoemission and Secondary Electron Emission from Lunar Surface Material. In R. J. L. Grard, editor, *Photon and Particle Interactions with Surfaces in Space*, *Astrophysics and Space Science Library*, 37:389, 1973.